

**Hybrid spin-nanomechanics
with single spins
in diamond mechanical oscillators**

Inauguraldissertation

zur
Erlangung der Würde eines Doktors der Philosophie
vorgelegt der
Philosophisch-Naturwissenschaftlichen Fakultät
der Universität Basel

von

ARNE BARFUSS

aus Marktredwitz, Deutschland

Basel, 2017

Originaldokument gespeichert auf dem Dokumentenserver der Universität Basel
<https://edoc.unibas.ch>



This work is licensed under a Creative Commons
Attribution-NonCommercial-NoDerivatives 4.0 International License.

The complete text may be reviewed here:

<http://creativecommons.org/licenses/by-nc-nd/4.0/>

Genehmigt von der Philosophisch-Naturwissenschaftlichen Fakultät
auf Antrag von
Prof. Dr. Patrick Maletinsky
Prof. Dr. Ania Bleszynski Jayich

Basel, den 14. November 2017

Prof. Dr. Martin Spiess
Dekan

Abstract

Hybrid spin-oscillator systems, formed by single spins coupled to mechanical oscillators, have attracted ever-increasing attention over the past few years, triggered largely by the prospect of employing such devices as high-performance nanoscale sensors or transducers in multi-qubit networks. Provided the spin-oscillator coupling is strong and robust, such systems can even serve as test-beds for studying macroscopic objects in the quantum regime. In this thesis we present a novel hybrid spin-oscillator system that consists of a diamond cantilever whose mechanical motion couples to the spin degree of freedom of embedded NV centers through crystal strain.

This thesis starts with a characterization of the coupling strength between NV spin and resonator motion. Static cantilever bending experiments reveal spin-strain coupling constants of several GHz per unit of strain, corresponding to a single phonon coupling strength $g_0 \approx \text{Hz}$. Although we demonstrate that our hybrid system resides deep in the resolved sideband regime, our current experimental conditions prevent bringing the diamond resonator to its motional ground state, since spin decoherence rate and mechanical heating rate exceed g_0 by several orders of magnitude. However, cooling the resonator, even to its motional ground state, is possible if cantilever dimensions are reduced to the nanometer scale and corresponding experiments are performed at cryogenic temperatures.

While spin-strain coupling is not favorable for such experiments in the quantum regime, it offers many other exciting features. In the second part of this thesis, we report on the implementation of a novel continuous decoupling scheme that protects the NV spin from environmental noise, increasing both Rabi oscillation decay time and inhomogeneous coherence time by two orders of magnitude. The remarkable coherence protection is explained by the robust, drift-free strain-coupling mechanism and the narrow linewidth of the high-quality diamond mechanical oscillators.

A major finding of this thesis is the demonstration of coherent spin manipulation with transverse AC strain fields, which is presented in the third part of this thesis. We show that AC strain driving not only addresses a magnetic dipole forbidden transition, but also allows working in the strong driving regime, in which the induced spin rotation frequency exceeds the initial spin splitting. Few systems have reached this regime, despite the appeal of studying dynamics beyond the rotating wave approximation. Additionally, continuous strain driving enhances the NVs spin coherence time by decoupling it from environmental magnetic noise. In the last part of this thesis, we combine coherent MW and strain spin driving to realize a three-level ∇ -system in the NV ground state by coherently addressing all three spin transitions. Our studies of the spin dynamics not only confirm the theoretical prediction that the global phase (i.e. the relative phase of the three driving fields) governs the occurring spin dynamics, but also that closed-contour driving shields the NV's spin from environmental noise without applying complicated decoupling

schemes. The corresponding decoupling mechanism is well explained by the effect of noise on the ∇ -system Hamiltonian. Based on our findings, we believe our closed-contour interaction scheme will have future applications in sensing and quantum information processing, for example as a phase sensor or as a test-bed for state transfer protocols.

Contents

Titel	a
Abstract	c
Contents	e
List of symbols and abbreviations	g
1. Introduction	1
2. The hybrid spin-oscillator system	5
2.1. Motivation	5
2.2. The Nitrogen-Vacancy center	6
2.2.1. Atomic and electronic structure	6
2.2.2. Optical properties under nonresonant excitation	12
2.3. The NV's response to external magnetic fields	14
2.3.1. DC magnetic fields	14
2.3.2. AC magnetic fields	15
2.3.3. Influence of environmental noise: Damping	21
2.3.4. Electron spin resonance	22
2.4. The NV's response to stress and strain	24
2.4.1. Strain coupling in $S=1$ ground and excited state	24
2.4.2. Quantifying strain and stress coupling	27
2.5. Strain and stress in cantilevers	33
2.5.1. Strain and stress under static bending	35
2.5.2. Strain and stress under external driving	40
2.6. Hybrid spin-oscillator systems in the quantum regime	44
2.6.1. Energy quantization of the harmonic oscillator	44
2.6.2. Bringing the resonator to its motional ground state	45
3. Characterizing spin-strain coupling	49
3.1. Experimental methods	49
3.1.1. Sample fabrication	49
3.1.2. Measurement techniques	53
3.2. Bending experiments	56
3.2.1. Static bending: characterization of strain coupling	56
3.2.2. AC bending: the resolved sideband regime	61
3.3. Conclusion and Outlook: the strong coupling regime	64
3.3.1. Status of our experiment	64
3.3.2. Approaches to reach the high cooperativity regime	65

4. Hybrid continuous dynamical decoupling	67
4.1. Motivation: Hybrid continuous dynamical decoupling	67
4.2. Experimental realization and NV characterization	68
4.3. A photon-phonon doubly-dressed spin	71
4.4. Coherence protection through double dressing	73
4.5. Conclusion	76
5. Strong mechanical driving of a single electron spin	77
5.1. Demonstration of coherent spin manipulation	77
5.1.1. Improvements to experimental setup	77
5.1.2. Mechanically induced Rabi oscillations	79
5.1.3. MW spectroscopy of the mechanically induced Autler-Townes effect	80
5.2. The strong driving regime	82
5.3. Protecting NV spin coherence by coherent strain driving	85
5.4. Summary and outlook	87
6. Phase-dependent spin dynamics under closed-contour interaction	89
6.1. Phase dependence of NV spin dynamics	90
6.2. Global driving phase for NV decoupling	93
6.3. Summary	97
6.4. Outlook	98
7. Summary and Outlook	103
7.1. Summary	103
7.2. Outlook	105
A. Appendix	109
A.1. Polarization dependence of microwave spin driving	109
A.2. Influence of NV coordinate system on spin-strain coupling Hamiltonian	110
A.3. Stress and strain coupling: How to include different NV orientations .	111
A.4. Notes on the harmonic oscillator	115
A.5. Characterizing spin-strain coupling in the NV S=1 ground state . . .	117
A.5.1. Simplified approach from Teissier <i>et al.</i> [1]	117
A.5.2. Characterizing spin-strain coupling - bending experiments . .	119
A.6. Frequency modulation with external driving	119
A.7. Single phonon coupling strength and mechanical Rabi frequency . . .	121
A.8. Strong mechanical driving: crossings and anti-crossings	123
A.9. Phase-dependent spin dynamics	126
A.9.1. Closed-contour Hamiltonian and time evolution	126
A.9.2. Creation of phase-locked driving fields	128
A.9.3. Analysis of environmental noise sources	129
A.10. Strain- and stress-coupling Hamiltonians for NV orientations NV1-NV4	138
B. Bibliography	I
Acknowledgement	XVII

List of symbols and abbreviations

General symbols:

t	time
T	environmental temperature
λ	optical wavelength
τ	spin evolution time
$\tau_{\pi/2}, \tau_{\pi}$	pulse lengths for $\pi/2$ - and π -pulses
ρ	density
S, I	total electron and nuclear spin
m_s, m_I	electron and nuclear spin quantum number

Coordinate systems:

x, y, z	NV coordinate system
$\tilde{x}, \tilde{y}, \tilde{z}$	cantilever coordinate system
X, Y, Z	crystal coordinate system

NV center::

^{14}N	nitrogen isotope
c_1, c_2, c_3, n	sp^3 atomic orbitals/dangling bonds
a'_1, a_1, e_x, e_y	molecular orbitals
$a_1^i e^i$	notation of molecular orbital electron population
$C_{3\nu}$	symmetry point group NV center
$A_{1,2}, E_{1,2}$	irreducible representations of $C_{3\nu}$
$e, C_3^{\pm}, \sigma_{1,2,3}$	symmetry operations of $C_{3\nu}$
$D_{\text{gs}}, D_{\text{es}}^{\parallel, \perp}$	zero-field splitting parameters
$P_{\text{gs}}, P_{\text{es}}$	quadrupolar coupling parameter
$A_{\text{gs}}^{\parallel, \perp}, A_{\text{es}}^{\parallel, \perp}$	hyperfine coupling constants
T_1	spin relaxation time
$T_2, T_2^*, T_{\varphi}, T_{2,\text{d.d}}^*$	spin coherence times
Γ_{NV}	NV decoherence rate
T_{decay}	Rabi decay time
$\lambda_{\text{es}}^{\parallel, \perp}$	spin-orbit coupling constants
$\tau_{ {}^1E_{1,2}\rangle}, \tau_{ {}^3E\rangle}$	optical NV lifetimes
Δ_Z	Zeeman splitting
$\Delta_{i,j}$	spin precession frequency component

$ ^3A_2\rangle$	S=1 ground state manifold
$ 0\rangle, -1\rangle, +1\rangle$	S=1 ground state spin sublevels
$ \uparrow\rangle, \downarrow\rangle$	spin up and spin down state
$ ^3E\rangle$	S=1 excited state manifold
$ A_{1,2}\rangle, E_{1,2}\rangle, E_{x,y}\rangle$	S=1 excited state sublevels
$ ^1E\rangle$	S=0 ground state manifold
$ ^1A_1\rangle, ^1E_{1,2}\rangle$	S=0 ground state sublevels

Mechanical oscillator:

n	number of phonons in mechanical mode
n_{th}	number of phonons in thermal equilibrium
l	cantilever length
w	cantilever width
t	cantilever thickness
u	static cantilever deflection
\tilde{u}	dynamic cantilever deflection
m_{eff}	effective cantilever mass
Q	mechanical quality factor
γ_{th}	mechanical heating/decoherence rate
N, n	number of cantilever phonons
Γ_m	cantilever damping rate
χ_m	mechanical susceptibility
$\Delta\omega_d$	mechanical linewidth
Δx_{zpm}	zero-point motion
$\Delta x, \Delta p$	uncertainties in cantilever position and momentum

External fields:

M	number of microwave photons
$\mathbf{B} = \{B_x, B_y, B_z\}$	external magnetic field in NV coordinate system
ω_d	mechanical driving frequency
ω_m	mechanical mode frequency
Ω_m	mechanical Rabi frequency
ω_{MW}	microwave field frequency
Ω_{MW}	microwave Rabi frequency
Ω_{opt}	optical Rabi frequency
Ω_{eff}	effective Rabi frequency
δ	driving field detuning
$\sigma_{\text{MW}}, \sigma_m$	width of Gaussian noise distribution
ϕ_i	individual driving field phase
Φ	total driving field phase (global phase)

Strain and stress coupling:

a_1, a_2, b, c	spin-strain coupling constants
$g_0^{\parallel, \perp}$	longitudinal/transverse single phonon coupling strength
$M_{\epsilon, i}^{\text{gs, es}}, M_{\sigma, i}^{\text{gs, es}}$	strain-/stress-induced level shifts
$M'_{\epsilon, i}, M'_{\sigma, i}$	strain-/stress-induced level shifts for different xyz
\mathbf{C} ($\tilde{\mathbf{C}}$)	stiffness tensor (in Voigt notation)
\mathbf{P}, P	uniaxial stress and amplitude
A_1, A_2, B, C	spin-stress coupling constants
NV1-4	NV orientations in [001]-oriented diamond
$\tilde{\mathbf{K}}$	coordinate system transformation
$\tilde{\mathbf{R}}_{\mathbf{p}}(\theta)$	rotation by angle θ about axis \mathbf{p}
E	Young's modulus
I_i	moment of inertia about axis i
$\mathbf{V} = V_0 \cdot \{V_x, V_y, V_z\}$	shear force of amplitude V_0
$\Delta_{\pm}^{\epsilon, \sigma}$	level shifts of $ \pm 1\rangle$ with respect to $ 0\rangle$
$\Delta_{ E_x\rangle, E_y\rangle}^{\sigma, \epsilon}$	orbital level shifts with respect to $ 0\rangle$
$\boldsymbol{\epsilon}, \boldsymbol{\sigma}$	strain and stress tensors
$\tilde{\boldsymbol{\epsilon}}, \tilde{\boldsymbol{\sigma}}$	strain and stress tensors in Voigt notation
$\epsilon_{ij}, \sigma_{ij}$	strain and stress tensor components
ϵ	strain amplitude
ν	Poisson ratio
$\Gamma_{\parallel, \perp}$	strain-induced cooling rates

States and operators:

$ \Psi\rangle, \Psi(t)\rangle$	qubit wave function and its time evolution
$E_{ i\rangle} = \hbar\omega_{ i\rangle}$	energy of state $ i\rangle$
$P_{ i\rangle} = c_{ i\rangle} ^2$	population in level $ i\rangle$
$ \pm_M\rangle$	photon-dressed spin states
$ \pm_N\rangle$	phonon-dressed spin states
$ \pm_{M,N}\rangle$	doubly-dressed spin states
\hat{a}^\dagger, \hat{a}	phonon raising/lowering operators
\hat{x}	position operator
\hat{p}	momentum operator
\hat{n}	phonon number operator
$\hat{\mathbf{S}}_+, \hat{\mathbf{S}}_-$	spin raising/lowering operators
$\hat{\mathbf{H}}_{\text{gs}}, \hat{\mathbf{H}}_{\text{es}}^{\text{RT,LT}}$	fine- and hyperfine S=1 Hamiltonian
$\hat{\mathbf{H}}_{\text{int}}^{\text{AC,DC}}$	DC/AC interaction Hamiltonian
$\hat{\mathbf{S}}_i$ with $i = x, y, z, 3$	S=1 spin matrices
$\hat{\mathbf{I}}_i$ with $i = x, y, z, 3$	I=1 spin matrices
$\hat{\boldsymbol{\sigma}}_i$ with $i = x, y, z, 2$	S=1/2 Pauli matrices
$\hat{\mathbf{H}}_{\text{gs}}^{\epsilon, \sigma}, \hat{\mathbf{H}}_{\text{es}}^{\epsilon, \sigma}$	strain- and stress coupling Hamiltonians

\hat{H}_{ho}	Hamiltonian harmonic oscillator
\hat{T}	unitary rotation operator
Constants:	
$h = 6.626068 \cdot 10^{-34} \text{ m}^2\text{kg/s}$	Planck's constant
$\hbar = 1.05457148 \cdot 10^{-34} \text{ m}^2\text{kg/s}$	reduced Planck's constant
$\mu_B = 9.274009994 \cdot 10^{-24} \text{ J/T}$	Bohr magneton
$k_B = 1.38064852 \cdot 10^{-23} \text{ m}^2\text{kg/s}^2\text{K}$	Boltzmann constant
$\{C_{11}, C_{12}, C_{44}\} = \{1040, 170, 550\} \text{ GPa}$	stiffness tensor components for diamond
$\gamma_{\text{NV}} = 2.79 \text{ MHz/G}$	gyromagnetic ratio NV spin
$\alpha_{\text{NV}} = \arccos(1/\sqrt{3}) = 54.74^\circ$	characteristic angle in NV geometry
$g_e \approx 2.0002$	NV electron g-factor
Abbreviations:	
AC	alternating current
AOM	acousto-optic modulator
Au	gold
Cr	chromium
CW	continuous wave
DC	direct current
ESR	electron spin resonance
FWHM	full width half maximum
HCDD	hybrid continuous dynamical decoupling
LT	low temperature
MW	microwave
NA	numerical aperture
NV	Nitrogen-Vacancy
NV^0	neutral NV center
NV^{-1}	negatively charged NV center
O_2	oxygen
PSB	phonon sideband
PSF	point-spread function
qubit	quantum bit
RWA	rotating wave approximation
RT	room temperature
Si	silicon
SiV	Silicon-Vacancy
Ti	titanium
ZPL	zero-phonon line

1. Introduction

Quantum two- or few-level systems are highly promising for future quantum information or metrology applications, as they offer suitable platforms to implement physical quantum bits (qubits). In the field of quantum information science, qubits serve as the main building block for novel quantum computation techniques [2, 3], and have been proposed to test and implement secure quantum communication protocols [4]. Furthermore, harnessing such systems provides an attractive route towards improving current measurement techniques. If prepared in a protected superposition state, qubits can be employed for high-performance characterization of environmental quantities such as mass or magnetic fields [5]. More advanced sensing schemes rely, for example, on squeezing effects, pushing the experimental noise floor below the quantum limit [6].

The exciting prospect of realizing quantum devices in the nearer future has triggered numerous theoretical and experimental studies in the last decades. These culminated in the identification and characterization of a remarkable variety of suitable few-level systems, such as quantum dots, ultracold atoms, superconducting qubits, and solid state spin defects. These systems are considered suitable for quantum applications as they are well decoupled from environmental fluctuations and offer long coherence times. In addition, their internal properties, i.e. the qubit's quantum state, can be coherently controlled and detected by applying external magnetic, electric or optical fields [7–11].

Despite the progress that has been made within the last years, there is still much work to be done until quantum devices become reality. A major challenge in quantum computation is the demand of implementing a network of interacting quantum systems by establishing long-range coupling between initially well isolated qubits [12]. This already complicated task is further hindered by the prospect that such quantum networks most likely need to constitute different types of quantum systems. For example, a quantum computer may rely on solid state spins as memory qubits due to their long coherence times, while using superconducting qubits for computational tasks due to their fast processing capabilities [13, 14]. Another challenge can be found in the field of high-performance sensing. Typically, weak external fields can be measured precisely if the qubit's superposition state decoheres slowly [15]. Future quantum sensing devices thus require the implementation of a coupling mechanism that links the qubit to its environment, but does not degrade its quantum mechanical properties.

Mechanical resonators offer a promising route to address these challenges. They can couple to many different types of two-level systems through a variety of coupling mechanisms (Fig. 1.1a). For example, mechanical resonators couple to photons through radiation pressure, to superconducting qubits via capacitive coupling and to spin qubits by magnetic field gradients [16–19]. As these coupling mechanisms are coherent, the transfer of information between different qubits is possible and

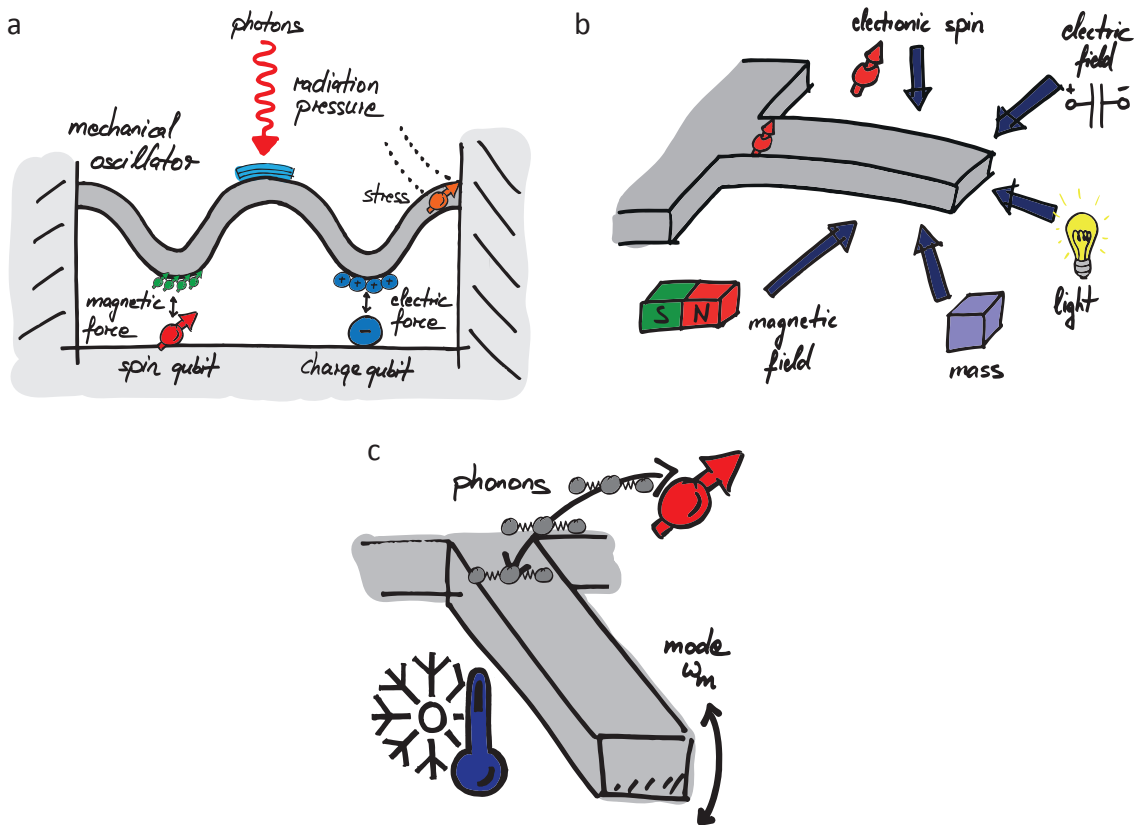


Figure 1.1.: Possible applications of hybrid spin-oscillator systems. a) Mechanical resonators couple to different types of qubits, thereby serving as transducer devices to build hybrid quantum networks for future quantum devices (after [13]). b) A mechanical oscillator can link the qubit to environmental fields without degrading its coherence properties, enabling high-performance sensing. c) If the qubit-oscillator coupling is strong enough, the qubit can be used to cool down the mechanical oscillator to its quantum ground state. Hybrid systems thus allow for studying macroscopic objects in the quantum regime.

the realization of hybrid qubit networks seems realistic [20]. Mechanical oscillators are moreover capable of linking well isolated two-level systems to their environment without degrading their precious decoherence properties. As illustrated in Fig. 1.1b, the resonator's motion is, for example, coupled to an embedded spin qubit by crystal strain. Consequently, the spin qubit might serve as a probe for any external signal that causes the resonator to deflect. Clearly, the performance of such a hybrid sensor would be determined by the individual properties of both quantum system and mechanical resonator, and the strength of the employed coupling mechanism.

Hybrid quantum systems not only enable further progress in the field of quantum information processing and metrology as described above. They also offer the opportunity to study the classical-to-quantum crossover by preparing the mechanical oscillator in non-classical states of motion. Recently, several groups successfully cooled mechanical oscillators to their quantum ground state [17, 21–23], created spin-phonon entanglement [24] or squeezed mechanical states [25, 26]. However, these experiments were performed using typical optomechanical systems, whose lin-

ear interactions limit the scope of future studies. For example, the creation of non-Gaussian mechanical states, believed to be beneficial for fault-tolerant quantum information processing and secure quantum communication schemes, requires the presence of non-linear interactions between qubit and resonator [27]. While such type of interaction is hard to realize in typical optomechanical setup, exploiting hybrid spin-oscillator systems in the strong-coupling regime, where the interaction can be nonlinear, might be able to address this open challenge [28–30].

Scope of this thesis

In this thesis, we report on the implementation and subsequent characterization of a novel hybrid spin-oscillator system, in which the mechanical motion of diamond cantilevers is coupled to the spin degree of freedom of embedded Nitrogen-Vacancy (NV) centers through crystal strain. Gaining a thorough understanding of the spin-strain coupling mechanism in this hybrid system and investigating its potential for future fundamental studies and applications in sensing or information processing are major goals of the experiments we perform.

We start with a theoretical description of the three main ingredients of our hybrid system in Chap. 2. While we review the most important aspects of NV centers and cantilevers, the focus of our theoretical description lies on understanding the employed coupling mechanism. For this reason, we explain in great detail how strain and stress coupling to the NV's spin and orbital degrees of freedom must be treated formally, and how such coupling can be studied experimentally.

Following a brief introduction to sample fabrication and employed experimental methods, we apply the developed formalism and quantify strain and stress coupling to a single NV spin in Chap. 3. Regarding the prospect of our hybrid spin-oscillator for future experiments in the quantum regime, we conclude that spin-induced resonator cooling is challenging and requires a cryogenic environment and significantly improved resonator geometries.

At this stage of the experiment, studying the classical-to-quantum crossover of our hybrid device is hard to realize. Yet the unique combination of diamond resonators and NV centers allows realizing several fascinating schemes in the context of high-performance sensing and coherent spin manipulation. In Chap. 4, we employ the parametric interaction between cantilever and spin to implement a novel coherence protection scheme, in which the spin precession frequency is locked to the oscillator mode. The remarkable coherence protection – both Rabi oscillation and spin decoherence time increase by two orders of magnitude – results from the nearly drift-free spin-strain coupling and the high-quality mechanical resonators we employ.

We proceed with demonstrating coherent NV spin manipulation using time-varying strain fields (Chap. 5). When studying the limits of this novel spin manipulation technique, we find that our hybrid system resides deep in the strong driving regime, and studying dynamics beyond the usually used rotating frame is possible. Additionally, continuous strain driving enhances the NVs spin coherence time by decoupling it from environmental magnetic noise. Our noise-isolating scheme therefore enables novel studies of weaker environmental noise sources, for example

electric noise originating from surface charge fluctuations. Our approach to strong coherent strain-driving of the NV spin has implications far beyond the coherence protection. By combining our strain-induced spin driving with coherent microwave spin manipulation, the NV's spin forms a three-level "∇-system", on which all three possible spin transitions can be coherently addressed. In Chap. 6 we present a detailed study of the spin dynamics of such a closed-contour interaction scheme and confirm the theoretical prediction that the global phase, i.e. the relative phase of the three driving fields, governs the occurring spin dynamics. Furthermore, we find that it shields the NV's spin from environmental noise and explain this novel decoupling mechanism by the symmetries of the underlying Hamiltonian.

Finally, in Chap. 7 we summarize the main results of this thesis and in particular discuss the prospect of orbital-strain coupling between NV and diamond resonator for experiments in the quantum regime. As this coupling mechanism is several orders of magnitude stronger than the spin-strain interaction we have studied so far, bringing the resonator to its quantum ground state should be within reach using this approach.

2. The hybrid spin-oscillator system

In the first chapter of this thesis we introduce our hybrid spin-oscillator system. To that end we briefly illustrate our motivation to work with a hybrid system consisting of NV centers embedded in and thus intrinsically coupled to the mechanical motion of diamond cantilevers through crystal strain. In the following, we investigate in detail the physical concepts and properties of the three components – NV centers, strain coupling and diamond cantilevers – relevant for the understanding of our experimental results.

2.1. Motivation

Existing hybrid systems feature many different combinations of quantum two- or few-level systems, mechanical resonators and coupling mechanisms. These include superconducting circuits coupled by changes in the magnetic flux [31] or capacitive coupling [17, 32, 33], ultracold atoms linked by radiation pressure forces [16, 34, 35], quantum dots as well as solid state spins and defects coupled by magnetic field gradients [18, 36, 37], or crystal strain [1, 38–42] to mechanical oscillators of different materials and shapes.

Due to their substantially different properties, each of these hybrid systems comes with its own advantages and challenges. Superconducting qubits for example are characterized by very strong interactions with mechanical motion. Consequently, they were integrated as control and detection elements in nanomechanical systems [32] and employed to establish coherent, single-phonon control of a mechanical oscillator prepared in its quantum ground state [17]. Despite these outstanding experimental achievements superconducting qubits suffer from fast decoherence as a direct consequence of the strong coupling to their environment, making them inappropriate candidates for storage qubits in quantum computers [13]. In addition, working with superconducting qubits requires experiments to be operated at a few tens of mK, posing a significant experimental challenge. Another example are ultracold atoms coupled to the mechanical motion of a resonator through radiation pressure. Such systems are usually characterized by excellent mechanical and qubit properties, enabling detailed studies of the interaction between internal atom degrees of freedom and the resonator. The intrinsically weak interaction due to radiation pressure can be overcome by coupling the resonator’s mechanical motion to the collective motion of an ensemble of atoms. Despite these promising characteristics, working with ultracold atoms is extremely challenging. Having this in mind, realizing quantum networks with ultracold atoms serving as the main building block seems possible, but will require significant effort.

To minimize experimental challenges but at the same time maintain the exciting prospects associated with hybrid systems, our quantum system of choice is the NV

center in diamond. In our experiments, its internal orbital and spin degrees of freedom will be coupled to the motion of a diamond cantilever through crystal strain. NV centers naturally feature convenient spin readout and initialization mechanisms and, as a result of the high Debye temperature and weak spin-orbit interaction strength of diamond, are characterized by relatively long coherence and relaxation times even at room temperature. These exciting inherent properties have triggered an explosion of research in the fields of quantum information processing and quantum sensing, making the NV center one of the best controlled solid state defects of our time [10, 43, 44]. A high-performance hybrid system however also requires a decent mechanical resonator. Exploiting diamond resonators is a convenient choice due to the outstanding material properties. First, diamond possesses excellent mechanical strength on account of its high Young's modulus and can be shaped into high quality resonators with quality factors $Q \sim 10^6$ [45–47]. Second, its large bulk bandgap makes diamond optically transparent, enabling optical NV readout. Strain coupling of cantilever motion to the qubit benefits from the mentioned properties, above all the high Young's modulus. Additionally, strain coupling is intrinsic as our NVs are embedded into the cantilevers. Our hybrid system thus comes with minimized fabrication complexity and simultaneously offers a quite robust and potentially strong qubit-resonator link. As we will see in this thesis, strain coupling enables a vast variety of experiments with potential for operation in a quantum regime, where the resonator is cooled to its motional ground state [20, 48, 49].

2.2. The Nitrogen-Vacancy center

2.2.1. Atomic and electronic structure

The NV center is a lattice defect in diamond and consists of a substitutional nitrogen atom¹ and a neighboring lattice vacancy (see Fig. 2.1a). As the diamond crystal structure belongs to the face-centered cubic lattice family and features two atoms per unit cell, the vacancy also has three carbon atoms as next-nearest neighbors. Consequently the NV center is of trigonal symmetry, with the symmetry axis passing through nitrogen atom and lattice vacancy. It's symmetry thus belongs to the C_{3v} point group which contains the six symmetry operations depicted in Fig. 2.1b. The underlying lattice structure also gives rise to the existence of four different NV orientations with symmetry axes pointing along the directions $[111]$, $[\bar{1}\bar{1}1]$, $[1\bar{1}\bar{1}]$ and $[\bar{1}\bar{1}\bar{1}]$.

The absence of a lattice atom leads to the formation of four tetrahedrally coordinated sp^3 atomic orbitals – c_1, c_2, c_3, n – of the carbon and nitrogen atoms surrounding the vacancy. The negatively charged NV center, which is at the focus of this thesis, has six unpaired electrons, five of which come from the nitrogen and carbon atoms and one from a donor atom nearby. The electrons occupy the molecular orbital states a'_1 , a_1 , e_x and e_y , which are linear combinations of the dangling bonds c_1, c_2, c_3, n and satisfy the C_{3v} symmetry of the NV [43, 50, 51]. The molecular orbital states can

¹Naturally occurring nitrogen consists of two stable isotopes, ^{14}N and ^{15}N . In this work we solely work with ^{14}N and therefore don't specify this in the following.

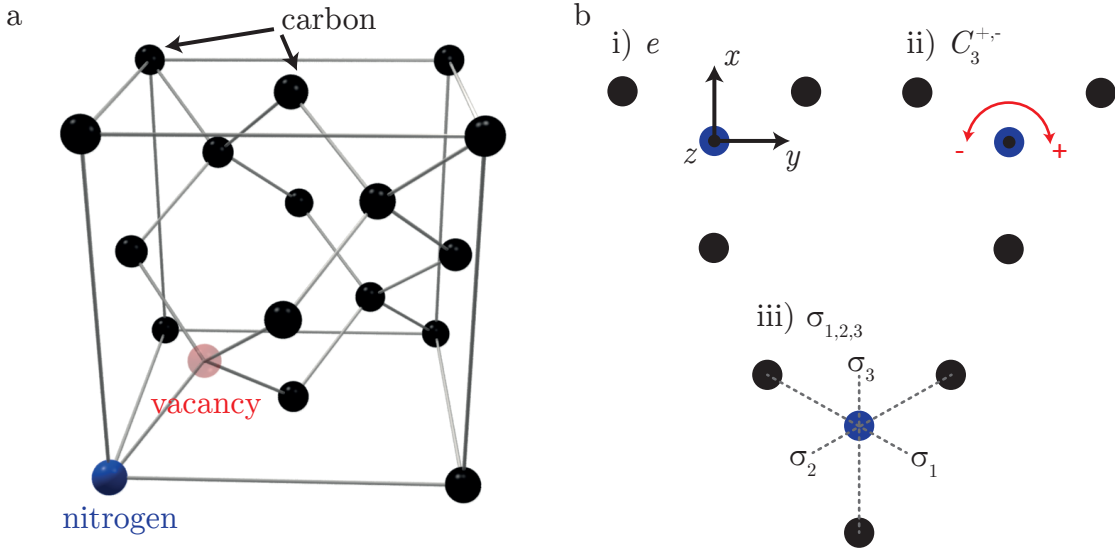


Figure 2.1.: Geometric structure and symmetry of the NV center. a) The NV center is a lattice defect in diamond and consists of a substitutional nitrogen atom (blue) and a neighboring vacancy (red). The defect's symmetry axis passes through both nitrogen atom and vacancy. b) The NV center is of trigonal symmetry and belongs to the $C_{3\nu}$ point group, which contains six symmetry operations: identity e , two rotations $C_3^{+, -}$ describing rotations of $\pm 2\pi/3$ about the NV symmetry axis (usually defined as the z axis) as well as three equivalent reflections $\sigma_{1,2,3}$. The reflection planes are defined such that each contains the symmetry axis as well as one of the three next-nearest neighbor carbon atoms.

be written as

$$\begin{aligned}
 a'_1 &= n - \lambda'(c_1 + c_2 + c_3) \\
 a_1 &= (c_1 + c_2 + c_3) + \lambda n \\
 e_x &= (2c_1 - c_2 - c_3)/\sqrt{6} \\
 e_y &= (c_2 - c_3)/\sqrt{2}
 \end{aligned} \tag{2.1}$$

where λ and λ' describe mixing between the carbon and nitrogen dangling bonds. Their spatial appearance (sketched in Fig. 2.2a) indicates that a'_1 and a_1 are invariant under the symmetry operations of the $C_{3\nu}$ point group (compare Fig. 2.1b) and thus are of A_1 symmetry (i.e. they belong to the irreducible representation A_1 of $C_{3\nu}$). The orbital states e_x and e_y however are antisymmetric and therefore belong to the two-dimensional irreducible representation E . They have permanent electric dipole moments along the x and y directions, making optical excitation of the NV center possible [43, 51]. The energetic order of the molecular orbital states can be obtained via electron-ion Coulomb interaction modeling and *ab initio* density functional theory calculations [51, 52]. While the a'_1 level is located within the diamond valance band, the remaining three levels are placed in the band gap and are thus effectively decoupled from bulk charge carriers (see Fig. 2.2b).

By distributing the six electrons among the molecular orbital states and considering the electronic spin we obtain the NV's unique level structure. In the ground

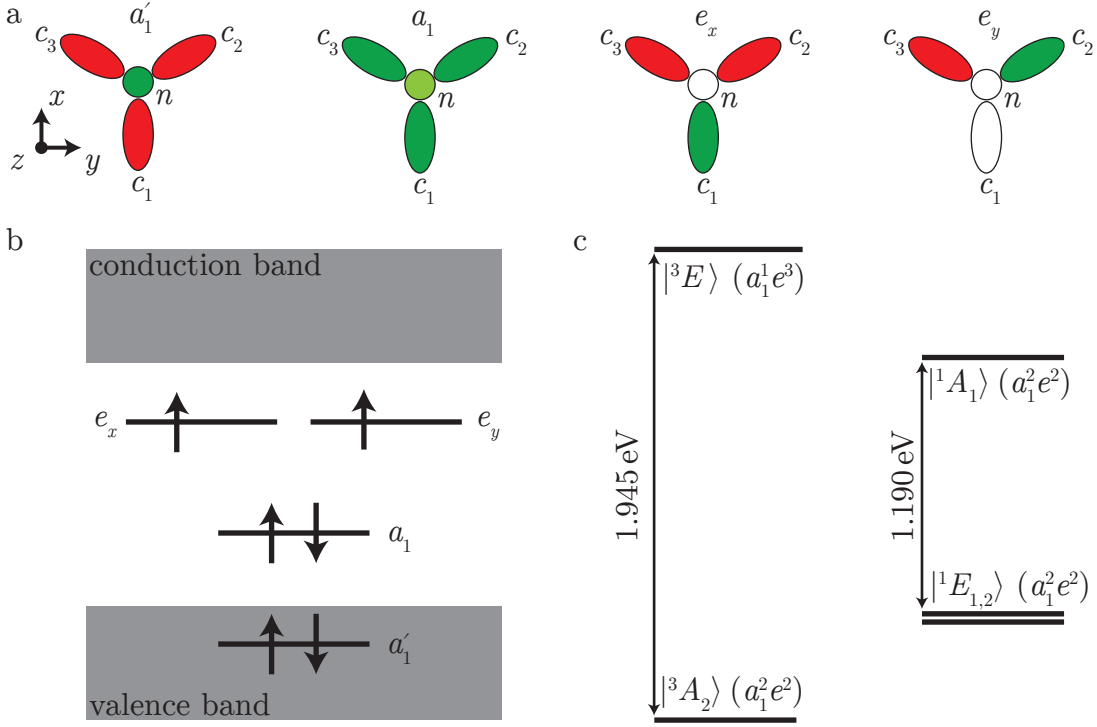


Figure 2.2.: Electronic structure of the NV center. a) Illustration of molecular orbitals a'_1 , a_1 , e_x and e_y which are linear superposition of NV dangling bonds c_1, c_2, c_3 and n (color code denotes occupation and sign of combination). b) The energetic ordering of the molecular orbitals is determined by electron-ion Coulomb interaction. The a'_1 level is lowest in energy and located within the diamond bulk valence band. The level a_1 and the degenerate levels e_x and e_y reside within the bulk band gap. c) Energetic ordering of singlet and triplet states. Triplet ground state $|^3A_2\rangle$ and excited state $|^3E\rangle$ manifolds are split by 1.945 eV due to electron-electron Coulomb interaction. The singlet ground state, which is located in between, consists of three levels which are split by 1.190 eV [43, 51].

state the lowest states in energy, a'_1 and a_1 , are filled with two electrons each while the remaining two are occupy the $e_{x,y}$ levels. This electronic configuration, labeled $a_1^2 e^2$, results in a spin-triplet ground state manifold

$$|^3A_2\rangle = |e_x e_y - e_y e_x\rangle \otimes \begin{cases} |\uparrow\uparrow\rangle \\ |\uparrow\downarrow + \downarrow\uparrow\rangle \\ |\downarrow\downarrow\rangle \end{cases} \quad (2.2)$$

where the label $|^3A_2\rangle$ indicates a total spin $S=1$ and an orbital symmetry A_2 .² The consideration of both orbital and spin symmetry, however, results in the symmetries E for the spin sublevels with spin projection $m_s = \pm 1$ ($|\uparrow\uparrow\rangle, |\downarrow\downarrow\rangle$ in (2.2)) and A_1 for $m_s = 0$ ($|\uparrow\downarrow + \downarrow\uparrow\rangle$ in (2.2)). The same electronic configuration but with total

²The irreducible representation A_2 of the point group C_{3v} describes a system which is invariant under $C_3^{+, -}$ but antisymmetric under reflections $\sigma_{1,2,3}$.

spin $S=0$ yields the NV singlet ground state with levels

$$\left. \begin{aligned} |{}^1E_1\rangle &= |e_x e_x - e_y e_y\rangle \\ |{}^1E_2\rangle &= |e_x e_y + e_y e_x\rangle \\ |{}^1A_1\rangle &= |e_x e_x + e_y e_y\rangle \end{aligned} \right\} \otimes |\uparrow\downarrow - \downarrow\uparrow\rangle \quad (2.3)$$

of E and A_1 symmetry. Due to the permanent electric dipole of e_x and e_y , we can optically excite an electron³ from the a_1 molecular orbital and obtain the electronic configuration $a_1^1 e^3$, which yields the NV triplet excited state with a total of six states

$$\begin{aligned} |A_1\rangle &= |E_-\rangle \otimes |\uparrow\uparrow\rangle - |E_+\rangle \otimes |\downarrow\downarrow\rangle \\ |A_2\rangle &= |E_-\rangle \otimes |\uparrow\uparrow\rangle + |E_+\rangle \otimes |\downarrow\downarrow\rangle \\ |E_1\rangle &= |E_-\rangle \otimes |\downarrow\downarrow\rangle - |E_+\rangle \otimes |\uparrow\uparrow\rangle \\ |E_2\rangle &= |E_-\rangle \otimes |\downarrow\downarrow\rangle + |E_+\rangle \otimes |\uparrow\uparrow\rangle \\ |E_x\rangle &= |X\rangle \otimes |\uparrow\downarrow + \downarrow\uparrow\rangle \\ |E_y\rangle &= |Y\rangle \otimes |\uparrow\downarrow + \downarrow\uparrow\rangle \end{aligned} \quad (2.4)$$

where $|E_\pm\rangle = |a_1 e_\pm - e_\pm a_1\rangle$ with $e_\pm = \mp(e_x \pm i e_y)$, $|X\rangle = (|E_-\rangle - |E_+\rangle)/2$ and $|Y\rangle = i(|E_-\rangle + |E_+\rangle)/2$ (for more details the reader is referred to [43, 51]). The labels again denote the levels' symmetries. Note that while levels $|E_{x,y}\rangle$ are also of E symmetry, they are named differently for distinction. Finally, electron-electron Coulomb interaction separates triplet ground and excited state as well as the singlet ground state levels $|{}^1A_1\rangle$ and $|{}^1E_{1,2}\rangle$, and we obtain the level structure as shown in Fig. 2.2c [43, 51].

So far we only considered electron-ion Coulomb interaction, which determines the ordering of the molecular orbital states, as well as electron-electron Coulomb interaction, which causes the singlet and triplet states to split. In our experiments, however, we primarily work with the NV's spin degree of freedom and thus need to consider spin-spin and spin-orbit interactions which determine the fine and hyperfine structure of the $|{}^3A_2\rangle$ and $|{}^3E\rangle$ manifolds. For the $S=1$ ground state $|{}^3A_2\rangle$, spin-orbit interactions vanish to first order as the underlying antisymmetric orbital wave function $|e_x e_y - e_y e_x\rangle$ has no orbital momentum [43].⁴ We therefore only consider spin-spin interactions, which split the spin sublevels by the zero-field splitting $D_{\text{gs}} = 2.87$ GHz (as depicted in Fig. 2.3). Additionally we need to account for hyperfine interactions as there is a non-zero electron spin density overlapping with the spatial position of the ${}^{14}\text{N}$ nucleus with nuclear spin $I = 1$. This interaction gives rise to the hyperfine structure shown in Fig. 2.3. Electric field gradients at the nuclear site couple to the electric quadrupole moment of the ${}^{14}\text{N}$ nuclear spin, which as a total spin $I = 1$, and shift the $m_I = \pm 1$ sublevels by the nuclear electric quadrupole parameter $P_{\text{gs}} = -5$ MHz with respect to $|m_I = 0\rangle$ and the non-zero nuclear magnetic dipole moment further causes the $|m_s = \pm 1, m_I = \pm 1\rangle$ states to split by the axial magnetic hyperfine parameter $A_{\text{gs}}^{\parallel} = -2.17$ MHz [43]. Contact hyperfine interactions, denoted by the non-axial magnetic hyperfine parameter A_{gs}^{\perp} ,

³An optical excitation is possible because the transition matrix elements for linear polarization along x and y , $\langle a|\hat{x}\mathbf{r}|e_x\rangle$ and $\langle a|\hat{y}\mathbf{r}|e_y\rangle$, differ from zero.

⁴Consequently, non-zero spin-strain coupling in the $S=1$ ground state exists due to spin-orbit coupling between $S=1$ ground and excited states. This effect is however small, as it is suppressed by the energy splitting between ground and excited state [53].

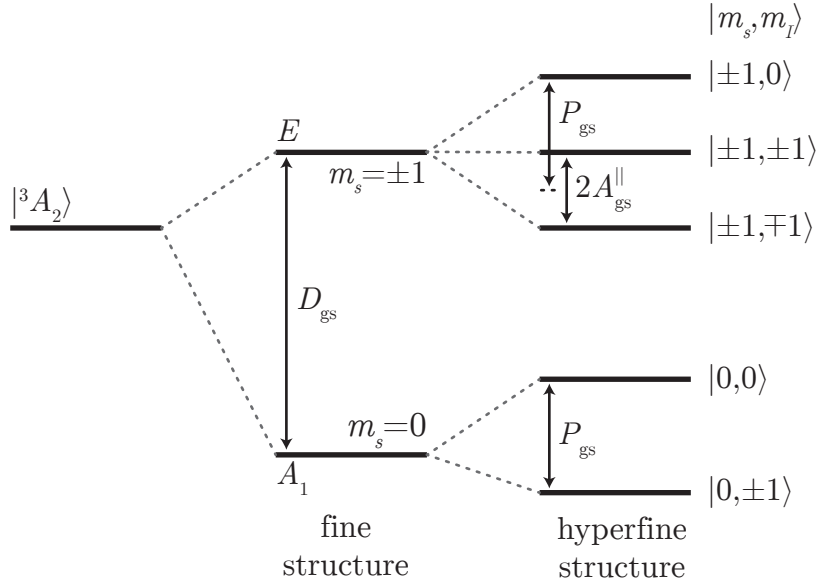


Figure 2.3.: Fine and hyperfine structure of the NV S=1 ground state. Spin-spin interactions split the spin sublevels $|m_s = 0\rangle$ and $|m_s = \pm 1\rangle$ by the zero-field splitting D_{gs} . Interactions with the nuclear spin of the ^{14}N nuclear spin cause the depicted hyperfine structure.

mix nearly degenerate states.⁵ The fine- and hyperfine structure of the NV S=1 ground state is then described by the Hamiltonian

$$\begin{aligned} \hat{H}_{gs}/h = & D_{gs}[(\hat{S}_z^2 - 2/3\hat{S}_3) \otimes \hat{I}_3] + A_{gs}^{\parallel} \hat{S}_z \otimes \hat{I}_z \\ & + A_{gs}^{\perp}[\hat{S}_x \otimes \hat{I}_x + \hat{S}_y \otimes \hat{I}_y] + P_{gs}[\hat{S}_3 \otimes (\hat{I}_z^2 - 2/3\hat{I}_3)] \end{aligned} \quad (2.5)$$

where h is Planck's constant and $\hat{S}_{x,y,z}$, $\hat{I}_{x,y,z}$ denote the S=1 electron and nuclear spin operators (\hat{S}_3 and \hat{I}_3 are corresponding identity matrices). Note that the terms $2/3\hat{S}_3$ and $2/3\hat{I}_3$ denote overall energy shifts of all involved levels and are therefore usually neglected.

While the S=1 ground state responds weakly to temperature⁶, we observe significant differences in the S=1 excited state level structure when comparing the high and low temperature limit. At low temperatures a total of six states can be spectroscopically observed, arising from spin and orbital degree of freedoms. Spin-orbit interactions $\lambda_{es}^{\parallel} = 5.3$ GHz and $\lambda_{es}^{\perp} = 0.2/\sqrt{2}$ GHz, as well as spin-spin interactions $D_{es}^{\parallel} = 1.42$ GHz and $D_{es}^{\perp} = 0.775$ GHz (values taken from [55]) result in the fine structure as depicted on the right of Fig. 2.4. The corresponding Hamiltonian is

$$\begin{aligned} \hat{H}_{es}^{LT}/h = & D_{es}^{\parallel}[\hat{\sigma}_2 \otimes (\hat{S}_z^2 - 2/3\hat{S}_3)] + D_{es}^{\perp}[\hat{\sigma}_z \otimes (\hat{S}_y^2 - \hat{S}_x^2) - \hat{\sigma}_x \otimes (\hat{S}_y\hat{S}_x + \hat{S}_x\hat{S}_y) \\ & - \lambda_{es}^{\parallel} \hat{\sigma}_y \otimes \hat{S}_z + \lambda_{es}^{\perp}[\hat{\sigma}_z \otimes (\hat{S}_x\hat{S}_z + \hat{S}_z\hat{S}_x) - \hat{\sigma}_x \otimes (\hat{S}_y\hat{S}_z + \hat{S}_z\hat{S}_y)] \end{aligned} \quad (2.6)$$

where $\hat{\sigma}_{x,y,z}$ denote the standard Pauli matrices that represent the orbital degree of freedom and $\hat{\sigma}_2$ is the two-dimensional identity matrix [43]. At high temperatures,

⁵The magnitude of A_{gs}^{\perp} is under debate. [43] lists values of -2.7 MHz and 2.1 MHz.

⁶ $dD_{gs}/dT = -78$ kHz/K [54]

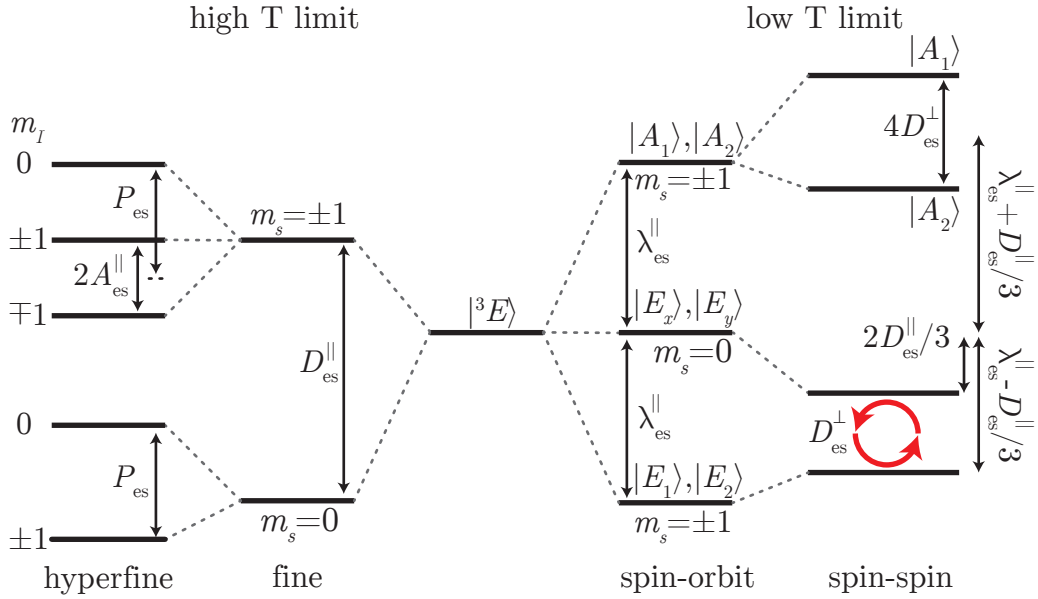


Figure 2.4.: Fine and hyperfine structure of the NV S=1 excited state. Right: At low temperatures the six states $|A_1\rangle$, $|A_2\rangle$, $|E_1\rangle$, $|E_2\rangle$, $|E_x\rangle$ and $|E_y\rangle$ are split by spin-spin ($D_{\text{es}}^{\parallel,\perp}$) and spin-orbit ($\lambda_{\text{es}}^{\parallel,\perp}$) interactions. The mixing of the $|E_{x,y}\rangle$ and $|E_{1,2}\rangle$ states due to the transverse spin-spin interaction term is indicated by red arrows. Left: At high temperatures the orbital degree of freedom vanishes as phonons mix the orbital states e_x and e_y , causing $\lambda_{\text{es}}^{\parallel} \rightarrow 0$. After including hyperfine interactions of the electron with the nuclear spin we obtain a level structure similar to the S=1 ground state.

however, the observable level structure of the S=1 excited state changes drastically. Spin-conserving phonon transitions mix the molecular orbital states (mainly e_x and e_y), and average over the orbital degree of freedom. We obtain a S=1 fine structure which is very similar to the S=1 ground state but with a smaller zero-field splitting $D_{\text{es}}^{\parallel}$ [43, 51, 55–58]. Similar considerations as for the S=1 ground state regarding hyperfine interactions of the electron spin with the nuclear spin of the ^{14}N atom result in the hyperfine structure as depicted in Fig. 2.4. While the nuclear electric quadrupolar parameter P_{es} has not been quantified yet, the axial and non-axial hyperfine coupling constants $A_{\text{es}}^{\parallel,\perp}$ for the excited state have been measured to be about 20 times larger than in the ground state [43, 59]. The difference in interaction strength is caused by the electronic configuration associated with the excited state featuring a larger unpaired spin density at the spatial position of the ^{14}N atom than the ground state configuration.⁷ The effective Hamiltonian for the S=1 excited state at high temperatures thus takes the form

$$\begin{aligned} \hat{H}_{\text{es}}^{\text{RT}}/h = & D_{\text{es}}^{\parallel} [(\hat{S}_z^2 - 2/3\hat{S}_3) \otimes \hat{I}_3] + A_{\text{es}}^{\parallel} \hat{S}_z \otimes \hat{I}_z \\ & + A_{\text{es}}^{\perp} [\hat{S}_x \otimes \hat{I}_x + \hat{S}_y \otimes \hat{I}_y] + P_{\text{es}} [\hat{S}_3 \otimes (\hat{I}_z^2 - 2/3\hat{I}_3)] \end{aligned} \quad (2.7)$$

⁷For the ground state, unpaired spins occupy the $e_{x,y}$ molecular orbital states which have little nitrogen contribution. In the excited state however, unpaired spins now also occupy the a_1 orbital state which has a larger overlap with the nitrogen's position.

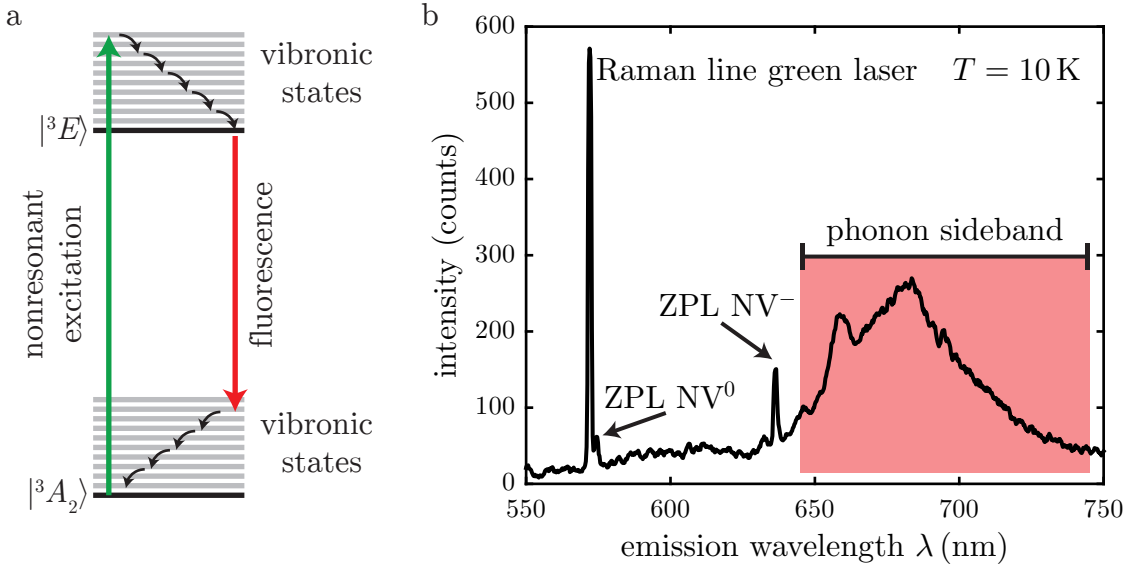


Figure 2.5.: NV emission under nonresonant excitation. a) When exciting the NV center non-resonantly, for example with green light, the system is pumped into vibronic states of the $S=1$ excited state and then experiences a radiationless, phonon-mediated decay into the $|^3E\rangle$ levels. The $|^3E\rangle$ levels have a radiative lifetime of a few ns, after which the system relaxes back into the $S=1$ ground state. This can either happen under phonon participation via the ground state vibronic states or directly without phononic contributions. The first process gives rise to emission into the phonon sideband, while the direct recombination causes emission into the zero-phonon line. b) Typical NV emission spectrum recorded at 10 K. The zero-phonon line of the negatively charged NV center is located at 637 nm and the phonon sideband extends from the zero-phonon line to about 750 nm. We also observe the ZPL of the neutral NV charge state as well as the Raman line of the green excitation laser.

with spin operators as defined above.

2.2.2. Optical properties under nonresonant excitation

The NV center in diamond is a versatile system with diverse applications in metrology and quantum information science [10, 44, 60–65]. While many applications rely on the NV’s level structure presented in the previous section, almost all (including our own) critically depend on the NV’s outstanding optical properties which are explained in the following.

The NV center can be optically excited from ground to excited state because the $e_{x,y}$ molecular orbitals possess permanent electric dipole moments (see Sec. 2.2.1). Light with $\lambda \approx 637$ nm resonantly excites the $|^3A_2\rangle \leftrightarrow |^3E\rangle$ transition. In contrast, nonresonant excitation with $\lambda < 637$ nm (typically a green laser with $\lambda = 532$ nm is used) can pump the NV into a continuum of vibronic states, which exist at slightly higher energies than the $S=1$ excited state due to vibrations in the diamond lattice (see Fig. 2.5a). Nonresonant excitation is followed by a fast, phonon-mediated relaxation into the $|^3E\rangle$ manifold [43]. The $S=1$ excited state is characterized by a

- the intersystem crossing from S=1 excited to S=0 ground state is more likely to occur for $m_s = \pm 1$ sublevels and
- the lifetime $\tau_{|{}^1E_{1,2}\rangle}$ of the metastable singlet state is significantly longer than the lifetime $\tau_{|{}^3E\rangle}$ of the triplet excited state.

Consequently the NV appears to be brighter when it was in the $m_s = 0$ ground state level at the time of optical excitation. It thereby offers a built-in optical mechanism to conveniently readout the spin state. Moreover, the presented optical dynamics also cause a net electronic spin polarization of $\sim 80\%$ into the $m_s = 0$ spin state [67].

2.3. The NV's response to external magnetic fields

The NV center is a suitable candidate for quantum information processing and sensing experiments because its spin state can be conveniently initialized and detected by optical means. This alone however does not make the NV such a promising experimental platform – its susceptibility to external magnetic fields is equally important. In this chapter we explain the NV S=1 ground state's response to constant (DC) as well as time-varying (AC) magnetic fields. We present how Zeeman splittings arise and why we can use transverse AC magnetic fields to coherently manipulate the NV's spin degree of freedom in the S=1 ground state. We finish this section with a short explanation of the influence of environmental fluctuations, which limit external spin control.

2.3.1. DC magnetic fields

External magnetic fields couple to the permanent magnetic moment associated with the NV's electronic spin and the interaction with a DC field is described by the Hamiltonian

$$\hat{\mathbf{H}}_{\text{int}}^{\text{DC}}/h = \gamma_{\text{NV}}\mathbf{B}\hat{\mathbf{S}} = \gamma_{\text{NV}}(B_x\hat{\mathbf{S}}_x + B_y\hat{\mathbf{S}}_y + B_z\hat{\mathbf{S}}_z) \quad (2.8)$$

where $\gamma_{\text{NV}} = g_e\mu_B = 2.79 \text{ MHz/G}$ with the electron g-factor $g_e \approx 2$ and the Bohr magneton μ_B . $B_{x,y,z}$ denote the magnetic field amplitudes defined in the NV coordinate system with the z axis being the NV symmetry axis and spin quantization axis, and $\hat{\mathbf{S}}_{x,y,z}$ are the S=1 spin operators. Expressing the spin operators in the Zeeman basis as

$$\hat{\mathbf{S}}_x = \frac{1}{\sqrt{2}} \begin{pmatrix} 0 & 1 & 0 \\ 1 & 0 & 1 \\ 0 & 1 & 0 \end{pmatrix} \quad \hat{\mathbf{S}}_y = \frac{-i}{\sqrt{2}} \begin{pmatrix} 0 & 1 & 0 \\ -1 & 0 & 1 \\ 0 & -1 & 0 \end{pmatrix} \quad \hat{\mathbf{S}}_z = \begin{pmatrix} 1 & 0 & 0 \\ 0 & 0 & 0 \\ 0 & 0 & -1 \end{pmatrix}, \quad (2.9)$$

allows writing $\hat{\mathbf{H}}_{\text{tot}} = \hat{\mathbf{H}}_{\text{gs}} + \hat{\mathbf{H}}_{\text{int}}^{\text{DC}}$ in matrix representation as

$$\hat{\mathbf{H}}_{\text{tot}}/h = \begin{pmatrix} D_{\text{gs}} + \gamma_{\text{NV}}B_z & \frac{\gamma_{\text{NV}}}{\sqrt{2}}(B_x - iB_y) & 0 \\ \frac{\gamma_{\text{NV}}}{\sqrt{2}}(B_x + iB_y) & 0 & \frac{\gamma_{\text{NV}}}{\sqrt{2}}(B_x - iB_y) \\ 0 & \frac{\gamma_{\text{NV}}}{\sqrt{2}}(B_x + iB_y) & D_{\text{gs}} - \gamma_{\text{NV}}B_z \end{pmatrix} \quad (2.10)$$

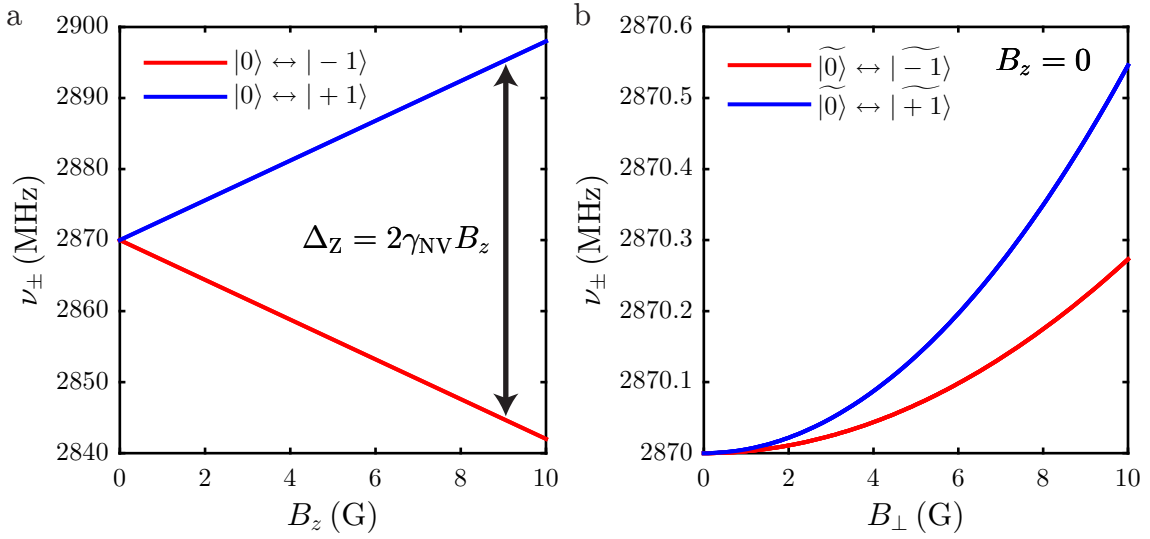


Figure 2.7.: The NV $S=1$ ground state's response to static external fields. a) Longitudinal DC magnetic fields introduce a Zeeman splitting Δ_Z between the $m_s = \pm 1$ spin sublevels, causing $\nu_+ \neq \nu_-$. b) Transverse DC magnetic fields $B_\perp = \sqrt{B_x^2 + B_y^2}$ mix and split the spin sublevels, consequently influencing ν_\pm as well. This effect is small and can usually be neglected in our experiments.

where we omitted all hyperfine terms for clarity. The magnetic field component B_z along the NV symmetry axis shifts the $m_s = \pm 1$ levels and introduces a Zeeman splitting $\Delta_Z = 2\gamma_{\text{NV}}B_z$. Consequently the transition frequencies $\nu_\pm = E_{|\pm 1\rangle} - E_{|0\rangle}$ vary linearly with B_z (see Fig. 2.7a). In contrast, transverse components $B_{x,y}$ mix and therefore shift the spin sublevels, causing a quadratic change in ν_\pm (see Fig. 2.7b). This effect however is small as long as $B_\perp = \sqrt{B_x^2 + B_y^2} \ll D_{\text{gs}}/\gamma_{\text{NV}}$, and we can usually neglect it in our experiments as we carefully align our magnetic fields to the z axis with $< 1^\circ$ mismatch.

2.3.2. AC magnetic fields

While DC magnetic fields cause static changes in the $S=1$ ground state, AC magnetic fields⁸ introduce a time-dependence to the system. To illustrate the effect of longitudinal and transverse MW fields on the NV center, we assume a MW field of the form $\mathbf{B}(t) = \{B_x \cos(\omega_{\text{MW}}t), 0, B_z \cos(\omega_{\text{MW}}t)\}$, which oscillates at frequency ω_{MW} . In analogy to (2.8) we can then write down an interaction Hamiltonian

$$\hat{\mathbf{H}}_{\text{int}}^{\text{AC}}/h = \gamma_{\text{NV}}(B_x \cos(\omega_{\text{MW}}t)\hat{\mathbf{S}}_x + B_z \cos(\omega_{\text{MW}}t)\hat{\mathbf{S}}_z). \quad (2.11)$$

In the following, we will now discuss the role of transverse and longitudinal MW components.

⁸Driving the NV spin transitions resonantly requires AC magnetic fields with frequencies in the GHz range. In this thesis we refer to such fields as microwave (MW) fields.

Transverse AC magnetic field: Rabi oscillations

The transverse MW field components are of great importance for our experiments. When the modulation frequency $\omega_{\text{MW}} \approx 2\pi\nu_{\pm}$, population transfer – known as Rabi oscillations – occurs between the coupled levels (see below) [70]. Applying a MW field resonantly to a magnetic dipole-allowed spin transition with $\Delta m_s = \pm 1$ thus enables manipulating its state, which is an essential ingredient for experiments in fields such as quantum computing or high-performance sensing.

The concept of Rabi oscillations is well understood and we will only highlight the main outcomes which are important for our measurements here (for more details on the following derivation refer to for example [71–74]). For a quasi-resonant oscillatory driving field it is most convenient to work with the two-level approximation, in which only the two levels, whose transition is addressed by the applied MW field, are considered. Such a scenario can be created in the NV's $S=1$ ground state by applying a static magnetic field along the quantization axis to split $|\pm 1\rangle$. Consequently only one of the two transitions can be driven near resonance and the second transition can be neglected. Alternatively one can apply a circularly polarized field, which drives the $|0\rangle \leftrightarrow |\pm 1\rangle$ transitions separately (see Appendix A.1).

In the following discussion we consider a two-level system which constitutes the states $|0\rangle$ and $|+1\rangle$ with energies $E_{|0\rangle} = 0$ and $E_{|+1\rangle} = \hbar\omega_+$ (the $|-1\rangle$ is split off by a static magnetic field, applied along the NV quantization axis). Furthermore, we only consider the transverse MW component of (2.11). The corresponding Hamiltonian $\hat{\mathbf{H}}_{\text{tot}}$ is time-dependent and has the form

$$\hat{\mathbf{H}}_{\text{tot}}/\hbar = \begin{pmatrix} \omega_+ & \Omega_{\text{MW}} \cos(\omega_{\text{MW}}t) \\ \Omega_{\text{MW}} \cos(\omega_{\text{MW}}t) & 0 \end{pmatrix} \quad (2.12)$$

where $\Omega_{\text{MW}}/2\pi = \gamma_{\text{NV}}B_x$ denotes the amplitude of the applied MW field. To describe the time evolution of our system, we assume the NV is in the pure state

$$|\Psi(t)\rangle = \sum_{i=0}^{+1} c_{|i\rangle}(t) e^{-iE_{|i\rangle}t/\hbar} |n\rangle = c_{|0\rangle}(t) |0\rangle + c_{|+1\rangle}(t) e^{-i\omega_+t} |+1\rangle \quad (2.13)$$

with a total population of $|c_{|0\rangle}(t)|^2 + |c_{|+1\rangle}(t)|^2 = 1$ for all t . The exponential term $e^{-i\omega_+t}$ accounts for the free evolution of $|\Psi(t)\rangle$ about the quantization axis.⁹

Solving the time-dependent Schrödinger equation $i\hbar\partial_t\Psi(t) = \hat{\mathbf{H}}_{\text{tot}}\Psi(t)$ leads to the coupled differential equations for $c_{|0\rangle}(t)$ and $c_{|+1\rangle}(t)$:

$$i\frac{d}{dt}c_{|0\rangle}(t) = \frac{\Omega_{\text{MW}}}{2} e^{i(\omega_{\text{MW}}-\omega_+)t} c_{|+1\rangle}(t) + \frac{\Omega_{\text{MW}}}{2} e^{-i(\omega_{\text{MW}}+\omega_+)t} c_{|+1\rangle}(t) \quad (2.14)$$

$$i\frac{d}{dt}c_{|+1\rangle}(t) = \frac{\Omega_{\text{MW}}}{2} e^{-i(\omega_{\text{MW}}-\omega_+)t} c_{|0\rangle}(t) + \frac{\Omega_{\text{MW}}}{2} e^{i(\omega_{\text{MW}}+\omega_+)t} c_{|0\rangle}(t). \quad (2.15)$$

For weak driving ($\Omega_{\text{MW}} \ll \omega_{\text{MW}}, \omega_+$) close to resonance ($|\omega_+ - \omega_{\text{MW}}| \ll \omega_{\text{MW}}, \omega_+$) we use the rotating wave approximation (RWA) and neglect the terms involving $e^{i(\omega_{\text{MW}}+\omega_+)t}$, since they oscillate very rapidly and give a negligible average contribution to the population transfer. Together with a beneficial change of variables

⁹This statement will be explained when we introduce the Bloch sphere.

($\tilde{c}_{|0\rangle}(t) = c_{|0\rangle}(t)e^{-i\delta t/2}$ and $\tilde{c}_{|+1\rangle}(t) = c_{|+1\rangle}(t)e^{i\delta t/2}$), (2.14) and (2.15) are transformed into time-independent expressions

$$i\frac{d}{dt}\tilde{c}_{|0\rangle}(t) = \frac{\delta}{2}\tilde{c}_{|0\rangle}(t) + \frac{\Omega_{\text{MW}}}{2}\tilde{c}_{|+1\rangle}(t) \quad (2.16)$$

$$i\frac{d}{dt}\tilde{c}_{|+1\rangle}(t) = \frac{\Omega_{\text{MW}}}{2}\tilde{c}_{|0\rangle}(t) - \frac{\delta}{2}\tilde{c}_{|+1\rangle}(t) \quad (2.17)$$

with the detuning $\delta = \omega_{\text{MW}} - \omega_+$. (2.16) and (2.17) have the general solution

$$\tilde{c}_{|0\rangle}(t) = \tilde{c}_{|0\rangle}(0) \left[\cos\left(\frac{\Omega}{2}t\right) - i\frac{\delta}{\Omega} \sin\left(\frac{\Omega}{2}t\right) \right] - i\frac{\Omega_{\text{MW}}}{\Omega}\tilde{c}_{|+1\rangle}(0) \sin\left(\frac{\Omega}{2}t\right) \quad (2.18)$$

$$\tilde{c}_{|+1\rangle}(t) = \tilde{c}_{|+1\rangle}(0) \left[\cos\left(\frac{\Omega}{2}t\right) + i\frac{\delta}{\Omega} \sin\left(\frac{\Omega}{2}t\right) \right] - i\frac{\Omega_{\text{MW}}}{\Omega}\tilde{c}_{|0\rangle}(0) \sin\left(\frac{\Omega}{2}t\right) \quad (2.19)$$

where Ω denotes the effective Rabi frequency with $\Omega = \sqrt{\Omega_{\text{MW}}^2 + \delta^2}$. For the initial conditions $c_{|0\rangle}(0) = 1$ and $c_{|+1\rangle}(0) = 0$, (2.18) and (2.19) simplify to

$$\tilde{c}_{|0\rangle}(t) = \cos\left(\frac{\Omega}{2}t\right) - i\frac{\delta}{\Omega} \sin\left(\frac{\Omega}{2}t\right) \quad (2.20)$$

$$\tilde{c}_{|+1\rangle}(t) = -i\frac{\Omega_{\text{MW}}}{\Omega} \sin\left(\frac{\Omega}{2}t\right). \quad (2.21)$$

The probabilities $P_{|0\rangle}(t) = |\langle 0|\Psi(t)\rangle|^2 = |\tilde{c}_{|0\rangle}|^2$ and $P_{|+1\rangle}(t) = |\langle +1|\Psi(t)\rangle|^2 = |\tilde{c}_{|+1\rangle}|^2$ to find our system in either the $|0\rangle$ or the $|+1\rangle$ spin sublevel are

$$P_{|0\rangle}(t) = \cos^2\left(\frac{\Omega}{2}t\right) + \frac{\delta^2}{\Omega_{\text{MW}}^2 + \delta^2} \sin^2\left(\frac{\Omega}{2}t\right) \quad (2.22)$$

$$P_{|+1\rangle}(t) = \frac{\Omega_{\text{MW}}^2}{\Omega_{\text{MW}}^2 + \delta^2} \sin^2\left(\frac{\Omega}{2}t\right). \quad (2.23)$$

and show coherent oscillations between $|0\rangle$ and $|+1\rangle$, denoted as Rabi oscillations. At $t = 0$ the system is fully in $|0\rangle$ as $P_{|0\rangle}(0) = 1$. For resonant driving ($\delta = 0$), the population then oscillates sinusoidally between the two states at frequency Ω_{MW} . $P_{|0\rangle}(t) = 1$ for $t = n \cdot 2\pi/\Omega$ with $n = 0, 1, 2, 3, \dots$ while $P_{|+1\rangle}(t) = 1$ for $t = n \cdot \pi/\Omega$ with $n = 1, 3, 5, \dots$, indicating that resonant driving allows complete population inversion between both levels throughout one period. A MW field applied for interaction time $\tau_\pi = \pi/\Omega$ is called a π -pulse as $\tau_\pi\Omega = \pi$. Similarly one can also define a $\pi/2$ -pulse as the oscillatory field which is applied for $\tau_{\pi/2} = \pi/2\Omega$.

Driving the two-level system slightly out of resonance, i.e. with $\delta \neq 0$, has two effects. First, the spin now oscillates at the effective Rabi frequency $\Omega = \sqrt{\Omega_{\text{MW}}^2 + \delta^2}$. Second, population is not fully transferred between $|0\rangle$ and $|+1\rangle$ as $P_{|0\rangle}(t) \neq 0$ for all t , limiting the contrast of the observed Rabi oscillation signal. Fig. 2.8 summarizes what has been discussed so far.

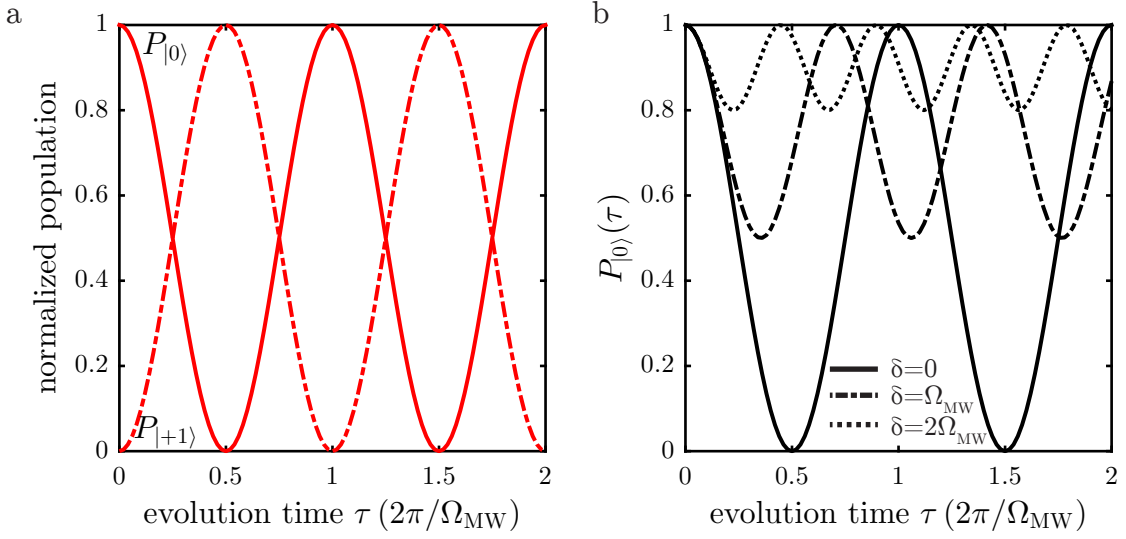


Figure 2.8.: The NV’s response to a transverse MW field. a) Driving a two-level system resonantly with a transverse MW field creates a superposition of the states that are coupled to each other and causes full population transfer at frequency Ω_{MW} . $P_{|0\rangle}$ is maximal (minimal) whenever $P_{|+1\rangle}$ is minimal (maximal). b) With increasing detuning δ the contrast decreases and the frequency at which the oscillations occur increases. Population in $|0\rangle$ is always finite for $\delta \neq 0$ when $P_{|0\rangle}(\tau = 0) \neq 0$.

Longitudinal AC magnetic field: Frequency modulation

For completeness, let us have a quick look at the influence of the B_z component. As we have seen in the previous section, static longitudinal fields induce a Zeeman splitting Δ_z between the $|\pm 1\rangle$ spin sublevels and thus lift the degeneracy of ν_{\pm} . Longitudinal AC fields, however, modulate ν_{\pm} periodically and sidebands appear in the spectra $S_{\pm}(t)$ of ν_{\pm} with

$$S_{\pm}(t) = A_{\pm} \sum_{-\infty}^{\infty} J_n \left(\frac{\gamma_{NV} B_z}{\omega_{MW}} \right) \cos[(2\pi\nu_{\pm} + n\omega_{MW})t] \quad (2.24)$$

where A_{\pm} denotes the amplitude of the non-modulated carriers and $J_n \left(\frac{\gamma_{NV} B_z}{\omega_{MW}} \right)$ are Bessel functions of first kind and n -th order, the argument to which is the modulation index $m = \gamma_{NV} B_z / \omega_{MW}$ (see App. A.6 for further information)[75]. In our experiments we usually work with $\omega_{MW} \approx 2\pi\nu_{\pm} \approx \text{GHz}$ and $\gamma_{NV} B_z \approx \text{MHz}$. Under this condition $\gamma_{NV} B_z / \nu_{\pm} \rightarrow 0$ and already the $n = \pm 1$ sidebands are so weak in amplitude that their existence is of no importance for our measurements.

Note that the longitudinal term of an AC magnetic field can nevertheless play an essential role in the framework of hybrid spin-oscillator systems in the sense that it can couple the mechanical motion of a resonator to a quantum two-level system (see Chap. 4) [18, 37, 76–78]. In the reported experiments NV centers were subject to an oscillating magnetic field, realized either by placing the NV on the tip of cantilever, which was oscillating in a magnetic field gradient, or by having a magnetized cantilever oscillating in close proximity to an NV. In both cases the NV experienced an oscillating magnetic field. It was possible to sense and drive the motion of the

resonator [18, 37], to study spin-dependent forces in a doubly dressed approach [78], and to study the coherence of this hybrid system [77]. Other experiments applied a longitudinal AC magnetic field using a nearby antenna structure to parametrically modulate the NV's transition frequencies in the $S=1$ ground state and observed locking of the NV spin dynamics onto the AC magnetic field [79]. These promising results suggest that magnetic coupling might be able to establish a strong coherent coupling between single electronic spin qubits and mechanical resonators [76].

The Bloch sphere

A pure state of the NV spin can in general be described by the arbitrary superposition state

$$|\Psi\rangle = c_{|0\rangle}|0\rangle + c_{|+1\rangle}|+1\rangle \quad (2.25)$$

with $|c_{|0\rangle}|^2 + |c_{|+1\rangle}|^2 = 1$. We can therefore represent $|\Psi\rangle$ as vector $\mathbf{R} = \{R_x, R_y, R_z\}$ with unit length, which is called the Bloch vector and defines the Bloch sphere. Both Bloch vector and sphere allow for the geometric interpretation of a quantum two-level system's interaction with driving fields.

As the Bloch vector \mathbf{R} describes a sphere, it is convenient to express it in terms of spherical coordinates (r, θ, φ) as

$$R_x = r \sin \theta \cos \varphi \quad (2.26a)$$

$$R_y = r \sin \theta \sin \varphi \quad (2.26b)$$

$$R_z = r \cos \theta \quad (2.26c)$$

with $r = 1$, θ being the polar angle and φ the azimuthal angle (see Fig. 2.9a). We define the north and the south pole of the sphere to correspond to the $|0\rangle$ and $|+1\rangle$ spin sublevels and rewrite (2.25) as [73]

$$|\Psi\rangle = \cos \frac{\theta}{2} |0\rangle + e^{-i\omega_+ t} \sin \frac{\theta}{2} |+1\rangle. \quad (2.27)$$

We see that, in the absence of external driving, the Bloch vector rotates at a constant angular frequency $-\omega_+$ around the quantization axis. It is therefore convenient to go to a rotating frame where the Bloch vector is stationary.

Let us now consider the interaction of our two-level system with an external driving field of amplitude Ω_{MW} and detuning δ . The Bloch vector in the mentioned rotating reference frame will precess about the rotation vector, defined as $\mathbf{U} = \{-\text{Re}(\Omega_{\text{MW}}), -\text{Im}(\Omega_{\text{MW}}), \delta\}$ [80], following the evolution

$$\frac{d\mathbf{R}}{dt} = \mathbf{U} \times \mathbf{R}. \quad (2.28)$$

For our applied MW field $\mathbf{B}(t) = B_{\perp} \{\cos(\omega_{\text{MW}} t), 0, 0\}$ (see (2.12)), we find $\mathbf{U} = \{-\Omega_{\text{MW}}, 0, \delta\}$ and the equations of motion for the Bloch vector are given by

$$\frac{d}{dt} R_x = -\delta R_y \quad (2.29a)$$

$$\frac{d}{dt} R_y = \Omega_{\text{MW}} R_z + \delta R_x \quad (2.29b)$$

$$\frac{d}{dt} R_z = \Omega_{\text{MW}} R_y. \quad (2.29c)$$

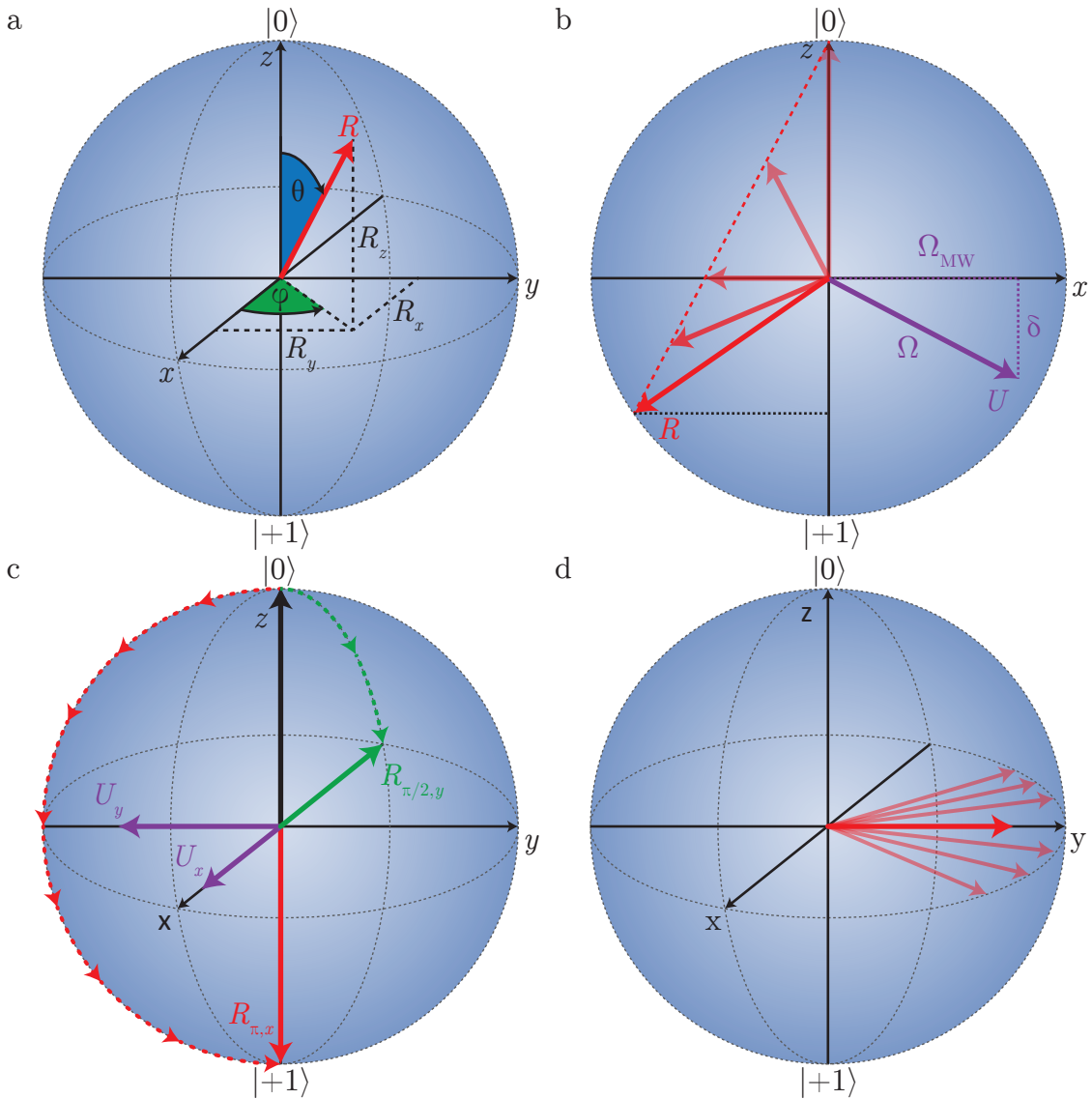


Figure 2.9.: The Bloch sphere as a geometrical representation of a two-level system. a) Any arbitrary, pure state $|\Psi\rangle$ of a two-level system can be described by a Bloch vector \mathbf{R} of length 1. The projection of $|\Psi\rangle$ on the z axis is a measure for the individual spin sublevel populations $P_{|0\rangle}$ and $P_{|+1\rangle}$. b) Applying an external driving field introduces the vector $\mathbf{U} = \{-\text{Re}(\Omega_{\text{MW}}), -\text{Im}(\Omega_{\text{MW}}), \delta\}$ about which the Bloch vector rotates. The length of \mathbf{U} is the effective Rabi frequency Ω . For non-zero detuning δ , \mathbf{U} points out of the equatorial plane and the maximum Rabi oscillation amplitude is reduced. c) When the driving field is applied for time $t = \tau_\pi$, the polar angle θ is changed by π . A pulse of length τ_π is thus called a π -pulse. d) Influence of T_2 dephasing. When the transition frequency ω_+ is fluctuating, $|\Psi\rangle$ is not a pure state anymore but a statistical mixture of many $|\Psi\rangle$ s and $|\mathbf{R}| < 1$. Other processes, for example fluctuations in Ω_{MW} , induce dephasing as well.

This is the geometrical representation of a Rabi oscillation, where the length $|\mathbf{U}| = \Omega = \sqrt{\Omega_{\text{MW}}^2 + \delta^2}$ determines the frequency of the rotation. As one can see in Fig. 2.9b, a detuning δ not only increases Ω . It also reduces the maximum Rabi contrast which in the Bloch sphere picture corresponds to the projection of \mathbf{R} on the z axis. Figs. 2.9b and 2.8b can thus be linked nicely. The geometrical representation of Rabi oscillations on the Bloch sphere also gives an intuitive explanation about the idea of π - or $\pi/2$ -pulses. Applying a transverse field resonantly for t_π to a two-level system in state $|\Psi\rangle = |0\rangle$ transfers the population entirely into $|+1\rangle$ and changes θ by π - hence the name π -pulse. In analogy one can define other pulses, for example the $\pi/2$ -pulse where θ changes by $\pi/2$ (compare Fig. 2.9c).

2.3.3. Influence of environmental noise: Damping

If the NV two-level system exclusively interacts with the applied driving field, Rabi oscillations will be observable for infinite interaction times τ . In reality, however, the NV is also subject to environmental fluctuations, causing Rabi oscillations to damp. In general, such damping processes are attributed to different types of interactions, giving rise to two time constants – the energy relaxation time T_1 and the coherence time T_2 .

T_1 processes depend on resonant noise at the NV transition frequency and influence the level populations through induced spin flips. The spin relaxation thus happens along the quantization axis and T_1 processes are therefore often referred to as longitudinal relaxation. For the NV center, T_1 is mainly determined by spin-phonon interactions which force the population distribution into a thermal equilibrium such that all spin sublevels in the NV $S=1$ ground state are equally populated. Additionally, at low temperatures cross relaxation with neighboring spins becomes important. NV T_1 times exhibit a strong temperature dependence and possible values range from \sim ms at room temperature to \sim min in cryogenic environments [81–84].

The Bloch-Redfield theory describes T_2 damping to arise from energy relaxation and pure dephasing [74, 85, 86]. Energy removal from the spin system will perturb any superposition phase between the states $|0\rangle$ and $|+1\rangle$. This takes place at a rate $1/2T_1$. Pure dephasing processes randomize the phase $e^{-i\omega_+t}$ of the corresponding wave function $|\Psi\rangle$ (see (2.13)) at rate $1/T_\varphi$ until all phase information about the superposition state is lost. A random change of the NV's transition frequency ν_+ can, for example, be introduced by interactions with impurities or phonons. These two processes combine to a total decoherence rate

$$\frac{1}{T_2} = \frac{1}{T_\varphi} + \frac{1}{2T_1}. \quad (2.30)$$

In the NV case, the coherence time T_2 is mostly limited by interactions with environmental fluctuating magnetic and electric fields, originating from surface charge fluctuations or nearby (nuclear and electron) spins. Reported T_2 values are therefore highly dependent on their surroundings and cover values from sub-microseconds for shallow NV centers at room temperature, to seconds at low temperatures with the NV hosted by artificially purified diamond material [54, 82, 83, 87–89]. Note that literature often discriminates between the inhomogeneous coherence time T_2^* and

the homogeneous coherence time T_2 . The term *inhomogeneous* refers to an observed or effective coherence time, which is reduced by slow environmental noise (for example fluctuating spins). T_2 is the true NV coherence time measured without the slow noise terms (this is for example achieved by applying dynamical decoupling sequences).

To include T_1 and T_2 processes into our description of Rabi oscillations, we modify (2.29) and obtain the rotating-frame Bloch equations

$$\frac{d}{dt}R_x = -\delta R_y - \frac{R_x}{T_2} \quad (2.31a)$$

$$\frac{d}{dt}R_y = \Omega_{\text{MW}}R_z + \delta R_x - \frac{R_y}{T_2} \quad (2.31b)$$

$$\frac{d}{dt}R_z = \Omega_{\text{MW}}R_y - \frac{R_z - R_z^{\text{th}}}{T_1} \quad (2.31c)$$

where R_z^{th} denotes the level population difference between $|0\rangle$ and $|+1\rangle$ in thermal equilibrium (for the NV center, $R_z^{\text{th}} = 0$ in thermal equilibrium) [71, 80].

The effect of damping can be nicely illustrated in the framework of the Bloch sphere. T_2 processes do not change the sublevel populations (i.e. R_z is not affected), but continuously modulate the level splitting $\hbar\omega_+$ and thus cause uncertainties in the azimuthal angle φ (Fig. 2.9d). In such a scenario, $|\Psi\rangle$ is not a pure state anymore but a statistical mixture of many $|\Psi\rangle$ (semitransparent red arrows) which differ slightly in φ . As a result, the length of the overall Bloch vector (solid red arrow) is reduced. Driving a Rabi oscillation under such circumstances would therefore be characterized by a Bloch vector slowly decreasing in length until $|\mathbf{R}| = 0$, indicating that the two-level system is in a state where both sublevels are equally populated but the information about the relative phase φ is lost. The NV's relaxation time T_1 at room temperature is mainly limited by spin-phonon interactions forcing the system into thermal equilibrium where all spin sublevels are equally populated. In the Bloch sphere picture the Bloch vector is pushed into the equatorial plane.

2.3.4. Electron spin resonance

Applying a transverse MW field not only allows for manipulation of the NV's spin degree of freedom. It is also essential to quantify the spin-strain coupling strength, where a measure of the strain-induced level shifts of $|0\rangle$ and $|\pm 1\rangle$ is required. For this purpose we employ optically detected electron spin resonance (ESR) of the NV (Fig. 2.10). To perform ESR measurements we continuously excite the NV center with green light and record the resulting red emission. We further apply a continuous wave (CW) MW field and sweep its frequency ω_{MW} across the region of interest. Due to the NV's spin-dependent fluorescence, the detected NV emission decreases significantly when ω_{MW} is near resonance to one of the allowed spin transitions. Fig. 2.10b shows the result of such a measurement. We observe two dips, corresponding to the $|0\rangle \leftrightarrow |\pm 1\rangle$ transitions, which are not degenerate here as an external static magnetic field B_z was applied. The MW frequency at which these dips occur now allows quantifying the relative position of $|\pm 1\rangle$ with respect to $|0\rangle$, thereby yielding information about type and strength of the applied strain (see Sec. 2.4).

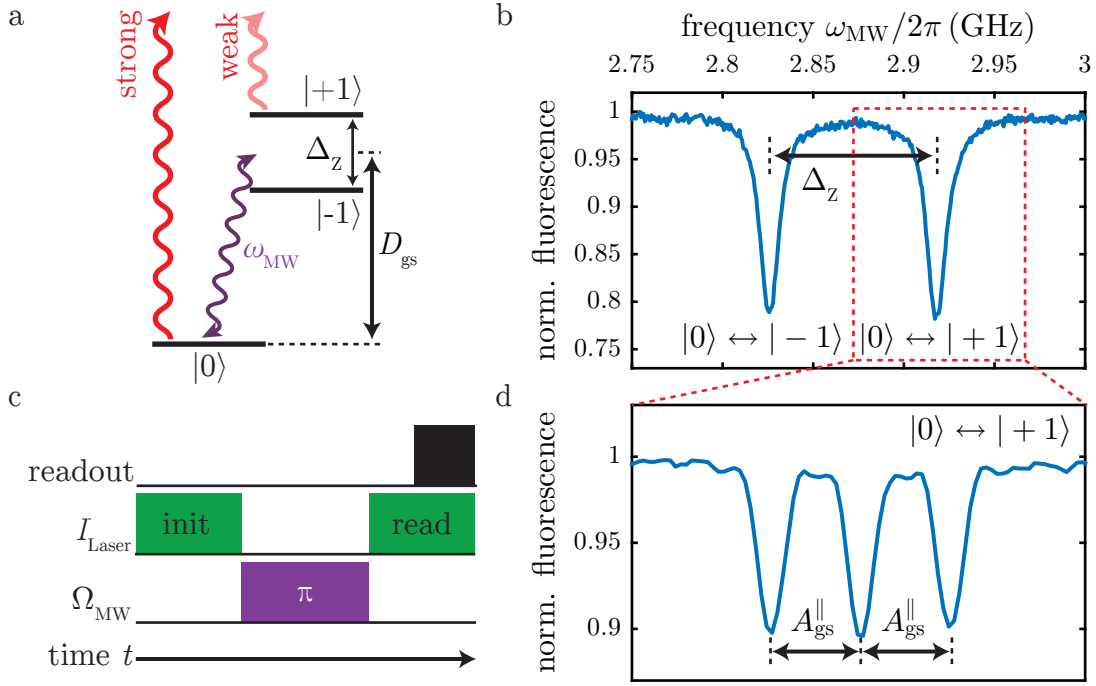


Figure 2.10.: CW and pulsed electron spin resonance. a) ESR measurements rely on the spin-dependent fluorescence of NV centers. NV emission is strong when the NV is in the $|0\rangle$ spin sublevel at the time of green illumination, but decreases for the $|\pm 1\rangle$ levels. Sweeping the frequency ω_{MW} of an applied transverse MW field allows determining relative level positions of $|0\rangle$ and $|\pm 1\rangle$. b) ESR under continuous green illumination of a single NV center (an external static magnetic $B_z \approx 18$ G field was applied along the NV symmetry axis). We observe two dips with $\sim 20\%$ readout contrast which correspond to the $|0\rangle \leftrightarrow |\pm 1\rangle$ spin transitions. c) Pulsed ESR sequence to minimize laser and MW power broadening. d) NV's hyperfine structure resulting from interactions with the nuclear spin of the ^{14}N atom. The observed dips are separated by $|A_{\text{gs}}^{\parallel}| = 2.17$ MHz (Sec. 2.2) and correspond to the nuclear spin quantum number $m_I = \{+1, 0, -1\}$ (from left to right).

For most of our experiments we also need to resolve the NV's hyperfine structure. To that end we perform pulsed ESR measurements where power broadening induced by the green excitation laser is fully eliminated and MW power broadening is reduced as much as possible. The ESR linewidth is then ultimately determined by the inhomogeneous coherence time T_2^* [90]. In the corresponding pulse sequence (Fig. 2.10c.) a green laser pulse initializes the NV in $|0\rangle$ and a subsequent MW π -pulse of duration t_π is applied to swap population between $|0\rangle$ and $|+1\rangle$ or $|-1\rangle$. Finally the NV spin state is readout by an optimized green readout pulse. To record such data as presented in Fig. 2.10d we apply the presented sequence and vary the MW frequency. For low enough MW amplitudes we can observe the NV's hyperfine structure, i.e. three nuclear sublevels m_I per electronic sublevel m_s , separated by $A_{\text{gs}}^{\parallel} = -2.17$ MHz, at maximized readout contrast.

2.4. The NV's response to stress and strain

The fact that NV centers respond to crystal stress has been known since the 1970s when Davies and Hamer investigated its influence on the NV's optical transitions [91]. Until five years ago, studies of strain coupling focused on probing the electronic level structure of the S=1 excited state [55, 58, 92], the S=1 ground state [1, 42, 92], and the S=0 ground state [93, 94]. Recently, several groups worldwide started characterizing strain coupling to single or few NV spins in the context of hybrid spin-oscillator systems. First publications, reporting on the general interaction between resonator and spin, found substantial evidence that bringing the system to its quantum ground state is in principle possible [1, 41, 42, 76, 95–98]. Further studies discovered that strain coupling allows for coherent control of the NV's spin degree of freedom [99, 100] and that such hybrid systems can have future sensing applications, for example in protecting NV centers from environmental noise through dynamical decoupling [99, 101, 102] or as the main ingredient of nanospin-mechanical sensors for mass spectrometry and force microscopy [103].

In the following section we give a theoretical description of how stress and strain affect the NV center's spin and orbital degrees of freedom. At first we explain the coupling Hamiltonians for the S=1 ground and excited state. Here we focus on the difference between transverse and longitudinal coupling and highlight their potential for future experiments. In the second part we link the coupling Hamiltonians to stress and strain defined in crystal and NV coordinate systems.

2.4.1. Strain coupling in S=1 ground and excited state

In general, crystal strain displaces the lattice atoms from their equilibrium positions. As a result, the NV's sp^3 atomic orbitals also shift, changing the molecular orbital states a'_1 , a_1 , e_x and e_y (see (2.1)). In particular, strain that distorts the lattice but maintains the NV's symmetry, e.g. longitudinal strain acting along the symmetry axis, changes the energy splitting between a_1 and e_x , e_y . Such strain components are usually referred to in literature as strain of A symmetry. In contrast, strain that breaks the symmetry of the NV center is of E symmetry. Such strain, for example acting transversely to the NV's symmetry axis, mixes and splits the e_x and e_y states and rotates the orientation of the NV's electric dipoles, changing the polarization of the optical transition between S=1 ground and excited state [51, 104, 105]. Any change of the molecular orbital states is translated into shifts and mixings of the S=1 and S=0 ground and excited state sublevels. We will restrict our discussion to the influence of strain on the S=1 ground state at room temperature as well as on the S=1 excited state at low temperatures.

S=1 ground state

The influence of strain on the NV's S=1 ground state at room temperature is described by the Hamiltonian

$$\hat{H}_{\text{gs}}^\epsilon/h = \underbrace{M_{\epsilon,z}^{\text{gs}} \hat{S}_z^2}_{\hat{H}_{\text{gs}}^{\epsilon,\parallel}} + \underbrace{M_{\epsilon,x}^{\text{gs}} (\hat{S}_y^2 - \hat{S}_x^2) + M_{\epsilon,y}^{\text{gs}} (\hat{S}_x \hat{S}_y + \hat{S}_y \hat{S}_x)}_{\hat{H}_{\text{gs}}^{\epsilon,\perp}} \quad (2.32)$$

where $\hat{\mathbf{S}}_3$ is the S=1 spin identity matrix, $\hat{\mathbf{S}}_{x,y,z}$ are the S=1 spin operators and $M_{\epsilon,i}^{\text{gs}}$ with $i = x, y, z$ denote the strain-induced level shifts [43], which will be related to applied stress/strain below. Note that earlier publications express $M_{\epsilon,z}^{\text{gs}} = d_{\parallel}^{\text{gs}} \epsilon_z$ and $M_{\epsilon,x,y} = d_{\perp}^{\text{gs}} \epsilon_{x,y}$ as the product of strain coupling constants $d_{\parallel,\perp}^{\text{gs}}$ and strain amplitudes $\epsilon_{x,y,z}$ defined purely along the NV's coordinate axes. In other words, strain was treated as a vector and shear components were neglected [1, 42, 43, 106]. Based on this assumption the terms longitudinal (strain along the NV's axis) and transverse (strain transverse to the NV's axis) coupling arose. However, we will see in the following discussion that this description is not sufficient to fully cover strain coupling, as strain must be treated as a tensor. Yet as the nomenclature is somewhat established we also make use of these terms throughout this thesis. Nevertheless, we want to emphasize that longitudinal coupling refers to strain of A symmetry and thus covers more than just strain purely along the symmetry axis. Similarly transverse coupling describes strain of E symmetry.

Expressing $\hat{\mathbf{H}}_{\text{gs}}^{\epsilon}$ in matrix form and in the Zeeman basis (with the spin operators given in (2.9), neglecting terms describing the hyperfine interaction with the ^{14}N nuclear spin for simplicity and setting $|0\rangle$ to zero energy) as

$$\hat{\mathbf{H}}_{\text{gs}}^{\epsilon}/h = \begin{pmatrix} M_{\epsilon,z}^{\text{gs}} & 0 & -(M_{\epsilon,x}^{\text{gs}} + iM_{\epsilon,y}^{\text{gs}}) \\ 0 & 0 & 0 \\ -(M_{\epsilon,x}^{\text{gs}} - iM_{\epsilon,y}^{\text{gs}}) & 0 & M_{\epsilon,z}^{\text{gs}} \end{pmatrix} \quad (2.33)$$

helps to understand the effect of transverse and longitudinal strain on the S=1 ground state spin sublevels. Longitudinal strain $\hat{\mathbf{H}}_{\text{gs}}^{\epsilon,\parallel}$ shifts both $|\pm 1\rangle$ sublevels by $M_{\epsilon,z}^{\text{gs}}$ with respect to $|0\rangle$. In contrast, the transverse term $\hat{\mathbf{H}}_{\text{gs}}^{\epsilon,\perp}$ mixes and subsequently splits the $|\pm 1\rangle$ states by $2\sqrt{(M_{\epsilon,x}^{\text{gs}})^2 + (M_{\epsilon,y}^{\text{gs}})^2}$. The total level shifts Δ_{\pm}^{ϵ} of states $|\pm 1\rangle$ in the NV's S=1 ground state are thus given by

$$\Delta_{\pm}^{\epsilon} = M_{\epsilon,z}^{\text{gs}} \pm \sqrt{(M_{\epsilon,x}^{\text{gs}})^2 + (M_{\epsilon,y}^{\text{gs}})^2}. \quad (2.34)$$

S=1 excited state

The influence of strain on the NV's S=1 excited state at low temperature is described by the Hamiltonian

$$\hat{\mathbf{H}}_{\text{es}}^{\epsilon}/h = M_{\epsilon,z}^{\text{es}} (\hat{\sigma}_2 \otimes \hat{\mathbf{S}}_3) + M_{\epsilon,x}^{\text{es}} (\hat{\sigma}_z \otimes \hat{\mathbf{S}}_3) - M_{\epsilon,y}^{\text{es}} (\hat{\sigma}_x \otimes \hat{\mathbf{S}}_3) \quad (2.35)$$

where $\hat{\mathbf{S}}_3$ is the S=1 spin identity matrix, $\hat{\sigma}_i$ with $i = x, y, z$ are Pauli matrices that represent the orbital degree of freedom and $\hat{\sigma}_2$ is the corresponding identity matrix. $M_{\epsilon,i}^{\text{es}}$ with $i = x, y, z$ denote the strain-induced level shifts in the S=1 excited state [43]. Note that due to the additional orbital degree of freedom and the non-vanishing spin-orbit coupling $M_{\epsilon,i}^{\text{es}} \approx 10^5 M_{\epsilon,i}^{\text{gs}}$ [13, 103, 105].

For a better understanding of the influence of strain on the NV's S=1 excited state we again express $\hat{\mathbf{H}}_{\text{es}}^{\epsilon}$ in matrix form. Written in the basis

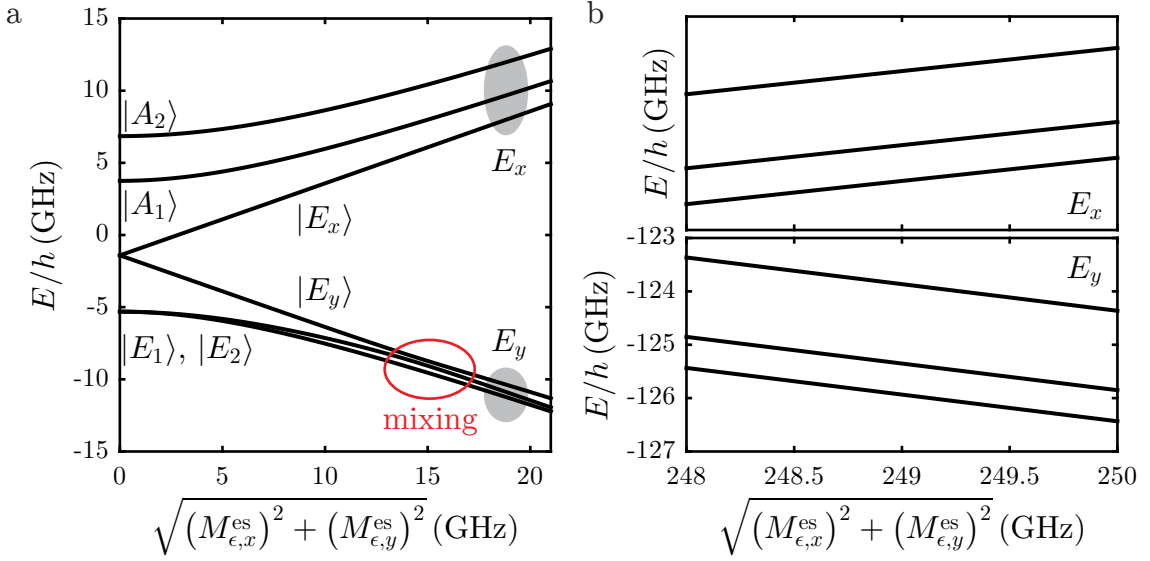


Figure 2.11.: Influence of transverse strain on the NV's S=1 excited state at low temperatures (longitudinal strain is not considered as it shifts all levels equally). a) Transverse coupling $M_{\epsilon,x}^{es}$ introduces a linear splitting of the two orbital branches E_x and E_y . Transverse strain $M_{\epsilon,y}^{es}$ also causes the orbital branches to separate and leads to a mixing of sublevels within the E_y branch (red circle). b) At large strain off-diagonal coupling terms are strongly suppressed. The two orbital branches are well separated and have a similar level structure, featuring three spin sublevels each.

$\{|A_1\rangle, |A_2\rangle, |E_x\rangle, |E_y\rangle, |E_1\rangle, |E_2\rangle\}$, we obtain

$$\hat{H}_{es}^{\epsilon}/h = \begin{pmatrix} M_{\epsilon,z}^{es} & 0 & 0 & 0 & 0 & 0 \\ 0 & M_{\epsilon,z}^{es} & 0 & 0 & 0 & 0 \\ 0 & 0 & M_{\epsilon,z}^{es} & 0 & 0 & 0 \\ 0 & 0 & 0 & M_{\epsilon,z}^{es} & 0 & 0 \\ 0 & 0 & 0 & 0 & M_{\epsilon,z}^{es} & 0 \\ 0 & 0 & 0 & 0 & 0 & M_{\epsilon,z}^{es} \end{pmatrix} + \begin{pmatrix} M_{\epsilon,x}^{es}/2 & 0 & 0 & -M_{\epsilon,y}^{es}/2 & 0 & 0 \\ 0 & M_{\epsilon,x}^{es}/2 & 0 & 0 & -M_{\epsilon,y}^{es}/2 & 0 \\ 0 & 0 & M_{\epsilon,x}^{es}/2 & 0 & 0 & -M_{\epsilon,y}^{es}/2 \\ -M_{\epsilon,y}^{es}/2 & 0 & 0 & -M_{\epsilon,x}^{es}/2 & 0 & 0 \\ 0 & -M_{\epsilon,y}^{es}/2 & 0 & 0 & -M_{\epsilon,x}^{es}/2 & 0 \\ 0 & 0 & -M_{\epsilon,y}^{es}/2 & 0 & 0 & -M_{\epsilon,x}^{es}/2 \end{pmatrix} \quad (2.36)$$

and quickly recognize that longitudinal strain shifts all six states equally. The first term in (2.35) is therefore usually neglected in literature. The transverse term $M_{\epsilon,x}^{es}$ separates the two orbital branches E_x and E_y , while $M_{\epsilon,y}^{es}$ similarly splits the orbital branches but also causes a mixing of sublevels within the E_y triplet. For large $M_{\epsilon,x}^{es}$, i.e. when the strain-induced level shifts are larger than spin-spin and spin-orbit interactions, the mixing is suppressed and the S=1 excited state levels separate into the two orbital branches with three spin sublevels each (see Fig. 2.11) [43, 107]. The experimental results of [55] nicely confirm this description.

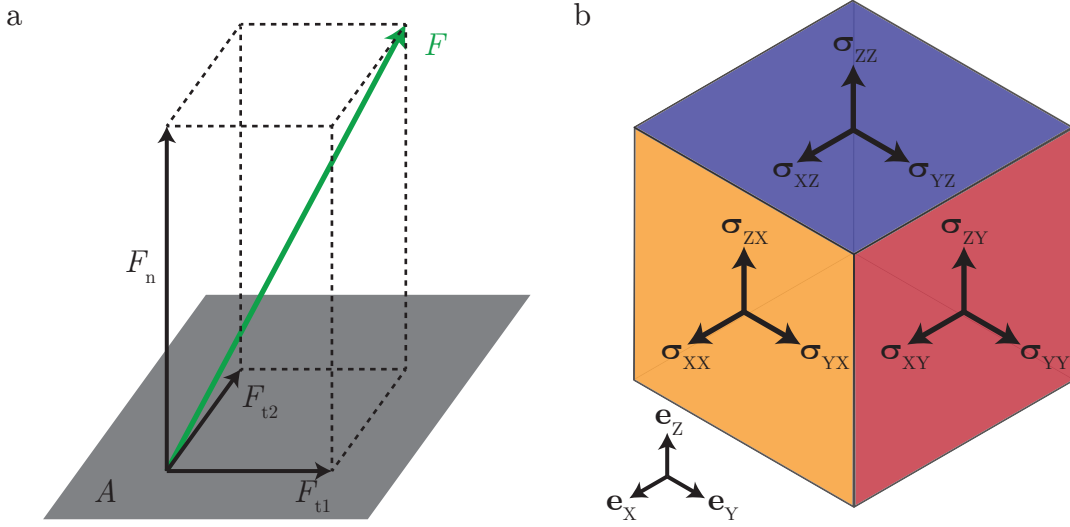


Figure 2.12.: Definition of stress. a) A force \mathbf{F} acting on a surface A can always be separated into a normal component F_n , causing normal stress F_n/A as well as two tangential components F_{t1} and F_{t2} , giving rise to the shear stresses F_{t1}/A and F_{t2}/A . b) Stress in a three-dimensional body due to external forces is described by the stress tensor $\boldsymbol{\sigma}$. Tensor components $\sigma_{ij} = dF_i/dA_j$ with $i, j \in \{X, Y, Z\}$ describe stress caused by a force along \mathbf{e}_i acting on a plane with normal vector along \mathbf{e}_j .

2.4.2. Quantifying strain and stress coupling

We will now discuss how stress-induced level shifts $M_{\epsilon,i}$ and $M_{\sigma,i}$ with $i = x, y, z$ depend on stress tensor components defined in different coordinate systems. We start with stress, but come to strain-induced level shifts afterwards. This will help us later to characterize our hybrid system with respect to spin-strain coupling efficiency and how this can be improved further.

Definition of strain, stress and stiffness tensors

We start our discussion with defining tensors for stress and strain. An external force acting on a body causes deformation and thus induces stress. The external force \mathbf{F} acting on the surface element A can always be separated into a normal component F_n as well as two tangential components F_{t1} and F_{t2} (see Fig. 2.12a). The normal component induces normal stress F_n/A , given in units of Pa, whereas the tangential components cause shear stresses F_{t1}/A and F_{t2}/A . Consequently we need nine stress components σ_{ij} with $i, j \in \{X, Y, Z\}$ to fully describe stress in a three-dimensional body caused by external forces (Fig. 2.12b). This approach results in the stress tensor $\boldsymbol{\sigma}_{XYZ}$ defined in the crystal coordinate system with $\mathbf{e}_X \parallel [100]$, $\mathbf{e}_Y \parallel [010]$ and $\mathbf{e}_Z \parallel [001]$ as

$$\boldsymbol{\sigma}_{XYZ} = \begin{pmatrix} \sigma_{XX} & \sigma_{XY} & \sigma_{XZ} \\ \sigma_{YX} & \sigma_{YY} & \sigma_{YZ} \\ \sigma_{ZX} & \sigma_{ZY} & \sigma_{ZZ} \end{pmatrix}. \quad (2.37)$$

The stress tensor components $\sigma_{ij} = dF_i/dA_j$ describe stress caused by a force along \mathbf{e}_i acting on a plane with normal vector along \mathbf{e}_j . As stress causes neither trans-

lational nor rotational movements, the condition $\sigma_{ij} = \sigma_{ji}$ needs to be fulfilled. Consequently, only six tensor components are independent of each other and the stress tensor is symmetric [108].

Strain in crystals is created by deformation and is defined as the relative displacement of lattice atoms from their equilibrium positions. In analogy to stress, strain is described by the symmetric tensor¹⁰

$$\boldsymbol{\epsilon}_{XYZ} = \begin{pmatrix} \epsilon_{XX} & \epsilon_{XY} & \epsilon_{XZ} \\ \epsilon_{YX} & \epsilon_{YY} & \epsilon_{YZ} \\ \epsilon_{ZX} & \epsilon_{ZY} & \epsilon_{ZZ} \end{pmatrix}. \quad (2.38)$$

The on-diagonal elements denote infinitesimal lattice distortions associated with a change in volume and the off-diagonal components are related to changes of angle between the basis vectors of the unstrained crystal [108].

For small strains or stresses a linear stress-strain relationship (Hooke's law) applies and we can convert strain into stress via

$$\boldsymbol{\sigma}_{XYZ} = \mathbf{C}_{XYZ} \boldsymbol{\epsilon}_{XYZ} \quad (2.39)$$

where \mathbf{C}_{XYZ} is the elastic stiffness tensor. Note that the stiffness tensor is a fourth rank tensor and in principle contains $3 \times 3 \times 3 \times 3 = 81$ independent elements. As stress and strain tensors are symmetric, this number is reduced to 36. For cubic crystals, such as diamond, symmetry arguments further reduce the number of independent elements to three (see [108] for a detailed explanation). In Voigt notation we can write the symmetric strain and stress tensors as

$$\tilde{\boldsymbol{\epsilon}}_{XYZ} = \begin{pmatrix} \epsilon_{XX} \\ \epsilon_{YY} \\ \epsilon_{ZZ} \\ \epsilon_{YZ} \\ \epsilon_{XZ} \\ \epsilon_{XY} \end{pmatrix} \quad (2.40)$$

and

$$\tilde{\boldsymbol{\sigma}}_{XYZ} = \begin{pmatrix} \sigma_{XX} \\ \sigma_{YY} \\ \sigma_{ZZ} \\ \sigma_{YZ} \\ \sigma_{XZ} \\ \sigma_{XY} \end{pmatrix} \quad (2.41)$$

and the elastic stiffness tensor reduces to a tensor of rank two and can be expressed as the 6×6 matrix

$$\tilde{\mathbf{C}}_{XYZ} = \begin{pmatrix} C_{11} & C_{12} & C_{12} & 0 & 0 & 0 \\ C_{12} & C_{11} & C_{12} & 0 & 0 & 0 \\ C_{12} & C_{12} & C_{11} & 0 & 0 & 0 \\ 0 & 0 & 0 & C_{44} & 0 & 0 \\ 0 & 0 & 0 & 0 & C_{44} & 0 \\ 0 & 0 & 0 & 0 & 0 & C_{44} \end{pmatrix} \quad (2.42)$$

with $\{C_{11}, C_{12}, C_{44}\} = \{1040, 170, 550\}$ GPa for diamond [108–110].

¹⁰For a definition of the strain tensor components see for example [108], starting on page 147.

Expressing stress-induced level shifts in terms of stress tensor components

To account for the anisotropic nature of spin-stress coupling we need to link the stress-induced level shifts $M'_{\sigma,i}$ with $i = x, y, z$ to the stress tensor components σ_{ij} . This exercise has been performed in 1967 by Hughes and Runciman [111]. The authors calculate level shifts of two excited state orbitals $|E_x\rangle$ and $|E_y\rangle$ of E symmetry with respect to an orbital ground state $|A\rangle$ of A symmetry and consider a trigonal center of C_{3v} symmetry oriented such that the center's coordinate axes point along $\mathbf{e}_x \parallel [\bar{1}10]$, $\mathbf{e}_y \parallel [\bar{1}\bar{1}2]$ and $\mathbf{e}_z \parallel [111]$. They derive a stress-coupling Hamiltonian of the form

$$\hat{\mathbf{H}}'_{\sigma,XYZ}/h = \begin{pmatrix} 0 & 0 & 0 \\ 0 & M'_{\sigma,z} - M'_{\sigma,x} & M'_{\sigma,y} \\ 0 & M'_{\sigma,y} & M'_{\sigma,z} + M'_{\sigma,x} \end{pmatrix} \quad (2.43)$$

written in the $\{|A\rangle, |E_x\rangle, |E_y\rangle\}$ basis and show that

$$M'_{\sigma,x} = B(2\sigma_{ZZ} - \sigma_{XX} - \sigma_{YY}) + C(2\sigma_{XY} - \sigma_{YZ} - \sigma_{XZ}) \quad (2.44a)$$

$$M'_{\sigma,y} = \sqrt{3}B(\sigma_{XX} - \sigma_{YY}) + \sqrt{3}C(\sigma_{YZ} - \sigma_{XZ}) \quad (2.44b)$$

$$M'_{\sigma,z} = A_1(\sigma_{XX} + \sigma_{YY} + \sigma_{ZZ}) + 2A_2(\sigma_{YZ} + \sigma_{XZ} + \sigma_{XY}) \quad (2.44c)$$

with the stress tensor defined in the crystal coordinate system. The parameters A_1 , A_2 , B and C are four coefficients required to fully characterize stress coupling [92]. They were determined to $A_1 = 4.86$ MHz/GPa, $A_2 = -3.7$ MHz/GPa, $B = -2.3$ MHz/GPa and $C = 3.5$ MHz/GPa for spin-stress coupling in the NV S=1 ground state [103]. Taking a closer look at (2.43) reveals that stress of A symmetry shifts the orbitals of E symmetry by $M'_{\sigma,z}$ with respect to $|A\rangle$. Stress distorting the lattice along the \mathbf{e}_x direction causes the $|E_x\rangle$ and $|E_y\rangle$ orbital states to split by $2M'_{\sigma,x}$. \mathbf{e}_y stress mixes and subsequently splits the $|E_x\rangle$ and $|E_y\rangle$ orbital states. The overall level shifts are given by

$$\Delta_{E_x,|E_y\rangle}^{\sigma,i} = M'_{\sigma,z} \pm \sqrt{(M'_{\sigma,x})^2 + (M'_{\sigma,y})^2}. \quad (2.45)$$

The results from Hughes and Runciman can be directly transferred to the S=1 ground and excited states of the NV center. To show this, we first convert the spin-strain coupling Hamiltonian $\hat{\mathbf{H}}_{\text{gs}}^\epsilon$ from (2.32) into a spin-stress coupling Hamiltonian $\hat{\mathbf{H}}_{\text{gs}}^\sigma$ by substituting strain-induced level shifts $M_{\epsilon,i}^{\text{gs}}$ with stress-induced level shifts $M_{\sigma,i}^{\text{gs}}$. For a direct comparison of the obtained $\hat{\mathbf{H}}_{\text{gs}}^\sigma$ with $\hat{\mathbf{H}}'_{\sigma,XYZ}$ ((2.43)), we then express $\hat{\mathbf{H}}_{\text{gs}}^\sigma$ not in the Zeeman basis but in the orbital basis $\{|A\rangle, |E_x\rangle, |E_y\rangle\}$. To that end we perform a basis transformation and write the S=1 spin operators as [106]

$$\hat{\mathbf{S}}_x = \begin{pmatrix} 0 & 0 & -i \\ 0 & 0 & 0 \\ i & 0 & 0 \end{pmatrix} \quad \hat{\mathbf{S}}_y = \begin{pmatrix} 0 & i & 0 \\ -i & 0 & 0 \\ 0 & 0 & 0 \end{pmatrix} \quad \hat{\mathbf{S}}_z = \begin{pmatrix} 0 & 0 & 0 \\ 0 & 0 & -i \\ 0 & i & 0 \end{pmatrix} \quad (2.46)$$

and obtain

$$\hat{\mathbf{H}}_{\text{gs}}^\sigma/h = \begin{pmatrix} 0 & 0 & 0 \\ 0 & M_{\sigma,z}^{\text{gs}} + M_{\sigma,x}^{\text{gs}} & -M_{\sigma,y}^{\text{gs}} \\ 0 & -M_{\sigma,y}^{\text{gs}} & M_{\sigma,z}^{\text{gs}} - M_{\sigma,x}^{\text{gs}} \end{pmatrix}. \quad (2.47)$$

Comparing our result from (2.47) with the expression (2.43), we find a strong similarity as the spin sublevels of the S=1 ground state have the same symmetry as the three orbital states that are considered in [111]. Comparing (2.43) and (2.47) yields

$$M_{\sigma,x}^{\text{gs}} = -M'_{\sigma,x} \quad (2.48a)$$

$$M_{\sigma,y}^{\text{gs}} = -M'_{\sigma,y} \quad (2.48b)$$

$$M_{\sigma,z}^{\text{gs}} = M'_{\sigma,z} \quad (2.48c)$$

and we find that the two expressions use opposite signs in the transverse level shifts. This is related to the different definitions of underlying NV and defect coordinate systems in [111] and [43]. Hughes and Runciman define their defect coordinate system such that the y axis is contained by one of the three mirror planes. In contrast, Doherty *et al.* define the x axis to lie within a mirror plane. Rotating $\hat{\mathbf{H}}_{\text{gs}}^{\epsilon}$ and $\hat{\mathbf{H}}_{\text{gs}}^{\sigma}$ about their quantization axis to account for the different coordinate systems resolves this issue (see App. A.2). Note that the different coordinate systems do not influence the overall level shifts (compare (2.34) and (2.45)). One has however to be careful with assigning signs to the stress coupling parameters A_1, A_2, B, C .

Before we continue our discussion, let us calculate expected level shifts for some uniaxial stresses. In general, if a uniaxial stress \mathbf{P} is applied to the crystal along an arbitrary direction, the elements σ_{ij} of the stress tensor are given by

$$\sigma_{ij} = P \cos(\mathbf{P}, \mathbf{e}_i) \cos(\mathbf{P}, \mathbf{e}_j) \quad (2.49)$$

where P denotes the stress amplitude and $(\mathbf{P}, \mathbf{e}_i)$ is the angle between the direction of \mathbf{P} and the crystal axis \mathbf{e}_i labeled by i [111]. For example, stresses along the [100], [110] and [111] directions result in the stress tensors

$$\boldsymbol{\sigma}_{XYZ}^{[100]} = P \begin{pmatrix} 1 & 0 & 0 \\ 0 & 0 & 0 \\ 0 & 0 & 0 \end{pmatrix} \quad \boldsymbol{\sigma}_{XYZ}^{[110]} = \frac{P}{2} \begin{pmatrix} 1 & 1 & 0 \\ 1 & 1 & 0 \\ 0 & 0 & 0 \end{pmatrix} \quad \boldsymbol{\sigma}_{XYZ}^{[111]} = \frac{P}{3} \begin{pmatrix} 1 & 1 & 1 \\ 1 & 1 & 1 \\ 1 & 1 & 1 \end{pmatrix} \quad (2.50)$$

and the corresponding level shifts in the S=1 ground state are (see (2.34), (2.44) and (2.48))

$$\Delta_{\pm}^{[100]}/P = A_1 \pm 2B \quad (2.51a)$$

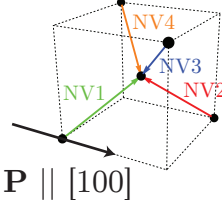
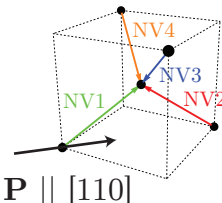
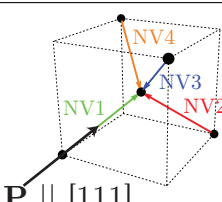
$$\Delta_{\pm}^{[110]}/P = A_1 + A_2 \pm (C - B) \quad (2.51b)$$

$$\Delta_{\pm}^{[111]}/P = A_1 + 2A_2. \quad (2.51c)$$

We emphasize that these level shifts are true for the NV coordinate system defined such that the y axis is contained by a mirror plane. Furthermore it becomes clear immediately why we need all four parameters A_1, A_2, B and C to fully describe stress coupling. Stress along the [100] direction shifts the $|\pm 1\rangle$ spin sublevels by $A_1 P$ whereas stress along [110] shifts them by $(A_1 + A_2)P$. A similar observation can be made regarding the stress-induced splitting of the $|\pm 1\rangle$ states, which is $4BP$ in the case of [100] stress and $2(C - B)P$ for [110] stress.

The formalism of Hughes and Runciman describes the influence of stress defined in crystal coordinates on a defect center with fixed orientation. Due to the structure

Table 2.1.: Overview NV orientations and the corresponding level shifts Δ_{\pm}^{σ} for states $|\pm 1\rangle$ for stresses along the [100], [110] and [111] directions. The NV coordinate system is defined such that the y axis is contained by one of the three mirror planes.

stress \mathbf{P}	NV orientation	Δ_{\pm}^{σ}/P
 $\mathbf{P} \parallel [100]$	NV1	$A_1 \pm 2B$
	NV2	
	NV3	
	NV4	
 $\mathbf{P} \parallel [110]$	NV1	$A_1 + A_2 \pm (C - B)$
	NV2	$A_1 - A_2 \pm (-B - C)$
	NV3	
	NV4	
 $\mathbf{P} \parallel [111]$	NV1	$A_1 + 2A_2$
	NV2	$A_1 - \frac{2}{3}A_2 \pm \frac{4}{3}C$
	NV3	
	NV4	

of the diamond lattice there are however four different NV orientations which might differ in their reaction to uniaxial stress. From now we label these orientations NV1-NV4. To calculate their response to stress we rotate the stress tensor, i.e. the crystal lattice, around NV1 (see App. A.3 for details on NV orientations, corresponding rotations and expressions for the expected level shifts $M'_{\sigma,i}$ for the four NV orientations). The resulting level shifts Δ_{\pm}^{σ} are summarized in Tab. 2.1 for different stress directions. Stress along the [100] direction affects all four NV orientations equally as they have the same orientation with respect to \mathbf{P} . In the case of $\mathbf{P} \parallel [110]$, we have to distinguish between two families of NV centers. NV1 and NV2 experience predominantly strain of A symmetry while NV3 and NV4 are subject to mostly transverse strain. For $\mathbf{P} \parallel [111]$, NV1 is oriented along \mathbf{P} and therefore no mixing of the $|\pm 1\rangle$ spin sublevels occurs. NV2-NV4 exhibit equal shifts and splittings.

Expressing level shifts in terms of strain in NV coordinate system

So far, we have considered crystal stress defined in the crystal coordinate system XYZ , thereby explaining the need for four parameters A_1 , A_2 , B and C to fully describe stress coupling for the four NV orientations. However, despite being more complicated, several research groups (including our own) describe the coupling mechanism in an NV-based hybrid system in terms of strain defined in the NV's coordinate system xyz [1, 13, 42]. To unify previous experimental findings, we will now show how the coupling is described in terms of strain. First, we are going to convert

the stress-induced level shifts $M'_{\sigma,i}$ from (2.44) into strain-induced level shifts $M'_{\epsilon,i}$ by replacing stress tensor components σ_{ij} with $i, j \in \{X, Y, Z\}$ with corresponding strain tensor components ϵ_{ij} with $i, j \in \{x, y, z\}$, i.e. defined in the coordinate system of NV1. We then include the NV orientations NV2-4 by expressing ϵ_{ij} in the corresponding, rotated NV coordinate systems.

To convert stress-induced level shifts $M'_{\sigma,i}$ defined in crystal coordinates XYZ into strain-induced level shifts $M'_{\epsilon,i}$ in crystal coordinates xyz of NV1, we need to substitute $\boldsymbol{\sigma}_{XYZ}$ by $\boldsymbol{\epsilon}_{xyz}$ in (2.44). Using (2.39) we derive the expression

$$\tilde{\boldsymbol{\sigma}}_{XYZ} = \tilde{\mathbf{C}}_{XYZ} \tilde{\mathbf{K}}^T \tilde{\boldsymbol{\epsilon}}_{xyz} \quad (2.52)$$

where $\tilde{\mathbf{K}}$ describes the coordinate system transformation $XYZ \rightarrow xyz$ with xyz being the coordinate system of NV1 (see App. A.3). Here $\tilde{\mathbf{K}}$ is given by

$$\tilde{\mathbf{K}} = \left(\tilde{\mathbf{R}}_{[\bar{1}10]}(\alpha_{\text{NV}}) \tilde{\mathbf{R}}_{[001]}(3\pi/4) \right)^{-1} \quad (2.53)$$

with $\alpha_{\text{NV}} = \arccos(1/\sqrt{3})$. We would like to point out that rotating the stiffness tensor requires working within the Voigt notation, in which $\tilde{\mathbf{C}}$ reduces to a 6×6 matrix and $\tilde{\boldsymbol{\epsilon}}$ and $\tilde{\boldsymbol{\sigma}}$ are 6×1 vectors (see (2.40), (2.41), (2.42)). Consequently, $\tilde{\mathbf{K}}$ and $\tilde{\mathbf{R}}$ are 6×6 matrices describing rotations in three-dimensional space (see App. A.3 for their derivation).

Performing the rotation in (2.52) allows expressing $M'_{\sigma,i}$ in terms of strain and we obtain the strain-induced level shifts

$$M'_{\epsilon,x} = b(\epsilon_{xx} - \epsilon_{yy}) + 2c\epsilon_{yz} \quad (2.54a)$$

$$M'_{\epsilon,y} = -2b\epsilon_{xy} - 2c\epsilon_{xz} \quad (2.54b)$$

$$M'_{\epsilon,z} = a_1\epsilon_{zz} + a_2(\epsilon_{xx} + \epsilon_{yy}) \quad (2.54c)$$

defined in the coordinate system of NV1. The four strain-coupling parameters

$$a_1 = A_1(C_{11} + 2C_{12}) + 2A_2C_{44} \quad (2.55a)$$

$$a_2 = A_1(C_{11} + 2C_{12}) - A_2C_{44} \quad (2.55b)$$

$$b = -B(C_{11} - C_{12}) - CC_{44} \quad (2.55c)$$

$$c = \sqrt{2}B(C_{11} - C_{12}) - \frac{1}{\sqrt{2}}CC_{44} \quad (2.55d)$$

are given in units of Hz/strain [112].¹¹

In analogy to stress coupling, we can now calculate the expected level shifts Δ_{\pm}^{ϵ} . Stresses along [100], [110] and [111] result in the stress tensors given in (2.50). Using

¹¹Expressing strain-coupling in NV coordinates is not advisable as the resulting expressions for Δ_{\pm}^{ϵ} (see (2.57)) are rather lengthy and, on first sight, depend on the employed coordinate systems. For example, in [103] the authors choose to work with an NV coordinate system different to the one we employ here, and their expressions for (2.54) are slightly different. One can however show that the overall level shifts are not affected if one starts from $\boldsymbol{\sigma}_{XYZ}$ and carefully performs the required operations to convert $XYZ \rightarrow xyz$ (see App. A.3).

the relation from (2.52) we find the corresponding strain tensors

$$\boldsymbol{\epsilon}_{xyz}^{[100]} = \epsilon \begin{pmatrix} \frac{(1-\nu)}{2} & \frac{(1+\nu)}{2\sqrt{3}} & -\frac{(1+\nu)}{\sqrt{6}} \\ \frac{(1+\nu)}{2\sqrt{3}} & \frac{(1-5\nu)}{6} & -\frac{(1+\nu)}{3\sqrt{2}} \\ -\frac{(1+\nu)}{\sqrt{6}} & -\frac{(1+\nu)}{3\sqrt{2}} & \frac{(1-2\nu)}{3} \end{pmatrix} \quad (2.56a)$$

$$\boldsymbol{\epsilon}_{xyz}^{[110]} = \epsilon \begin{pmatrix} \frac{1-\nu-\gamma(1+\nu)}{2} & 0 & 0 \\ 0 & \frac{1-5\nu+\gamma(1+\nu)}{6} & \frac{-1-\nu-\gamma(1+\nu)}{3\sqrt{2}} \\ 0 & \frac{-1-\nu-\gamma(1+\nu)}{3\sqrt{2}} & \frac{1-2\nu+\gamma(1+\nu)}{3} \end{pmatrix} \quad (2.56b)$$

$$\boldsymbol{\epsilon}_{xyz}^{[111]} = \epsilon \begin{pmatrix} \frac{1-2\nu-\gamma(1+\nu)}{3} & 0 & 0 \\ 0 & \frac{1-2\nu-\gamma(1+\nu)}{3} & 0 \\ 0 & 0 & \frac{1-2\nu+2\gamma(1+\nu)}{3} \end{pmatrix} \quad (2.56c)$$

with $\gamma = (C_{11}-C_{12})/C_{44}$, the Poisson ratio $\nu = C_{12}/(C_{11}+C_{12})$ and strain amplitude $\epsilon = P/E$, where P is the applied stress and $E = (C_{11}-C_{12})(C_{11}+2C_{12})/(C_{11}+C_{12})$ is the Young's modulus [108]. The associated level shifts obtained through combining (2.54) and (2.56) are

$$\Delta_{\pm}^{[100]}/\epsilon = \frac{(1-2\nu)}{3}(a_1 + 2a_2) \pm \frac{(2+2\nu)}{3}(b - \sqrt{2}c) \quad (2.57a)$$

$$\begin{aligned} \Delta_{\pm}^{[110]}/\epsilon &= \frac{a_1}{3}(1-2\nu+\gamma(1+\nu)) + \frac{a_2}{3}(2-4\nu-\gamma(1+\nu)) \\ &\pm \frac{2}{3} \left[\frac{c}{\sqrt{2}}(1+\nu+\gamma(1+\nu)) + \frac{b}{2}(-1-\nu+2\gamma(1+\nu)) \right] \end{aligned} \quad (2.57b)$$

$$\Delta_{\pm}^{[111]}/\epsilon = \frac{a_1}{3}(1-2\nu+2\gamma(1+\nu)) + \frac{2a_2}{3}(1-2\nu-\gamma(1+\nu)). \quad (2.57c)$$

To find the strain-induced level shifts for all four NV orientations, we follow the same approach as for stress and transform the coordinate system of the strain tensors from (2.56) accordingly (see App. A.3, where the rotations are listed in detail). The obtained level-shifts are summarized in Tab. 2.2.¹²

Before we continue we would like to point out that the formalism above also applies to both the S=1 excited state and the S=0 ground state manifold. The latter features two degenerate levels of E symmetry ($|^1E_1\rangle$ and $|^1E_2\rangle$, see Sec. 2.2.1), and $|^1A_1\rangle$, which is of A symmetry. Consequently the formalism of Hughes and Runciman applies [94]. Furthermore, if one considers a subsystem spanned by $|0\rangle$ in the S=1 ground state and the $|E_x\rangle$ and $|E_y\rangle$ excited state levels, one finds the same reaction to stress as described above. Longitudinal coupling shifts $|E_x\rangle$ and $|E_y\rangle$ with respect to $|0\rangle$, while transverse coupling mixes and splits the $|E_x\rangle$ and $|E_y\rangle$ states [51, 107]. The subsystem $\{|0\rangle, |E_1\rangle, |E_2\rangle\}$, however, cannot be described by the presented formalism as the involved excited state levels belong to the same orbital branch.

2.5. Strain and stress in cantilevers

In the last section of our first chapter we are going to introduce the physical concepts of a mechanical resonator. Naturally, as strain and stress play a crucial role

¹²The Mathematica script used for calculation is provided in App. A.10.

Table 2.2.: Overview of NV orientations and the strain-included level shifts Δ_{\pm}^{ϵ} caused by stresses along the [100], [110] and [111] directions.

stress \mathbf{P}	NV orientation	$\Delta_{\pm}^{\epsilon}/\epsilon$
$\mathbf{P} \parallel [100]$	NV1	$\frac{(1-2\nu)}{3}(a_1 + 2a_2) \pm \frac{(2+2\nu)}{3}(b - \sqrt{2}c)$
	NV2	
	NV3	
	NV4	
$\mathbf{P} \parallel [110]$	NV1	$\frac{a_1}{3}(1 - 2\nu + \gamma(1 + \nu)) + \frac{a_2}{3}(2 - 4\nu - \gamma(1 + \nu)) \pm \frac{2}{3} \left[\frac{c}{\sqrt{2}}(1 + \nu + \gamma(1 + \nu)) + \frac{b}{2}(-1 - \nu + 2\gamma(1 + \nu)) \right]$
	NV2	
	NV3	
	NV4	
$\mathbf{P} \parallel [111]$	NV1	$\frac{a_1}{3}(1 - 2\nu + 2\gamma(1 + \nu)) + \frac{2a_2}{3}(1 - 2\nu - \gamma(1 + \nu))$
	NV2	
	NV3	
	NV4	

in our experiments, we mainly concentrate on the derivation of stress and strain tensors in our cantilever. We do this for both static bending and AC excitation and therefore present a short description of the cantilever's equation of motion under external driving, with special focus on the concepts of quality factor and mechanical susceptibility. As working with hybrid systems promises exciting experiments in the resonator's motional ground state, we conclude this section by presenting the quantum mechanical description of an harmonic oscillator and discuss its interaction with a surrounding thermal bath.

2.5.1. Strain and stress under static bending

Let us start with stress and strain in a cantilever caused by a static external force \mathbf{F} . We begin our discussion, which mainly follows [113], by defining sign conventions for shear force, bending moment, coordinate directions, beam deflection, lateral forces and strain or stress. In general we consider a cantilever of length l , which has a rectangular cross section of width w and thickness t and we assume $l \gg w, t$. The cantilever coordinate system is chosen such that length l is defined along $\mathbf{e}_{\tilde{x}}$, width w along $\mathbf{e}_{\tilde{y}}$ and thickness t along $\mathbf{e}_{\tilde{z}}$ (see Fig. 2.13a). The \tilde{x} axis has its origin at the left-hand end of the beam and \tilde{y} and \tilde{z} are defined with respect to the cross section's centroid. Points that lie within a beam of rectangular cross section are therefore described by $\tilde{x} \in [0, l]$, $\tilde{y} \in [-w/2, w/2]$ and $\tilde{z} \in [-t/2, t/2]$. Lateral deflection u is chosen to be positive along $\mathbf{e}_{\tilde{z}}$. Shear forces \mathbf{V} are defined positive, if they cause the beam to rotate clockwise. For example, an external force with $\mathbf{F} \parallel -\mathbf{e}_{\tilde{z}}$ applied at positive \tilde{x} would rotate the beam clockwise about the \tilde{y} axis and would therefore be considered as a positive shear force \mathbf{V} . The same holds for $\mathbf{F} \parallel +\mathbf{e}_{\tilde{y}}$ applied at positive \tilde{x} where one would observe a clockwise rotation about the \tilde{z} axis. Moments are defined positive if they cause a sagging behavior of the beam where the top surface becomes concave and the bottom surface convex. The reverse tendency is referred to as hogging and is consequently associated with a negative bending moment. Finally, tension (compression) relates to positive (negative) strain and stress.

The effect of pure bending

To find the normal stresses in a beam caused by bending, we first consider the case of pure bending, in which the bending moment M is constant over the beam and no transverse shear forces are applied. Fig. 2.13 depicts such a scenario where a positive moment $M_{\tilde{y}}$ is applied such that the beam bends about the \tilde{y} axis. Originally horizontal lines become arcs of circles, and lines which were originally vertical (green dashed lines) now lie along radii of these circles, meeting at the center of curvature O . The finite curvature leads to a compression of the beam for $\tilde{z} > 0$, indicating that the beam's length decreases and thus $\epsilon, \sigma < 0$. In contrast, the lower half of the beam with $\tilde{z} < 0$ is under tension and the beam is stretched here. The plane at $\tilde{z} = 0$ also bends but does not change in length. It is therefore referred to as the neutral plane, as it extends along the length l and the width w of the beam.

In order to proceed with finding expressions for normal strain and stress due to bending we first define the radius of curvature of the neutral plane as R_c . For

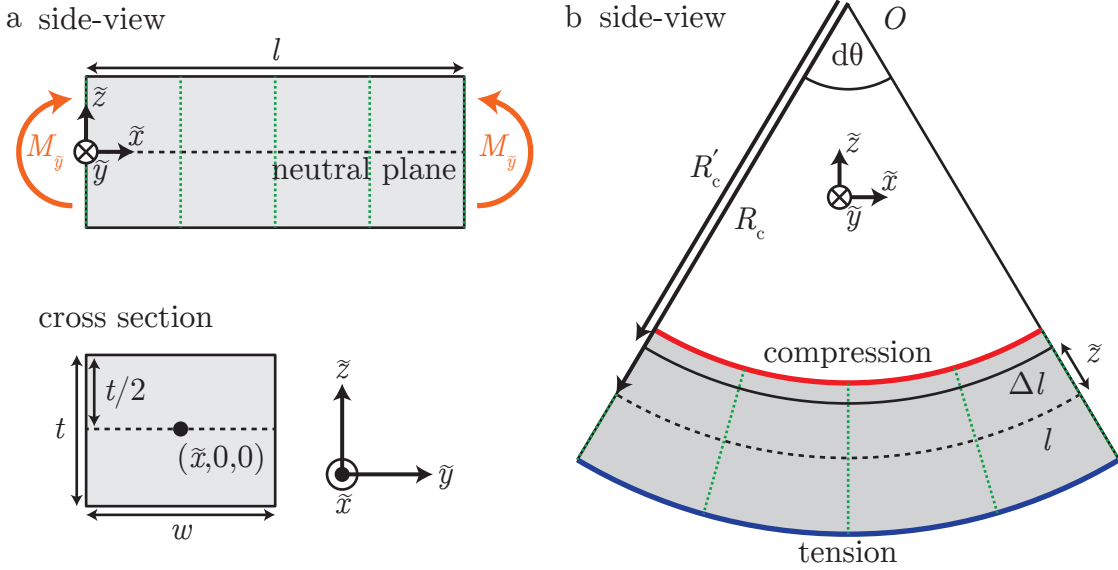


Figure 2.13.: Pure bending of a beam. a) We consider a beam of length l defined along $e_{\tilde{x}}$, width w along $e_{\tilde{y}}$ and thickness t along $e_{\tilde{z}}$. \tilde{x} is measured from the left-hand end of the beam. \tilde{y} and \tilde{z} have their origin at the centroid of the rectangular cross section. $M_{\tilde{y}}$ indicates the bending moment from b. b) When applying a positive bending moment $M_{\tilde{y}}$, the beam is compressed for $\tilde{z} > 0$ and stretched for $\tilde{z} < 0$. The neutral plane, indicated by the black dashed line, does not feel any stress and its length l remains unchanged. Planes that were perpendicular to the neutral plane in the originally straight beam (green dashed lines) remain perpendicular under pure bending as no transverse stress occurs.

small bending, i.e. small angles $d\theta$, we can then express the normal strain $\epsilon_{\tilde{x}}(\tilde{z})$ at a distance \tilde{z} above the neutral plane as

$$\epsilon_{\tilde{x}}(\tilde{z}) = \frac{\Delta l - l}{\Delta l} = \frac{R'_c d\theta - R_c d\theta}{R_c d\theta} = \frac{-\tilde{z}}{R_c} \quad (2.58)$$

where $R'_c = (R_c - \tilde{z})$. Applying Hooke's law yields the expression for normal stress $\sigma_{\tilde{x}}(\tilde{z})$

$$\sigma_{\tilde{x}}(\tilde{z}) = \frac{-\tilde{z}E}{R_c} \quad (2.59)$$

where E is the Young's modulus of the beam's material. As one can clearly see, stress and strain are maximized at the beam's top and bottom surfaces, i.e. for $\tilde{z} = \pm t/2$ and vanish at the position of the neutral plane – hence the name.

At this point, our expressions for strain and stress are linked to the radius of curvature R but not to the applied moment $M_{\tilde{y}}$ which is responsible for the observed deformation. To express $M_{\tilde{y}}$ in terms of stress and strain we need to consider the equilibrium of moments applied to the beam's cross section. For equilibrium of moments the stress distribution at the beam cross section must cause a resulting bending moment which is equal in magnitude to the applied external moment $M_{\tilde{y}}$. We can therefore write

$$M_{\tilde{y}} = \int_{-t/2}^{+t/2} -\sigma_{\tilde{x}}(\tilde{z})w\tilde{z}d\tilde{z} = \frac{E}{R_c} \int_{-t/2}^{+t/2} w\tilde{z}^2 d\tilde{z} = \frac{E}{R_c} I_{\tilde{z}} \quad (2.60)$$

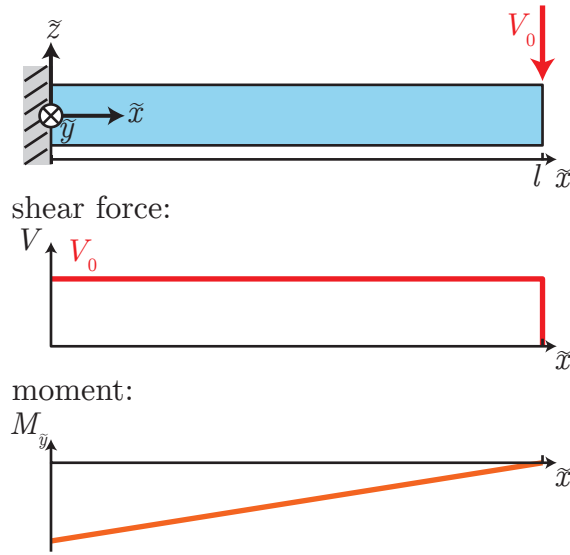


Figure 2.14.: Beam bending with a transverse force. A positive shear force V_0 pushes the cantilever downwards and induces a negative external moment. As the shear force V_0 remains constant across the beam, the induced moment increases linearly from tip to root.

where $I_i = \int_A i^2 dA$ is the moment of inertia about the i axis with $i \in \{\tilde{x}, \tilde{y}, \tilde{z}\}$. For example, a cantilever with rectangular cross section of thickness t and width w is characterized by $I_{\tilde{z}} = wt^3/12$. Combining (2.59) and (2.60), we find the sought-after relation

$$\sigma_{\tilde{x}}(\tilde{z}) = \frac{-\tilde{z}M_{\tilde{y}}}{I_{\tilde{z}}} \quad (2.61)$$

between stress and applied moment, which is usually referred to as the flexural formula [113, 114]. Note that a moment applied about the \tilde{y} axis causes constant stress along the \tilde{x} axis but varies with distance \tilde{z} from the neutral plane. The moment of inertia $I_{\tilde{z}}$ describes the beam's resistance against deflection along the \tilde{z} direction.

Beam bending with a transverse force

So far we talked about a rather general beam which was in the state of pure bending, i.e. it was subject to an external moment but not to forces applied transverse to the beam's \tilde{x} axis. In such a scenario stress is normal to the $\tilde{y}\tilde{z}$ -plane, is constant along the beam, and only depends on the distance \tilde{z} from the neutral plane.

In our static bending experiment, however, we deal with a slightly different scenario. We work with a cantilever beam of length l fixed at $\tilde{x} = 0$ and apply a transverse or shear force of magnitude V_0 at the tip of the beam such that it points along $-\mathbf{e}_{\tilde{z}}$ (remember that such a force is considered to be positive under our sign conventions). This force induces a moment $M_{\tilde{y}}(\tilde{x})$ with

$$M_{\tilde{y}}(\tilde{x}) = -(l - \tilde{x})V_0 \quad (2.62)$$

and needs to be negative for $\tilde{x} \in [0, l]$ as it causes the cantilever to deflect downwards. The applied moment vanishes at $\tilde{x} = l$ and takes its maximum value at the root of

the cantilever for $\tilde{x} = 0$ (see Fig. 2.14). As long as the considered beam is a true beam and satisfies $l \gg w, t$, we can apply the formulas we derived for pure bending [113, 114]. Normal strain $\sigma_{\tilde{x}}(\tilde{x}, \tilde{z})$, induced by a transverse force V_0 applied at the beam's tip, is thus given by (see (2.61))

$$\sigma_{\tilde{x}}(\tilde{x}, \tilde{z}) = \frac{\tilde{z}(l - \tilde{x})V_0}{I_{\tilde{z}}}. \quad (2.63)$$

Obviously, bending the cantilever downwards induces tensile stress in the top half of the beam and compressive stress in the lower half. Moreover, $\sigma_{\tilde{x}}(\tilde{x}, \tilde{z})$ decreases linearly from root to tip and from the neutral plane towards top and bottom surfaces.

In contrast to pure bending, bending through a transverse force not only induces normal stress but also causes shear stress $\sigma_{\perp}(\tilde{z})$ with

$$\sigma_{\perp}(\tilde{z}) = \frac{V_0}{2I_{\tilde{z}}} \left[\left(\frac{t}{2} \right)^2 - \tilde{z}^2 \right] \quad (2.64)$$

in the system.¹³ Note that in contrast to normal stress in (2.63), the shear stress does not depend on the position \tilde{x} along the cantilever. It vanishes at the top and bottom surfaces and is maximized near the neutral plane.

To link this discussion to the stress-induced level shifts $M'_{\sigma,i}$ from (2.44), we need to write down the stress tensor corresponding to a shear force pushing a cantilever downwards. To that end we consider an arbitrary force $\mathbf{V} = \{V_x, V_y, V_z\}$ that is applied to a cantilever as shown in Fig. 2.15. The cantilever is oriented such that $\tilde{x} \parallel X \parallel [100]$, $\tilde{y} \parallel Y \parallel [010]$ and $\tilde{z} \parallel Z \parallel [001]$, i.e. such that its coordinate system coincides with the crystal coordinate system used in Sec. 2.4.2 to quantify the influence of stress on the NV center. The axial component $V_{\tilde{x}} \parallel X$ causes a constant normal stress $\sigma_{XX} = V_{\tilde{x}}/A$ along the beam where $A = wt$ is the cross-sectional area. The transverse component $V_{\tilde{z}} \parallel -Z$ induces normal stress $\sigma_{XX} = V_{\tilde{z}}\tilde{z}(l - \tilde{x})/I_{\tilde{z}}$ as well as shear stresses $\sigma_{XZ} = \sigma_{ZX} = V_{\tilde{z}}[(t/2)^2 - \tilde{z}^2]/2I_{\tilde{z}}$ with $I_{\tilde{z}} = wt^3/12$. In analogy, the transverse component $V_{\tilde{y}} \parallel -Y$ causes normal stress $\sigma_{XX} = V_{\tilde{y}}\tilde{y}(l - \tilde{x})/I_{\tilde{y}}$ and shear stresses $\sigma_{XY} = \sigma_{YX} = V_{\tilde{y}}[(w/2)^2 - \tilde{y}^2]/2I_{\tilde{y}}$ with $I_{\tilde{y}} = tw^3/12$. All in all we find the final stress tensor

$$\boldsymbol{\sigma} = \begin{pmatrix} \frac{V_{\tilde{x}}}{wt} + (l - \tilde{x}) \left(\frac{\tilde{z}V_{\tilde{z}}}{I_{\tilde{z}}} + \frac{\tilde{y}V_{\tilde{y}}}{I_{\tilde{y}}} \right) & \frac{V_{\tilde{y}}}{2I_{\tilde{y}}} \left[\left(\frac{w}{2} \right)^2 - \tilde{y}^2 \right] & \frac{V_{\tilde{z}}}{2I_{\tilde{z}}} \left[\left(\frac{t}{2} \right)^2 - \tilde{z}^2 \right] \\ \frac{V_{\tilde{y}}}{2I_{\tilde{y}}} \left[\left(\frac{w}{2} \right)^2 - \tilde{y}^2 \right] & 0 & 0 \\ \frac{V_{\tilde{z}}}{2I_{\tilde{z}}} \left[\left(\frac{t}{2} \right)^2 - \tilde{z}^2 \right] & 0 & 0 \end{pmatrix}. \quad (2.65)$$

Under the assumption of a purely transverse force along \tilde{z} , i.e. $V_{\tilde{x}} = V_{\tilde{y}} = 0$ and NV centers located close to the top surface, the stress tensor simplifies to

$$\boldsymbol{\sigma} = P(\tilde{x}, \tilde{z}) \begin{pmatrix} 1 & 0 & 0 \\ 0 & 0 & 0 \\ 0 & 0 & 0 \end{pmatrix} \quad (2.66)$$

with $P(\tilde{x}, \tilde{z}) = \frac{\tilde{z}V_{\tilde{z}}}{I_{\tilde{z}}}(l - \tilde{x})$ being the stress amplitude. We would like to point out that pushing along $-\tilde{z}$ on a cantilever oriented along the $[100]$ direction introduces stress

¹³For details on the derivation refer to p. 256 ff. in [113].

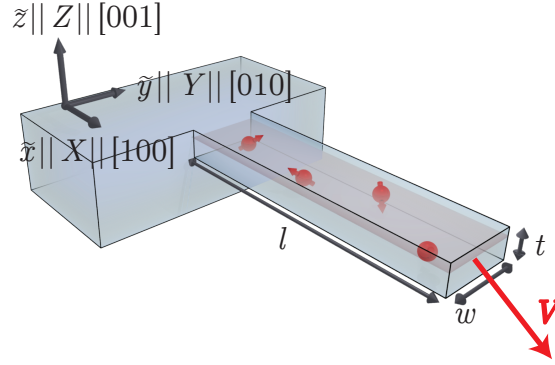


Figure 2.15.: Cantilever under influence of an external force V . The cantilever's coordinate system is defined such that it coincides with the crystal coordinate system we have used to describe stress coupling. An arbitrary force \mathbf{V} applied to the end facet bends the cantilever and induces stress.

along the $[100]$ direction. Consequently stress in cantilevers of different orientations can be obtained by making an appropriate coordinate system transformation. The corresponding strain tensor is then obtained via Hooke's law (see (2.39)).

We now know how to calculate stress and strain tensors for an external force \mathbf{V} applied to the tip of the cantilever. Yet it might be desirable to express stress in terms of cantilever deflection u , for example when the applied force is not known but the cantilever's deflection due to an external force can be measured. From Euler-Bernoulli beam theory we know that a force V_z applied at the beam's end causes a beam deflection $u(\tilde{x})$ of the form [110]

$$u(\tilde{x}) = \frac{V_z}{EI_z} \left(\frac{l\tilde{x}^2}{2} - \frac{\tilde{x}^3}{6} \right). \quad (2.67)$$

We can thus link the applied force V_z to the maximum beam displacement $u(l)$ via the expression

$$V_z = \frac{3EI_z}{l^3} u(l). \quad (2.68)$$

The stress amplitude $P(\tilde{x}, \tilde{z})$ from (2.66) becomes

$$P(\tilde{x}, \tilde{z}) = \frac{3\tilde{z}E}{l^3} (l - \tilde{x}) u(l) \quad (2.69)$$

where $u(l)$ now represents the cantilever deflection measured at $\tilde{x} = l$. In case the external force is not applied at the tip of the cantilever, but at a position a with $0 < a < l$, (2.69) becomes

$$P(\tilde{x}, \tilde{z}) = \frac{\tilde{z}V_z}{I_z} (a - \tilde{x}) = \frac{3\tilde{z}E}{a^3} (a - \tilde{x}) u(a). \quad (2.70)$$

Finally, using $\frac{1}{R_c} \approx \frac{d^2}{d\tilde{x}^2} u(\tilde{x})$ one can link the beam deflection $u(\tilde{x})$ to the induced stress $P(\tilde{x}, \tilde{z})$ via the relation

$$P(\tilde{x}, \tilde{z}) = E\epsilon(\tilde{x}, \tilde{z}) = \frac{-\tilde{z}E}{R_c} \approx \tilde{z}E \frac{d^2}{d\tilde{x}^2} u(\tilde{x}) \quad (2.71)$$

where R_c is the radius of curvature of the neutral plane [110]. To check this statement we can consider the beam deflection caused by a positive shear force $V_{\tilde{z}}$ applied to the tip of a cantilever (see (2.67)) and obtain

$$P(\tilde{x}, \tilde{z}) = \frac{\tilde{z}V_{\tilde{z}}}{I_{\tilde{z}}}(l - \tilde{x}) \quad (2.72)$$

using the relation from (2.71). This is the exact same result as the one we got by consideration of external moments and we will later use this simple relation to extract stress profiles of an externally driven cantilever beam.

2.5.2. Strain and stress under external driving

While static cantilever bending constitutes an important tool to characterize the coupling mechanism of our hybrid system, most of our experiments rely on AC strain fields. To create such AC strain fields the cantilever is externally driven, and its oscillatory amplitude $\tilde{u}(\tilde{x}, t)$ now not only depends on spatial position \tilde{x} but also on time t . The general equation of motion for a long thin beam of uniform cross section that is oscillating in one dimension is

$$EI \frac{\partial^4}{\partial x^4} \tilde{u}(\tilde{x}, t) + \rho A \frac{\partial^2}{\partial t^2} \tilde{u}(\tilde{x}, t) = F(\tilde{x}, t) \quad (2.73)$$

where $A = wt$ is the cross-sectional area, ρ the density of the beam's material, E the corresponding Young's modulus, I the moment of inertia and $F(\tilde{x}, t)$ is an arbitrary, external driving force [110, 115]. Note that (2.73) describes both in-plane and out-of-plane vibrations of the beam. Out-of-plane modes oscillate along the $\mathbf{e}_{\tilde{z}}$ direction and are characterized by $I_{\tilde{z}} = wt^3/12$ whereas in-plane deflections along $\mathbf{e}_{\tilde{y}}$ go with $I_{\tilde{y}} = tw^3/12$. In the following we use the common ansatz $\tilde{u}(\tilde{x}, t) = \tilde{u}(\tilde{x})\tilde{u}(t)$ and treat the time-dependent part $\tilde{u}(t)$ and spatial component $\tilde{u}(\tilde{x})$ of (2.73) separately.

Spatial dependence of deflection $\tilde{u}(\tilde{x})$

To find an expression for the spatial component $\tilde{u}(\tilde{x})$ we solve the wave equation (2.73), choosing the ansatz $\tilde{u}(\tilde{x}, t) = \tilde{u}(\tilde{x})e^{-i\omega_m t}$.¹⁴ In this case the spatial component $\tilde{u}(\tilde{x})$ must satisfy the differential equation

$$\frac{\partial^4}{\partial x^4} \tilde{u}(\tilde{x}) = \left(\frac{\rho A}{EI} \right) \omega_m^2 \tilde{u}(\tilde{x}). \quad (2.74)$$

Defining $\beta = (\rho A/EI)^{1/4} \omega_m^{1/2}$ and choosing the Ansatz $\tilde{u}(\tilde{x}) \propto \exp(\kappa \tilde{x})$ we find the general solution

$$\tilde{u}(\tilde{x}) = \tilde{a} \cos(\beta \tilde{x}) + \tilde{b} \sin(\beta \tilde{x}) + \tilde{c} \cosh(\beta \tilde{x}) + \tilde{d} \sinh(\beta \tilde{x}) \quad (2.75)$$

with amplitudes $\tilde{a}, \tilde{b}, \tilde{c}, \tilde{d}$ to be determined by imposing boundary conditions [110]. For our cantilever $\tilde{u}(0) = 0$, $\frac{d}{d\tilde{x}} \tilde{u}(0) = 0$, $\frac{d^2}{d\tilde{x}^2} \tilde{u}(l) = 0$, $\frac{d^3}{d\tilde{x}^3} \tilde{u}(l) = 0$ and we find that the allowed values for beta β_n are from a discrete set and satisfy

$$\cos(\beta_n l) \cosh(\beta_n l) + 1 = 0, \quad (2.76)$$

¹⁴In this simplified situation the cantilever is not driven, but oscillates freely. For the driven solution for $\tilde{u}(\tilde{x}, t)$ please refer to p. 293ff. in [110] or [115].

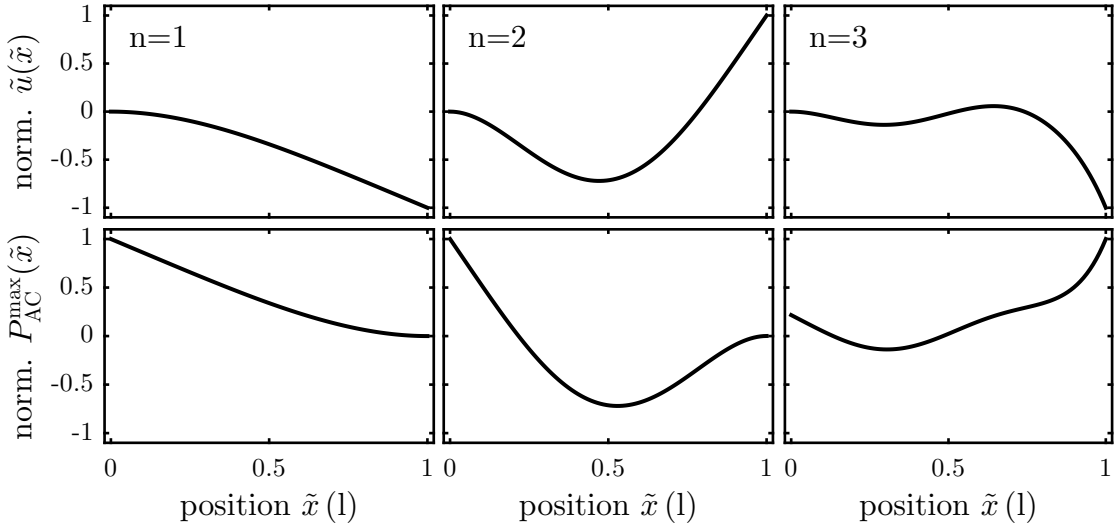


Figure 2.16.: Deflection (top) and stress (bottom) profiles, normalized to maximum values, for the first three eigenmodes of an externally driven cantilever.

which has the numerical solutions $\beta_n l = 1.875, 4.694, 7.855, 10.996$ for $n = 1, 2, 3, 4$. As β_n takes discrete values the cantilever's eigenfrequency $\omega_{m,n}$ does as well, following the relation

$$\omega_{m,n} = \sqrt{\frac{EI}{\rho A}} \beta_n^2. \quad (2.77)$$

Furthermore, the amplitudes are given by $\tilde{a}_n = -\tilde{c}_n$ and $\tilde{b}_n = -\tilde{d}_n$ and

$$\tilde{u}_n(\tilde{x}) = \tilde{a}_n (\cos(\beta_n \tilde{x}) - \cosh(\beta_n \tilde{x})) + \tilde{b}_n (\sin(\beta_n \tilde{x}) - \sinh(\beta_n \tilde{x})) \quad (2.78)$$

where $\tilde{a}_n/\tilde{b}_n = -1.3622, -0.9819, -1.008, -1.000$ for the first four eigenmodes [110].

Since we now know the spatial component $\tilde{u}(\tilde{x})$ we can compare the different eigenmodes with respect to their stress profiles. To that end we employ (2.71) and find the expression

$$P_{AC}^{\max}(\tilde{x}) = \gamma_n \left[-\cos(\beta_n \tilde{x}) - \cosh(\beta_n \tilde{x}) + \frac{\tilde{b}_n}{\tilde{a}_n} (-\sin(\beta_n \tilde{x}) - \sinh(\beta_n \tilde{x})) \right] \quad (2.79)$$

with $\gamma_n = \tilde{a}_n \beta_n^2 E t / 2$. Deflection and stress profiles for the first three eigenmodes, normalized to their maximum values, are shown in Fig. 2.16. One can clearly see that the induced stress varies along the cantilever depending on the excited mode. For example, it is maximized close to the cantilever's root for the first and second eigenmode but minimized for the third. Also for $n > 1$ stress is varying between tension and compression when moving along the beam. For experimental reasons we focus on the first eigenmode and thus work with NV centers that are positioned as close as possible to both the cantilever's root and its top or bottom surface.

Time dependence of deflection $\tilde{u}(t)$ without external driving

To investigate the time-dependent component $\tilde{u}(t)$ of (2.73), we employ the concept of effective mass and approximate our cantilever by a point mass $m_{\text{eff},n}$ that is placed

at the point of maximum deflection, i.e. at $\tilde{x} = l$, and connected to a spring with the effective spring constant $k_{\text{eff},n}$. For one-dimensional motion of a resonator with uniform cross-sectional area A , the effective mass of the n -th resonator mode is given by [115]

$$m_{\text{eff},n} = \rho A \int_0^l d\tilde{x} |\tilde{u}_n(\tilde{x})|^2 \quad (2.80)$$

where $\tilde{u}(\tilde{x})$ describes the spatial mode profile of the resonator mode. For example, when considering cantilever beams (see (2.78)), we find $m_{\text{eff},n}/m_0 = 0.25$ where $m_0 = \rho w l t$ is the geometric mass of the beam [115]. As the ratio $m_{\text{eff},n}/m_0$ is constant for all modes, we usually refer to the effective mass as m_{eff} .

Approximating the cantilever by a point mass of mass m_{eff} placed at the point of maximum deflection allows using the formalism developed for a classical, damped harmonic oscillator. When considering free oscillations, the time-dependent deflection $\tilde{u}(t)$ of the oscillator is described the differential equation

$$\ddot{\tilde{u}}(t) + 2\Gamma_m \dot{\tilde{u}}(t) + \omega_m^2 \tilde{u}(t) = 0 \quad (2.81)$$

where $\Gamma_m = b/2m_{\text{eff}}$ is the oscillator's damping rate. b characterizes the damping force and $\omega_m = \sqrt{k_{\text{eff}}/m_{\text{eff}}}$ represents the undamped eigenfrequency [116]. With the Ansatz $\tilde{u}(t) = A \exp(i\omega t)$ we find the general solution

$$\tilde{u}(t) = \left(\tilde{A}_1 e^{i\omega_{\text{eff}} t} + \tilde{A}_2 e^{-i\omega_{\text{eff}} t} \right) e^{-\Gamma_m t} \quad (2.82)$$

where $\omega_{\text{eff}} = \sqrt{\omega_m^2 - \Gamma_m^2}$ is the effective frequency at which the resonator oscillates and the amplitudes $\tilde{A}_{1,2}$ have to be determined by imposing boundary conditions. One recognizes that the resonator oscillates at a smaller frequency compared to its undamped eigenfrequency and that its oscillations damp out on a timescale $T_{\text{damp}} = 1/\Gamma_m$. We can further distinguish between three regimes with respect to the ratio Γ_m/ω_m :

- For weak damping, $\Gamma_m/\omega_m < 1$, we work in the so-called underdamped regime. The resonator oscillates at frequency ω_{eff} and its amplitude gradually decreases to zero.
- For $\Gamma_m/\omega_m = 1$ the oscillator is critically damped and returns to a steady state as quickly as possible. Oscillations do not occur, but overshoots can be observed.
- When $\Gamma_m/\omega_m > 1$ the oscillator returns to a steady state and no oscillations occur. This process, however, takes significantly longer than for critical damping.

Because the resonator we work with in our experiments resides in the underdamped regime, we restrict our following discussion to this particular case. With the boundary conditions $\tilde{u}(t=0) = \tilde{A}$ and $\dot{\tilde{u}}(t=0) = 0$ we find the solution

$$\tilde{u}_0(t) = \tilde{A} \cos(\omega_{\text{eff}} t) e^{-\Gamma_m t}. \quad (2.83)$$

It is common to introduce the quality factor Q , which compares the energy that is stored in the oscillator with the amount of energy that is lost during one oscillation cycle. For a weakly damped harmonic oscillator it can be approximated with $Q \approx \omega_m/2\Gamma_m$ (see App. A.4) [116].

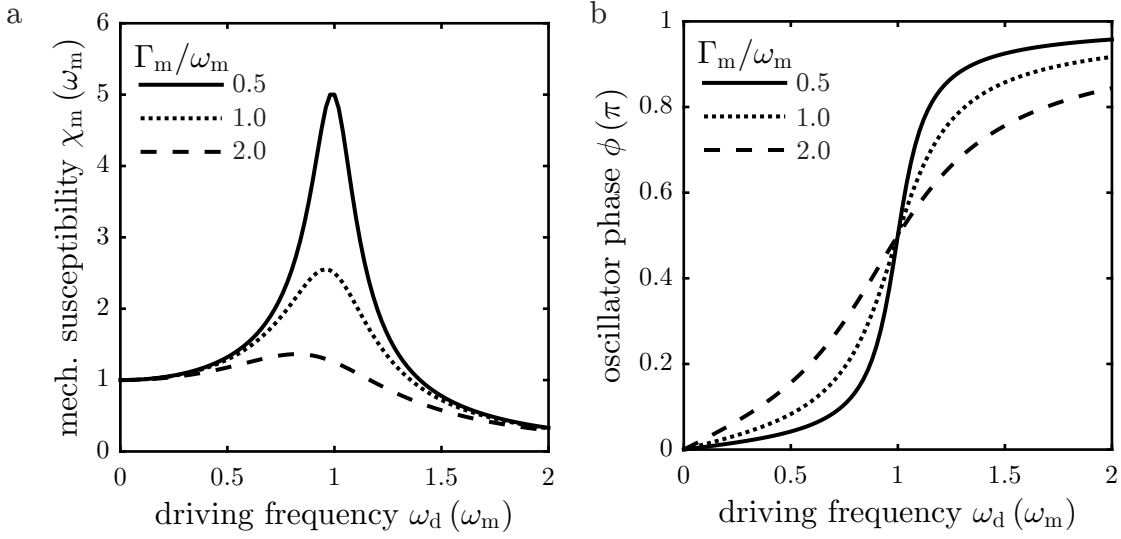


Figure 2.17.: Amplitude and phase spectrum of a driven, damped harmonic oscillator. a) The oscillation amplitude peaks at $\omega_d = \omega_{\text{res}} = \sqrt{\omega_m^2 - 2\Gamma_m^2}$. For decreased damping the peaking behavior becomes more pronounced and the resonance frequency approaches the undamped eigenfrequency. Low frequency driving always induces small oscillations while for high driving frequencies the resonator cannot follow the external drive and no deflection occurs. b) The phase difference between oscillator and driving force exhibits a similar behavior. The oscillator follows the force for low driving frequencies and thus oscillations are induced. Fast driving however causes the oscillator to oscillate fully out of phase and its oscillation amplitude approaches zero. Strong damping broadens the transition region from in phase to out of phase oscillations.

Time dependence of deflection $\tilde{u}(t)$ with external driving

In our experiment we excite the cantilever through external driving, modeled by a force $F(t) = F_0 \cos(\omega_d t)$ oscillating at the driving frequency ω_d . To include the driving force we modify (2.81) and obtain the differential equation

$$\ddot{\tilde{u}}(t) + 2\Gamma_m \dot{\tilde{u}}(t) + \omega_m^2 \tilde{u}(t) = \tilde{F} \cos(\omega_d t) \quad (2.84)$$

with $\tilde{F} = F_0/m_{\text{eff}}$ [116]. The solution of this equation is of the form

$$\tilde{u}(t) = \tilde{u}_0(t) + \tilde{u}_F(t) \quad (2.85)$$

where $\tilde{u}_0(t)$ denotes the solution of the free harmonic oscillator (see (2.83) or (2.82)) and $\tilde{u}_F(t)$ describes the cantilever's reaction to external driving. Choosing the Ansatz $\tilde{u}_F(t) = D \cos(\omega_d t - \phi)$ we find

$$\tilde{u}_F(t) = \frac{\tilde{F}}{\sqrt{(\omega_m^2 - \omega_d^2)^2 + (2\Gamma_m \omega_d)^2}} \cos \left[\omega_d t - \arctan \left(\frac{2\Gamma_m \omega_d}{\omega_m^2 - \omega_d^2} \right) \right] \quad (2.86)$$

(see App. A.4 for a detailed derivation). As (2.86) only contains undamped, oscillating terms whereas $\tilde{u}_0(t)$ is a damped oscillation, the free oscillations will disappear

due to damping, and $\tilde{u}_F(t)$ is the steady-state solution of the driven harmonic oscillator.

We want to finish this part of our discussion with two short comments important for our experimental work. First, the parameter $\chi(\omega_d) = D/\tilde{F}$ is usually called the mechanical susceptibility and links oscillation amplitude D and driving frequency ω_d . As one can easily check, the resonator's amplitude peaks when driven at $\omega_{\text{res}} = \sqrt{\omega_m^2 - 2\Gamma_m^2}$, which is slightly below the undamped eigenfrequency. For decreased damping the peaking behavior becomes more pronounced (see Fig. 2.17a). As strain and stress are proportional to the cantilever's oscillation amplitude D we choose $\omega_d \approx \omega_{\text{res}}$. Second, the Q factor for the driven harmonic oscillator is given by $Q = \omega_m/2\Gamma_m$ if the resonator is excited at its undamped eigenfrequency. One can show that weak damping allows the approximation $Q \approx \omega_m/\Delta\omega_d$ where $\Delta\omega_d$ is the width of the amplitude distribution $D(\omega_d)$ (see App. A.4). In other words, we can obtain a good approximation for the Q factor of our resonator by measuring the amplitude response to driving frequency and extracting $\Delta\omega_d$ from $D(\omega_d)$.

2.6. Hybrid spin-oscillator systems in the quantum regime

2.6.1. Energy quantization of the harmonic oscillator

Before we discuss possible, strain-based cooling schemes for our hybrid device, we need to introduce the energy quantization of our harmonic oscillator and derive its zero-point fluctuations Δx_{zpm} . The latter are an important benchmark for the estimation of the stress-induced single phonon coupling strength and thus the question whether or not we can perform experiments in the quantum regime with our hybrid system. The total energy of a classical, free harmonic oscillator (see (2.81)) is

$$E_{\text{tot}} = \frac{p^2}{2m_{\text{eff}}} + \frac{k_{\text{eff}}}{2} x^2 \quad (2.87)$$

where p denotes the momentum and x the oscillator's position.¹⁵ For the transition to the quantum world we make use of the correspondence principle and transform the classical variables into their quantum mechanical counterparts, i.e. $x \rightarrow \hat{x}$ and $p \rightarrow \hat{p}$ with

$$\hat{x} = \sqrt{\frac{\hbar}{2m_{\text{eff}}\omega_m}} (\hat{a} + \hat{a}^\dagger) \quad (2.88)$$

and

$$\hat{p} = \frac{\sqrt{2m_{\text{eff}}\hbar\omega_m}}{2i} (\hat{a} - \hat{a}^\dagger). \quad (2.89)$$

\hat{a}^\dagger and \hat{a} are the creation and annihilation operators of phonons in the eigenmode with frequency ω_m . The Hamiltonian of the harmonic oscillator can then be written as

$$\hat{H}_{\text{ho}} = \hbar\omega_m \left(\hat{a}^\dagger \hat{a} + \frac{1}{2} \right) \quad (2.90)$$

¹⁵Note that we denote the oscillator's position with x instead of \tilde{u} in order to follow the standard notion for a one-dimensional harmonic oscillator.

where $\hat{n} = \hat{a}^\dagger \hat{a}$ denotes the number of phonons in mode ω_m . When \hat{H}_{ho} acts on the energy eigenstates $|n\rangle$ of the system

$$\hat{H}_{\text{ho}}|n\rangle = E_n|n\rangle = \hbar\omega_m \left(n + \frac{1}{2} \right) |n\rangle \quad (2.91)$$

we see that even for $n = 0$ phonons in mode ω_m the system has a non-zero energy $E_0 = \hbar\omega_m/2$, which is therefore called the zero-point energy. We further realize that the mechanical oscillator is characterized by a quantized energy ladder where the levels are spaced by the energy of one phonon or $\hbar\omega_m$ for $n > 1$.

The non-zero ground state energy gives rise to the zero-point motion Δx_{zpm} , which describes the Gaussian-distributed position of the oscillator around the origin in phase space. This is a consequence of the Heisenberg uncertainty relation $\Delta x \Delta p \geq \hbar/2$ and we can thus use the latter in combination with (2.87) to find

$$\Delta x_{\text{zpm}} = \sqrt{\frac{\hbar}{2m_{\text{eff}}\omega_m}}. \quad (2.92)$$

Due to the interaction of the resonator with its environment of temperature T , it is in general hard to measure Δx_{zpm} as the resonator is usually not in its ground state, but in a state of thermal equilibrium with mean phonon number

$$n_{\text{th}} = \left(e^{\frac{\hbar\omega_m}{k_B T}} - 1 \right)^{-1} \quad (2.93)$$

in mode ω_m . Consequently, if the phonon number $n < n_{\text{th}}$, the corresponding mode will be heated and n follows the equation

$$\frac{d}{dt}n(t) = -2\Gamma_m(n(t) - n_{\text{th}}) \quad (2.94)$$

where $2\Gamma_m = \omega_m/Q$ quantifies the resonator's coupling to the thermal bath (see App. A.4). Assuming the resonator to be initially in its ground state with $n(t=0) = 0$, the evolution of the mean phonon number is described by

$$n(t) = n_{\text{th}}(1 - e^{-2\Gamma_m t}) \quad (2.95)$$

and we can express the thermal heating rate or thermal decoherence rate γ_{th} as

$$\gamma_{\text{th}} = \frac{d}{dt}n(t) = 2\Gamma_m n_{\text{th}} \simeq \frac{k_B T}{\hbar Q} \quad (2.96)$$

where we used the high-temperature limit in which $n_{\text{th}} \simeq k_B T / \hbar\omega_m$ [29]. Note that γ_{th} is given in units of $\text{Hz} \times \text{rad}$.

2.6.2. Bringing the resonator to its motional ground state

A key long-term goal for our hybrid mechanical devices is to cool and study the mechanical resonator close to its quantum ground state, where the number of phonons n in the resonator's mode of interest is < 1 . The thermal occupation number n_{th} of a resonator mode with frequency ω_m at temperature T (see (2.93)) is however well

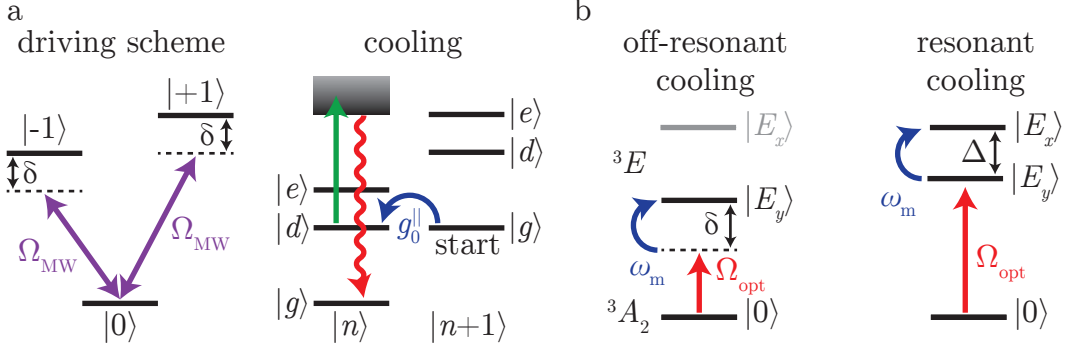


Figure 2.18.: Cooling schemes for NV-mechanical oscillator hybrid systems. a) In the S=1 ground state two MW fields with equal Rabi frequency Ω_{MW} and detuning δ address the $|0\rangle \leftrightarrow |\pm 1\rangle$ spin transitions, thereby creating new eigenstates $|d\rangle$, $|g\rangle$ and $|e\rangle$. For $\omega_{dg} \approx \omega_m$, longitudinal strain coupling enables the transition $|g\rangle|n+1\rangle \rightarrow |d\rangle|n\rangle$, effectively removing one phonon per scattering event from the resonator mode. Subsequent optical pumping restarts a cycle and the resonator is cooled. b) Phonon cooling schemes in the S=1 excited state are built on longitudinal and transverse coupling to the NV’s orbital degree of freedom. In the off-resonant cooling scheme a laser of optical Rabi frequency Ω_{opt} is detuned from the $|0\rangle \leftrightarrow |E_y\rangle$ transition by $\delta = -\omega_m$. Longitudinal strain removes a phonon from the resonator and the NV decays via spontaneous emission. In the resonant cooling scheme, the $|E_x\rangle$ and $|E_y\rangle$ orbital states are separated by $\Delta = \omega_m$, for example through an external electric field. A laser applied resonantly to the $|0\rangle \leftrightarrow |E_y\rangle$ transition prepares the NV in the $|E_y\rangle$. Transverse strain then excites the NV to the $|E_x\rangle$ state under removal of a resonator phonon.

above unity even if a GHz-resonator is cooled to mK-temperatures.¹⁶ Obviously, working with higher frequency resonators and/or lower environmental temperatures can do the trick, as demonstrated in [17]. Yet working under such extreme conditions is in general very challenging and cannot always be realized. Conventional cooling is therefore considered to be an essential prerequisite for bringing the resonator to its quantum ground state, but additional cooling techniques are required.

Strain coupling in principle allows for realizing such cooling schemes in both the S=1 ground and excited states. In the ground state a combination of optical pumping, MW driving and longitudinal strain was proposed for this purpose (see Fig. 2.18a) [13, 76]. Two MW fields with driving strength Ω_{MW} and detuning δ address the $|0\rangle \leftrightarrow |\pm 1\rangle$ spin transitions and create the dark state $|d\rangle = (|+1\rangle - |-1\rangle)/\sqrt{2}$ as well as the dressed states $|g\rangle = \cos\theta|0\rangle - \sin\theta(|+1\rangle + |-1\rangle)/\sqrt{2}$ and $|e\rangle = \sin\theta|0\rangle + \cos\theta(|+1\rangle + |-1\rangle)/\sqrt{2}$ with $\tan\theta = -\sqrt{2}\Omega_{\text{MW}}/\delta$. The eigenenergies $\hbar\omega_{|g\rangle,|e\rangle} = \hbar(-\delta \pm \sqrt{\delta^2 + 2\Omega^2})/2$ and $\hbar\omega_{|d\rangle} = -\hbar\delta$ can be tuned via the parameters δ and Ω_{MW} (for $\delta < 0$, $|g\rangle$ is the lowest state in energy). If $\omega_{dg} = \omega_{|d\rangle} - \omega_{|g\rangle}$ becomes comparable to the mechanical frequency ω_m , spin-phonon interactions of strength $g_0^{\parallel} \propto M_{\epsilon,z}^{\text{gs}}$ enable the transition $|g\rangle|n+1\rangle \rightarrow |d\rangle|n\rangle$ where $|n\rangle$ denotes the state of the mechanical resonator with n phonons. The cooling protocol itself begins with an optical pulse, which resonantly excites the NV to its excited state manifold,

¹⁶ $k_B T/h = 20.9 \text{ GHz/K}$, so for $T = 100 \text{ mK}$ and $\omega_m/2\pi = 1 \text{ GHz}$, $n_{\text{th}} = 12.6$.

to initialize the system in $|g\rangle|n+1\rangle$. The transition $|g\rangle|n+1\rangle \rightarrow |d\rangle|n\rangle$ then cools the mechanical mode and a second laser pulse brings the system into $|g\rangle|n\rangle$. Repeating this cycle is predicted to cool MHz frequency mechanical resonators to their ground state if the initial temperature of the system is low ($T < 1$ K) and the system resides in the strong coupling regime, in which the coupling strength g_0^\parallel is larger than both the thermal decoherence rate γ_{th} of the mechanical resonator (see (2.96)) and the spin decoherence rate of the NV center [76].

Working with strain coupling to the NV's orbital degree of freedom allows realizing two additional cooling schemes which involve the $|0\rangle$ spin sublevel of the S=1 ground state as well as the $|E_x\rangle$ and $|E_y\rangle$ orbital states (see Fig. 2.18b) [49, 95]. In the off-resonant cooling scheme a laser with optical Rabi frequency Ω_{opt} is detuned from the $|0\rangle \leftrightarrow |E_y\rangle$ transition by $\delta = -\omega_m$. Longitudinal strain coupling thus enables a phonon-assisted transition to the $|E_y\rangle$ level under removal of a resonator phonon. The excited NV center subsequently relaxes back to the ground state through spontaneous emission of a photon. The cooling rate Γ_\parallel is found to be

$$\Gamma_\parallel = \frac{1}{4\pi^2} \frac{g_0^{\parallel 2} \Omega_{\text{opt}}^2}{\Gamma_{\text{NV}} \omega_m^2} \quad (2.97)$$

where Γ_{NV} is the lifetime-limited decay rate of the optical transition and $g_0^\parallel \propto M_{\epsilon_i z}^{\text{es}}$ describes the longitudinal strain-orbit coupling strength (see App A.7) [49, 105].¹⁷ The off-resonant cooling scheme requires the system to reside in the resolved sideband regime, where $\omega_m > \Gamma_{\text{NV}}$ such that the red sideband of the transition can be addressed without driving the carrier. It also requires the system to be in a regime of high cooperativity $C = g_0^{\parallel 2} / 2\pi\gamma_{\text{th}}\Gamma_{\text{NV}} > 1$ (see (3.20)). These requirements reveal significant challenges of the off-resonant cooling scheme. Reaching the high cooperativity regime usually demands the usage of very small resonator structures with eigenfrequencies in the GHz range. Large ω_m , however, lead to a strong decrease of Γ_\parallel and cooling the resonator off-resonantly becomes less efficient.

To overcome this drawback, a second cooling scheme was proposed (see Fig. 2.18b). A laser resonantly drives the $|0\rangle \leftrightarrow |E_y\rangle$ transition and thus prepares the system in $|E_y\rangle$. Transverse strain couples the $|E_x\rangle$ and $|E_y\rangle$ levels if their frequency difference Δ is tuned to the phonon frequency ω_m . In this case the system is excited to the $|E_x\rangle$ state by removing a single phonon from the resonator. The associated cooling rate Γ_\perp is found to be

$$\Gamma_\perp = \frac{1}{4\pi^4} \frac{g_0^{\perp 2} \Omega_{\text{opt}}^2}{\Gamma_{\text{NV}}^3} \quad (2.98)$$

and does not depend on the phonon frequency ω_m anymore. Note that both off-resonant and resonant cooling schemes were proposed to utilize strain coupling to the NV's S=1 excited state. Yet it should in principle be possible to realize similar schemes in the S=1 ground state as both strain components exist there as well. In such schemes, the long spin lifetime T_1 prohibits spontaneous relaxation of the absorbed phonon energy. This obstacle could be overcome via external optical pumping, similar to the scheme proposed in [76] and presented in Fig. 2.18a.

¹⁷In the equations for Γ_\perp and Γ_\parallel , we define Γ_{NV} in units of Hz and g_0^\parallel , ω_m and Ω_{opt} in units of $\text{Hz} \times \text{rad}$.

Finally, we would like to quickly discuss the prospects of transverse strain. Two of the three cooling schemes presented above hinge upon the existence of longitudinal coupling and can therefore be realized with strain and magnetic field gradients. Transverse strain coupling, however, distinguishes our hybrid system, because it does not exist in the case of magnetic coupling. Additionally, transverse strain not only serves as the foundation for the resonant cooling scheme shown in Fig. 2.18b, it was also predicted to lead to unusual spin dynamics as well engineered, long-range interactions between distant qubits [117, 118]. In particular, Hamiltonian (2.32) indicates that transverse strain couples the $|\pm 1\rangle$ spin sublevels in the $S=1$ ground state. This transition is characterized by $\Delta m_s = \pm 2$ and is thus difficult to drive with conventional transverse MW fields. Combining magnetic field and strain driving hence allows studying multi-level dynamics in a closed-contour interaction scheme, in which all three spin transitions are addressed by individual, coherent driving fields (see Chap. 5). Such driving schemes are fundamentally interesting and can have impact on sensing applications, but due to selection rules have been barely studied so far. The action of transverse strain on NV spin ensembles can furthermore be used to generate spin-squeezed states in large ensembles of NV centers. These states are characterized by a reduced spin variance along one quadrature and could enable for example magnetometry with a precision below the quantum projection noise limit. Such experiments, however, require working in a regime with high cooperativity C and with a large number of spins with ideally identical reaction to transverse strain. Squeezed states can be created if the squeezing parameter $\xi = 2/\sqrt{JC} < 1$, where J is the total spin angular momentum [118].

3. Characterizing spin-strain coupling

In this chapter we introduce our experimental approach to realize a hybrid spin-oscillator system and characterize the coupling of a diamond cantilever to the spin degree of freedom of embedded NV centers through crystal strain. We start with a brief overview of sample fabrication and discuss persisting challenges that need to be addressed for future experiments, followed by a short explanation of the employed measurement techniques. We then present an analysis, that is based on DC strain, of the coupling mechanism and quantify the spin-strain coupling strength of our hybrid device. Furthermore, we demonstrate operation in the resolved sideband regime by applying AC strain. We finish this chapter by examining the prospects of our system to perform experiments in the quantum regime and discuss the possibility to reach the strong coupling regime in the $S=1$ NV ground state.

3.1. Experimental methods

3.1.1. Sample fabrication

Our group's general approach to diamond fabrication is well presented in [119], and we will not discuss it here in detail. Yet [119] focuses on the fabrication of all-diamond scanning probes for nanoscale magnetometry and in such the fabrication process and related problems differ slightly from ours. We therefore sketch our fabrication procedure here and highlight the existing issues we are facing.

Our process starts with $4 \times 4 \text{ mm}^2$ single-crystal, ultra-pure diamond slabs grown along the [001] direction and polished to a thickness of $\sim 50 \mu\text{m}$. Internal crystal stress, resulting from the polishing, is limited to a minimum by performing a stress relief etch where $\sim 5 \mu\text{m}$ of material is removed. Shallow NV centers are created by implantation of ^{14}N ions at 12 keV, resulting in NV depths of $(17 \pm 6) \text{ nm}$ (calculated with SRIM [120]), and subsequent annealing in high vacuum ($p \approx 1 \cdot 10^{-7} \text{ mbar}$) up to 1200°C for several hours (Fig. 3.1).

Prior to structuring cantilevers, we thin down further a $700 \times 1000 \mu\text{m}^2$ large area of the diamond slab to $\sim 10 \mu\text{m}$ using inductively coupled reactive ion etching (ICP-RIE, Sentech SI 500), where we alternate between argon chlorine (ArCl_2) and oxygen (O_2) chemistry. During this deep etch, as well as throughout all following etching steps, the not-to-be-etched parts of the diamond slab are protected with a $100 \mu\text{m}$ thick, lasercut quartz mask (SPI, #01006-AB). To protect the NV centers from plasma damage, the NV sample side is coated with a protective double layer of 5 nm chromium (Cr) and 50 nm gold (Au) using an e-beam evaporation system (AJA International). From here on, several steps (Fig. 3.2) are necessary to fabricate cantilevers. First, we apply a $\sim 500 \text{ nm}$ thick layer of FOX-16 negative electron beam resist (Dow Corning) onto the resulting membrane via spin-coating. TI Prime (MicroChemicals) serves as an adhesion promoter and is applied prior to spinning

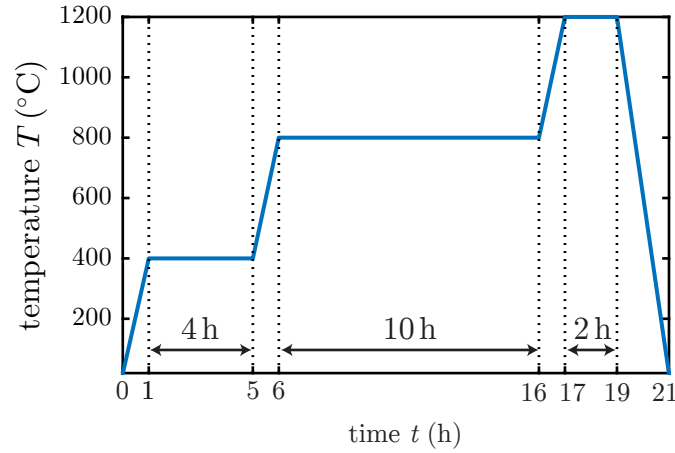


Figure 3.1.: Sample annealing procedure for NV creation. Annealing is performed in high vacuum with a base pressure of $p \approx 1 \cdot 10^{-7}$ mbar. Ramp times are vary between 1 h and two 2 h, depending on whether temperature is increased or decreased.

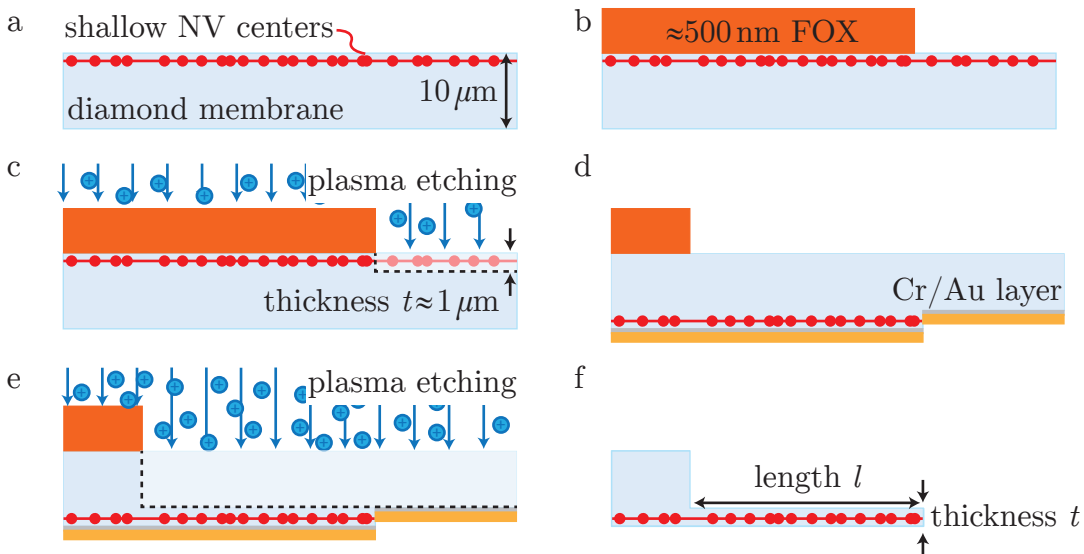


Figure 3.2.: Cantilever fabrication procedure. a) We usually start with a $\sim 10 \mu\text{m}$ thick diamond membrane that contains shallow implanted NV centers. b+c) Cantilever etch masks, written with e-beam lithography, are transferred about $t = 1 \mu\text{m}$ deep into the diamond membrane using oxygen reactive ion etching. t determines the final cantilever thickness d) A protective double layer of 5 nm chromium and 50 nm gold is applied to the NV side of the membrane and another etch mask, necessary to create a step at the cantilevers' roots, is patterned onto the membrane's backside. e+f) Oxygen reactive ion etching is used to release the cantilevers.

Table 3.1.: Spincoating parameters for e-beam resist FOX-16. TI Prime increases adhesion between FOX and the diamond surface. This recipe results in layers of about 500 nm thickness.

step	material	rotational speed (RPM)	spinning time (sec)	baking time(sec) / temperature (°C)
1	TI Prime	6000	60	120/120
2	FOX	6000	60	300/90
3	FOX	6000	60	600/90

the resist (Tab. 3.1). After spin-coating, we use e-beam lithography (30 keV, 10 μm aperture) and subsequent developing for 30 sec in a tetramethylammonium hydroxide solution (Sigma-Aldrich) to pattern cantilever etch masks into the e-beam resist. Second, we employ oxygen plasma etching to transfer the cantilever etch masks into the diamond membrane. The etch depth $t \approx 1 \mu\text{m}$ determines the thickness of the final cantilever structures. To decouple the cantilevers as best as possible from the bulk material and thus to increase their Q , we fabricate a step in thickness at the cantilevers' bases. To that end we again coat the membrane's NV side with a protective Cr/Au layer, flip the diamond and fabricate another set of etch masks on it. The Cr/Au layer protects the NV centers from being etched away in the following oxygen plasma step that releases the cantilevers. The cantilevers we employ are 3 – 5 μm wide, 0.5 – 1 μm thick and between 15 – 45 μm long (Fig. 3.3a). After fabrication and cleaning, the sample is attached to a small silicon (Si) chip (SPI, crystalbond 509) to ensure safe handling.

While our current cantilever quality is sufficient for the work presented in this thesis, our future endeavors require high Q resonators. Significant improvements to our fabrication procedure are thus required to overcome presently existing issues (Fig. 3.3). High Q devices are characterized by a high surface quality and minimized clamping losses to the substrate [45–47]. Our current cantilevers do not meet these criteria and suffer from three main problems. First, the FOX layer detaches from the substrate while etching, leading to rounded edges and degraded NV centers in close proximity. Second, the physical plasma component is rather strong and leads to significant "trenching" at the cantilevers' roots. Such trenches cause a non-uniform cross section, constitute potential breaking points and in addition might alter the strain profile significantly. Third, the use of massive quartz protection masks results in a thickness gradient of up to 4 μm across the produced membrane. Consequently, our cantilevers usually show a slightly varying thickness transverse to their long axis, i.e. along their width.

There are even further issues not related to the Q factor. To protect the NV centers from plasma induced degradation we apply a Cr/Au protection layer to the membrane. This layer, however, does not seem to withstand the plasma treatment during a deep etch and we frequently encounter that it strongly degrades on the first $\sim 100 - 200 \mu\text{m}$ of the membrane. We have to assume that the NV centers in the corresponding area are affected, limiting our device yield. The last issue we

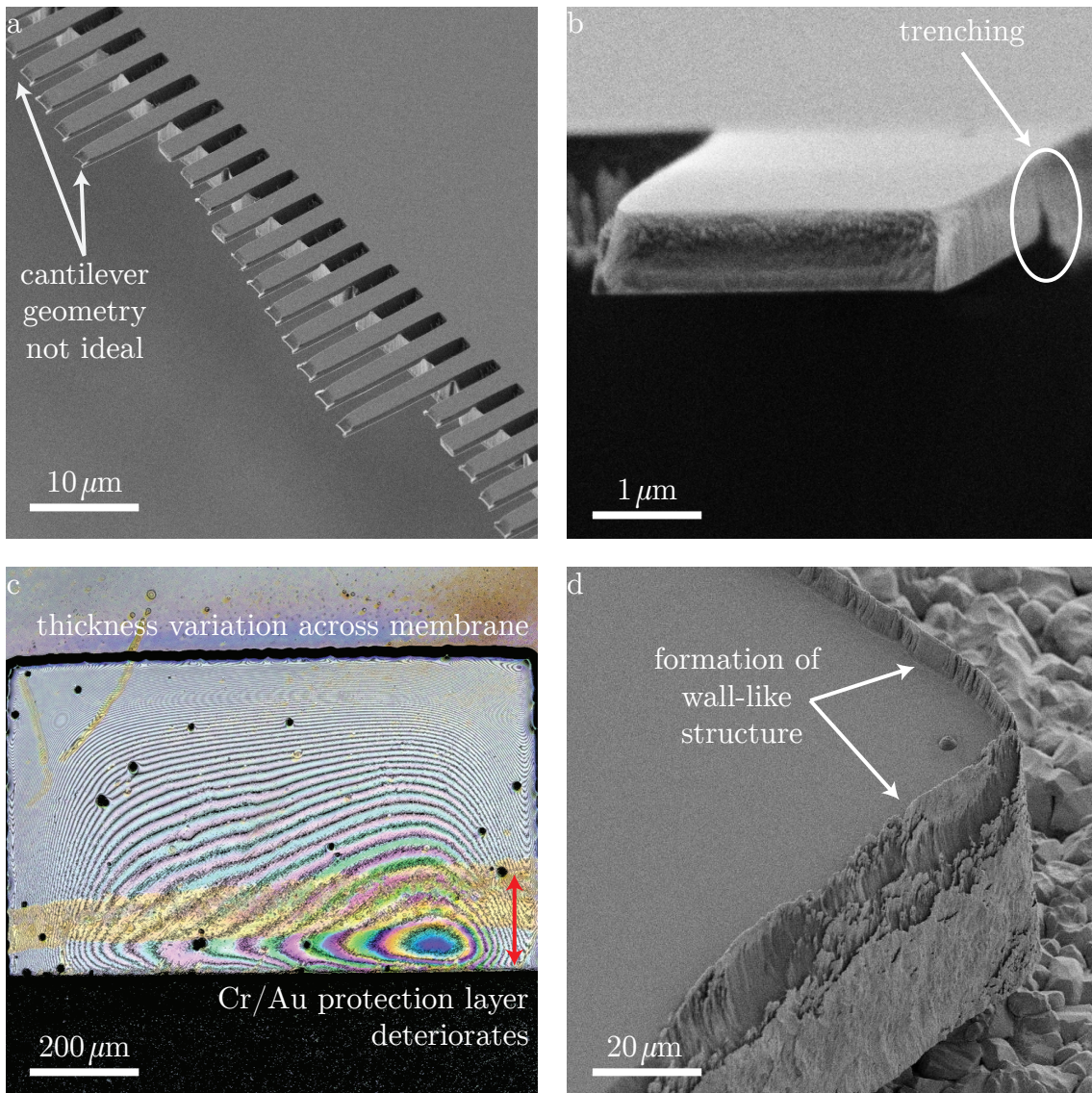


Figure 3.3.: Persisting fabrication issues. a) Scanning electron microscope image showing a typical sample after fabrication. Despite the application of TI Prime for adhesion improvement, the FOX layer lifts mainly at the cantilever tips while etching, resulting in rounded edges. b) Strong physical plasma components cause 100 – 200 nm deep trenches at the cantilevers' roots, creating potential breaking points. c) The usage of massive quartz protection masks leads to thickness variations of up to 4 μm across the membrane. Quite frequently we find that parts of the Cr/Au protection layer do not withstand the plasma treatment and we have to assume that NV centers in the corresponding areas strongly degrade. d) The physical component of the applied plasmas attacks the carrier wafer and sputters particles onto the diamond membrane, leading to the formation of wall-like structures predominantly at the membrane's edges.

want to mention here is related to the carrier wafer material of our etching reactor. To minimize surface roughness to below 1 nm we work with carrier wafers made from amorphous aluminum oxide. Reactive ion etching sputters the carrier wafer and Al_2O_3 particles adsorb onto the sample. Throughout our etching processes a massive, wall-like structure forms. Its presence is especially problematic when thin membranes are produced, as it needs to be physically removed for further processing, usually leading to significant membrane damage.

To overcome the presented issues, to minimize the number of fabrication steps, and to enable large area fabrication, we plan to employ the diamond-on-insulator technique from [45–47], where a diamond slab is bonded to a SiO_2 substrate using a thin SiO_2 intermediate layer. The whole diamond slab could then be thinned down to the desired cantilever thickness. In this case, quartz masks for protection are obsolete and thickness variations should be minimized. Implementing a plasma based on oxygen fluorine chemistry should help to avoid the formation of wall-like structures at the diamond's edges. Replacing TI Prime with a thin layer of titanium should solve the adhesion problem. Finally, a wet etching process of the SiO_2 layer underneath the sample could be employed to create the desired step at the cantilevers' roots. Note that the application of Cr/Au protection layers becomes obsolete if NV centers are implanted after bonding and subsequent thinning, but prior to cantilever structuring.

3.1.2. Measurement techniques

Scanning confocal microscopy

Our experiments are performed in a homebuilt confocal microscope setup at room temperature and at atmospheric pressure [121–123]. A 532 nm laser (Laser Quantum, Torus 200) is coupled into the confocal system through a dichroic mirror (Semrock, LM01-552-25). A microscope objective (Olympus, XLMFLN40x, NA= 0.8) is used to focus the laser light onto the sample, which is placed on a micropositioner (Attocube, ANSxyz100). Red fluorescence photons are collected by the same microscope objective, transmitted through the dichroic mirror and coupled into a single mode optical fibre (Thorlabs, SM600), which acts as a pinhole for confocal detection. Photons are detected using an avalanche photodiode (Excelitas, SPCM-AQRH-13). Scan control and data acquisition are achieved using a digital acquisition card (National Instruments, NI-6733). The microwave signal for spin manipulation is generated by a signal generator (Stanford Research Systems, SRS384), amplified (Mini-Circuits, ZHL-42W+) and delivered to the sample using a homebuilt near-field microwave antenna mounted on a manual xyz positioning stage. Laser, microwave and detection signals are gated using microwave switches (Mini-Circuits, ZASWA-2-50DR+), controlled through digital pulses generated by a fast pulse generator (SpinCore, PulseBlasterESR-PRO 500). Gating of the laser is achieved using a double pass acoustic optical modulator (Crystal Technologies, 3200-146). A permanent magnet placed in proximity to the sample allows introducing a Zeeman splitting. For better field control, we later replaced the permanent magnet with a set of Helmholtz coils (see Chap. 5).

AC and DC strain fields are at the heart of our experiments. To induce AC strain fields we mechanically excite our diamond cantilevers at their eigenfrequencies

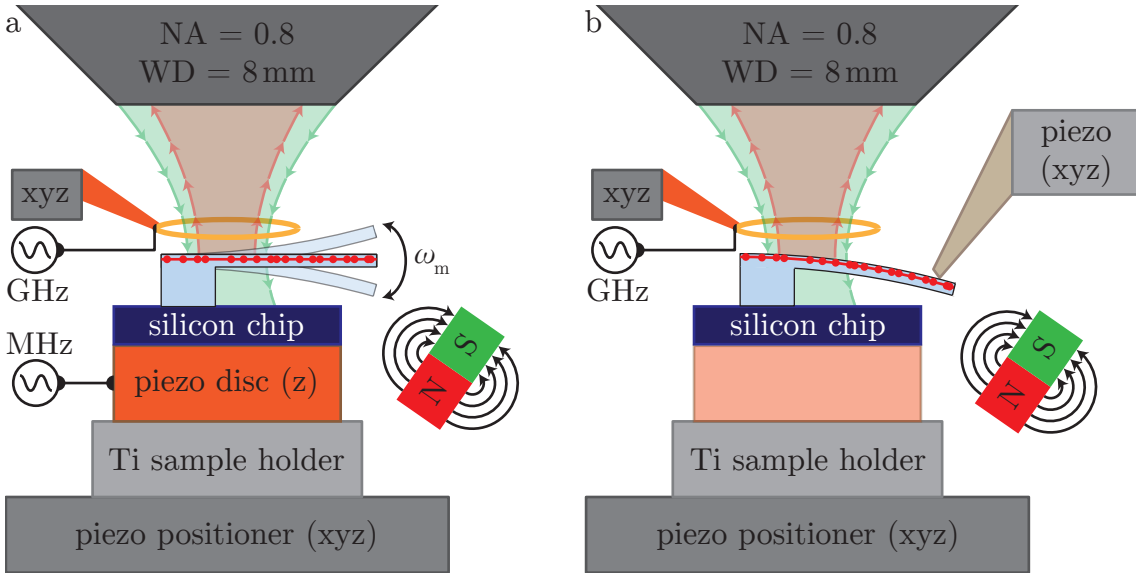


Figure 3.4.: Creation of AC and DC strain fields. a) AC strain fields are induced by mechanical excitation of the diamond cantilever at its mechanical eigenfrequency ω_m . To that end the cantilever is mounted on a piezoelectric disc that is driven by an AC voltage of variable amplitude and frequencies in the MHz range. b) A tungsten tip, mounted to a piezoelectric actuator, pushes the cantilever up or down and thus creates DC tensile or compressive strain at the NV's position.

$\omega_m/2\pi$ which are in the order of 1 – 10 MHz. To that end the sample is mounted on a piezoelectric disc (PI ceramics, PIC255) that is driven by an AC voltage V_{AC} (Keysight Technologies, 33622A). Varying V_{AC} controls the deflection amplitude and thus regulates the strain field's strength (see below). To ensure drift free, robust excitation we attach the piezoelectric disc to a titanium (Ti) sample holder, that is screwed onto the piezoelectric scanner, with a two-component epoxy (UHU, plus endfest). The sample itself is fixed to a Si chip, which in turn is glued to the piezoelectric disc with crystalbond (Fig. 3.4a). DC strain is created by static beam bending (Fig. 3.4b). We employ a tungsten tip (Omniprobe, Autoprobe 250) mounted on a piezoelectric actuator (Attocube, ANSxyz100) to statically bend the cantilever.

Optical readout of cantilever motion

To fully characterize strain coupling we determine the induced strain's amplitude via the cantilever deflection (compare (2.71)). For DC strain, the beam deflection is given by the applied piezo displacement of the tungsten tip as the tip's spring constant is orders of magnitude larger than the spring constant of the diamond cantilevers we employ [1].¹ For AC strain, we estimate the mechanical susceptibility χ_m of our cantilevers by monitoring the deflection of the non-clamped end of the

¹The cantilever spring constant is given by $k_{cant} = 3EI/l^3$. With $E = 1200$ GPa, $I = wt^3/12$ and $\{w, l, t\} = \{3, 1, 40\}$ μm we find $k_{cant} \approx 14$ N/m. To calculate k_{tip} , we approximate the tungsten tip by a tapered rod of circular cross section. Under this assumption, $k_{tip} = 3EIr^3/l^3$ where $r = d_{root}/d_{tip}$ is the ratio of the rods' diameters at root and tip and $I = \pi d_{tip}^4/64$. With $d_{root} = 500$ μm , $d_{tip} = 1$ μm , a taper of 10° and $E = 411$ GPa, we find $k_{tip} \approx 8200$ N/m.

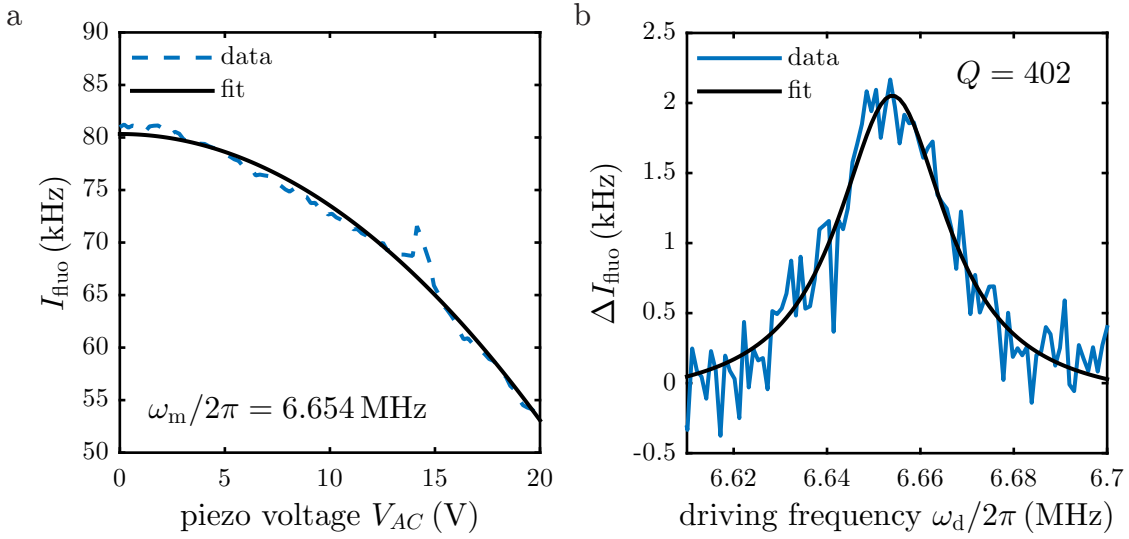


Figure 3.5.: Optical determination of mechanical susceptibility χ_m , cantilever eigenfrequency ω_m , and quality factor Q . a) To determine the mechanical susceptibility χ_m we record NV fluorescence I_{fluo} at the cantilever’s tip and vary the piezo voltage V_{AC} . The cantilever’s amplitude increases and the detected count rate drops, as the NV spends less time in the detection volume of our confocal microscope. We link χ_m to the detected count rate as described in the text and fit the recorded data accordingly. b) A similar approach is used to measure the cantilever’s eigenfrequency ω_m as well as its quality factor Q . We fix V_{AC} to a constant value, here 2 V, and sweep the driving frequency ω_d . The resulting curve can be fitted with a Lorentzian distribution to determine eigenfrequency and Q factor.

cantilever as a function of excitation voltage V_{AC} . To that end, we measure NV fluorescence originating from the cantilever end and record the drop in detected NV fluorescence as a function of V_{AC} . An approximate calibration of the cantilever excitation amplitude is then possible through the knowledge of the point-spread function (PSF) of our confocal microscope.

To formalize this situation, we assume an approximative axial PSF given by a Gaussian

$$I_{\text{PSF}}(z) = e^{-4 \ln 2 \left(\frac{z}{\Delta z}\right)^2} \quad (3.1)$$

with a full width at half maximum (FWHM) of $\Delta z = 1.26\lambda/\text{NA}^2$ [124], where λ is the wavelength of detected fluorescence (for $\lambda = 750$ nm, $\text{NA} = 0.8$ we obtain $\Delta z = 1477$ nm). The time-averaged collected NV fluorescence can then be calculated as

$$\begin{aligned} I_{\text{fluo}}(\tilde{u}_{\text{max}}) &= \int_0^{2\pi/\omega_m} I_{\text{PSF}}(\tilde{u}_{\text{max}}(\omega_m) \sin(\omega_m t)) dt \\ &= 2\pi e^{-2\left(\frac{\tilde{u}_{\text{max}}(\omega_m)}{\Delta z}\right)^2} I_0\left(2 \ln 2 \left(\frac{\tilde{u}_{\text{max}}(\omega_m)}{\Delta z}\right)^2\right) \end{aligned} \quad (3.2)$$

assuming the oscillator is driven on resonance, i.e. $\omega_d = \omega_m \approx \omega_{\text{res}}$ (see Sec. 2.5). $I_0(z)$ is the zeroth order modified Bessel function of first kind. The induced cantilever

motion is small compared to the width of the axial PSF and we obtain to second order in z an NV fluorescence rate

$$I_{\text{fluo}}(V_{\text{AC}}) = \alpha \left[1 - 2 \left(\frac{\chi_{\text{m}} V_{\text{AC}}}{\Delta z} \right)^2 \right] \quad (3.3)$$

where we used the relation $\tilde{u}_{\text{max}}(\omega_{\text{m}}) = \chi_{\text{m}}(\omega_{\text{m}}) V_{\text{AC}}$ and α is a proportionality factor. Fig. 3.5a shows recorded NV fluorescence for an exemplary cantilever of thickness $t = 1 \mu\text{m}$ and length $l = 45 \mu\text{m}$ as a function of V_{AC} along with the fit to the quadratic function given in (3.3), which yields $\chi_{\text{m}} = (26 \pm 4) \text{ nm/V}$ and $\alpha = (80.3 \pm 0.3) \text{ kHz}$.

The cantilevers mechanical resonance frequency ω_{m} is determined with a similar approach. We apply mechanical excitation at a constant piezo excitation amplitude ($V_{\text{AC}} = 2 \text{ V}$ in Fig. 3.5b) and vary the drive frequency ω_{d} . The resulting variation of NV fluorescence counts as a function of ω_{d} is fitted to a Lorentzian (see App. A.4) from which eigenfrequency ω_{m} and width $\Delta\omega_{\text{d}}$ are extracted. The Q factor can thus be obtained by $Q = \omega_{\text{m}}/\Delta\omega_{\text{d}}$. For the cantilever we investigated here, $\omega_{\text{m}} = 6.654 \text{ MHz}$, $\Delta\omega_{\text{d}} = 16.55 \text{ kHz}$ and hence $Q = 402$.

3.2. Bending experiments

We now present bending experiments which we performed to characterize our hybrid system with respect to its spin-strain coupling strength (the results presented in the following are published in [1]). First, we concentrate on static cantilever bending and quantify strain and stress coupling. Note that our original treatment in [1] is oversimplified, as it neglects shear strain and the Poisson effect. Additionally it contains a few minor mistakes. Nevertheless, for reasons of completeness, our original approach to the characterization of spin-strain coupling is presented in App. A.5.1, where we also amend the existing minor mistakes. In the following, we use the correct formalism from Sec. 2.4 and quantify stress and strain coupling parameters A_1, A_2, B, C and a_1, a_2, b, c , respectively. We then turn our attention to the dynamics of our hybrid system by applying AC strain.

The sample we investigated here (Fig. 3.6) contained NV centers implanted at 12 keV and $5 \cdot 10^{-10} \text{ ions/cm}^2$ (the implantation was performed by the company Ion Beam Services, France). These implantation parameters resulted in a defect density slightly too high for our experiments (i.e. it was very difficult to locate single NVs). The diamond cantilevers were fabricated as described in the previous section and were aligned to within a few degrees to the [110] direction (not [100], as stated in [1]). Cantilever dimensions were in the range of $(10 - 50) \times (3.5) \times (0.2 - 1) \mu\text{m}^3$ for length l , width w and thickness t , respectively. The corresponding resonance frequencies $\omega_{\text{m}}/2\pi$ of the fundamental out of plane flexural mode of our cantilevers lay in a range of 1 – 10 MHz with Q factors ~ 400 . The relatively modest values of Q are caused by clamping losses and our experimental conditions under atmospheric pressure, but did not pose a limitation to our experiments.

3.2.1. Static bending: characterization of strain coupling

For a complete description of strain and stress coupling we need to determine the coupling parameters A_1, A_2, B, C (for stress) and a_1, a_2, b, c (for strain). To that

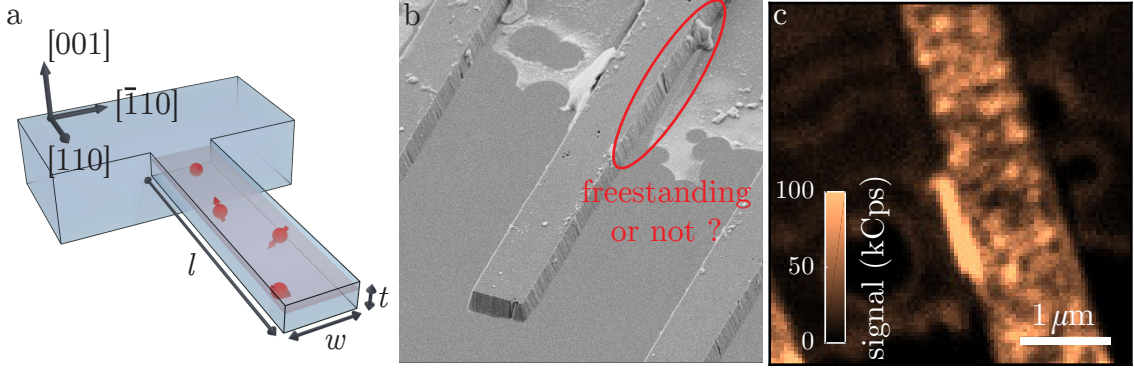


Figure 3.6.: Characteristics of the employed sample for our bending experiments. a) Schematic of a typical cantilever, indicating alignment to within a few degrees along the $[110]$ direction. Cantilever dimensions are in the range of $(10-50) \times (3.5) \times (0.2-1) \mu\text{m}^3$ for length l , width w and thickness t , respectively. b) Scanning electron microscope picture of cantilevers employed in this work. Imperfections during fabrication caused non-regular cross section throughout the beams, thin diamond membranes connected neighboring cantilevers and the cantilevers' lengths were not well defined. c) Fluorescence map recorded with our scanning confocal microscope. NV centers were implanted at an energy of 12 keV and a density of $5 \cdot 10^{-10}$ ions/ cm^2 , resulting in a rather high NV density, making it difficult to identify single NV centers.

end we follow the procedure presented in Sec. 2.4, i.e. we describe the coupling in our hybrid system in terms of lattice stress and extract values for A_1, A_2, B, C by comparing NV centers from families NVA and NVB. Strain coupling parameters a_1, a_2, b, c can then be obtained via (2.55).

Spin-stress coupling is described by the Hamiltonian

$$\hat{H}_{\text{gs}}^{\sigma}/h = \underbrace{M_{\sigma,z}^{\text{gs}} \hat{S}_z^2}_{\hat{H}_{\text{gs}}^{\sigma,\parallel}} + \underbrace{M_{\sigma,x}^{\text{gs}} (\hat{S}_y^2 - \hat{S}_x^2) + M_{\sigma,y}^{\text{gs}} (\hat{S}_x \hat{S}_y + \hat{S}_y \hat{S}_x)}_{\hat{H}_{\text{gs}}^{\sigma,\perp}} \quad (3.4)$$

with the stress-induced level shifts (compare (2.44) and (2.48))

$$M'_{\sigma,x} = -M_{\sigma,x}^{\text{gs}} = B(2\sigma_{ZZ} - \sigma_{XX} - \sigma_{YY}) + C(2\sigma_{XY} - \sigma_{YZ} - \sigma_{XZ}) \quad (3.5a)$$

$$M'_{\sigma,y} = -M_{\sigma,y}^{\text{gs}} = \sqrt{3}B(\sigma_{XX} - \sigma_{YY}) + \sqrt{3}C(\sigma_{YZ} - \sigma_{XZ}) \quad (3.5b)$$

$$M'_{\sigma,z} = M_{\sigma,z}^{\text{gs}} = A_1(\sigma_{XX} + \sigma_{YY} + \sigma_{ZZ}) + 2A_2(\sigma_{YZ} + \sigma_{XZ} + \sigma_{XY}) \quad (3.5c)$$

defined in the crystal coordinate system XYZ (see Sec. 2.4). The corresponding stress tensor for a cantilever aligned to the $[110]$ direction is (see (2.50))

$$\sigma_{XYZ}^{[110]} = \frac{P_{[110]}}{2} \begin{pmatrix} 1 & 1 & 0 \\ 1 & 1 & 0 \\ 0 & 0 & 0 \end{pmatrix} \quad (3.6)$$

where the stress amplitude for shallow NV centers ($z = t/2$) located at the cantilever's base ($x = 0$) is given by (compare (2.69))

$$P_{[110]} = P(0, t/2) = \frac{3}{2} \frac{t}{l^2} Eu, \quad (3.7)$$

where u is the cantilever tip displacement and E is the Young's modulus of diamond (see Sec. 2.4.2). To quantify the four coupling constants A_1, A_2, B, C we investigate NV centers from both families NVA and NVB. The overall level shifts (see (2.45))

$$\Delta_{\pm}/P_{[110]} = M'_{\sigma,z} \pm \sqrt{(M'_{\sigma,x})^2 + (M'_{\sigma,y})^2} \quad (3.8)$$

induced by stress along the [110] direction are given by (Tab. 2.1)

$$\Delta_{\pm}^A/P_{[110]} = (A_1 + A_2) \pm (C - B) \quad (3.9a)$$

$$\Delta_{\pm}^B/P_{[110]} = (A_1 - A_2) \pm (-C - B) \quad (3.9b)$$

for NV families NVA and NVB. Performing the calculations

$$\Delta_+^A + \Delta_-^A = 2(A_1 + A_2)P_{[110]} \equiv \Delta_{\parallel}^A P_{[110]} \quad (3.10a)$$

$$\Delta_+^A - \Delta_-^A = 2(C - B)P_{[110]} \equiv \Delta_{\perp}^A P_{[110]} \quad (3.10b)$$

$$\Delta_+^B + \Delta_-^B = 2(A_1 - A_2)P_{[110]} \equiv \Delta_{\parallel}^B P_{[110]} \quad (3.10c)$$

$$\Delta_+^B - \Delta_-^B = 2(-C - B)P_{[110]} \equiv \Delta_{\perp}^B P_{[110]} \quad (3.10d)$$

yields four equations describing the level shifts ($\Delta_{\parallel}^{A,B}$) and splittings ($\Delta_{\perp}^{A,B}$) for NVA and NVB due to uniaxial stress. Assuming homogeneous stress fields, we can thus determine the coupling constants via the relations

$$A_1 = (\Delta_{\parallel}^A + \Delta_{\parallel}^B)/4 \quad (3.11a)$$

$$A_2 = (\Delta_{\parallel}^A - \Delta_{\parallel}^B)/4 \quad (3.11b)$$

$$B = -(\Delta_{\perp}^A + \Delta_{\perp}^B)/4 \quad (3.11c)$$

$$C = (\Delta_{\perp}^A - \Delta_{\perp}^B)/4. \quad (3.11d)$$

We determined $\Delta_{\pm}^{A,B}$, $\Delta_{\parallel}^{A,B}$ and $\Delta_{\perp}^{A,B}$ for five NV centers following the described procedure (see App. A.5.2 for data and fits). This approach yields the values

$$A_1 = (-12.4 \pm 3.4) \text{ MHz/GPa} \quad (3.12a)$$

$$A_2 = (6.9 \pm 3.4) \text{ MHz/GPa} \quad (3.12b)$$

$$B = (-6.2 \pm 1.0) \text{ MHz/GPa} \quad (3.12c)$$

$$C = (7.1 \pm 1.0) \text{ MHz/GPa}. \quad (3.12d)$$

for A_1, A_2, B, C . The given errors denote the variation among the available sets of data and contain 68% of the observed values. Fig. 3.7 shows two of the five evaluated data sets (left: NVA, right: NVB). The white dashed lines in the top graphs are obtained by evaluating (3.9) with the values for A_1, A_2, B, C from (3.12). The observed discrepancy for the NV of family NVB largely arises from the small number of NV centers we analyzed and increasing statistics should strongly improve our analysis (see App. A.5.2). Fig. 3.8 compares experimental data from [1] (see Fig. A.1) with the theoretically expected shifts and yields a very good agreement between theory and experiment. The strain coupling constants a_1, a_2, b, c

$$\begin{aligned} a_1 &= (-9.5 \pm 5.1) \text{ GHz/strain} \\ a_2 &= (-20.9 \pm 4.8) \text{ GHz/strain} \\ b &= (1.5 \pm 1.0) \text{ GHz/strain} \\ c &= (-10.4 \pm 1.2) \text{ GHz/strain}. \end{aligned} \quad (3.13)$$

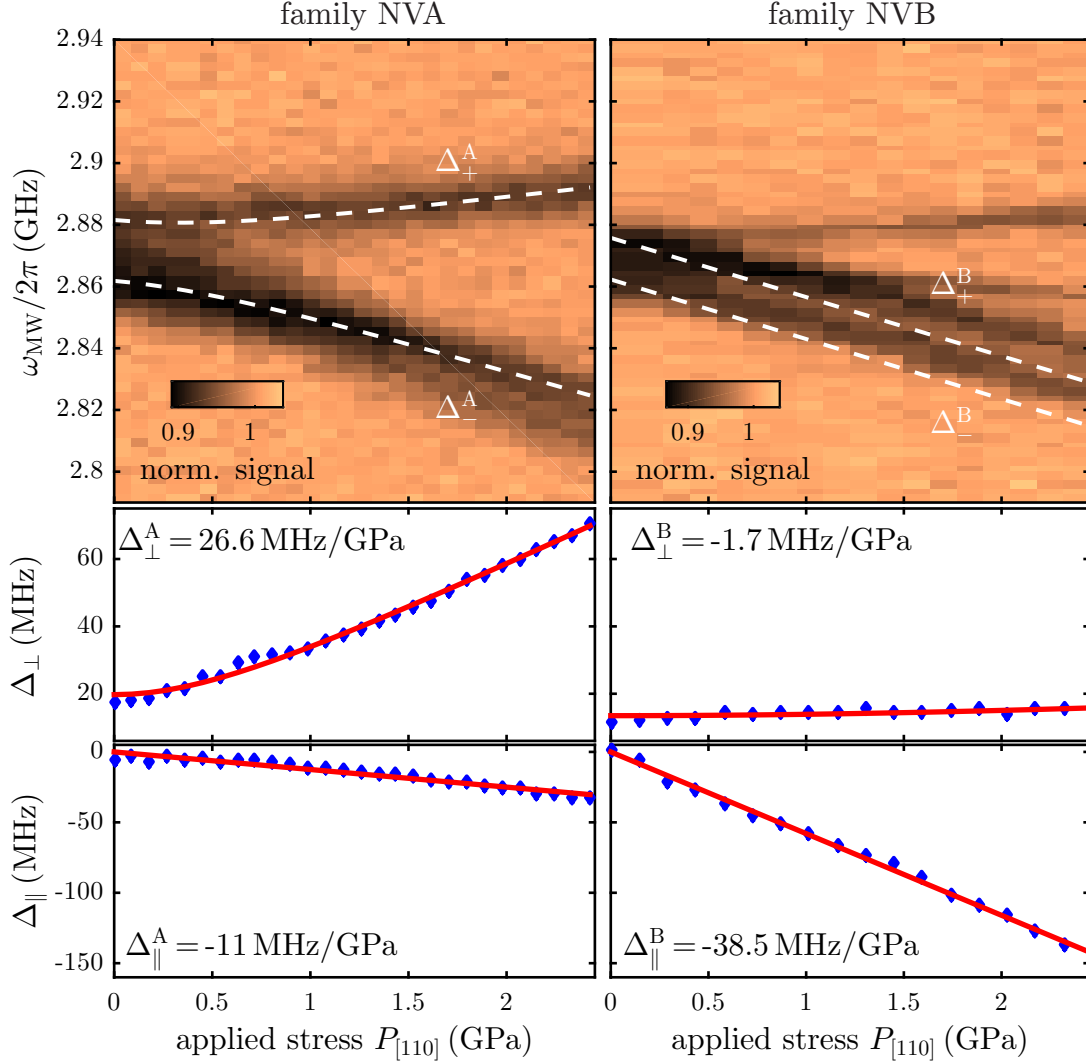


Figure 3.7.: Determination of stress coupling constants A_1, A_2, B, C . We characterized NV centers of both families NVA and NVB and extracted level shifts $\Delta_{\parallel} = (\Delta_{+} + \Delta_{-})$ (bottom row; data represented by blue dots, fit by red line) and level splittings $\Delta_{\perp} = (\Delta_{+} - \Delta_{-})$ (middle row; data represented by blue dots, fit by red line). Stress coupling constants A_1, A_2, B, C were then determined as described in the text. The white lines in the top graph denote calculated level shifts based on the extracted values for A_1, A_2, B, C . The investigated NV centers all showed significant intrinsic strain, lifting the sublevel degeneracy at zero applied external stress. The additional features in the graph of NVB stem from another NV center that was simultaneously measured.

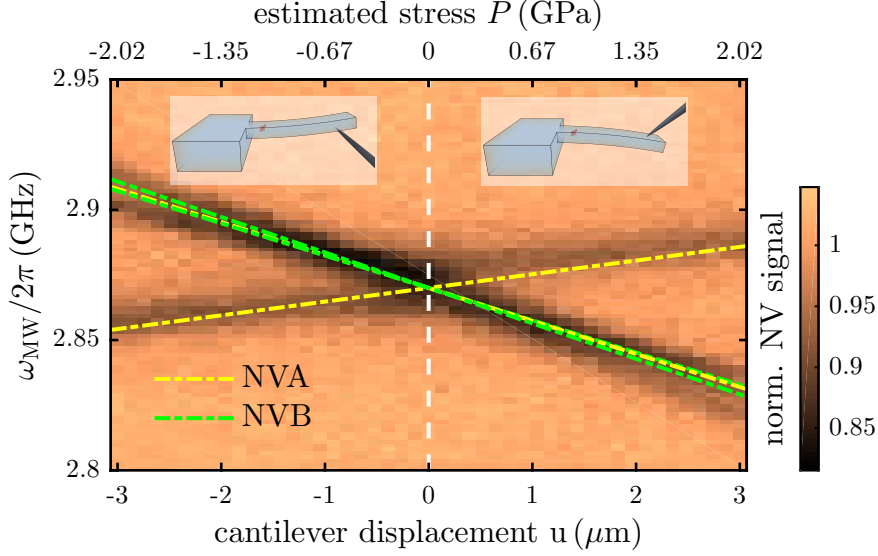


Figure 3.8.: Comparing experimental data with expected stress-induced level shifts (yellow lines denote NV family NVA and green lines represent NV orientation NVB). Expected level shifts are calculated with (3.9) and stress coupling parameters from (3.12). Our data most likely contains two NVs, one from each family NVA and NVB.

are obtained via the relation (2.55).

Recently, Barson *et al.* [103] reported similar values for the stress coupling constants, obtained through applying uniaxial stress to a diamond cube in a diamond anvil cell (see Tab. 3.2 for a comparison of both sets of values). Both experiments predict stress level shifts in the order of a few MHz/GPa. Yet they differ by a factor ~ 2 and the signs of A_1 and A_2 are flipped. The origin of the discrepancy in sign between our findings and the results from [103] seems to lie in different sign conventions for stress and coupling parameters B and C . In their work, Barson *et al.* define compressive stress to be positive and further relate it to a stress-induced increase of the NV zero-field splitting D_{gs} . In our analysis, however, compressive stress is negative and increases D_{gs} (see Fig. 3.8). The different sign convention for applied stress consequently inverts the stress axis and flips the signs of all four coupling parameters. In addition, Barson *et al.* describe the stress-induced splitting of the $|\pm 1\rangle$ spin sublevels with expressions $2(B - C)P$ and $2(B + C)P$ for NVs of family NVA and NVB (see supplementary material of [103]). In our analysis, however, the signs of B and C are flipped (see (3.9)). Taking both aspects into account explains the observed discrepancy in sign. The difference in amplitude could be caused by uncertainties in the calibration of the applied stress with respect to cantilever deflection. As seen in Fig. 3.6 the cantilevers employed for this work did not have perfect geometry, i.e. the cross section was not constant along their length, and thin diamond membranes connected neighboring structures. Both factors can lead to a different stress distribution than assumed during our analysis. On top of that, our stress calibration relies on correctly determined cantilever dimensions as well as a precise knowledge of the deflection amplitude and the point where our tungsten needle pushed on the cantilever. It is most likely that our determination

Table 3.2.: Comparing stress coupling constants from [1] and [103]. The two sets of values differ by a factor of ~ 2 as well as in the signs of A_1 and A_2 .

parameter	Teissier <i>et al.</i> [1]	Barson <i>et al.</i> [103]
	MHz/GPa	MHz/GPa
A_1	-12.4 ± 3.4	4.86 ± 0.02
A_2	6.9 ± 3.4	-3.7 ± 0.2
B	-6.2 ± 1.0	-2.3 ± 0.3
C	7.1 ± 1.0	3.5 ± 0.3

of cantilever length l is not entirely correct (compare Fig. 3.6b). Uncertainties in l pose a serious problem as $P \propto l^{-2}$. Reducing the measured values for l by 25% results in values for stress coupling parameters almost identical in amplitude to [103]. Unfortunately, as this particular sample was destroyed, there is no chance to retake data to verify our results. We thus suggest to perform similar experiments on well defined structures to reduce the uncertainty in cantilever dimensions.

3.2.2. AC bending: the resolved sideband regime

We now turn our attention to the dynamics of our hybrid spin-oscillator system. To measure the systems response to AC strain, we applied a mechanical drive to the diamond cantilever by means of a piezoelectric transducer driven at a frequency ω_d with voltage V_{AC} (compare Subsec. 3.1.2). We then characterized the resulting dynamical spin-cantilever interaction through high-resolution pulsed ESR spectroscopy. For this experiment, we chose an NV of family NVB, where the induced strain field acts mostly longitudinally. Additionally we applied a magnetic field $B_z = 26$ G along the NV axis such that our discussion can be restricted to the two-level subspace spanned by $|0\rangle$ and $|-1\rangle$ and mixing of $|1\rangle$ and $|-1\rangle$ by transverse strain can be neglected. Under these conditions the spin-stress coupling Hamiltonian from (2.32) is modified to

$$\hat{H}_{AC}/h = M_{\sigma,z}^{\max} \cos(\omega_d t) \hat{\sigma}_z \quad (3.14)$$

where the maximum level shift

$$M_{\sigma,z}^{\max} = \alpha_z^\sigma \tilde{u}_{\max} = (A_1 - A_2) \frac{3}{2} \frac{t}{l^2} E \chi_m V_{AC} \quad (3.15)$$

depends on cantilever dimensions, mechanical susceptibility and peak driving amplitude.² The quantity α_z^σ denotes the stress-induced level shift per cantilever displacement and static bending experiments yielded $\alpha_z^\sigma = -17.9$ MHz/ μm for the NV center investigated here (i.e. $t \approx 1$ μm and $l \approx 37$ μm).

The result of dynamic strain-modulation can be seen in Fig. 3.9a, where we choose $\omega_d = \omega_m = 2\pi \times 6.659$ MHz and compare pulsed ESR spectra of the $|0\rangle \leftrightarrow |-1\rangle$

²We note that in this limit our model is equivalent to spin-oscillator systems coupled through magnetic field gradients [18, 37, 76].

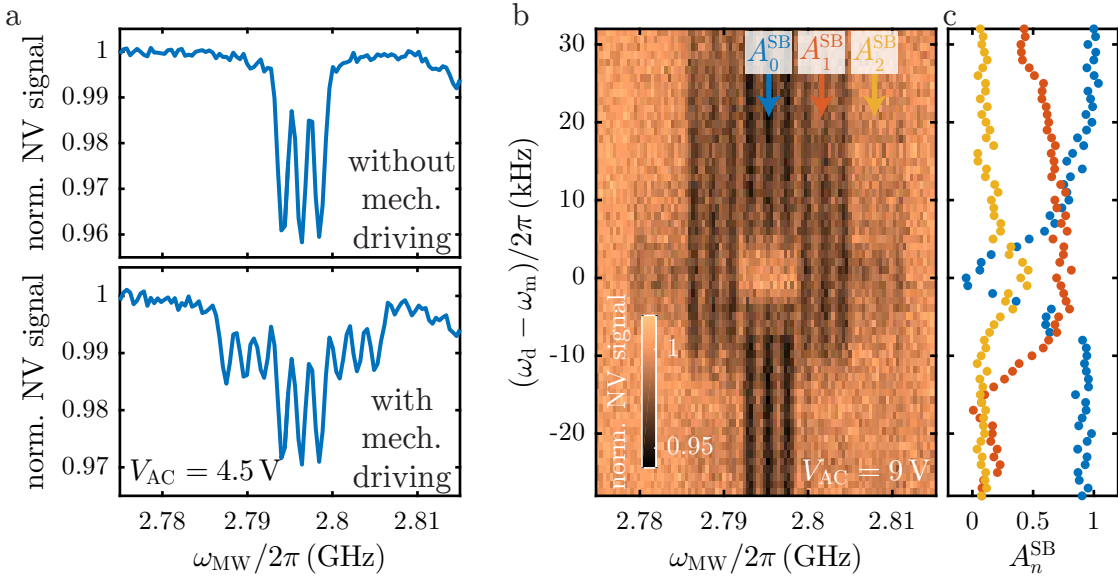


Figure 3.9.: Pulsed ESR measurements under mechanical driving. a) Pulsed ESR trace of a stress-coupled NV in the absence (upper trace) and presence (lower trace) of resonant mechanical excitation. Without excitation, the ESR line exhibits a splitting into three hyperfine components. Mechanical driving at an amplitude $V_{AC} = 4.5$ V induces sidebands to this central carrier at frequencies $\omega_{\pm} \pm \omega_m$, where $\omega_{\pm}/2\pi = 2.796$ GHz is the bare ESR frequency of the investigated $|0\rangle \leftrightarrow |-1\rangle$ transition. b) Evolution of the ESR sidebands as a function of mechanical drive frequency ω_d at an excitation amplitude $V_{AC} = 9$ V. A resonant behavior is observed with a maximal sideband amplitude appearing when $\omega_d = \omega_m$. c) Sideband amplitudes A_n^{SB} of the carrier signal ($n = 0$, blue) and the two higher-order sidebands ($n = 1, 2$ in red and yellow, respectively) as determined by a Lorentzian fit to the observed ESR dips. A slight asymmetry in the sideband amplitudes with respect to ω_d is caused by the onset of a mechanical nonlinearity of the diamond mechanical oscillator.

transition in the presence and absence of the mechanical excitation. Without mechanical drive (upper trace), we observed the well established hyperfine structure of the NV electron spin, which consists of three ESR lines split by the ^{14}N hyperfine coupling constant $\omega_{\parallel}^{\text{gs}} = 2\pi A_{\parallel}^{\text{gs}}$ (see also Fig. 2.10). Upon resonant mechanical excitation two clearly resolved, mechanically induced sidebands appear for each of the three hyperfine ESR lines at detunings $\pm\omega_m$, respectively. This experiment demonstrates that our system resides well within the resolved sideband regime of spin-oscillator coupling, since the ESR linewidth $\Delta\omega < \omega_m$ by a factor of three (here $\Delta\omega \approx 2\pi \times 1.8$ MHz).

To prove the resonant character of our coupling and the mechanical origin of the observed sidebands, we extended the experiment presented in Fig. 3.9a by sweeping $\omega_d/2\pi$ over a frequency range of ± 30 kHz around $\omega_m/2\pi$, while monitoring the NV's ESR spectrum (Fig. 3.9b). Clearly, sidebands are maximized in amplitude under resonant driving when $\omega_d \approx \omega_m$. Furthermore, the frequency range over which sidebands can be observed (Fig. 3.9c) matches $\Delta\omega_m = Q/\omega_m = 6.659 \text{ MHz}/402 =$

16.6 kHz as expected from our cantilever's characteristics. This observation demonstrates that the observed sidebands are indeed induced by the mechanical oscillator and in particular excludes sidebands occurring through accidental modulation of the NV spin splitting by electric or magnetic stray fields.

Finally, we investigate the evolution of the motion-induced sidebands as a function of the mechanical driving strength. Figure 3.10a shows a series of pulsed ESR traces recorded at various strengths of piezo excitation V_{AC} with $\omega_d = \omega_m$. For increasing V_{AC} , we observe an increase of the sideband amplitude and eventually the appearance of higher-order sidebands up to order $n = 3$. As expected (see App. A.6 as well as [125]), the amplitude A_n^{SB} of the n -th sideband follows $J_n^2(M_{\sigma,z}^{\max}/\omega_m)$, where $J_n(x)$ is the n -th order Bessel function of the first kind (Fig. 3.10b). Besides being a further confirmation of the sidebands' mechanical nature, this measurement allows us to verify the stress coupling parameters A_1, A_2 . In this dynamical spin-stress coupling mode we can extract the modulation depth $m = M_{\sigma,z}^{\max}/\omega_m$ as a function of drive amplitude and use an estimated mechanical susceptibility $\chi_m \approx 26 \text{ nm/V}$ of our system to relate m to V_{AC} . This estimate yields $\alpha_z^\sigma \approx 72 \text{ MHz}/\mu\text{m}$ and lies within a factor of four of our static measurement of α_z^σ , which is reasonable, given the uncertainty in our estimation of χ_m .

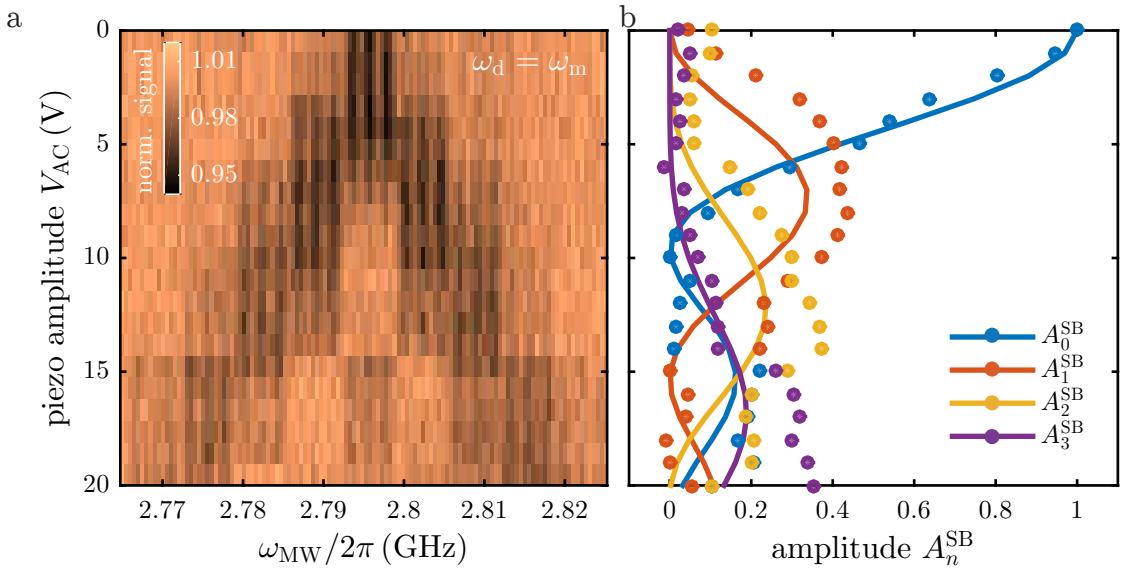


Figure 3.10.: Sideband amplitudes versus mechanical driving strength. a) Amplitude of ESR sidebands for increasing excitation voltage V_{AC} of the mechanical oscillator. b) Relative amplitudes A_n^{SB} of carrier signal (blue) and sidebands as a function of excitation amplitude (dots). We determined the amplitudes by Lorentzian fits to the ESR peaks in a) and normalized the dips in each line by the total measured ESR signal strength. Sidebands of order $n = 1, 2, 3$ are color-coded in orange, yellow and purple, respectively. Lines indicate squares of n -th order Bessel functions.

3.3. Conclusion and Outlook: the strong coupling regime

With spin-stress/strain coupling and the resolved sideband regime clearly established, the question arises to what extent our system is amenable to future experiments in the quantum regime and in particular whether the high cooperativity regime can be reached. To discuss this question we introduce the cooperativity C , which is the key figure of merit of our spin-oscillator system and compares the coupling strength against both spin and resonator decoherence rates. We present the status quo of our experiment and highlight possible approaches to reach the high cooperativity regime in the future.

3.3.1. Status of our experiment

To define the single phonon coupling strength, we introduce the position operator $\hat{x} = \Delta x_{\text{zpm}} (\hat{a} + \hat{a}^\dagger)$ (see (2.88)) and rewrite (3.4) as (see App. A.7 for a detailed derivation)

$$\hat{H}_{\text{gs}}^\sigma/h = \frac{g_0^\parallel}{2\pi} (\hat{a} + \hat{a}^\dagger) \hat{S}_z^2 - \frac{g_0^\perp}{2\pi} (\hat{a} + \hat{a}^\dagger) (\hat{S}_+^2 + \hat{S}_-^2). \quad (3.16)$$

$g_0^{\parallel,\perp}$ describe the induced level shifts of longitudinal and transverse stress caused by the zero-point motion of the resonator, and are given by (see App. A.7)

$$g_0^{\parallel,\perp} = 2\pi\alpha_{z,\perp}^\sigma \Delta x_{\text{zpm}}. \quad (3.17)$$

Here $\alpha_{z,\perp}^\sigma$ represents the induced level shifts, caused by longitudinal or transverse stress, per cantilever displacement. $\Delta x_{\text{zpm}} = \sqrt{\hbar/(2m_{\text{eff}}\omega_m)}$ is the cantilever's zero-point motion, which depends on eigenfrequency ω_m and effective mass m_{eff} of the resonator (see Subsec. 2.5.2). Furthermore, the NV spin decoherence rate is

$$\Gamma_{\text{NV}} = 1/T_2, \quad (3.18)$$

where T_2 denotes the spin NV coherence time. The oscillators thermal decoherence rate is (see (2.96))

$$\gamma_{\text{th}} = \frac{k_B T}{\hbar Q}, \quad (3.19)$$

and depends on the bath temperature T and the cantilever's quality factor Q .

To reach the high cooperativity regime, the single phonon coupling rate needs to be higher than the spin decoherence rate Γ_{NV} and the thermal decoherence rate γ_{th} of the resonator. The cooperativity

$$C = \frac{1}{2\pi} \frac{\left(g_0^{\parallel,\perp}\right)^2}{\gamma_{\text{th}}\Gamma_{\text{NV}}} \quad (3.20)$$

compares longitudinal and transverse coupling strengths $g_0^{\parallel,\perp}$ to the individual decoherence rates of spin and resonator; $C > 1$ denotes the desired high cooperativity regime where $\left(g_0^{\parallel,\perp}\right)^2 > 2\pi\gamma_{\text{th}}\Gamma_{\text{NV}}$.

In the experiments we present in this thesis, we employ solely the $n = 1$ out-of-plane flexural mode of a cantilever beam and hence

$$\omega_{m,1} = \sqrt{\frac{EI_z}{\rho A}} \beta_1^2 \quad (3.21)$$

where $I_z = wt^3/12$, $A = wt$ and $\beta_1 l = 1.875$ (see Sec. 2.5). The investigated NV centers are usually located at the cantilever's root and close to its top surface. When focusing on longitudinal coupling, i.e. an NV from family NVB under the presence of an external magnetic field, $\alpha_z^\sigma = (A_1 - A_2) \frac{3}{2} \frac{t}{l^2} E$ (see (3.15)) and we can express g_0^\parallel as

$$\begin{aligned} g_0^\parallel &= 2\pi |\alpha_z^\sigma| \cdot \Delta x_{z\text{pm}} \\ &= 2\pi |(A_1 - A_2)| \frac{3}{2} \frac{t}{l^2} E \cdot \sqrt{\frac{140 \hbar}{66 m_0 \omega_{m,1}}} \\ &= 2\pi \left[12 \left(\frac{140}{66} \right)^2 \left(\frac{3}{2 \cdot 1.875} \right)^4 \right]^{\frac{1}{4}} \cdot E |(A_1 - A_2)| \cdot \left(\frac{\hbar}{wl^3 \sqrt{E\rho}} \right)^{\frac{1}{2}} \\ &\approx 220 \cdot \left(\frac{\hbar}{wl^3 \sqrt{E\rho}} \right)^{\frac{1}{2}} \end{aligned} \quad (3.22)$$

in units of GHz \times rad, where we used $m_{\text{eff}} = m_0/4$ [115], the cantilever's mass $m_0 = \rho wlt$ and $\rho = 3.5 \text{ g/cm}^3$ is the density of diamond. For our typical cantilever dimensions ($t \approx 1 \mu\text{m}$ and $l \approx 35 \mu\text{m}$) and $E = 992 \text{ GPa}$ (see (2.56)) we find $g_0^\parallel/2\pi \approx 0.2 \text{ Hz}$. As our experiments are operated at room temperature ($T = 300 \text{ K}$) and in air, our cantilevers have relatively modest factors $Q \approx 400$ and are thus characterized by a thermal decoherence rate of $\gamma_{\text{th}}/2\pi \approx 15.6 \text{ GHz}$. Typical T_2 times for our shallow implanted NV centers at room temperature are $T_2 \approx 100 \mu\text{s}$ and $\Gamma_{\text{NV}} \approx 10 \text{ kHz}$. Our current devices are thus characterized by a cooperativity of $C = 3.1 \cdot 10^{-16} \ll 1$.

3.3.2. Approaches to reach the high cooperativity regime

We want to point out that in our current experiments we have made no effort to optimize our hybrid system with respect to cooperativity. In the following we briefly discuss two possible approaches to boost C .

First, it becomes clear from (3.22) that $g_0^{\parallel,\perp} \propto \sqrt{1/wl^3}$. The single phonon coupling strength is largely determined by cantilever dimensions and can thus be boosted by shrinking our resonator. Furthermore, our experiments were performed at room temperature and in air. Both aspects give rise to large γ_{th} , and we can thus lower the thermal decoherence rate of our resonator significantly by operating our setup at cryogenic temperatures and in vacuum. Additionally, lowering the temperature T also increases T_2 , as values $\sim s$ have been reported [89]. When assuming a cantilever with dimensions $l = 1 \mu\text{m}$, $t = 0.1 \mu\text{m}$ and $Q = 2.5 \cdot 10^6$ coupled to an NV center with $T_2 = 1 \text{ s}$ at $T = 100 \text{ mK}$ we find $g_0^\parallel/2\pi = 144 \text{ Hz}$, $\gamma_{\text{th}}/2\pi = 8.3 \text{ kHz}$ and $\Gamma_{\text{NV}} = 1 \text{ Hz}$. Together this yields a cooperativity of $C = 2.49$. Reaching these parameters is, however, most likely to be at the limit of what we can possibly achieve.

While Q factors of up to $6 \cdot 10^6$ have been demonstrated, these values were reported for large structures with eigenfrequencies in the kHz range [46]. Making resonators significantly smaller will most likely decrease Q due to an increased surface contributions to internal losses [46, 47]. Furthermore, corresponding eigenfrequencies will increase drastically as well – the cantilever described above, for instance, is characterized by $\omega_{m,1}/2\pi \approx 272$ MHz. Assuming a constant Qf_m product, the projected Q factor of such a device would be $Q \approx 100$ and thus much lower than the value we assumed. Other obstacles arise from the NV's proximity to resonator surfaces, which will deteriorate the spin coherence time T_2 , as well as from the assumed temperature of 100 mK, which is very low and challenging to realize. All in all, miniaturizing the cantilever will certainly help boost g_0 . Reaching the high cooperativity regime seems to be possible, but will be difficult. Certainly, great efforts in sample fabrication and NV engineering are required.

Besides miniaturizing the resonator, a second option would be to increase the stress-induced level shift per cantilever displacement. To that end we could not only bend the cantilever but also apply a torque, i.e. by twisting the cantilever. This would add additional, off-diagonal elements σ_{XY} and σ_{XZ} in the stress tensor (for further details see [110], p. 214) which contribute to a stress-induced level shift via the A_2 term in $M_{\sigma,z}$ (see for example (2.44)). Twisting our currently used cantilever with dimensions in the μm range by 1° would induce stress of several tens of GPa, which is about one order of magnitude more than the stress induced by static bending. Despite this promising outlook, further investigations regarding possible resonator geometries and their structural integrity are necessary to fully estimate the potential of torsional stress.

4. Hybrid continuous dynamical decoupling

In this chapter we study the parametric interaction between the NV's electronic spin and the diamond mechanical resonator. To that end we apply an AC strain field and focus on the longitudinal coupling term. Under coherent microwave driving of the spin, this parametric drive leads to a locking of the spin Rabi frequency to the oscillator mode in the megahertz range. Both the Rabi oscillation decay time and the inhomogeneous spin coherence time increase by two orders of magnitude under this condition. We present routes to prolong the dephasing times even further, potentially to the relaxation time limit. The remarkable coherence protection that our hybrid spin-oscillator system offers is reminiscent of recently proposed concatenated continuous dynamical decoupling schemes and results from our robust, drift-free strain-coupling mechanism and the narrow linewidth of the high-quality diamond mechanical oscillator employed. The results presented here have been published in [102].

4.1. Motivation: Hybrid continuous dynamical decoupling

Solid-state spins rank among the most promising sources for quantum information processing and sensing, due to their ease of use and the in-principle scalability they offer. Exploiting their quantum nature for computation or sensing however requires quantum coherence to be preserved for a time long compared to the speed of their coherent manipulation. The spin relaxation time T_1 , exceeding seconds for NV centers [81], sets the fundamental limit to these coherence times and spin manipulation rates in the GHz range have been demonstrated [126]. Despite these encouraging prospects, reaching relaxation-limited Rabi decay times for NV spins remains highly challenging due to the significant influence of additional noise sources in the spins' environment as well as in the driving fields.

Various approaches to enhance spin coherence times towards the relaxation time limit have been put forward. Most notably, dynamical decoupling – a method of filtering out environmental noise through either pulsed [127] or continuous [99, 101, 128, 129] driving – can isolate the spins from the low-frequency environmental fluctuations responsible for dephasing. In this regard, pulsed schemes have proven especially effective [89]. They are robust to pulse errors [130] and even allow for decoherence protected quantum gates [64]. However, such schemes come at the cost of increased experimental complexity and potentially harmful high intensity driving pulses. Decoupling schemes relying on continuous driving, on the other hand, are experimentally simpler to realize [128, 129] as in general no pulsing is re-

quired. Unfortunately, the effectiveness of continuous dynamical decoupling schemes is limited by the spin's sensitivity to the ubiquitous low-frequency fluctuations of the driving field.

One way to overcome this obstacle is to apply higher order, concatenated driving fields. Each additional field decouples the spin from the driving field fluctuations of the preceding driving field. In principle this procedure can be iterated ad infinitum and may then yield relaxation limited coherence times [131]. The application of many consecutive decoupling fields, however, also brings disadvantages. First, it exposes the spin to significant driving field powers. Second, it sets intrinsic constraints to the speed at which the final protected spin states can be coherently manipulated. Finally, it again increases the experimental complexity. New approaches to continuous dynamical decoupling are therefore required to yield fully robust spin systems which are of practical use to quantum information processing and sensing.

In this chapter we demonstrate a novel and efficient approach to continuous dynamical decoupling that is based on the parametric interaction of a single electronic spin with a mechanical resonator. We employ a coherent microwave drive for first order decoupling and use the spin-oscillator longitudinal strain coupling to protect the spin from amplitude fluctuations in the microwave field. This hybrid continuous dynamical decoupling (HCDD) scheme builds on two key advances over past approaches [131]:

- Second order decoupling is achieved by a parametric drive along the quantization axis of the undriven spin. The second order driving field is thus orthogonal to the first order drive, irrespective to the phase between these two fields. This significantly simplifies the experimental approach and is in contrast to the conventional dynamical decoupling by concatenated driving, where phase-locking between the driving fields is required to ensure the necessary orthogonality.
- Our second order decoupling field is based on crystal strain and transduced to the spin through a mechanical oscillator. The cantilever's resonant behavior effectively acts as a low-pass filter and thus minimizes amplitude noise, yielding a highly stable, second order driving field amplitude.

A concatenation of only two driving fields thereby results in coherence times nearly two orders of magnitude longer than that of an undriven spin, while also maintaining a final dressed state splitting in the MHz range. By using mechanical oscillators with even higher quality-factors, our scheme should allow us to prolong coherence times even further and ultimately reach the limit imposed by energy relaxation.

4.2. Experimental realization and NV characterization

The experiments presented in this chapter were performed on single NV centers embedded in singly-clamped cantilever diamond mechanical oscillators (Fig. 4.1b). The cantilevers were fabricated from ultra-pure, single-crystal diamond as described in Chap. 3, i.e. they were aligned to the [110] direction. NV centers were created at densities well below $1 \mu\text{m}^{-2}$ by ^{14}N ion implantation at 12 keV and $1 \cdot 10^{-9}$ ions/cm² and subsequent high-temperature annealing to 1200 °C. AC strain was introduced by exciting the cantilever at its eigenfrequency of $\omega_m/2\pi = 5.81$ MHz through a

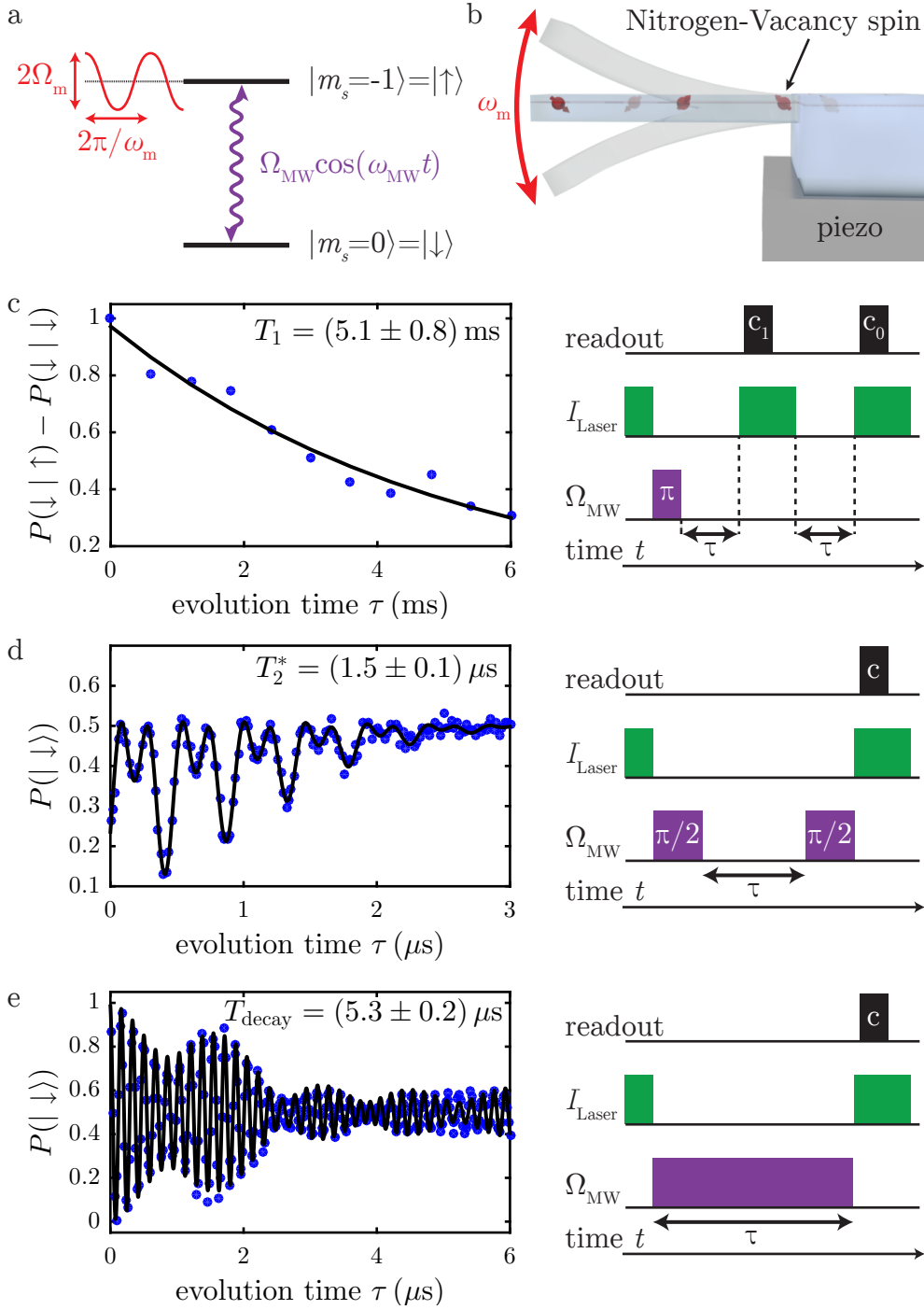


Figure 4.1.: Experimental setting and relevant spin relaxation and coherence times. a) NV spin sublevels involved in our experiment. The resonant driving field and parametric strain-drive are indicated by purple and red wavy lines, respectively. b.) Schematic of the experimental device. An NV spin is embedded in a diamond cantilever, which is actuated using a nearby piezoelectric transducer to generate AC strain for parametric driving. c) Measurement of spin-relaxation time T_1 , d) inhomogeneous spin coherence time T_2^* and e) coherent Rabi oscillations of the NV spin, with corresponding measurement pulse sequences. Exponential and Gaussian fits (black) to the data (blue) yield $T_1 = (5.1 \pm 0.8)$ ms, $T_2^* = (1.5 \pm 0.1)$ μ s and $T_{\text{decay}} = (5.3 \pm 0.2)$ μ s.

piezoelectric actuator placed underneath the sample.¹ All our experiments were performed under ambient conditions.

For our experiments we consider the dynamics of the effective two-level system formed by $|0\rangle := |\downarrow\rangle$ and $|-1\rangle := |\uparrow\rangle$. The third spin sublevel $|+1\rangle$ is split off in energy by a static magnetic field $B_z = 10.7$ G and ignored in the following. In addition to near-resonant microwave driving with transverse magnetic fields of frequency ω_{MW} and amplitude Ω_{MW} , we employ parametric driving by time-varying longitudinal strain fields of frequency ω_m and amplitude Ω_{MW} . The effective Hamiltonian for the two-level system spanned by $\{|\downarrow\rangle, |\uparrow\rangle\}$ then reads

$$\hat{H}/h = (D_{\text{gs}} - \gamma_{\text{NV}}B_z + \Omega_m \cos(\omega_m t))\hat{\sigma}_z + \Omega_{\text{MW}} \cos(\omega_{\text{MW}} t)\hat{\sigma}_x \quad (4.1)$$

with $\hat{\sigma}_i$ the Pauli matrices along direction $i \in \{x, z\}$ and $\gamma_{\text{NV}} = 2.8$ MHz/G the NV gyromagnetic ratio. Here, the MW Rabi frequency $\Omega_{\text{MW}}/2\pi = \gamma_{\text{NV}}B_\perp$ with B_\perp being the amplitude of the applied transverse MW field. The parametric spin drive's amplitude $\Omega_m = g_0^\parallel \tilde{u}_{\text{max}}/\Delta x_{\text{zpm}}$ with \tilde{u}_{max} the maximum cantilever displacement, Δx_{zpm} the cantilever's zero-point motion and $g_0^\parallel/2\pi \approx 0.1$ Hz the longitudinal zero-phonon coupling strength as defined in App. A.7.²

To provide a baseline for our subsequent measurements, we first characterize the investigated NV center with respect to the relevant spin relaxation times in the absence of mechanical driving. The NV population decay time T_1 was determined using the experimental pulse sequence illustrated in Fig. 4.1c. Following initialization in $|\downarrow\rangle$ ($|\uparrow\rangle$) we measure the difference $\Delta P = P(\downarrow|\uparrow) - P(\downarrow|\downarrow)$ as function of the variable delay τ , where $P(i|j)$ is the population in state $|i\rangle$ after initialization in state $|j\rangle$ (with $i, j \in \{\downarrow, \uparrow\}$). Here we obtain ΔP directly from the transient NV fluorescence photons c_1 and c_0 as $\Delta P(\tau) = (c_1(\tau) - c_0(\tau))/(c_1(0) - c_0(0))$. We find $T_1 = (5.1 \pm 0.8)$ ms through an exponential fit (Fig. 4.1c).

The inhomogeneous spin coherence time T_2^* was determined using a typical Ramsey sequence (see Fig. 4.1d) [132]. We initialize our two-level system in $|\downarrow\rangle$ and apply a near-resonant MW $\pi/2$ -pulse to create a superposition state of the form $|\Psi(t=0)\rangle = (|\uparrow\rangle + |\downarrow\rangle)/\sqrt{2}$. We then let the system evolve under the influence of external fluctuations and after time τ apply a second $\pi/2$ -pulse to measure $P(|\downarrow\rangle) = |\langle\downarrow|\Psi(t=\tau)\rangle|^2$. The observed Gaussian decay (blue curve in Fig. 4.1d) is well fit by the expression

$$S_{\text{Ramsey}}(\tau) = e^{-(\tau/T_2^*)^2} \sum_{m_I \in \{-1, 0, 1\}} \beta_{m_I} \cos(2\pi\delta_{m_I}\tau + \phi_{m_I}) \quad (4.2)$$

where β , δ and ϕ are the population, microwave-detuning and initial phase for the hyperfine states $|\downarrow, m_I\rangle$. The fit (black lines in Fig. 4.1d) yields an inhomogeneous spin coherence time of $T_2^* = (1.5 \pm 0.1)$ μs .

Similarly, we determined the decay time T_{decay} of the spin's Rabi oscillations by pulsed, coherent driving of the $|\downarrow\rangle \leftrightarrow |\uparrow\rangle$ transition with a near-resonant MW field

¹While the data presented here was taken on just one NV center, we point out that the investigated decoupling scheme is by no means difficult to realize and works on every NV center subject to longitudinal strain.

²As shown in the previous chapter, all NV centers in our cantilever geometry are subject to both transverse and longitudinal coupling. In the experiments presented here we can neglect the transverse coupling term in first order due to the presence of the static magnetic field B_z .

of variable duration τ (Fig. 4.1e). The observed Rabi oscillations (blue curve) show a pronounced beating pattern that results from the $A_{\text{gs}}^{\parallel} = -2.17$ MHz hyperfine-splitting between the NV electronic spin and the ^{14}N nuclear spin (Fig. 2.10). Our data are well fit by

$$S_{\text{Rabi}}(\tau) = e^{-(\tau/T_{\text{R}})^2} \sum_{m_I \in \{-1, 0, 1\}} \beta_{m_I} \cos(\Omega_{\text{eff}}^{m_I} \tau + \phi_{m_I}) \quad (4.3)$$

where $\Omega_{\text{eff}}^{m_I} = \sqrt{\Omega_{\text{MW}}^2 + \delta_{m_I}^2}$ are the effective Rabi frequencies of the three hyperfine transitions. From the fit, we find $\Omega_{\text{MW}}/2\pi = 5.81$ MHz and $T_{\text{decay}} = (5.3 \pm 0.2) \mu\text{s}$. Despite our strong MW driving the observed Rabi decay time is three orders of magnitude shorter than the relaxation-limit set by T_1 [74].

The Gaussian decay-envelope of our Rabi oscillations suggests that slowly fluctuating noise sources are responsible for the excess decoherence we observed. While both Ω_{MW} and δ_{m_I} may fluctuate, in our experiment, where $\Omega_{\text{MW}} \gtrsim 2\delta_{m_I}$, only the former contributes to first order to dephasing.

4.3. A photon-phonon doubly-dressed spin

In the presence of continuous and resonant MW driving the eigenstates of the driven spin system become the MW dressed states [131, 133]

$$|\pm_M\rangle = (|\downarrow, M\rangle \pm |\uparrow, M-1\rangle) / \sqrt{2} \quad (4.4)$$

with energy difference $\hbar\Omega_{\text{MW}}$ and M the number of microwave photons dressing the spin (i.e. the mean photon number in the coherent microwave field which drives the spin). The Rabi decay time T_{decay} can be interpreted as the MW dressed state relaxation time [85].

To further prolong T_{decay} , we decouple $|\pm_M\rangle$ from fluctuations in Ω_{MW} by applying the longitudinal AC strain field, which near-resonantly and coherently drives the $|+M\rangle \leftrightarrow |-M\rangle$ transition (Fig. 4.2b) and consequently leads to higher-order or doubly-dressed states – the main principle underlying dynamical decoupling by concatenated continuous driving [131]. Such driving is enabled by the coupling term $\Omega_{\text{m}} \cos(\omega_{\text{m}} t) \hat{\sigma}_z$ (see (4.1)), which drives the desired transition at a rate Ω_{m} as $\langle +M | \hat{\sigma}_z | -M \rangle \neq 0$. Resonance of that second drive tone with the dressed state energy splitting is achieved by adjusting Ω_{MW} such that $\Omega_{\text{MW}} \approx \omega_{\text{m}}$.³

To demonstrate second order dressing and the subsequent coherence protection, we performed resonant Rabi oscillation measurements up to an evolution time $\tau_{\text{max}} = 16 \mu\text{s}$ at variable Ω_{MW} and in the presence of a parametric, cantilever-induced strain-drive of fixed amplitude $\Omega_{\text{m}}/2\pi = 4.1$ MHz. Fig. 4.2a shows the Fourier transformation of each experimental Rabi oscillation as a function of Ω_{MW} . For Ω_{MW} far from the dressed-state transition energy (i.e. for $|\Omega_{\text{MW}} - \omega_{\text{m}}| \gtrsim \Omega_{\text{m}}$), the spin precession dynamics are dominated by a single peak at frequency $\Omega_{\text{MW}}/2\pi$, as expected for conventional, coherent spin driving (white dashed line in Fig. 4.2a). The very weak, additional spectral features visible for $\Omega_{\text{MW}} < \omega_{\text{m}}$ stem from the

³We tune Ω_{MW} since ω_{m} is fixed and given by the cantilever geometry. Yet our decoupling scheme would also work the other way around.

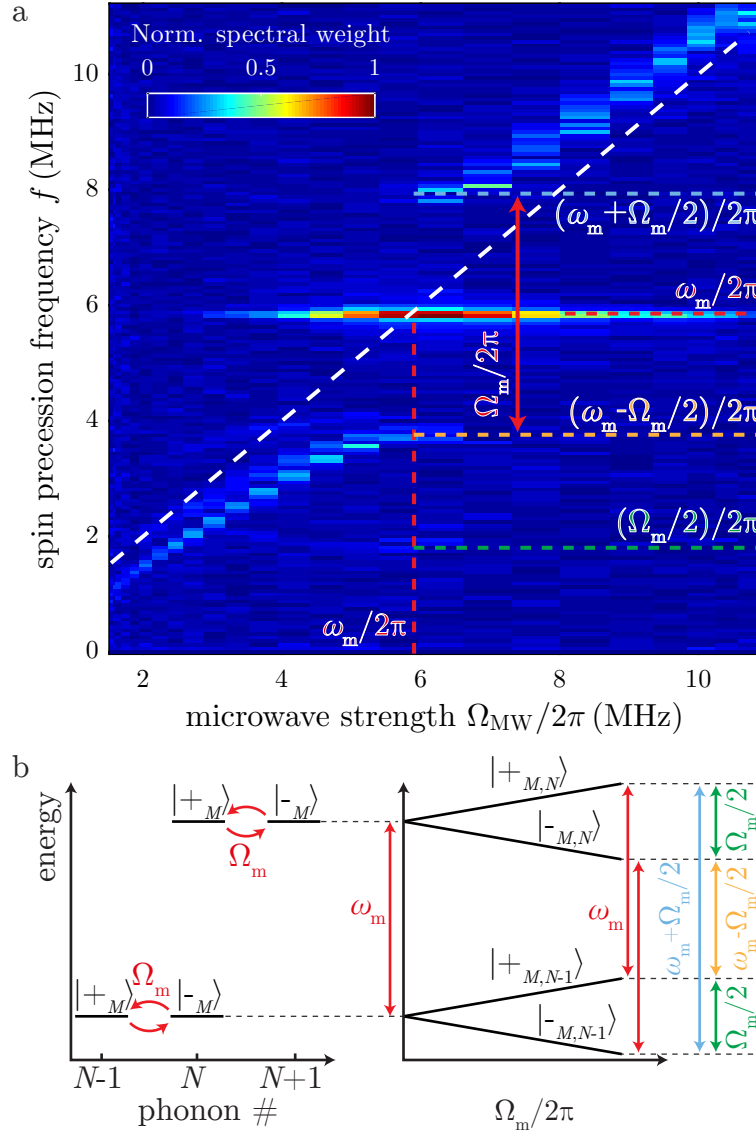


Figure 4.2.: A photon-phonon doubly-dressed spin. a) Spin precession frequency spectrum under combined microwave drive and parametric mechanical strain-driving as a function of microwave Rabi frequency Ω_{MW} . The spectra were obtained by Fourier-transforming the experimentally acquired Rabi oscillation data for each Ω_{MW} . The white dashed line follows $f = \Omega_{\text{MW}}/2\pi$, i.e. the precession frequency expected for pure microwave driving within the rotating wave approximation. Colored dashed lines indicate the characteristic frequencies occurring in the spin precession spectrum of the doubly-dressed spin. b) Eigenenergies ($\hbar = 1$) of the doubly-dressed spin under resonant microwave and parametric driving with $\Omega_{\text{MW}} = \omega_m$. Left: Energies of MW dressed spin states $|\pm_M\rangle$ as a function of phonon number in the cantilever. For resonant driving $|+_{M,N-1}\rangle$ and $|-_{M,N}\rangle$ are degenerate and coupled by the parametric drive with amplitude Ω_m (red arrows), leading to the doubly-dressed states $|\pm_{M,N}\rangle$ (see text). Right: Eigenenergies of $|\pm_{M,N}\rangle$ and $|\pm_{M,N-1}\rangle$ as a function of Ω_m . Colored arrows indicate allowed dressed-state transitions, which are reflected by corresponding features in the spin precession spectrum shown in a).

two additional, hyperfine-split NV spin transitions that are off-resonantly driven. For $\Omega_{\text{MW}} \approx \omega_{\text{m}} = 2\pi \times 5.81 \text{ MHz}$, however, we observe a spectrum that shares striking similarities with the well-known Mollow-triplet in quantum electrodynamics: the measured coherent spin oscillations peak at a single frequency $\omega_{\text{m}}/2\pi$, irrespective of the exact value of Ω_{MW} . Additionally, two weak side bands appear at $(\omega_{\text{m}} \pm \Omega_{\text{m}}/2)/2\pi$. Such spin-oscillator frequency-locking was previously observed for NV centers in diamond nanocrystals parametrically driven by the magnetic fields from a nearby antenna [79] or by the mechanical motion of a spin in a strong magnetic field gradient [78].

This phenomenon of frequency-locking is at the heart of our hybrid continuous decoupling scheme and indeed efficiently decouples the NV spin from environmental fluctuations. The parametric drive couples the microwave dressed states $|\pm_M\rangle$ and thereby yields new eigenstates $|\pm_{M,N}\rangle$, now doubly-dressed by M MW photons and N cantilever phonons [79]. For resonant strain-driving with $\Omega_{\text{MW}} = \omega_{\text{m}}$

$$|\pm_{M,N}\rangle = (|-_{M,N}\rangle \pm |+_{M,N}\rangle)/\sqrt{2} \quad (4.5)$$

where $|+_{M,N}\rangle$ is split from $|-_{M,N}\rangle$ by an energy $\hbar\Omega_{\text{m}}/2$. The resulting, doubly-dressed energy spectrum is illustrated in Fig. 4.2b as a function of mechanical driving strength Ω_{m} , along with the possible transitions allowed between adjacent dressed states. These transitions are indeed also observed in the experimentally measured spin-precession spectra (colored dashed lines in Fig. 4.2a). The transition with the largest spectral weight, $|\pm_{M,N}\rangle \leftrightarrow |\pm_{M,N-1}\rangle$, occurs at $\omega_{\text{m}}/2\pi$ and corresponds to a transition that changes the phonon number N at constant microwave photon number M .

4.4. Coherence protection through double dressing

The data presented in Fig. 4.2a indicate how doubly dressing using mechanically induced parametric strain driving protects the Rabi oscillations from environmental noise and prolongs their decay time. All involved energy levels are insensitive to first-order to fluctuations of Ω_{MW} around ω_{m} . Notably the central peak at a precession frequency $\omega_{\text{m}}/2\pi$ is insensitive to arbitrary orders. The same holds for vulnerability to microwave detunings (i.e. $\omega_{\text{MW}}/2\pi \neq D_{\text{gs}} - \gamma_{\text{NV}}B_z$). The only perturbation which affects the energies of the doubly-dressed states to first order are fluctuations in mechanical driving strength Ω_{m} , which are intrinsically low due to the resonant behavior of our cantilever (see below).

This coherence protection through double dressing is already visible in the width of the dominant central frequency component (Fig. 4.2a), which is significantly narrower than all other spectral features but still limited by the measurement bandwidth $1/\tau_{\text{max}}$. To determine the intrinsic linewidth of this spectral feature, we conducted long-time Rabi oscillation measurements for resonant driving at $\Omega_{\text{MW}} = \omega_{\text{m}}$. The result (Fig. 4.3) shows sustained, coherent Rabi oscillations at frequency $\omega_{\text{m}}/2\pi$ with a characteristic exponential decay over $T_{\text{decay}} = (2.9 \pm 0.3) \text{ ms}$. This value is close to three orders of magnitude longer than the Gaussian decay time determined earlier (see Fig. 4.1) without parametric mechanical driving, and the exponential decay we find indicates that the decay is induced by rapidly fluctuating noise sources, i.e. not by microwave power fluctuations.

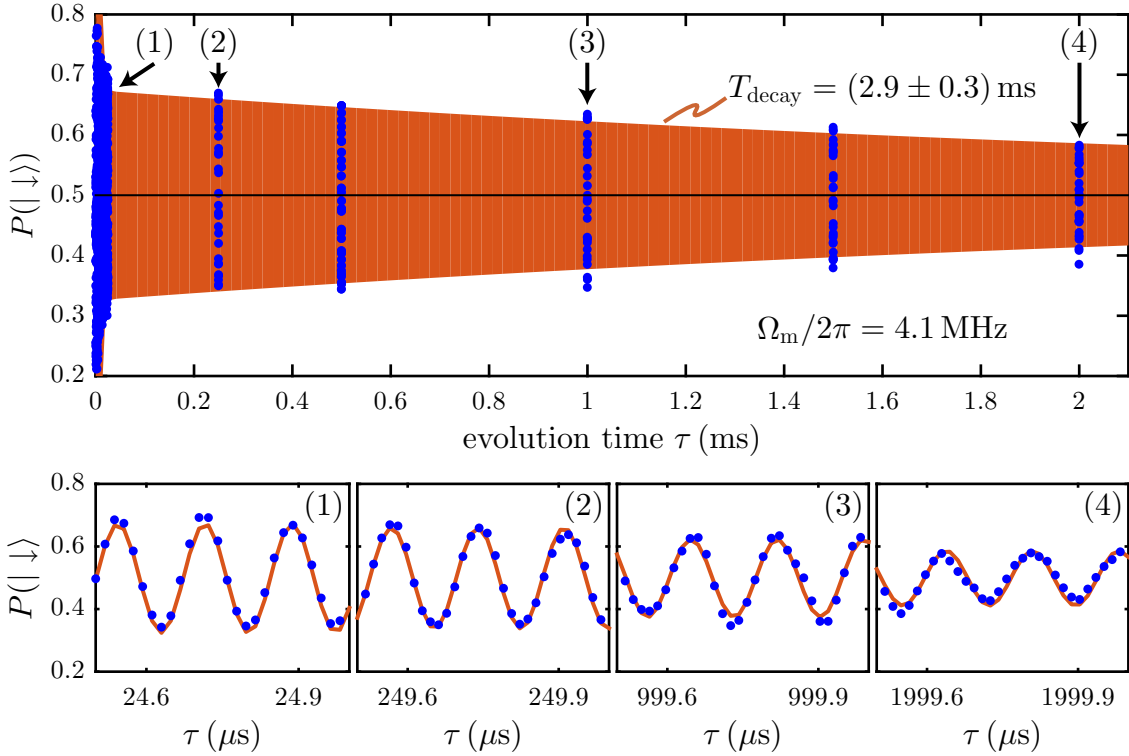


Figure 4.3.: Observation of long lasting Rabi oscillations. Single spin Rabi oscillations stabilized by parametric, mechanical driving with $\Omega_m/2\pi = 4.1$ MHz. Data (blue dots) are well-fit by an exponentially damped oscillation (orange) with decay time $T_{\text{decay}} = (2.9 \pm 0.3)$ ms and a spin-precession (Rabi) frequency of 5.83 MHz. The quickly decaying transient at $\tau < 10 \mu\text{s}$ corresponds to the sidebands observed in Fig. 4.2a (see also Fig. 4.4). The sub-panels show zoomed views over the measurement intervals labeled (1) – (4) and confirm that the slowly decaying signal indeed consists of monochromatic Rabi oscillations at the mechanical frequency $\omega_m/2\pi$.

The measured Rabi oscillations under parametric driving allows us to directly assess the coherence time $T_{2,\text{d.d.}}^*$ of the doubly-dressed spin states $|\pm_{M,N}\rangle$. As indicated in Fig. 4.2b, $|+_{M,N}\rangle$ and $|-_{M,N}\rangle$ are split in energy by $\Omega_m/2$, whose fluctuations of standard deviation σ_{Ω_m} thus directly set the inhomogeneous coherence time of the two-level system formed by $|\pm_{M,N}\rangle$ as $T_{2,\text{d.d.}}^* = 1/\sqrt{2\pi}\sigma_{\Omega_m}$ [134]. To assess $T_{2,\text{d.d.}}^*$ we determined the decay time of the transient oscillations of the observed Rabi oscillations by measuring the width of the Mollow-triplet sidebands [131], which are mutually split by Ω_m (Fig. 4.2a). Figure 4.4a shows that these transient oscillations decay for $\Omega_m/2\pi = 200$ kHz with a Gaussian decay time $T_{2,\text{d.d.}}^* = 59 \mu\text{s}$.

The doubly-dressed coherence time monotonically increases with mechanical driving strength Ω_m (Fig. 4.4b) [99, 131]. This increase however does not persist beyond $\Omega_m/2\pi = 800$ kHz (for which $T_{2,\text{d.d.}}^* = (110 \pm 17) \mu\text{s}$), due to increased mechanical amplitude noise (presumably due to nonlinearities of our diamond oscillator) at these high driving amplitudes. This deterioration is already visible in Fig. 4.3, where $\Omega_m/2\pi = 4.1$ MHz and the initial, transient amplitude oscillations decay on a fast timescale $T_{2,\text{d.d.}}^* \approx 4 \mu\text{s}$. Extending $T_{2,\text{d.d.}}^*$ further by increasing Ω_m would be possible through mechanical oscillators which yield higher strain fields while avoiding

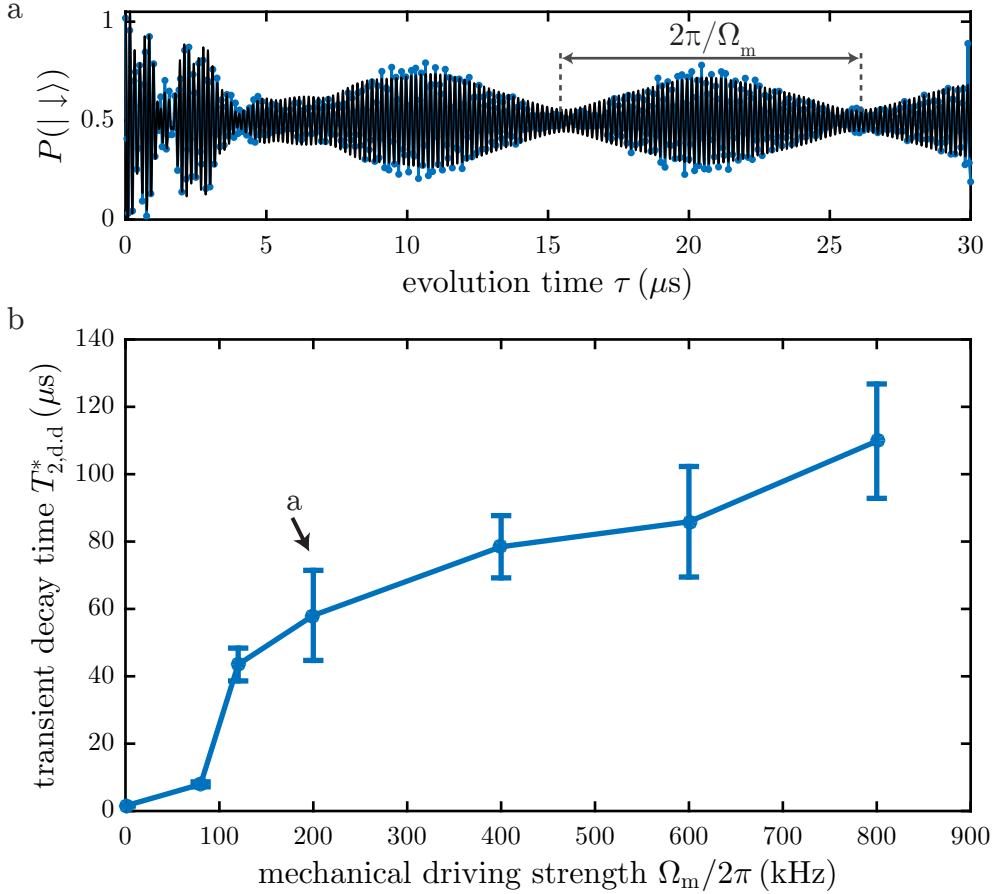


Figure 4.4.: Dependence of doubly-dressed coherence time on mechanical driving strength. a) Decay of transient Rabi oscillations for resonant parametric driving ($\Omega_{\text{MW}} = \omega_m$) and $\Omega_m/2\pi \approx 200$ kHz. The transient is dominated by a beat-note at Ω_m , i.e. the transient generates the Mollow-triplet sidebands visible in Fig. 4.2. The decay time of the beat-note (or, equivalently, the sideband linewidth) is a measure of the coherence time $T_{2,d,d}^*$ of the doubly-dressed spin states [131]. For $\tau \lesssim 5 \mu\text{s}$ we observe contributions from the off-resonantly driven, hyperfine-split NV spin transitions. b.) Coherence time $T_{2,d,d}^*$ as a function of mechanical driving strength Ω_m , demonstrating increased coherence protection for stronger mechanical driving. The observed coherence time saturates around $T_{2,d,d}^* \sim 100 \mu\text{s}$, presumably due to technical limitations in our experiment (see text).

nonlinearities when driven at high amplitudes [100].

Our novel continuous decoupling scheme takes advantage of double-dressing with photons and phonons to enhance spin coherence of NV spins. In that sense, it bears strong similarity to the recently demonstrated decoupling by concatenated driving [131]. In the presented work, however, we also take advantage of the properties of our diamond mechanical oscillator for amplitude noise filtering, which in principle eliminates the need for further, higher-order decoupling fields. Indeed, mechanical resonators in general act as low pass filters for amplitude-noise, with a cut-off frequency set by the mechanical linewidth $f_c = \Delta\omega_m/2\pi = \omega_m/2\pi Q$. For our experiment under ambient conditions we find $Q \approx 530$, and therefore $f_c \approx 11$ kHz, which still poses an important limitation to the coherence protection we can achieve. We note that under vacuum conditions $Q \gtrsim 10^6$ was reported for diamond mechanical oscillators [47], which would then yield $f_c \approx 5$ Hz $\ll 1/T_1$ and allow decoupling from the environment and driving field noise up to the ultimate limit imposed by the spin lifetime T_1 [131].

4.5. Conclusion

To conclude, we have demonstrated a novel hybrid continuous dynamical decoupling scheme for a single spin that combines resonant microwave excitation with parametric driving of the spin by using strain generated in a nanomechanical oscillator. With this approach we decoupled the spin from environmental noise and extended both the coherence time from the typical $T_2^* = 1.5 \mu\text{s}$ to $T_{2,\text{d.d.}}^* \gtrsim 100 \mu\text{s}$ and the Rabi decay time from $5.3 \mu\text{s}$ to about 2.9 ms. Next experimental steps may include the use of high quality-factor mechanical oscillators for coherence protection up to the T_1 -limit and the demonstration of coherent manipulation of dressed spin states. Our work thereby offers attractive perspectives for employing hybrid continuous dynamical decoupling of NV center spins for applications in quantum information processing and quantum sensing.

5. Strong mechanical driving of a single electron spin

Quantum devices for sensing and computing applications require coherent quantum systems, which can be manipulated in fast and robust ways. Such quantum control is typically achieved using external electromagnetic fields, which drive the system's orbital [135], charge [8] or spin [7, 10] degrees of freedom. However, most existing approaches are characterized by certain experimental or fundamental limitations. They require complex and unwieldy gate structures and with few exceptions [136, 137] are limited to the regime of weak coherent driving.

In this chapter we present a novel approach to coherently drive a single NV spin using crystal strain which brings vital advantages compared to established methods relying on electromagnetic fields. Such strain fields can be straightforwardly engineered in our hybrid system (see Chap. 3) and offer a direct coupling mechanism to embedded NV centers [1, 41, 42]. Since they are intrinsic to our system, strain fields are immune to drifts in the coupling strength. Additionally, strain does not generate spurious stray fields, which are unavoidable with electric or magnetic driving and which can cause unwanted dephasing or heating of the environment.

In our approach we create transverse AC strain in our hybrid system and induce long-lasting, coherent oscillations of the embedded single NV centers' spins. We perform direct spectroscopy of the emerging phonon-dressed states and observe hallmarks of the strong driving regime [138, 139], where the spin rotation frequency significantly exceeds the spin splitting. Finally, we employ our continuous strain driving to enhance the NV's spin coherence time [140]. Our room-temperature experiments thereby constitute an important step towards strain-driven, integrated quantum devices and open new perspectives to investigate unexplored regimes of strongly driven multi-level systems [141] and to study exotic spin dynamics in hybrid spin-oscillator devices [117]. The presented results have been published in [99].

5.1. Demonstration of coherent spin manipulation

5.1.1. Improvements to experimental setup

To perform the experiments presented in the following, several improvements to the experimental setup from Chap. 3 were made. First, a new sample, implanted at 12 keV and $1 \cdot 10^{-10}$ ions/cm² (Innovion, USA), with a slightly lower NV density was employed. Identifying single NVs was possible, but still challenging. The cantilevers were structured as previously explained and thus aligned to the [110] crystal direction

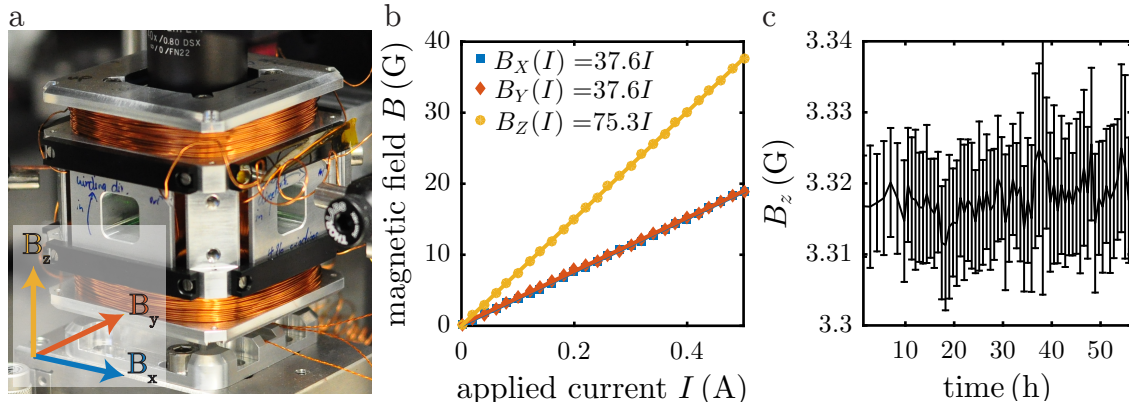


Figure 5.1.: Homebuilt magnetic field coils. a) Six coils, two per coordinate axis, are arranged in a Helmholtz-like setup, where the spatial separation of two corresponding coils matches their diameter. b) The X, Y -pairs have 426 windings per coil and create a magnetic field of 37.6 G/A while the Z -pair with 328 windings per coil is capable of creating magnetic fields of 75.3 G/A. c) The applied magnetic field B_z (here measured via the Zeeman splitting Δ_z of an NV center) is highly stable over time and shows fluctuations in the order of ± 5 mG only. The error bars denote 95% confidence fit intervals.

with dimensions in the range of $(0.2 - 1) \times 3.5 \times (15 - 25) \mu\text{m}^3$ for thickness, width and length.¹

Second, to study resonant strain driving of the $|-1\rangle \leftrightarrow |+1\rangle$ spin transition a purely longitudinal magnetic field B_z needs to be applied such that $\omega_m = 2\pi\Delta_z$. To that end we replaced the static magnet from Chap. 3 with a three-axis magnetic field generated by three homebuilt coil pairs, driven by constant-current sources (Agilent, E3644A) (Fig. 5.1). The coil pairs are arranged in a Helmholtz-like setup where the spatial separation between corresponding coils matches their diameter (X, Y -pairs) or their radius (Z -pair). The X, Y -pairs feature a radius of $r_{X,Y} = 2$ cm and 426 windings, giving rise to magnetic fields of $B_{X,Y} = 37.6$ G/A. The Z -pair is larger ($r_Z = 3$ cm) and with 383 windings creates a magnetic field of $B_Z = 75.3$ G/A. We control the three coil pairs separately and can align the resulting magnetic field to within $< 1^\circ$ to a desired NV direction.² The applied magnetic field is highly stable over time with observed fluctuations usually below 5 mG (Fig. 5.1c).

¹For the measurements we presented here three individual NV centers on three separate cantilevers were studied. The NVs were characterized by different zero-field splittings $D_{\text{gs}}^{\#1} = 2.870$ GHz, $D_{\text{gs}}^{\#2} = 2.871$ GHz and $D_{\text{gs}}^{\#3} = 2.8725$ GHz, most likely caused by varying intrinsic strain environments. As our experiment relies on a significant transverse strain component, all NV centers belonged to orientation family NVA, i.e. were predominantly oriented along the cantilever axis. The corresponding cantilevers had eigenfrequencies of $\omega_m^{\#1}/2\pi = 6.83$ MHz, $\omega_m^{\#2}/2\pi = 9.18$ MHz and $\omega_m^{\#3}/2\pi = 5.95$ MHz, respectively.

²The alignment procedure, originally established by Jean Teissier and Arne Barfuss, is nicely illustrated in the supplementary material of [62].

5.1.2. Mechanically induced Rabi oscillations

Coherent strain driving of NV spins is based on the sensitive response of the NV spin states to strain in the diamond host lattice. The strain-coupling Hamiltonian for transverse strain takes the form (see App. A.7)

$$\hat{H}_{\text{gs}}^{\perp}/\hbar = -g_0^{\perp} (\hat{a} + \hat{a}^{\dagger}) \left(e^{i\varphi} \hat{S}_+^2 + e^{-i\varphi} \hat{S}_-^2 \right) \quad (5.1)$$

where g_0^{\perp} denotes the transverse single phonon coupling strength and $\hat{S}_{+(-)}$ and \hat{a}^{\dagger} (\hat{a}) are the raising (lowering) operators for spin and phonons, respectively. Even though already demonstrated in Chap. 3 we again want to emphasize here that transverse strain leads to a direct coupling of the two electronic spin states $|-1\rangle$ and $|+1\rangle$ [1]. In the case of near-resonant, AC strain, coherent manipulation of the dipole-forbidden transitions $|-1, m_I\rangle \leftrightarrow |+1, m_I\rangle$ is possible [41]. In other words, transverse strain drives transitions where the electronic spin quantum number m_s differs by two units of angular momentum but the nuclear spin quantum number m_I remains constant. For a classical (coherent) phonon field at angular frequency ω_m , (5.1) can be rewritten as

$$\hat{H}_{\text{gs}}^{\perp}/\hbar = -\Omega_m \cos(\omega_m t) \left(e^{i\varphi} \hat{S}_+^2 + e^{-i\varphi} \hat{S}_-^2 \right) \quad (5.2)$$

where the mechanical Rabi frequency $\Omega_m = g_0^{\perp} \tilde{u}_{\text{max}}/\Delta x_{\text{zpm}}$ describes the amplitude of the strain drive, with Δx_{zpm} and \tilde{u}_{max} the cantilever's zero-point motion and peak amplitude, respectively. Typical values for the cantilevers and NVs employed in this chapter are $\Delta x_{\text{zpm}} \approx 1 \cdot 10^{-14}$ m and $g_0^{\perp}/2\pi \approx 0.2$ Hz.

To demonstrate the coherent character of our AC strain drive, we first performed strain-driven Rabi oscillations between $|-1\rangle$ and $|+1\rangle$ for a given hyperfine manifold (here we present data for $m_I = 1$ as indicated in Fig. 5.2a and b, but any other value of m_I works as well). To that end, we prepare the NV in $|-1, +1\rangle$ by applying an appropriate sequence of laser and microwave pulses (Fig. 5.2c). Specifically, a green laser pulse polarizes the NV in the $m_s = 0$ spin manifold and a subsequent MW π -pulse, resonant with the $|0, +1\rangle \leftrightarrow |-1, +1\rangle$ transition, completes the initialization process. We then let the NV spin evolve for a variable time τ under the influence of our coherent AC strain field generated by constantly exciting the cantilever at a fixed peak amplitude $\tilde{u}_{\text{max}} \approx 100$ nm.³ After this evolution we measured the resulting population in $|-1, 1\rangle$ with a pulse sequence analogous to our initialization protocol. As expected, we observed strain-induced Rabi oscillations (Fig. 5.2d) with $\Omega_m/2\pi = (1.14 \pm 0.01)$ MHz and hardly any damping over the 30 μ s observation time. Importantly and in contrast to a study on NV ensembles [41] that was published prior to ours, this damping timescale is not limited by ensemble-averaging since our experiment was performed on a single NV spin. We however want to point out an experimental difficulty visible in Fig. 5.2d. Due to the finite quality factor $Q \approx 300$ of the cantilever employed here, its ring-up and ring-down times $t_{\text{up,down}} = 1/\Gamma_m = 2Q/\omega_m \approx 88$ μ s are much longer than the typical timescales of our applied

³The cantilever used here had an eigenfrequency of $\omega_m/2\pi = (6.83 \pm 0.02)$ MHz and a mechanical susceptibility of $\chi_m = 12$ nm/V. Consequently we applied a driving voltage of $V_{\text{AC}} = 8$ V to reach $\tilde{u}_{\text{max}} \approx 100$ nm (compare Chap. 3).

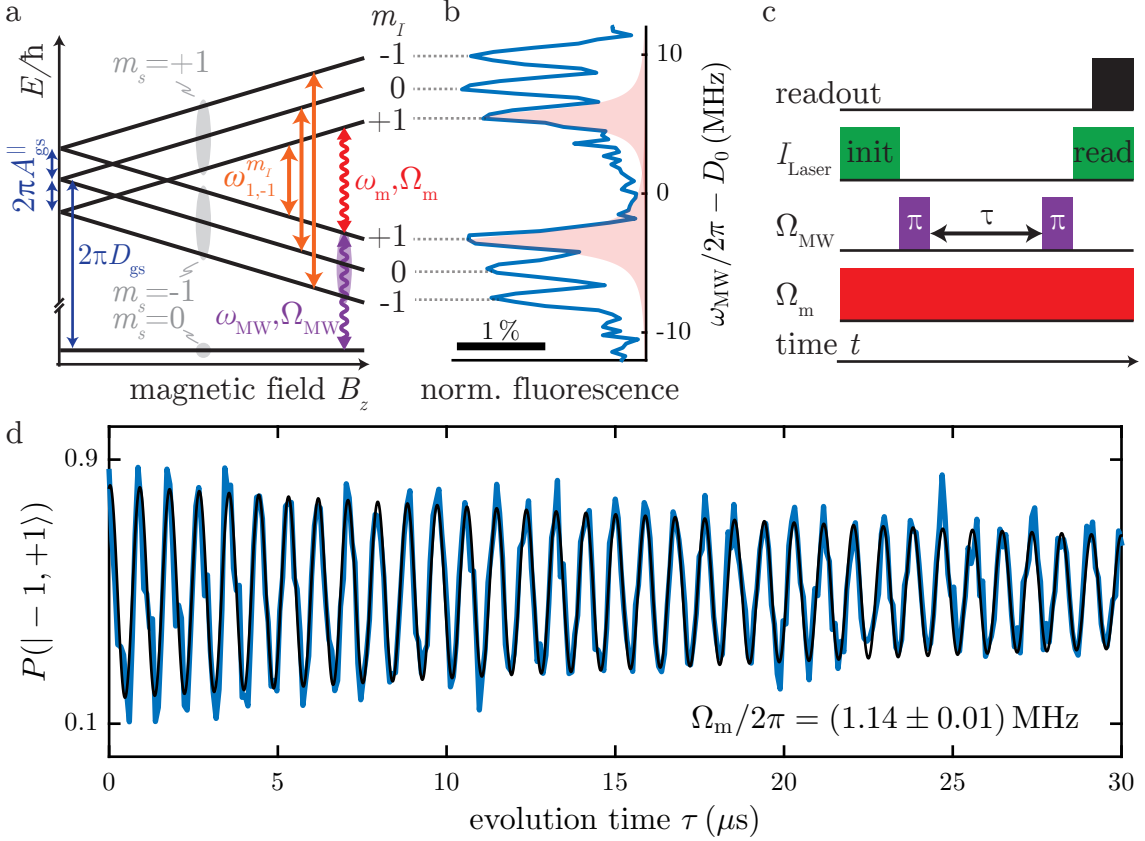


Figure 5.2.: Demonstration of strain-induced coherent spin manipulation. a) Energy levels of the NV spin as a function of magnetic field applied along the NV axis. Electronic spin states $|m_s = \pm 1\rangle$ split into three levels each due to hyperfine interactions with the NV's ^{14}N nuclear spin ($I = 1$, $A_{\text{gs}}^{\parallel} = -2.17$ MHz). Wavy lines indicate strain (red) and microwave (violet) fields of frequency ω and strength Ω . b) Pulsed ESR measurement of a single NV center, showing the NV's hyperfine structure. In the data presented here we drive hyperfine levels with $m_I = +1$. c) Pulse sequence employed to observe strain-induced Rabi oscillations. d) Strain-driven Rabi oscillations (data in blue, exponential fit to damped Rabi oscillations in black).

sequences (typical π -pulses are $\tau_{\pi} \approx 200 - 700$ ns long). We therefore have to apply our AC strain field continuously. In addition, to avoid unwanted population in the $|-1, 0\rangle$ and $|-1, -1\rangle$ hyperfine states during the initialization process, our MW π -pulses are of non-zero length. Both aspects limit the contrast of our mechanical Rabi oscillation signal to about 80%.

5.1.3. MW spectroscopy of the mechanically induced Autler-Townes effect

We obtain further insight into the strength and dynamics of our coherent strain-driving mechanism from pulsed ESR spectroscopy of the strain-coupled NV spin states, $|+1\rangle$ and $|-1\rangle$. For this, we employed a weak microwave tone at frequency

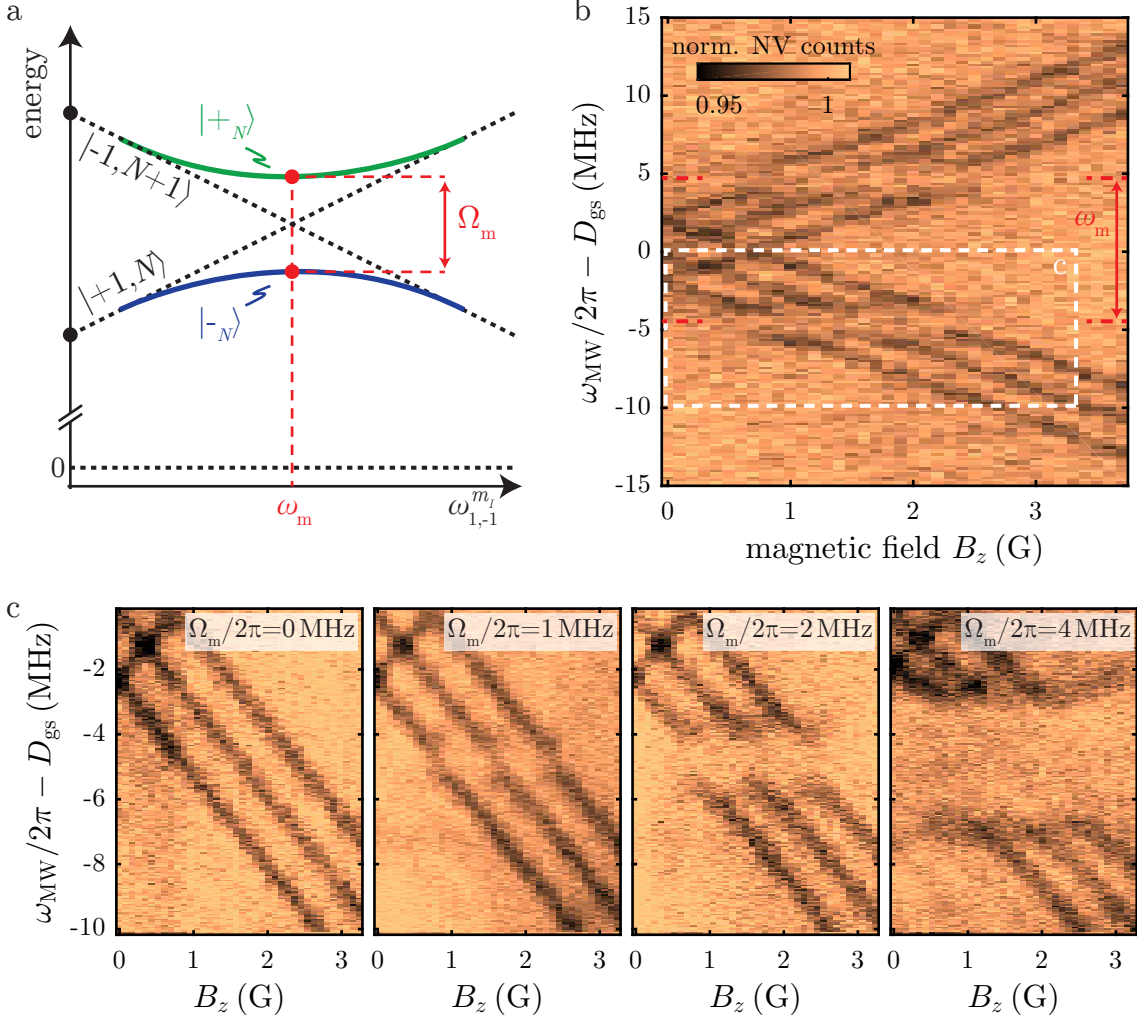


Figure 5.3.: Mechanically induced Autler-Townes effect probed by microwave spectroscopy. a) Eigenenergies of the joint spin-phonon system with basis-states $|m_s, N\rangle$, where m_s and N denote the electronic spin quantum number and the number of phonons in the cantilever, as a function of the spin splitting $\omega_{1,-1}^{m_I}$. Strain couples $|+1, N\rangle$ and $|-1, N+1\rangle$ and, whenever the resonance condition $\omega_{1,-1}^{m_I} = \omega_m$ is fulfilled, leads to new eigenstates $|+N\rangle$ and $|-N\rangle$ with energy splitting Ω_m (see text). b) Microwave spectroscopy of phonon-dressed states using a weak microwave probe with frequency ω_{MW} . For $m_I = -1, 0$ and 1 , resonance is separately established at $B_z \approx 0.9, 1.6$ and 2.3 G. c) Dependence of the energy gap between $|+N\rangle$ and $|-N\rangle$ on mechanical driving strength. As expected, the gap scales linearly with Ω_m for each hyperfine state. Data was recorded over a parameter range indicated by white dashed lines in b).

$\omega_{\text{MW}}/2\pi$ to probe the $|0\rangle \leftrightarrow |\pm 1\rangle$ transitions as a function of applied magnetic field B_z in the presence of the coherent strain field. This strain field has a striking effect on the NV's ESR spectrum (Fig. 5.3) in that it induces excitation gaps at $\omega_{\text{MW}} - 2\pi D_{\text{gs}} = \pm\omega_{\text{m}}/2$, i.e. for $B_z \approx 0.9, 1.6$ and 2.3 G (note that we used a cantilever with $\omega_{\text{m}}/2\pi = 9.18$ MHz for these experiments). At these values of B_z the AC strain field in the cantilever is resonant with a given hyperfine transition, i.e. the energy splitting $\hbar\omega_{1,-1}^{m_I}$ between $|-1, m_I\rangle$ and $|+1, m_I\rangle$ equals $\hbar\omega_{\text{m}}$ (Fig. 5.2a). The energy gaps which we observe in the ESR spectra under resonant strain driving are evidence of the Autler-Townes effect – a prominent phenomenon in quantum electrodynamics [133, 142], which has previously been observed in atoms and molecules [143], quantum dots [144], and superconducting qubits [145]. Our observation of the Autler-Townes effect was performed on a single electronic spin in the microwave domain and to the best of our knowledge constitutes the first observation of the Autler-Townes effect under ambient conditions.

The observed Autler-Townes splitting can be understood by considering the joint energetics of the NV spin states and the quantized strain field containing N phonons used to drive the spin (Fig. 5.3a) [133]. The joint basis states $|m_s, N\rangle$ consist of NV spin states $|m_s\rangle$, where we omit the nuclear spin quantum number m_I for simplicity, dressed by N phonons in the cantilever. As one phonon is required, strain couples $|+1, N\rangle$ to $|-1, N+1\rangle$ and leads to new eigenstates $|\pm_N\rangle$. These states anti-cross on resonance, i.e. for $\omega_{1,-1}^{m_I} = \omega_{\text{m}}$, where $|\pm_N\rangle = (|+1, N\rangle \pm |-1, N+1\rangle)/\sqrt{2}$ are split by the energy $\hbar\Omega_{\text{m}}$. In other words the dressed eigenstates are separated by an energy that corresponds to the mechanical Rabi frequency. As $\Omega_{\text{m}} \propto \tilde{u}_{\text{max}}$ we expect the splitting to increase linearly with the driving field amplitude which we control through the strength of piezo excitation V_{AC} . The corresponding experiment confirms this expectation (Fig. 5.3c).

5.2. The strong driving regime

To investigate the limits of our coherent strain-induced spin driving and study the resulting spin dynamics, we performed detailed dressed-state spectroscopy as a function of driving strength Ω_{m} (Fig. 5.4a). To that end, we first set B_z such that $\omega_{1,-1}^{m_I=1} = \omega_{\text{m}}$ and then performed pulsed ESR spectroscopy for different values of Ω_{m} . Note that we used a cantilever with $\omega_{\text{m}}/2\pi = 5.95$ MHz for these experiments. For weak driving with $\Omega_{\text{m}} < \omega_{\text{m}}$ the dressed states $|\pm_N\rangle$ emerging from the resonantly coupled states $|m_s = -1, m_I = 1\rangle$ and $|m_s = +1, m_I = 1\rangle$ split linearly with Ω_{m} as expected from the rotating wave approximation. However for $\Omega_{\text{m}} \approx \omega_{1,-1}^{m_I=1}$ the linear relationship breaks down due to multi-phonon couplings involving states which belong to different sub-spaces spanned by $|\pm_N\rangle$ and $|\pm_M\rangle$ with $N \neq M$ (see App. A.8) [133]. This observation is closely linked to the breakdown of the rotating wave approximation [126, 137] and indicates the onset of the strong driving regime we achieve in our experiment.

For even larger Rabi frequencies Ω_{m} , the dressed states evolve into a characteristic sequence of crossings and anti-crossings (see App. A.8 for a more detailed explanation). The (anti-)crossings occur in the vicinity of $\Omega_{\text{m}} = q\omega_{\text{m}}$, with q an odd (even) integer and are related to symmetries of our strain-coupling Hamiltonian (5.1), which

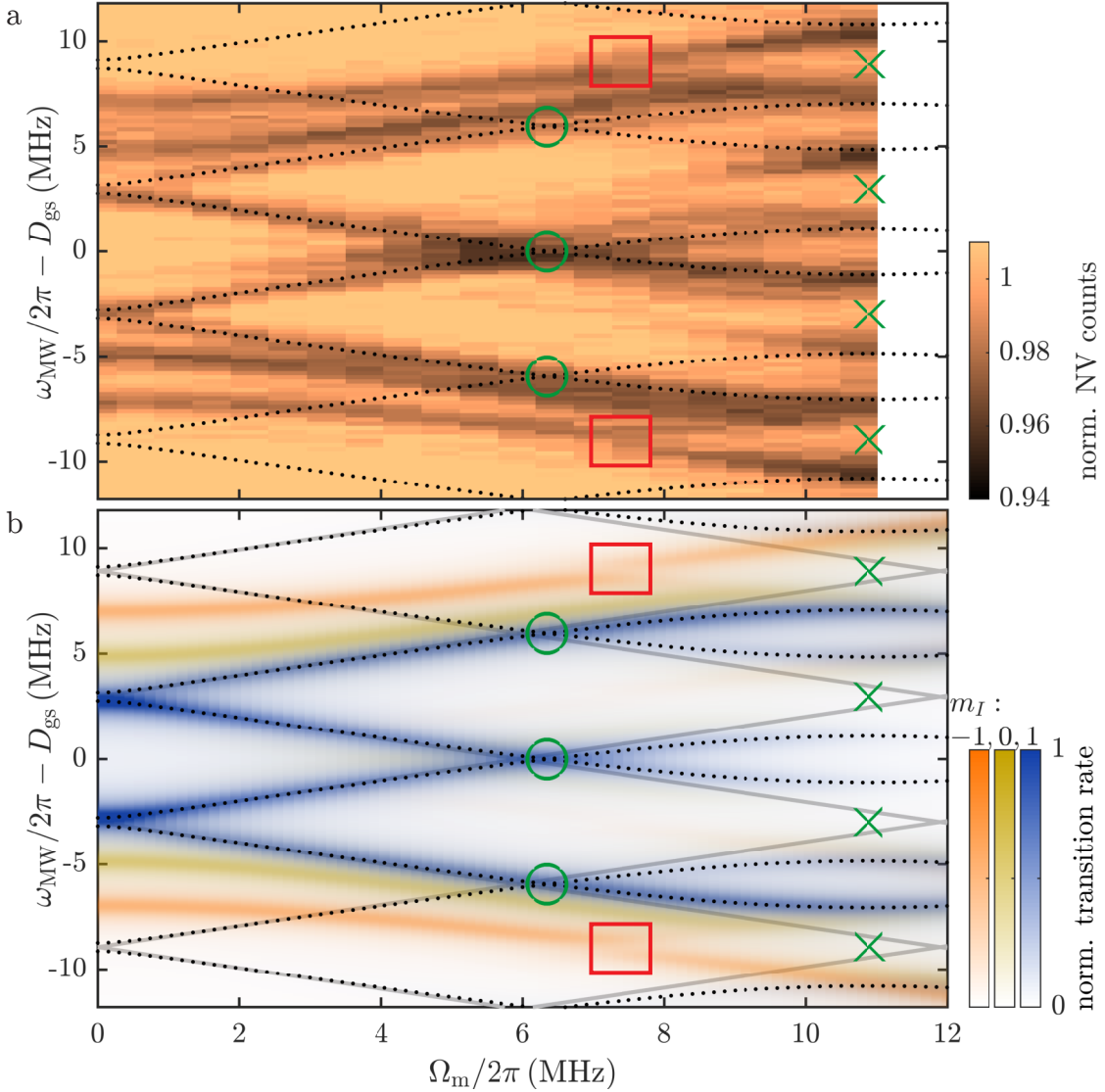


Figure 5.4.: Dressed-state spectroscopy of our strongly driven NV spin. a) Microwave spectroscopy of the mechanically driven NV spin at $B_z = 1.8$ G where $\omega_m = \omega_{1,-1}^{m_I=+1}$ as a function of driving strength Ω_m . The resonantly coupled states $|\pm 1, +1\rangle$ at $\omega_{\text{MW}}/2\pi - D_{\text{gs}} = \pm 2.98$ MHz first split linearly with Ω_m and then evolve into a sequence of crossings and anti-crossings (green circles and crosses, respectively) with higher-order dressed states. These (anti-)crossings indicate the strong driving regime. b) Calculated transition rates from $|m_s = 0\rangle$ to the dressed states obtained by Fermi's Golden rule (see text). Blue, yellow and orange shaded transitions correspond to the hyperfine manifolds $m_I = +1, 0$ and -1 , respectively. In both panels, black dots indicate the calculated dressed-state energies for $m_I = +1$. Grey lines in b) show the same under the rotating wave approximation. Deviations between black dots and the gray lines indicate the onset of the strong driving regime. Red squares mark $q = 2$ anti-crossings of the far detuned $m_I = -1$ manifolds (see text).

changes the phonon number by one and the spin quantum number by two units [133]. Our experiment allows us to clearly identify the $q = 1$ and $q = 2$ (anti-)crossings (green circles and crosses in Fig. 5.4a) and thereby demonstrates that we reside well within the strong driving regime ($\Omega_m > \omega_{1,-1}^{m_I}$) of a driven two-level system.⁴ Note that the anti-crossings are slightly shifted from the values $2\omega_m$. These shifts are a result of the Bloch-Siegert shift [146], which is neglected in the rotating wave approximation (see App. A.8). Furthermore, we point out that the $q = 2$ anti-crossing is also visible in the $m_I = 0$ and $m_I = -1$ manifolds, where the strain-driving field is detuned by 4.2 MHz and 8.4 MHz, respectively (since $m_I = +1$ is resonantly driven, these values are given by twice and four times the hyperfine splitting). For $m_I = -1$, this anti-crossing is visible as a weak splitting of the $m_I = -1$ ESR lines at $\Omega_m/2\pi \approx 7.5$ MHz, $\omega_m/2\pi - D_{\text{gs}} \approx \pm 9$ MHz (red squares in Fig. 5.4). As a result of the strong detuning, this splitting is much smaller than for the resonantly driven $m_I = +1$ transition.

We have carried out an extensive numerical analysis to compare our experimental findings to theoretical expectations. Following [139] we employ Floquet theory to treat the time dependence of the strain-induced spin driving $\hat{\mathbf{H}}_{\text{gs}}^\perp = -\hbar\Omega_m \cos(\omega_m t) \left(e^{i\varphi} \hat{\mathbf{S}}_+^2 + e^{-i\varphi} \hat{\mathbf{S}}_-^2 \right)$, beyond the rotating wave approximation. The key idea here is to map the Hamiltonian with periodic time dependence on an infinite-dimensional, but time-independent Floquet Hamiltonian \mathcal{H}_F . We can then solve the eigenvalue problem $\mathcal{H}_F|u_j\rangle = \hbar\omega_j|u_j\rangle$ with standard methods to obtain quasi-energies $\hbar\omega_j$ and corresponding eigenvectors $|u_j\rangle$. Treating the weak microwave drive up to second order in drive strength we find the rate for the system to leave the initial state with Fermi's golden rule as [139]

$$\mathcal{P} = \frac{1}{\hbar^2} \sum_{i,f} \frac{\gamma_{fi} |\langle u_f | \hat{\mathbf{H}}_{\text{MW}} | u_i \rangle|^2}{(\omega_f - \omega_i - \omega_{\text{MW}})^2 + \frac{\gamma_{fi}^2}{4}}, \quad (5.3)$$

where γ_{fi} denotes the corresponding linewidths of final and initial state and the MW driving Hamiltonian is $\hat{\mathbf{H}}_{\text{MW}} = \sum_{m_I} \hbar\Omega_{\text{MW}} (|+1, m_I\rangle\langle 0, m_I| + |-1, m_I\rangle\langle 0, m_I| + \text{H.c.})$ with driving strength Ω_{MW} , assuming a linearly polarized MW field.

The result is shown in Fig. 5.4b and demonstrates quantitative agreement of the model with our experimental findings.⁵ However, for the largest values of Ω_m , some discrepancies of the transition strengths between data and model remain. We tentatively assign these to uncertainties in microwave polarization, to possible variations of linewidths with Ω_m and to our particular pulsed ESR detection scheme [90]. Our

⁴We would like to point out that several notions of *strong driving* are employed in literature. In our work presented here we refer to a situation, where the strength of the driving field Ω_m exceeds the splitting $\omega_{1,-1}^{m_I}$ of the two coupled spin hyperfine levels. We note that some authors employ a slightly different notion of strong driving and define this regime as one in which the driving strength Ω_m exceeds the systems dissipation rates ([144] would be one such example). In our definition, such a regime would correspond to the coherent driving regime where the coupling strength is larger than the linewidth of the involved levels (and one can for example observe an Autler-Townes splitting with level spectroscopy, as demonstrated above).

⁵For the simulations shown in Fig. 5.4b we assumed an initial state $|u_i\rangle = |m_s = 0, m_I\rangle$ and linewidths $\gamma_{fi} = \gamma = 1$ MHz, and summed the result over all nuclear spin quantum numbers $m_I \in \{-1, 0, 1\}$.

calculation further shows that over our range of experimental parameters, Ω_m is linear in \tilde{u}_{\max} and reaches a maximum of $\Omega_m/2\pi \sim 10.75$ MHz. This value was at the time of the experiment limited by the maximally achievable piezo driving strength as well as the structural integrity of our resonators. Increasing the Q factor, for example by going to vacuum, will lead to higher cantilever deflections at identical piezo driving and larger Ω_m will be possible. Another option to extend our experiment beyond the $q = 2$ anti-crossings would be to work with low eigenfrequency cantilevers with $\omega_m/2\pi = 2$ MHz. By applying a maximum driving strength $\Omega_m/2\pi \approx 11$ MHz, we should observe (anti-)crossings up to fifth order.

5.3. Protecting NV spin coherence by coherent strain driving

As we know from Chap. 4, continuous coherent driving can be employed to protect a quantum system from its noisy environment and thereby increase its coherence times [101, 102, 129, 131, 140]. For NV spins, decoherence is predominantly caused by environmental magnetic field noise which normally couples linearly to the NV spin through the Zeeman Hamiltonian $\hat{H}_Z = \gamma_{\text{NV}} B_z \hat{S}_z$ (Fig. 5.2a). Conversely, for the dressed states $|\pm_N\rangle$ we create by coherent strain-driving, $\langle \pm_N | \hat{H}_Z | \pm_N \rangle = 0$ and the lowest order coupling to magnetic fields is only quadratic (Fig. 5.3a). The dressed states are thus less sensitive to magnetic field fluctuations and should exhibit increased coherence times, compared to the undriven NV.

To demonstrate such coherence enhancement by continuous driving we performed Ramsey spectroscopy [132] on our strain-driven NV spin. To that end, we adjusted B_z such that $\omega_{1,-1}^{m_I=1} = \omega_m$ (we used a cantilever with eigenfrequency $\omega_m/2\pi = 6.83$ MHz) and employed the sequence presented in Fig. 5.5a. We drove the spin with $\Omega_m/2\pi = 1.68$ MHz and applied a pulsed MW probe field of strength $\Omega_{\text{MW}}/2\pi = 1.29$ MHz and frequency $\omega_{\text{MW}}/2\pi - D_{\text{gs}} \approx 6.83/2$ MHz. This value of $\omega_{\text{MW}}/2\pi$ corresponds to a spectral position roughly in the center of the two dressed state transitions of the $m_s = +1$ spin manifold (see inset in Fig. 5.5b). The microwave Rabi frequency Ω_{MW} was thereby strong enough to drive both detuned dressed state transitions but also induced some population in $|+1, -1\rangle$ and $|+1, 0\rangle$. These populations led to the fast oscillating and highly damped signal visible for $\tau \lesssim 5 \mu\text{s}$ in Fig. 5.5b.

In order to fit the Ramsey data in Fig. 5.5b, we used a sum of cosines with Gaussian decays [132] for both dressed states and the uncoupled hyperfine states. As the dressed state coherences decay on a different timescale as compared to the bare hyperfine states we employed the fitting function

$$S_{\text{Ramsey}}^{\text{DS}}(\tau) = e^{-(\tau/T_{2,\text{DS}}^*)^2} \sum_{i=+,-} \beta_{\text{DS},i} \cos(2\pi\delta_{\text{DS},i}\tau + \phi_{\text{DS},i}) + \sum_{m_I=-1,0} e^{-(\tau/T_{2,m_I}^*)^2} \beta_{m_I} \cos(2\pi\delta_{m_I}\tau + \phi_{m_I}) \quad (5.4)$$

where β , δ and ϕ are the population, microwave-detuning and initial phase for the hyperfine states $|+1, m_I\rangle$ and dressed states $|\pm_N\rangle$ (indicated by the subscript DS). Our approach yielded the decay time $T_{2,\text{DS}}^* = (16.4 \pm 0.6) \mu\text{s}$ for the dressed states.

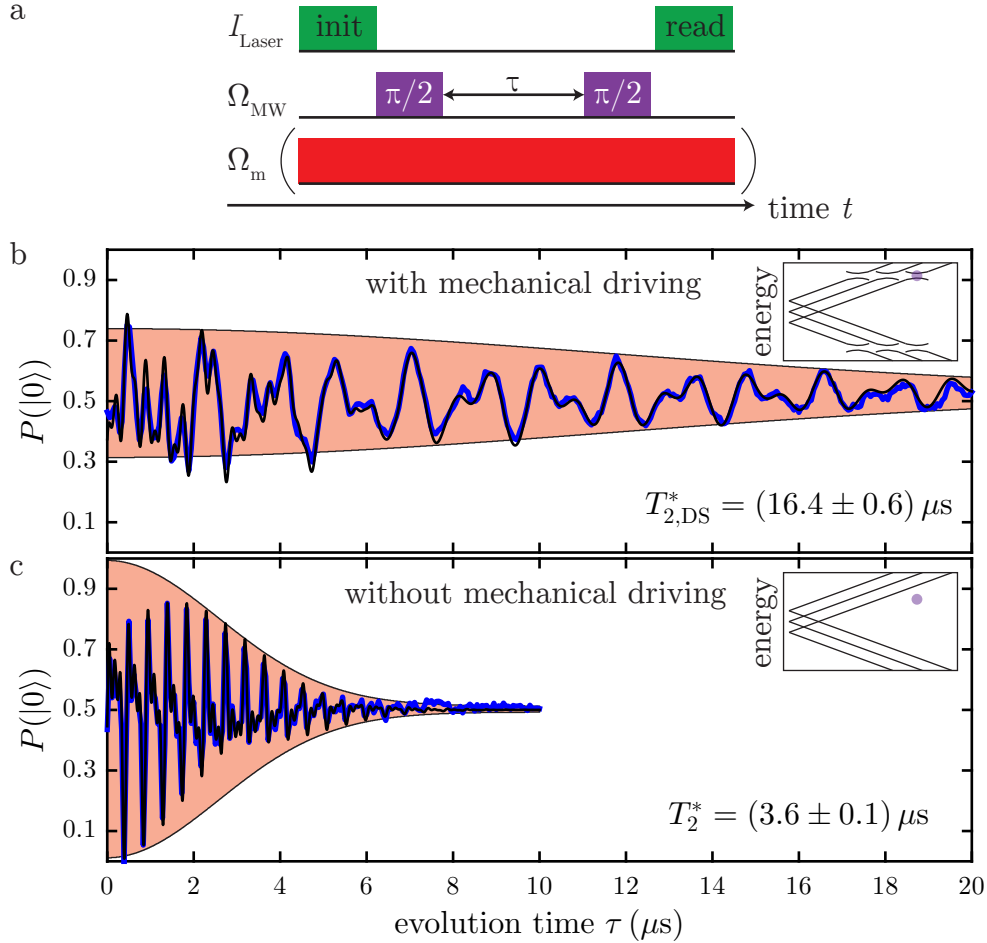


Figure 5.5.: Protecting NV spin coherence by coherent strain driving. a) Employed sequence to measure free induction decay with and without mechanical driving. b) Spin coherence decay of $|\pm_N\rangle$ (for $m_I = +1$) as measured by Ramsey interferometry between the state $|m_s = 0\rangle$ and the $|m_s = +1\rangle$ manifold. The probability for the NV to occupy the $|m_s = 0\rangle$ manifold after the sequence is denoted as $P(|0\rangle)$. The inset illustrates the NV spin's eigenenergies as a function of B_z and indicates the magnetic field and microwave frequencies employed (purple dot) with respect to the dressed-state spectrum shown in Fig. 5.3b. c) Measurement of NV spin coherence time in the undriven case, as determined by Ramsey spectroscopy between $|m_s = 0\rangle$ and $|m_s = +1\rangle$, in the absence of mechanical driving. Inset as in a). In both panels, the orange envelope indicates the coherence decay extracted from our fit (black) to the data (blue).

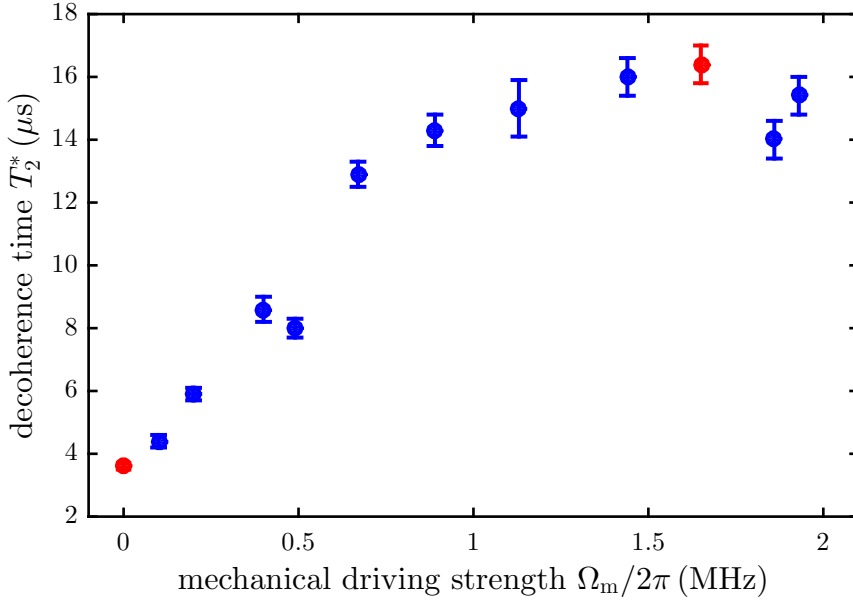


Figure 5.6.: Decoherence time T_2^* versus mechanical driving strength Ω_m . Each data point corresponds to the decay-time of a Ramsey interference signal recorded analogously to the ones shown in Fig. 5.5 (denoted by red markers). Overall we observe a linear increase of spin coherence for low Ω_m . T_2^* peaks at $\Omega_m/2\pi \approx 1.5$ MHz and decreases for higher driving strengths, most likely due to the onset of technical noise in the driving field. Error bars in T_2^* indicate 95% confidence intervals for the nonlinear least-squares parameter estimates.

To compare the dressed state decay time to the undriven case we repeated our experiment and applied the pulse sequence from Fig. 5.5a with $\Omega_m/2\pi = 0$ and $\omega_{\text{MW}}/2\pi - D_{\text{gs}} \approx 1$ MHz (see data in Fig. 5.5c). In the undriven case the fitting function

$$S_{\text{Ramsey}}(\tau) = e^{(-\tau/T_2^*)^2} \sum_{m_i=0,\pm 1} \beta_{m_i} \cos(2\pi\delta_{m_i}\tau + \phi_{m_i}) \quad (5.5)$$

is slightly simplified as only the three undriven levels are populated. We found the bare NV coherence time of $T_2^* = (3.6 \pm 0.1) \mu\text{s}$ (Fig. 5.5c) and compared to the driven coherence time of $T_{2,\text{DS}}^* = (16.4 \pm 0.6) \mu\text{s}$ this demonstrates a significant enhancement of T_2^* caused by our continuous, mechanical drive.

Our decoupling protocol is readily tuneable. For increasing Ω_m we have observed an initially monotonic, approximately linear increase of T_2^* , which saturates for $\Omega_m/2\pi \gtrsim 1$ MHz (Fig. 5.6). For further increasing driving strengths, the observed T_2^* decreased again. We assign this current limitation to the onset of technical noise in the driving field [102, 131, 140], whose mitigation might lead to further improvements of T_2^* in the future (compare Chap. 4).

5.4. Summary and outlook

To summarize, we employed AC transverse strain and coherently manipulated the NV's spin degree of freedom. From an experimental point of view our findings

demonstrate advantages over established spin control approaches. These usually employ unwieldy gate structures to apply external electric or magnetic fields, which are prone to fluctuations. In contrast, strain driving is intrinsic to the system and hence offers a drift-free coupling mechanism. From a physics point of view, AC strain driving allows working in the strong driving regime, in which the induced spin rotation frequency exceeds the initial spin splitting. Few systems have achieved this, despite the appeal of studying dynamics beyond the usually used rotating frame. Previously, only superconducting qubits at mK temperatures achieved sufficiently strong driving fields. Our room temperature experiments thus offer a more accessible route. Additionally, continuous strain driving enhances the NVs spin coherence time by decoupling it from environmental magnetic noise. Our noise-isolating scheme enables novel studies of weaker environmental noise sources, e.g. electric noise induced by charge fluctuations. Further studies of the remaining decoherence processes under mechanical driving, which remain largely unexplored until now, offer an exciting avenue to be pursued in the future. Besides this, the demonstrated coherence protection will be impactful for any quantum technology where pulsed decoupling protocols cannot be employed (such as DC electric field sensing).

Our approach to strong coherent strain-driving of a single electronic spin will have implications far beyond the coherence protection and dressed-state spectroscopy that we have demonstrated in this work. By combining our strain-drive with coherent microwave spin manipulation, our NV spin forms a three-level ∇ -system, on which all three possible spin transitions can be coherently addressed. This setting is known to lead to unconventional spin dynamics [117], which here could be observed on a single-spin basis and exploited for sensing and quantum manipulation. We will discuss ongoing spin dynamics under closed-contour driving in great detail in Chap. 6. On a more far-reaching perspective, our experiments lay the foundation for exploiting diamond-based hybrid spin-oscillator systems for quantum information processing and sensing, where our system forms an ideal platform for implementing proposed schemes for spin-induced phonon cooling and lasing [49] or oscillator-induced spin squeezing [118].

6. Phase-dependent spin dynamics under closed-contour interaction

The experiments we have presented so far essentially relied on two NV spin sublevels driven by a single coherent field. Such two-level quantum systems are the most common platform for experiments in the quantum regime as they offer a large diversity of observable physical phenomena and simultaneously minimize experimental challenges. In this chapter we expand our experiment and include all three spin sublevels of the NV's $S=1$ ground state. While this increases experimental complexity, it allows us to observe previously inaccessible spin dynamics of three-level systems under closed-contour interaction.

Three-level quantum systems have been at the forefront of experimental and theoretical investigations in quantum optics ever since the discovery of coherent population trapping and electromagnetically induced transparency in the 1970's [147–150]. Typically, such quantum systems are prepared in V- or Λ -type configurations by coupling two electronic states to a common third state through separate, coherent driving fields. This approach enables studying a wide variety of physical effects, such as light storage in atomic vapor [151], novel frequency standards for atomic clocks [152, 153] or stimulated Raman adiabatic passage for enhanced quantum control [154, 155]. The diversity of three-level quantum systems can in principle be further increased by driving all available transitions coherently by three individual driving fields (Fig. 6.1a). In such a scenario the global phase $\Phi = \phi_1 + \phi_3 - \phi_2$, i.e. the relative phase of the driving fields, offers a new and largely unexplored control parameter for coherent dynamics in quantum optics. It is predicted to significantly determine the system's dynamics [117], to control quantum interference phenomena [117], and lead to phase-dependent transmission and absorption [156–158].

Yet here we face an important limitation of many traditional approaches to quantum optics: selection rules make it difficult to couple all three levels solely by optical excitation. As combining optical and non-optical driving fields in a phase-locked manner to overcome this hurdle is experimentally challenging as well, previous researchers struggled to unambiguously demonstrate the influence of global phase. Although they have detected some effect in transmission and absorption measurements [159–162], the proposed phase dependence of occurring dynamics remains largely unexplored. The only exception to this is [163], where the circulation of microwave photons in three coupled superconducting qubits was measured. Yet, this study does not offer a complete characterization of the influence of global phase on occurring dynamics.

In this chapter we report on the implementation of a closed-contour interaction scheme in the ∇ -system formed by the $S=1$ ground state spin sublevels of the NV center. Using a unique combination of MW and strain driving, we perform a detailed study of the driving phase's influence on spin dynamics. Remarkably, the global

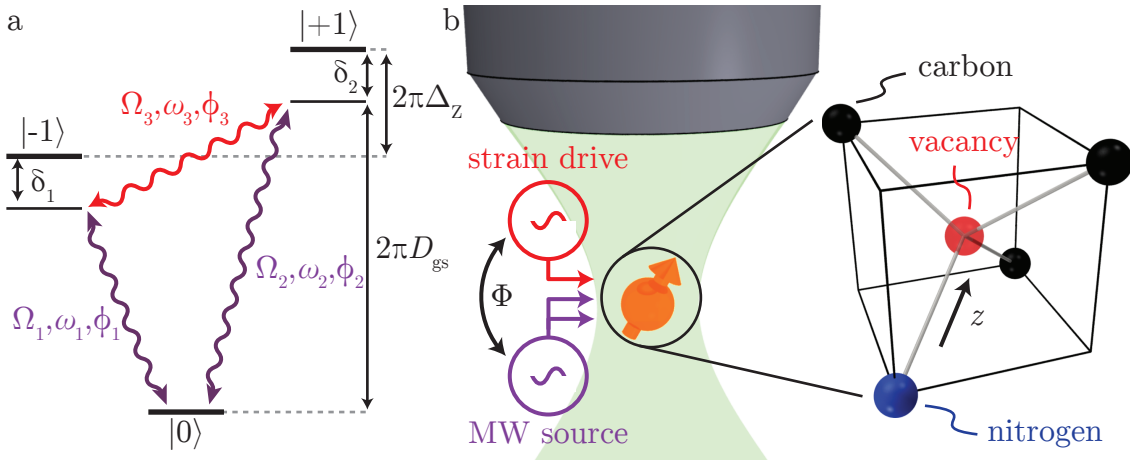


Figure 6.1.: Realization of a closed-contour interaction in the $S=1$ ground state of the NV center. a) Schematic representation of the investigated three-level system, driven by three fields. All three spin-transitions of the NV's ground state can be coherently driven by MW fields ($|\Delta m_s| = 1$ transitions, purple arrows) and by strain ($|\Delta m_s| = 2$, red arrow). The driving fields have frequency ω_i , amplitude (Rabi frequency) Ω_i and phase ϕ_i ($i \in \{1, 2, 3\}$). b) Spin dynamics under closed-contour interaction is investigated using a confocal microscope for optical initialization and readout of the NV spin. Driving fields are generated by MW sources and a function generator, which are mutually phase-locked to control the global interaction phase $\Phi = \phi_1 + \phi_3 - \phi_2$.

phase emerges as a handle to decouple the NV spin from environmental noise and thereby prolongs its coherence time under continuous driving. This discovery offers interesting perspectives for future applications in quantum sensing and quantum information processing.

6.1. Phase dependence of NV spin dynamics

To experimentally realize closed-contour interaction dynamics, we combine conventional, coherent MW driving of the $|0\rangle \leftrightarrow |\pm 1\rangle$ transitions and AC transverse strain driving of the $|-1\rangle \leftrightarrow |+1\rangle$ transition (Fig. 6.1). Since transverse strain only couples hyperfine sublevels with the same nuclear quantum number m_I (see Chap. 5), we restrict our experiments to hyperfine levels with $m_I = +1$. We generate the AC transverse strain field by exciting the mechanical resonator of our hybrid spin-oscillator system at its eigenfrequency (in this case $\omega_3/2\pi = 9.2075$ MHz) using a nearby piezoelectric actuator (see Chap. 5). The mechanical Rabi frequency Ω_3 is controlled by the amplitude of piezo excitation. To establish resonant driving of the $|-1\rangle \leftrightarrow |+1\rangle$ transition, we further apply a static magnetic field B_z along the NV axis such that $2\pi\Delta_Z = \omega_3$. Two transverse MW fields at frequencies $\omega_{1,2} = 2\pi D_{gs} \pm \omega_3/2$ address the $|0\rangle \leftrightarrow |\pm 1\rangle$ transitions and are delivered to the NV center using a homebuilt near-field microwave antenna.¹ The MW Rabi frequencies

¹In contrast to the experiments presented in previous chapters, here the MW antenna is formed by a 30 nm thick Au wire bonded across the cantilever.

$\Omega_{1,2}$ are set by the MW power delivered to the antenna. The three fields are created in a phase-locked manner, which is essential for our closed-contour interaction scheme to work (see App. A.9.2 for experimental details on field creation).

If the three-photon resonance $\omega_1 + \omega_3 = \omega_2$ is fulfilled, our closed-contour interaction scheme is described by the time-independent Hamiltonian (see App. A.9 for derivation)

$$\hat{\mathbf{H}}_{\text{cc}}/\hbar = \frac{1}{2} \begin{pmatrix} 2\delta_1 & \Omega_1 & \Omega_3 e^{i\Phi} \\ \Omega_1 & 0 & \Omega_2 \\ \Omega_3 e^{-i\Phi} & \Omega_2 & 2\delta_2 \end{pmatrix}, \quad (6.1)$$

written in the basis $\{|-1\rangle, |0\rangle, |1\rangle\}$, where $\delta_{1,2}$ are the MW-detunings from the $|0\rangle \leftrightarrow |\pm 1\rangle$ transitions. For $\omega_1 + \omega_3 = \omega_2$, the global phase $\Phi = \phi_1 + \phi_3 - \phi_2$ is well defined, where ϕ_i with $i = 1, 2, 3$ are the individual driving field phases. Experimentally, we focus on the case of resonant and symmetric driving, for which $\delta_1 = \delta_2 = 0$ and $\Omega_i = \Omega, \forall i$. Under such conditions, the eigenstates $|\Psi_k\rangle$ and eigenenergies E_k of $\hat{\mathbf{H}}_{\text{cc}}$ are

$$|\Psi_k\rangle = \frac{1}{\sqrt{3}} \left(e^{i\frac{\Phi+k4\pi}{3}}, 1, e^{-i\frac{\Phi-k2\pi}{3}} \right) \quad (6.2)$$

$$E_k/\hbar = \Omega \cos\left(\frac{\Phi - k2\pi}{3}\right) \quad (6.3)$$

with $k \in \{-1, 0, 1\}$ and Φ the global phase, imprinted on the system by the three coherent driving fields.

We study the closed-contour interaction dynamics by measuring the time evolution of the $|0\rangle$ spin population $P_{|0\rangle}(\tau)$ for different values of Φ with $\Omega/2\pi$ set to 500 kHz. To that end, we apply the pulse sequence shown in the inset to Fig. 6.2a to the NV. For each value of Φ , a green laser pulse initializes the NV spin in $|\Psi(\tau=0)\rangle = |0\rangle$, which can be expressed as a linear superposition of the three $|\Psi_k\rangle$

$$|\Psi(\tau=0)\rangle = (|\Psi_{-1}\rangle + |\Psi_0\rangle + |\Psi_1\rangle)/\sqrt{3}. \quad (6.4)$$

To monitor the time evolution

$$|\Psi(\tau)\rangle = e^{-i\hat{\mathbf{H}}_{\text{cc}}\tau/\hbar} |\Psi(0)\rangle, \quad (6.5)$$

we let the system evolve under the influence of the three driving fields and read out the population in $|0\rangle$,

$$P_{|0\rangle}(\tau) = |\langle 0|\Psi(\tau)\rangle|^2, \quad (6.6)$$

by applying a green readout laser pulse after a variable evolution time τ . The resulting data (Fig. 6.2a) show oscillations of $P_{|0\rangle}(\tau)$ in time, featuring a pronounced π -periodic dependence of the population dynamics on Φ .

We additionally monitor the populations $P_{|-1\rangle}(\tau)$ and $P_{|+1\rangle}(\tau)$ of spin sublevels $|\pm 1\rangle$ for $\Phi = 0, \pm\pi/2$ (Fig. 6.2b). To that end, we apply a MW π -pulse resonant with the $|0\rangle \leftrightarrow |1\rangle$ or $|0\rangle \leftrightarrow |-1\rangle$ transition at the end of the evolution time τ (dashed box in the inset of Fig. 6.2a) to swap the population between $|0\rangle$ and $|\pm 1\rangle$. The resulting spin dynamics are shown in Fig. 6.2b and demonstrate the time-reversal symmetry breaking character of the global phase at $|\Phi| = \pi/2$ [163]. In particular, at $\Phi = +\pi/2$ ($-\pi/2$) the spin exhibits clockwise (counterclockwise)

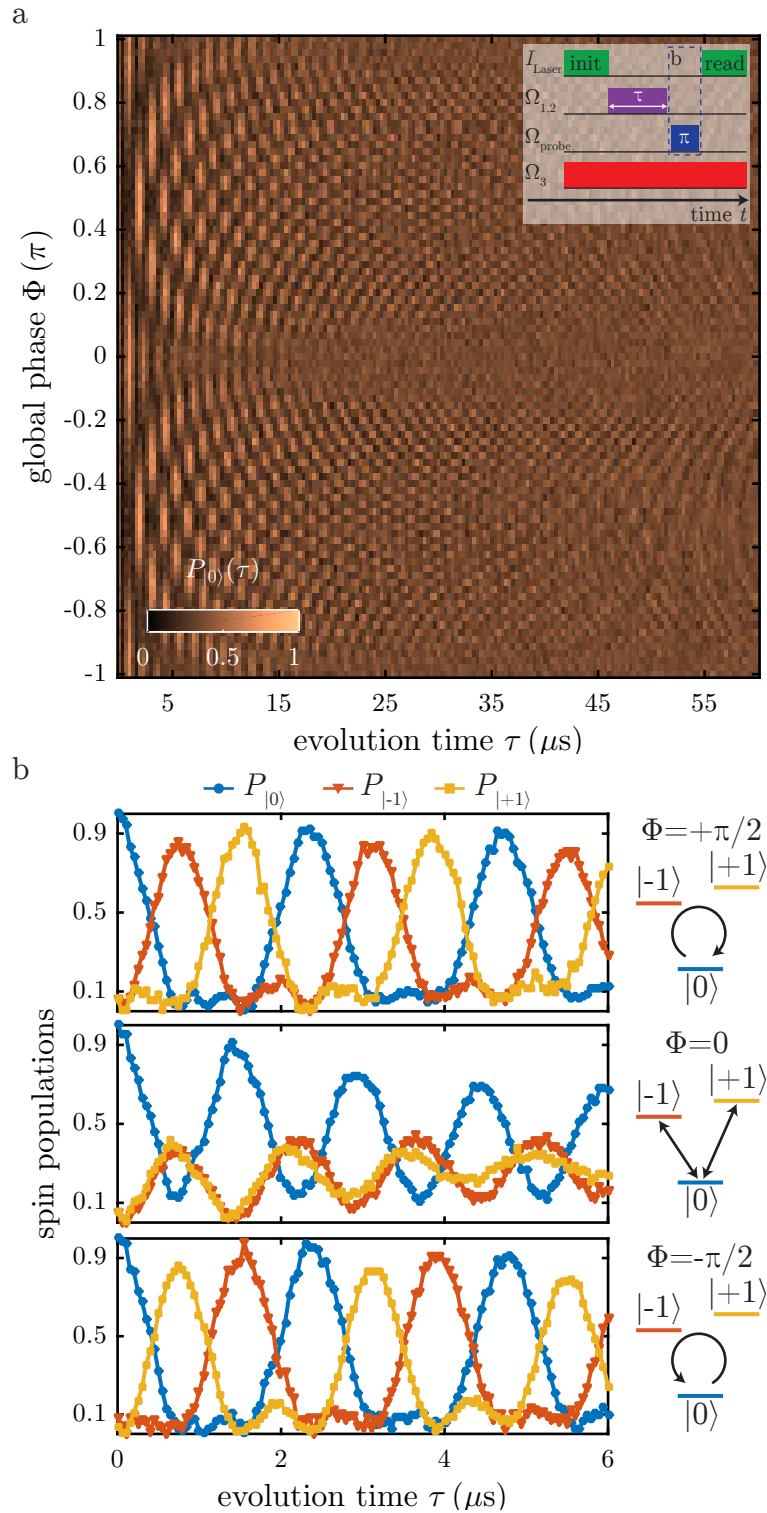


Figure 6.2.: Closed-contour spin dynamics controlled by global phase Φ . a) Time evolution of the population in $|0\rangle$, $P_{|0\rangle}(\tau)$, as a function of global phase Φ after initialization in $|0\rangle$. Closed-contour driving of the NV spin leads to periodic evolution of $P_{|0\rangle}(\tau)$ due to quantum-interference in the NV ground state. Period and decay times of the interference pattern strongly depend on Φ . b) Level populations $P_{|0\rangle}(\tau)$ (blue), $P_{|-1\rangle}(\tau)$ (red) and $P_{|+1\rangle}(\tau)$ (yellow) for $\Phi = \pi/2, 0$ and $-\pi/2$ (top, middle and bottom panel). For $\Phi = +\pi/2$ ($\Phi = -\pi/2$) population is shuffled clockwise (counterclockwise) through the three-level ∇ -system, while for $\Phi = 0$ it alternates between $|0\rangle$ and an equal superposition of $|\pm 1\rangle$.

circulation of population between the three spin sublevels $|0\rangle$, $|+1\rangle$ and $|-1\rangle$, with a period $T_{\pm\pi/2} = 4\pi/\sqrt{3}\Omega$ (see App. A.9.1 for derivation). Indeed, Roushan *et al.* connect the circulation of population at $\Phi = \pm\pi/2$ to chiral currents interacting with a synthetic magnetic field whose flux is given by Φ , demonstrating tunable gauge fields and strong particle interactions [163]. Conversely, for $\Phi = 0, \pm\pi$ the spin level population oscillates between $|0\rangle$ and an equal superposition of $|\pm 1\rangle$ in a "V"-shaped trajectory (Fig. 6.2b, middle) at a period $T_{0,\pm\pi} = 4\pi/3\Omega$. The time evolution of the spin populations revealed in Fig. 6.2b thus offers intuition for the strong influence Φ has on the effective Rabi frequencies we observe in Fig. 6.2a. Our experimental findings are in excellent agreement with theoretical expectations (see App. A.9.3 for further discussion).

6.2. Global driving phase for NV decoupling

In addition to observing spin dynamics under closed-contour interaction, our experiment also allows us to directly probe the eigenenergies E_k (solid lines in Fig. 6.3a, see (6.3)) of the driven three-level system. After spin-initialization in the superposition state $|\Psi(\tau = 0)\rangle$ (see (6.4)), each individual component $|\Psi_k\rangle$ acquires a dynamical phase $E_k\tau/\hbar$ that governs the time evolution of the NV spin (see App. A.9.1 for a detailed explanation). $P_{|0\rangle}(\tau)$ thus oscillates at frequencies $\Delta_{i,j} = (E_i - E_j)/h$ with $i \neq j \in \{-1, 0, 1\}$, as indicated by the colored arrows and lines in Fig. 6.3a+b. A Fourier transformation of $P_{|0\rangle}(\tau)$ from Fig. 6.2a will thus reveal $\Delta_{i,j}$ and thereby the eigenenergies of the driven NV spin for any given Φ . The resulting frequency spectrum is plotted in Fig. 6.3c and shows an overall good agreement between data and the expected spin precession frequencies for the undisturbed system ($\delta_{1,2} = 0$), represented by colored lines and obtained via (6.3)). However, discrepancies between expected and measured frequencies exist around $\Phi = 0, \pm\pi$, where we find anti-crossings instead of degenerate spin precession frequencies in our measured spectra.

The appearance of these anti-crossings indicates the presence of environmental fluctuations, disturbing our closed-contour interaction scheme. In particular, our system is subject to amplitude noise in the driving fields, causing Rabi frequencies Ω_i to vary throughout our experiment. Additionally, environmental magnetic fluctuations and changes in the zero-field splitting D_{gs} lead to variations in the detunings $\delta_{1,2}$ in (6.1) (see App. A.9.3 for a detailed study of the most important noise sources). For symmetric and resonant driving, degeneracies occur between $|\Psi_{-1}\rangle$ and $|\Psi_0\rangle$ at $\Phi = -\pi$, $|\Psi_{-1}\rangle$ and $|\Psi_{+1}\rangle$ at $\Phi = 0$, and between $|\Psi_0\rangle$ and $|\Psi_{+1}\rangle$ at $\Phi = +\pi$ (black lines in Fig. 6.3a). Environmental fluctuations, however, lead to asymmetric and/or non-resonant driving with $\Omega_1 \neq \Omega_2 \neq \Omega_3$ and/or $\delta_1 \neq \delta_2 \neq 0$, ultimately lifting these degeneracies (as indicated by green, dotted lines in Fig. 6.3a, which we obtained through solving \hat{H}_{cc} with $\delta_1/2\pi = -\delta_2/2\pi = 50$ kHz). While this simple approach nicely illustrates the effect of environmental noise on the spin dynamics of our driven three-level system, it is not a proper description of our experiment, as the interplay between the different noise sources is far more complex. In App. A.9.3, we discuss in great detail how we carefully model the influence of environmental noise. The resulting spin precession frequency spectrum is shown in Fig. 6.3d and reveals an excellent match with our experimental data.

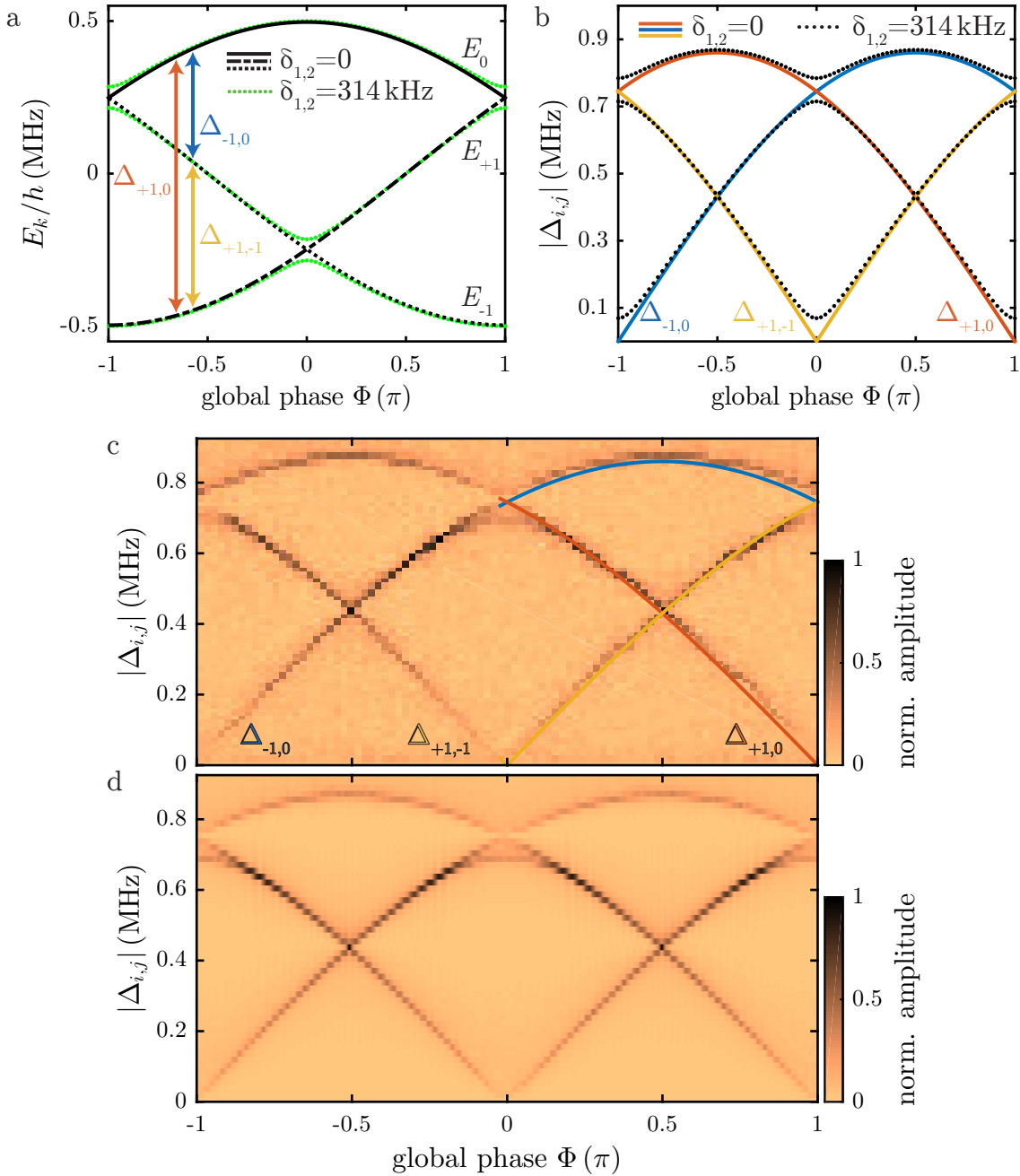


Figure 6.3.: Eigenenergies and precession frequencies of the driven NV spin under closed-contour interaction. a) Calculated eigenenergies $E_{0,\pm 1}/h$ as a function of Φ for zero (black solid and dashed lines) and non-zero (green dotted lines) detunings $\delta_{1,2}$. Environmental fluctuations disturb the closed-contour interaction system whenever two eigenstates are nearly degenerate and anti-crossings appear. Colored arrows indicate the expected spin precession frequencies $\Delta_{i,j}$. b) Spin precession frequencies $|\Delta_{i,j}|$ as a function of Φ for zero (colored solid lines) and non-zero (black dotted lines) detunings. The formation of anti-crossings for $\Phi \approx 0, \pm\pi$ indicates an increased vulnerability to environmental noise. c) Fourier transforming the data shown in Fig. 6.2a reveals the precession frequencies of the driven NV spin. Colored lines represent spin precession frequencies of the undisturbed system. d) Simulated spectrum taking environmental fluctuations into account, showing excellent agreement with experimental data in panel c (see App. A.9.3 for further information regarding the employed model).

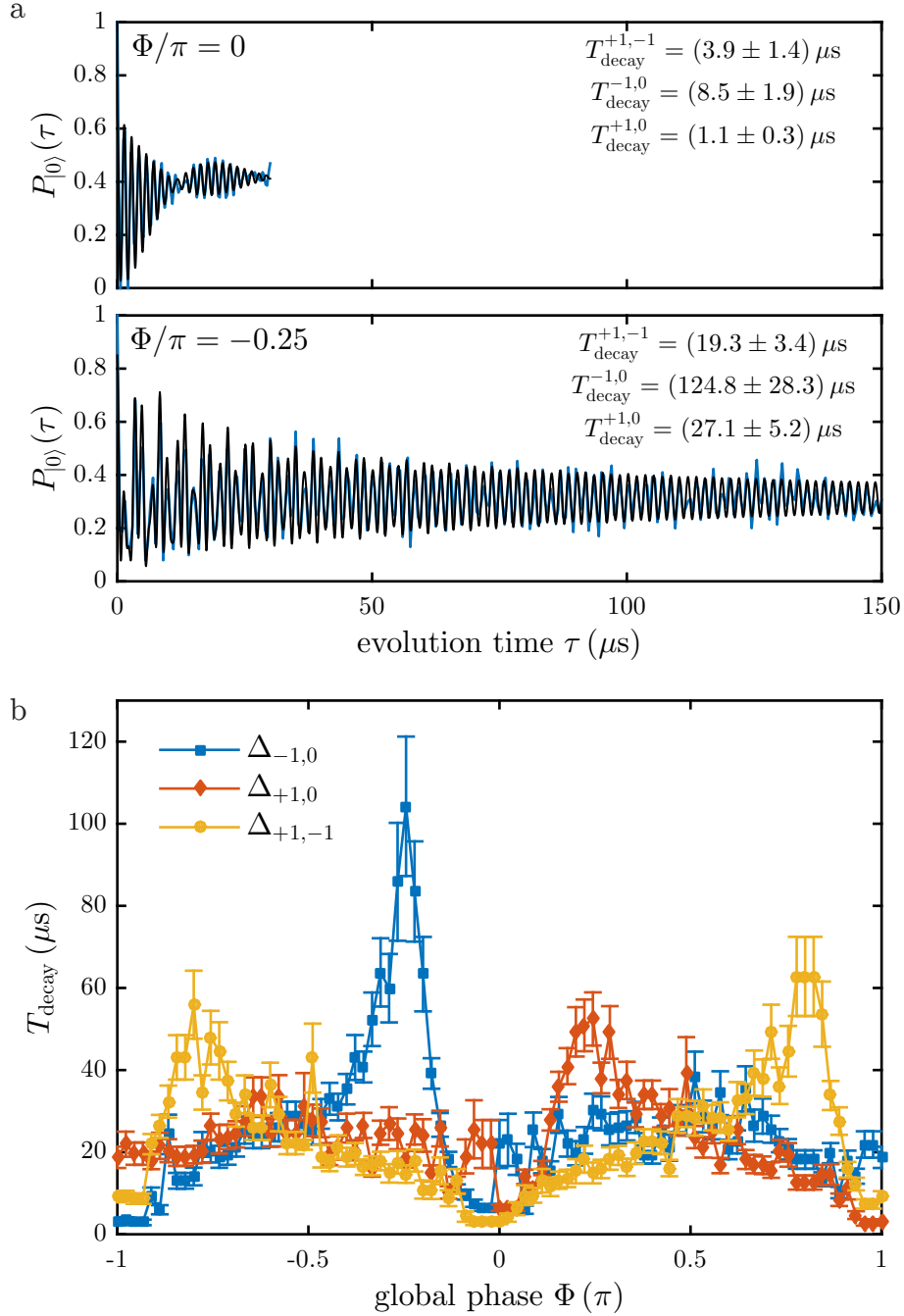


Figure 6.4.: Dependence of Rabi decay time T_{decay} on global phase Φ . a) Time evolution $P_{|0\rangle}(\tau)$ taken for $\Phi = 0$ (top) and $\Phi = 0.25\pi$ (bottom). The data (blue) is fitted by a sum of three exponential decays, yielding decay times that vary between a few μs ($\Phi = 0$) and $> 120 \mu\text{s}$ ($\Phi = -0.25\pi$). Note that the given decay time values differ slightly from those presented in panel b, as the linecuts were taken separately and thus under a different noise environment. b) Phase dependence of T_{decay} obtained by fitting data from Fig. 6.2a. The observed asymmetry with respect to $\Phi = 0$ stems from slow environmental drifts, for instance of the zero-field splitting. Error bars denote 95 % confidence intervals of the fits.

The existence of anti-crossings in the spin precession frequency spectrum indicates that the system's eigenstates are most vulnerable to environmental fluctuations for $\Phi \approx 0, \pm\pi$ and protected elsewhere. We therefore expect the decay time T_{decay} of the observed oscillation fringes to vary with Φ , showing minima at $\Phi \approx 0, \pm\pi$. The interference pattern in Fig. 6.2a qualitatively confirms these expectations. Oscillation fringes vanish quickly for $\Phi \approx 0, \pm\pi$ but last significantly longer in between. We can further deduce two important aspects from the spin's precession frequency spectrum (Fig. 6.3c). First, for a given Φ the three frequency components are characterized by different peak amplitudes, indicating that the decay times $T_{\text{decay}}^{+1,-1} \neq T_{\text{decay}}^{+1,0} \neq T_{\text{decay}}^{-1,0}$ are in general not equal.² Second, we can expect $T_{\text{decay}}^{+1,-1}$ to peak around $\Phi \approx \pm 0.75\pi$ and $T_{\text{decay}}^{\pm 1,0}$ at $\Phi \approx \pm 0.25\pi$, as for these Φ the spectral amplitude of the corresponding $\Delta_{i,j}$ is maximized.

For a quantitative analysis of Rabi decay times and their expected dependence on Φ , we fit the data of Fig. 6.2a with the function

$$S_{\text{Rabi}}(\tau) = \sum_{i,j} \beta_{i,j} \cos(2\pi\Delta_{i,j}\tau + \phi_{i,j}) e^{(-\tau/T_{\text{decay}}^{i,j})} \quad (6.7)$$

where $\beta_{i,j}$, $\Delta_{i,j}$ and $\phi_{i,j}$ denote amplitude, frequency and phase of the three spin precession frequency components $(i,j) = \{(-1,0), (+1,0), (+1,-1)\}$. We find a significant phase dependence of Rabi decay time (Fig. 6.4), which confirms our previous expectations. Rabi decay times are minimized for $\Phi = 0, \pm\pi$, where the oscillation fringes damp out within a few μs . In contrast, around $\Phi = \pm 0.25\pi$ and $\pm 0.75\pi$, we observe much longer decay times that vary between 50 – 120 μs . Our findings can be qualitatively explained by the specific reactions of $|\Psi_k\rangle$ and their corresponding energies E_k to environmental noise (see Fig. 6.3a):

- E_0 is not affected by noise for $\Phi = 0$, but strongly responds at $\Phi = \pm\pi$.
- E_{+1} is most susceptible to fluctuations for $\Phi = 0, +\pi$, while no reaction occurs at $\Phi = -\pi$ and $+\pi/2$.
- E_{-1} , however, strongly reacts to noise for $\Phi = -\pi, 0$, and is robust at $\Phi = -\pi/2$ and π .

As maximum robustness of E_i and E_j with $i \neq j$ never occurs at the same value of global phase, spin precession frequency components $\Delta_{i,j} = (E_i - E_j)/h$ are most efficiently protected at intermediate Φ ($\Delta_{+1,-1}$ at $\pm 0.75\pi$, $\Delta_{+1,0}$ at $+0.25\pi$ and $\Delta_{-1,0}$ at -0.25π). The relative driving phase Φ thus not only controls the spin dynamics in our closed-contour interaction scheme. It also serves as a handle to decouple the system from environmental fluctuations, effectively protecting the NV spin.

In addition to the remarkable coherence protection, we also observe an unexpected, yet strong asymmetry of decay times with respect to $\Phi = 0$ (Fig. 6.4b). Based on our previous discussion of spin dynamics (Fig. 6.2), the underlying eigenenergy spectra, and their response to fluctuations (Fig. 6.3), we would expect a symmetric behavior, i.e. decay times at $\Phi = \pm 0.25\pi, \pm 0.75\pi$ to be of the same magnitude. Our simulations indicate that slow fluctuations (for instance variations of the

²Long-living frequency components are not only indicated by narrower peaks in the Fourier transformation, but also by larger amplitudes. In our way of plotting, the linewidth is difficult to estimate and we therefore refer to the peak intensity as a measure for decay time.

zero-field splitting caused by small changes in environmental temperature), which happen on timescales comparable to our data acquisition time, to be the origin of this observed asymmetry (see discussion in App. A.9.3). Such influences are currently not avoidable, but could be suppressed by performing our experiments in a more stable environment, e.g. in vacuum and/or under cryogenic conditions.

6.3. Summary

In summary, we have realized a closed-contour interaction scheme in the NV's ground state by combining coherent MW and strain driving. We present a detailed study of the resulting spin dynamics and confirm the theoretical prediction that the global phase governs the occurring spin dynamics, i.e. it allows for controlling how population is shuffled between the three NV ground state spin sublevels. Furthermore we find that the relative driving phase shields the NV spin from environmental noise without having to apply complicated decoupling schemes. The decoupling mechanism and its phase dependence are well explained by the eigenenergies of the underlying Hamiltonian and their response to environmental noise. Carefully performed simulations yield a remarkable degree of consistency with our experimental findings and identify slow variations in the zero-field splitting D_{gs} to cause the observed asymmetry in the phase dependence of Rabi decay times.

To increase the coherence protection even further, we propose to repeat the presented measurements in a better controlled environment, for example by placing our hybrid system in a cryostat. This would eliminate slow drifts in D_{gs} and lead to cleaner decay time spectra. Additionally, our experiments were performed with relatively modest driving strengths of $\Omega/2\pi = 500$ kHz. As presented in Chap. 4 and Chap. 5, MW and strain driving strengths of several MHz are possible and increasing Ω would further suppress the influence of all noise sources. Our simulations indicate that Rabi decay times of up to 1.2 ms are possible for $\Omega/2\pi \approx 800$ kHz, if the relative driving field amplitude fluctuations can be reduced to approximately 10 % of their current levels.

Besides the existing technical issues, we believe that our closed-contour interaction scheme can have an impact on future applications in sensing and quantum information processing. The emerging eigenstates $|\Psi_k\rangle$ have a unique structure in the sense that they are superpositions of all three NV spin sublevels. Possible fluctuations thus affect them all in a similar fashion, and qubits spanned by $|\Psi_k\rangle$ are intrinsically protected. Moreover, the demonstrated phase-dependent decoupling by continuous driving suggests significantly enhanced coherence times of $|\Psi_k\rangle$ compared to the undriven NV center. As the states $|\Psi_{\pm 1}\rangle$ at $\Phi = \pm\pi/2$ are moreover completely decoupled from magnetic fluctuations, but have energies which depend linearly on phase, one could imagine to realize a built-in sensor to study phase noise in our hybrid system. Another interesting perspective is the combination of closed-contour dynamics with optical transitions for phase-controlled coherent population trapping [156]. This could either be done using an optical Λ -scheme, where the ground state levels are coupled by strain, or through an optical V-scheme, where the interaction contour is closed by driving optical excited state transitions [49]. Such schemes might prove useful for sensing applications in quantum optics.

6.4. Outlook

To estimate the impact of our coherence-protected closed-contour interaction eigenstates $|\Psi_k\rangle$ on sensing applications, we recently performed first experiments regarding the characterization of their coherence times T_2^* . In fact, the Rabi decay time measurements from Fig. 6.4 already constitute a simultaneous measurement of closed-contour interaction coherence times for all three qubits, spanned by $|\Psi_i\rangle$ and $|\Psi_j\rangle$ with $i \neq j$. By performing Ramsey measurements on a single of these qubits, we should therefore be able to reproduce the observed phase dependence from Fig. 6.4 in a way that is easier to understand. These studies, however, require the initialization of our driven three-level system in a single state $|\Psi_k\rangle$ instead of a superposition state $\sum_k |\Psi_k\rangle$, which we realize via phase-dependent, adiabatic state preparation (Fig. 6.5a+b).

To achieve such preparation, we start with the NV S=1 ground state and apply our AC strain field resonant with the $|-1\rangle \leftrightarrow |+1\rangle$ transition. The eigenstates under such conditions are $|0\rangle$ and $|\pm\rangle = (|-1\rangle \pm |+1\rangle)/\sqrt{2}$, and applying a green initialization pulse allows for preparing the NV in state $|0\rangle$. We then adiabatically increase the MW driving amplitudes until $\Omega_{1,2} = \Omega_3$ (see App. A.9.2 for the creation of such amplitude ramps). For $\Phi > 0$ ($\Phi < 0$), state $|0\rangle$ evolves into $|\Psi_{+1}\rangle$ ($|\Psi_{-1}\rangle$) and, as only $|0\rangle$ was initially populated, our closed-contour system is adiabatically prepared in a pure eigenstate of the driven system if $\Omega_{1,2}$ was increased slowly enough. By applying our standard readout pulse we finally probe $P_{|0\rangle}(\tau)$, which will approach 1/3 without showing any oscillation fringes if the adiabatic state preparation was successful (see App. A.9.1 for a detailed explanation).

The achievable state preparation fidelity, i.e. how well we manage to initialize in only one of the three states $|\Psi_k\rangle$, is closely linked to amplitude sweep rate ν_Ω via the Landau-Zener transition probability

$$P_{LZ} = e^{-2\pi \frac{\Delta^2}{4\nu_\Omega}}, \quad (6.8)$$

where Δ denotes the energy splitting between involved eigenstates [164]. For an abrupt onset of the driving fields $\nu_\Omega = \infty$ and $P_{LZ} = 1$ follows, indicating that all involved levels are populated. Preparing the system in a single eigenstate $|\Psi_k\rangle$ cannot be realized under such conditions. In contrast, if the driving fields are increased adiabatically, i.e. with $\nu_\Omega = 0$, $P_{LZ} = 0$ and adiabatic state preparation is achieved. Consequently, the sweeping rate ν_Ω needs to be small compared to the smallest energy gap Δ between involved states. For instance, at a global phase $\Phi = \pm\pi/2$ the smallest energy difference occurs at $\Omega_{1,2} = 0$ with $\Delta = |E_0 - E_{\pm 1}| = \Omega_3/2$ (see Fig. 6.5a). Here, the maximum sweep rate is limited by the amplitude of the applied strain drive.

In Fig. 6.5c+d, we compare amplitude sweeps of different shapes (error-function-like and parabolic increase) for different ramping times t_{ramp} , which denotes the timescale on which we ramp from $\Omega_{1,2} = 0$ to $\Omega_{1,2} = \Omega_3$. As expected, we find that increasing t_{ramp} improves our state preparation fidelity as indicated by weaker oscillation fringes in the time evolution of $P_{|0\rangle}(\tau)$. Ramping $\Omega_{1,2}$ in a parabolic fashion proved to be more effective as the system is almost fully prepared in $|\Psi_{+1}\rangle$ for $t_{\text{ramp}} = 5 \mu\text{s}$ whereas the error functional sweep requires a factor of four longer ramping times. This can be explained by comparing the size of Δ and the applied

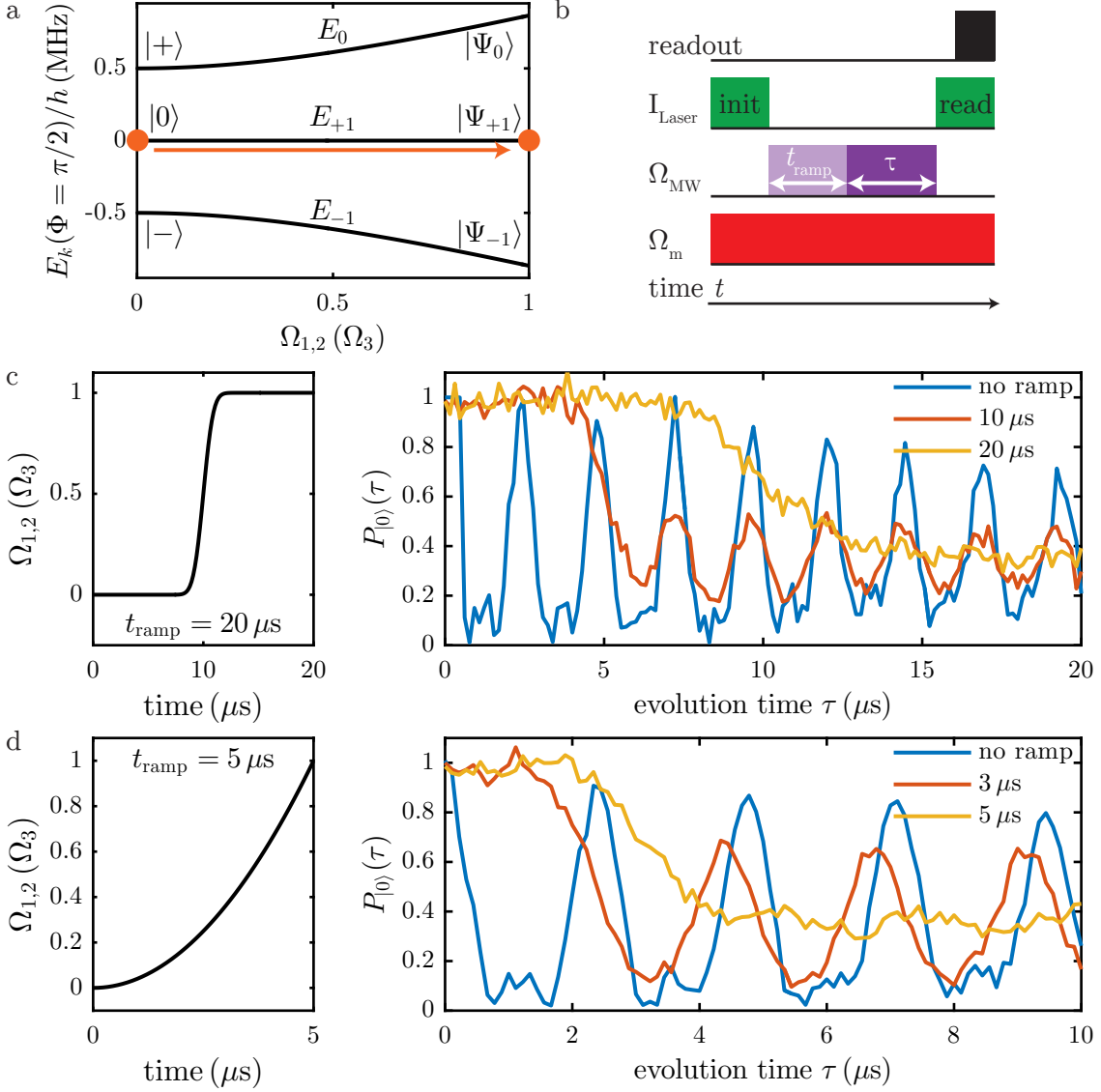


Figure 6.5.: Adiabatic state preparation in the NV's S=1 ground state. a+b) We initialize the spin in state $|0\rangle$ and slowly ramp the MW amplitudes $\Omega_{1,2}$. State $|0\rangle$ is thus converted into a single eigenstate $|\Psi_k\rangle$ (for $\Phi = \pm\pi/2$, $|0\rangle \rightarrow |\Psi_{\pm 1}\rangle$). Note that continuously applying the AC strain field is a prerequisite for this scheme to work, since this lifts the level degeneracy at $\Omega_{1,2} = 0$ and induces a non-zero energy gap Δ . c+d) Comparing state preparation fidelity at $\Phi = +\pi/2$ for different amplitude ramp functions. Ramping MW driving amplitudes in a parabolic fashion almost fully prepares the system in $|\Psi_{+1}\rangle$ for $t_{\text{ramp}} = 5 \mu\text{s}$, whereas the error-function-like approach is less effective and t_{ramp} increases significantly. The amplitude of the observed oscillation fringes in $P_{|0\rangle}(\tau)$ serves as a measure for the preparation fidelity.

ramping rate ν_Ω . Δ increases with $\Omega_{1,2}$ at $\Phi = +\pi/2$ (Fig. 6.5a), and ν_Ω can be increased during the MW amplitude ramp as well. As ν_Ω is proportional to the slope of the applied ramp function, it is continuously increased in case of the parabolic ramp. The same is not true for the error-function approach and adiabatic state preparation becomes less efficient.

After demonstrating state preparation, we continued with first experiments regarding manipulation and subsequent characterization of the driven eigenstates $|\Psi_k\rangle$ (Fig. 6.6). To that end we change the applied pulse sequence slightly. First, we apply a third MW probe field of frequency ω_{probe} and amplitude Ω_{probe} to manipulate the driven system after preparation in a single eigenstate, for example $|\Psi_{+1}\rangle$. Second, to investigate the influence of our probe field at evolution time τ , we adiabatically transfer our system from the driven basis $\{|\Psi_{-1}\rangle, |\Psi_0\rangle, |\Psi_{+1}\rangle\}$ back to the NV basis $\{|-1\rangle, |0\rangle, |+1\rangle\}$ by ramping $\Omega_{1,2}$ to zero. This intermediate step is necessary to monitor $P_{|\Psi_{+1}\rangle}(\tau)$ (using the standard NV readout procedure is not sufficient for this task as all three eigenstates $|\Psi_k\rangle$ are characterized by 1/3 population in $|0\rangle$).

Fig. 6.6b demonstrates manipulation of the closed-contour eigenstates $|\Psi_k\rangle$ at $\Phi = +\pi/2$ through pulsed ESR measurements. We applied the sequence from Fig. 6.6a, featuring a parabolic amplitude ramp with $t_{\text{ramp}} = 12 \mu\text{s}$ as well as a fixed evolution time $\tau_\pi = 5 \mu\text{s}$, and varied ω_{probe} . Whenever ω_{probe} is resonant with one of the allowed $|\Psi_{+1}\rangle \leftrightarrow |\Psi_{-1}\rangle$ and $|\Psi_{+1}\rangle \leftrightarrow |\Psi_0\rangle$ transitions, we observe a decrease in recorded NV emission. Setting ω_{probe} resonant to one of these transitions and applying the appropriate pulse sequence (Fig. 6.6c) then allows performing Rabi oscillation measurements, as demonstrated in Fig. 6.6d for the qubit spanned by the states $|\Psi_{+1}\rangle$ and $|\Psi_0\rangle$. Finally, we perform Ramsey experiments to determine the coherence time of the closed-contour interaction eigenstates $|\Psi_{+1}\rangle$ and $|\Psi_{-1}\rangle$ where $\tau_{\pi/2} = 1500 \text{ ns}$ and $\Phi/\pi = 0.55$. (Fig. 6.6e+d). First measurements indicate coherence times of several tens of μs , i.e. coherence times that are significantly longer than the bare NV spin coherence of $T_2^* \approx 2 \mu\text{s}$.

The experiments presented above are still in an early state, yet they already demonstrate the potential of our closed-interaction contour scheme. We are curious to see how coherence times changes with global phase Φ . In particular, we are interested in the question whether coherence time measurements on individual closed-contour interaction qubits do reproduce the previously observed phase dependence of Rabi decay times (Fig. 6.4b). The preliminary results from Fig. 6.6 are promising, as they are in agreement with the previously determined $T_{\text{decay}}^{+1,-1} \approx 40 \mu\text{s}$ measured for $\Phi/\pi = 0.55$. Due to the possibility to prepare our system in two different sets of basis states in a very controlled way, we can also test advanced state preparation protocols with respect to their vulnerability to environmental fluctuations, whose origins and amplitudes can be tuned via the global phase Φ . We plan to demonstrate this proposal using the fast adiabatic state preparation protocol presented in [165, 166].

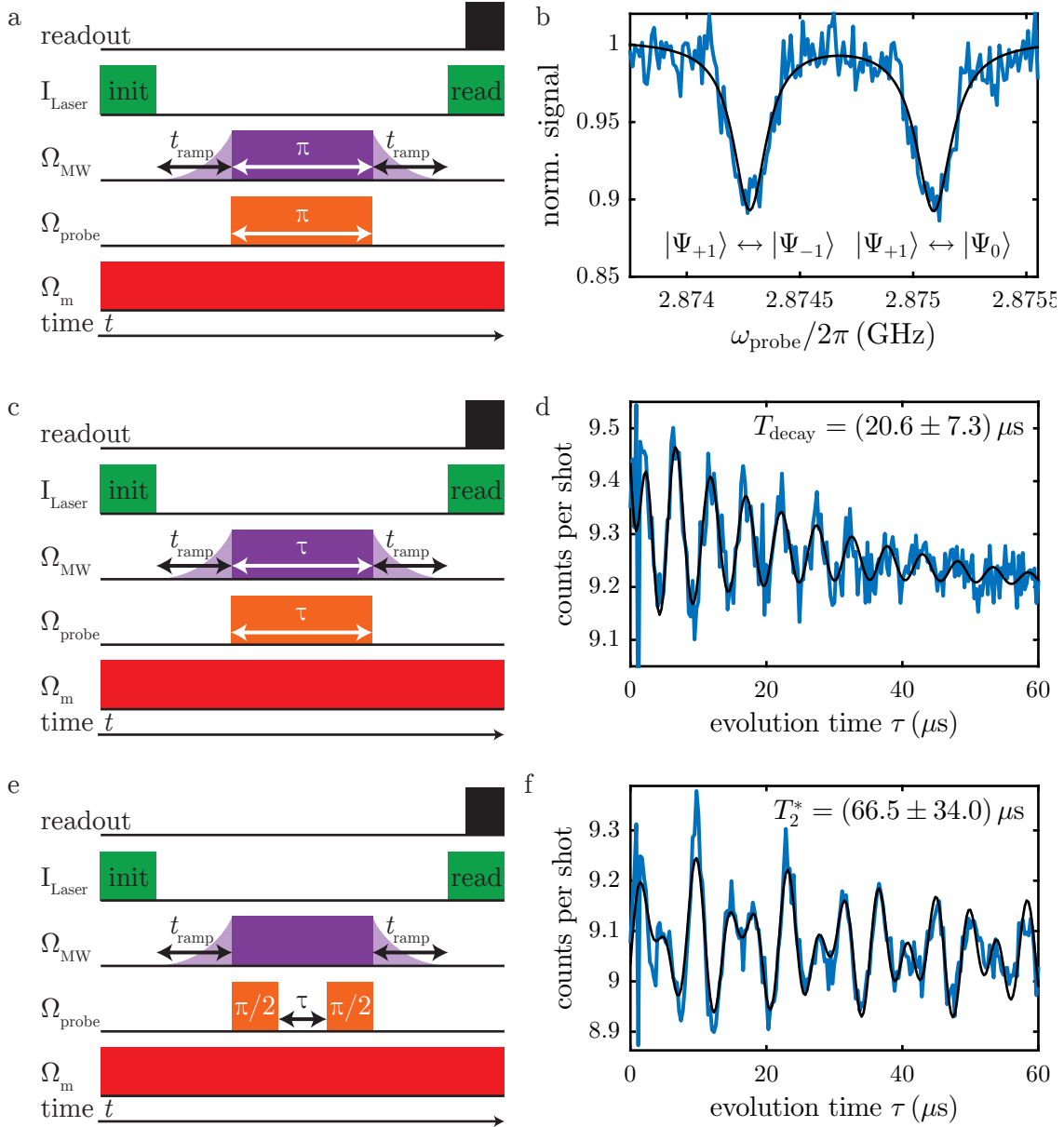


Figure 6.6.: Manipulation and coherence of the NV spin driven in a closed interaction contour. a) Sequence for pulsed ESR spectroscopy of the eigenstates $|\Psi_k\rangle$ at $\Phi/\pi = 0.5$. To manipulate and characterize these, we apply an additional, weak MW probe field once the system is prepared in an eigenstate $|\Psi_{+1}\rangle$. To readout the spin manipulation of this field via the $|0\rangle$ spin sublevel, we further adiabatically convert the system back into the NV basis $\{|-1\rangle, |0\rangle, |+1\rangle\}$ by ramping $\Omega_{1,2}$ to zero. b) Pulsed ESR spectroscopy of the eigenstates $|\Psi_k\rangle$, obtained by applying the presented sequence with $t_{\text{ramp}} = 12 \mu\text{s}$ and $\tau_\pi = 5 \mu\text{s}$ at $\Phi = +\pi/2$. Whenever ω_{probe} is resonant with one of the allowed $|\Psi_{+1}\rangle \leftrightarrow |\Psi_{-1}\rangle$ and $|\Psi_{+1}\rangle \leftrightarrow |\Psi_0\rangle$ transitions, we observe a decrease in recorded NV emission. c+d) Rabi oscillations measured on the $|\Psi_{+1}\rangle \leftrightarrow |\Psi_0\rangle$ transition for $\Phi/\pi = 0.5$, featuring an effective Rabi frequency of 192 kHz. e+f) Ramsey spectroscopy indicates coherence times of the $|\Psi_{+1}\rangle \leftrightarrow |\Psi_{-1}\rangle$ in the order of several tens of μs , measured with $\tau_{\pi/2} = 1500 \text{ ns}$ and at $\Phi/\pi = 0.55$. The origin of the observed beating is currently not clear.

7. Summary and Outlook

Hybrid spin-oscillator systems, formed by single spins coupled to mechanical oscillators, have attracted ever-increasing attention over the last years. As outlined in Chap. 1 this development was largely triggered by the prospect of employing such devices as high-performance nanoscale sensors or transducers in multi-qubit networks. Provided the spin-oscillator coupling is strong and robust, such systems can even serve as test-beds for studying macroscopic objects in the quantum regime. In this thesis we intensively studied our hybrid spin-oscillator system, that consists of a diamond cantilever, whose mechanical motion is coupled to the spin degree of freedom of embedded NV centers through crystal strain. The unique combination of NV centers, diamond resonators, and spin-strain coupling enabled several interesting room temperature experiments in the NV $S=1$ ground. Our results constitute an important step towards strain-driven quantum devices, and reveal new perspectives for future sensing applications.

7.1. Summary

We started the investigation of our hybrid spin-oscillator device by quantifying the coupling strength between NV spin and resonator motion. Static cantilever bending revealed spin-strain coupling constants of several GHz per unit of strain, corresponding to a single phonon coupling strength $g_0 \approx \text{Hz}$. By applying time-varying strain fields, we demonstrated that our hybrid system resides deep in the resolved sideband regime, which is a prerequisite for several schemes proposed to prepare and study the mechanical oscillator in its quantum ground state. Implementing corresponding cooling schemes, however, also requires the spin-strain coupling strength to exceed spin decoherence rate Γ_{NV} and cantilever heating rate γ_{th} – a regime characterized by a cooperativity $C = 2\pi g_0^2 / \Gamma_{\text{NV}} \gamma_{\text{th}} > 1$. Reaching such a regime is, however, impossible under our current experimental conditions. Yet several possibilities to boost the cooperativity, such as miniaturizing our cantilevers or going to cryogenic temperatures, exist. While these enable reaching cooperativities above unity, they simultaneously come at significant experimental challenges. We therefore believe that working with the NV's excited state is favorable, if our hybrid system is to be studied in the cantilever's motional ground state (see discussion below).

While the NV's spin and its coupling to strain is not the first choice for such experiments in the quantum regime, it offers many other exciting features we explored. In Chap. 4 we report on the implementation of a novel continuous decoupling scheme that protects the NV spin from environmental noise. In this scheme, we combined microwave and AC strain fields to lock the spin precession frequency to the cantilever's mode frequency in the MHz range. Under this condition, both Rabi oscillation decay time and inhomogeneous coherence time increased by two orders of magnitude. The remarkable coherence protection of our hybrid spin-oscillator

system relies on concatenated continuous dynamical decoupling and results from the robust, drift-free strain-coupling mechanism and the narrow linewidth of the high-quality diamond mechanical oscillator we employed. Improving the resonators' quality factors, for example by operating the system in vacuum, will further prolong coherence times, potentially to the relaxation time limit.

At the heart of this thesis stand our efforts to use transverse AC strain for coherent spin manipulation, which we demonstrate in Chap. 5. From an experimental point of view our findings manifest advantages over established spin control approaches. These usually employ unwieldy gate structures to apply external electric or magnetic fields, which are additionally prone to fluctuations. In contrast, strain driving is intrinsic to the system and hence offers a drift-free driving mechanism. From a physics point of view, AC strain driving not only addresses a magnetic dipole forbidden transition. It also allows working in the strong driving regime, in which the induced spin rotation frequency exceeds the initial spin splitting. Few systems have reached this regime, despite the appeal of studying dynamics beyond the usually used rotating frame. Previously, only superconducting qubits at mK temperatures achieved sufficiently strong driving fields and our room temperature experiments offer a more accessible route. Additionally, continuous strain driving enhances the NVs spin coherence time by decoupling it from environmental magnetic noise. Our noise-isolating scheme will thus enable novel studies of weaker environmental noise sources. Further studies of the remaining decoherence processes under mechanical driving, which remain largely unexplored until now, offer another exciting avenue to be pursued. Besides this, the demonstrated decoherence protection will have impact on any quantum technology where pulsed decoupling protocols cannot be employed.

Our approach to strong coherent strain-driving of the NV spin has implications far beyond the coherence protection that we demonstrated in Chap. 5. Under combined MW and strain driving, the NV's spin forms a three-level ∇ -system, on which all three possible spin transitions can be coherently addressed. This setting is known to lead to unconventional spin dynamics [117] which had been barely studied so far due to experimental limitations. In Chap. 6 we present a detailed study of the spin dynamics of such a closed-contour interaction scheme and confirm the theoretical prediction that the global phase, i.e. the relative phase of the three driving fields, governs the occurring spin dynamics. Furthermore, we discovered that it shields the NV's spin from environmental noise without applying complicated decoupling schemes. The corresponding decoupling mechanism is well explained by the symmetries of the underlying Hamiltonian and their response to noise. Based on our findings, we believe our closed-contour interaction scheme to have impact on future applications in sensing and quantum information processing, for example as phase sensor or as test-bed for state transfer protocols. First experiments, where we studied the decoherence of the NV's spin eigenstates under closed-contour interaction, indicate coherence times up to one order of magnitude longer compared to the undriven NV – a highly interesting avenue we will pursue in the future.

7.2. Outlook

Besides studying spin coherence under closed-contour driving, cooling the resonator of our hybrid system to its motional ground state will be one of our main goals in the future. As discussed in Chap. 3, such an undertaking is challenging to realize when working with the NV center's ground state due to the relatively weak spin-strain coupling. Employing orbital-strain coupling in the NV center's $S=1$ excited state manifold, however, might help to overcome this hurdle. Recently, orbital-strain coupling constants of several PHz/strain have been reported [105], making orbital-strain coupling five orders of magnitude stronger than spin-strain coupling. We therefore estimate the corresponding single phonon coupling strength $g_0/2\pi \approx 22$ kHz, assuming our current cantilever dimensions of $t \approx 1 \mu\text{m}$ and $l \approx 35 \mu\text{m}$. This remarkable boost in g_0 is compensated to some extent by the relevant NV decoherence now being limited by the optical lifetime $\tau_{|3E\rangle} = 6 - 14$ ns [167]. The cooperativity C therefore benchmarks g_0 against cantilever heating rate $\gamma_{\text{th}} = k_B T / \hbar Q$ and NV decoherence rate $\Gamma_{\text{NV}} = 1/\tau_{3E} \approx 100$ MHz. For our current devices – if operated at $T = 8$ K and with quality factors of $Q = 10^5$ – we find $\gamma_{\text{th}}/2\pi = 1.7$ MHz and $C = 3 \times 10^{-6}$. The orbital-strain cooperativity increases by about five orders of magnitude with respect to the spin-strain cooperativity. Still, our current devices are far from the high cooperativity regime.

As discussed in Chap. 3, reducing cantilever dimensions is an effective ways to increase C . For a cantilever with dimensions $(l \times t \times w) = (1 \times 0.1 \times 0.1) \mu\text{m}^3$, operated at $T = 8$ K, and assuming $Q = 10^5$, we obtain $g_0/2\pi = 14.4$ MHz, $\gamma_{\text{th}}/2\pi = 1.7$ MHz and $\Gamma_{\text{NV}} = 100$ MHz. Together this yields a cooperativity of $C = 1.24$. On first sight, this does not seem to be an improvement compared to our estimations from Chap. 3, where we found a spin-strain cooperativity of $C = 2.49$, assuming identical cantilever dimensions, $Q = 2.5 \times 10^5$ and $T = 0.1$ K. Taking a second look, however, reveals the advantages of working with orbital-strain coupling in the NV's excited state in the sense that these values have been estimated for $T = 8$ K instead of mK temperatures. Even though our group has now access to an appropriate dilution refrigerator, working at temperatures in the mK range is without doubt challenging and reaching temperature of a few Kelvin should be much easier. Second, achieving quality factors of 2.5×10^5 for such small structures is difficult. Clearly, the lower the required quality factor is, the less demanding sample fabrication will be.

Yet, when estimating the orbit-strain cooperativity, we assumed a comparably large quality factor of $Q = 10^5$. However, when working with the NV excited state, the quality factor is less critical, especially in the context of resonator ground state cooling. As explained in Chap. 2, cooling rates for off-resonant (Γ_{\parallel}) and resonant (Γ_{\perp}) cooling are given by

$$\Gamma_{\parallel} = \frac{1}{4\pi^2} \frac{g_0^{\parallel 2} \Omega_{\text{opt}}^2}{\Gamma_{\text{NV}} \omega_m^2} \quad (7.1)$$

and

$$\Gamma_{\perp} = \frac{1}{4\pi^4} \frac{g_0^{\perp 2} \Omega_{\text{opt}}^2}{\Gamma_{\text{NV}}^3} \quad (7.2)$$

respectively [49]. With an optical Rabi frequency of $\Omega_{\text{opt}}/2\pi = 100$ MHz (values up to 400 MHz have been demonstrated [167]) and a mechanical eigenfrequency of

$\omega_m/2\pi = 272$ MHz (which is the eigenfrequency of the cantilever considered above), we find cooling rates of $\Gamma_{\parallel} = 0.3$ MHz and $\Gamma_{\perp} = 5.8$ MHz, assuming $g_0^{\parallel}/g_0^{\perp} = 0.83$ (see App. A.7). Comparing these with the heating rate $\gamma_{\text{th}} = k_B T/\hbar Q = 2\pi \times 1.7$ MHz of our cantilever yields final phonon numbers of

$$\bar{n}_{\parallel} = \frac{\gamma_{\text{th}}}{2\pi\Gamma_{\parallel}} = 5.95 \quad (7.3a)$$

$$\bar{n}_{\perp} = \frac{\gamma_{\text{th}}}{2\pi\Gamma_{\perp}} = 0.29. \quad (7.3b)$$

Under these circumstances, cooling the resonator with transverse coupling can bring it to its quantum ground state. Lower Q factors can be accounted for to some extent by increasing the optical Rabi amplitude Ω , on which both cooling rates depend quadratically. For example, with $Q = 5000$ and $\Omega_{\text{opt}}/2\pi = 250$ MHz, the resonant cooling scheme would still yield $\bar{n}_{\perp} = 0.93$.

Despite this promising prospect, we still have to worry about the NV coherence time Γ_{NV} . For the estimations given above we assumed Γ_{NV} to be purely lifetime limited. It is however known that NV centers in proximity to surfaces exhibit significantly broadened optical transitions due to spectral diffusion [167, 168]. Already in our current structures, which are by far larger than the resonators we would need to employ for the proposed cooling experiments, we observed inhomogeneously broadened optical linewidths in the order of $\Gamma_{\text{NV}}^* \approx 1$ GHz, and cooling rates $\Gamma_{\parallel,\perp}$ decrease by a factor $\Gamma_{\text{NV}}/(\Gamma_{\text{NV}} + \Gamma_{\text{NV}}^*) = 0.09$, as spectral diffusion broadens the line without causing dissipation [49]. Assuming the same Γ_{NV}^* for the proposed nanoscale resonator, we find $\bar{n}_{\parallel} = 65.5$ and $\bar{n}_{\perp} = 3.2$, which are both increased by one order of magnitude. A major challenge will therefore be the reduction of spectral diffusion while simultaneously decreasing cantilever dimensions. It might well be possible that we need to abandon the employed cantilever geometry and switch to other types of resonators, for example pillars, optomechanical crystals or surface acoustic wave structures [13, 169–172]. Such devices are characterized by similar coupling strengths as the introduced sub-micron cantilevers and in addition support mechanical modes with frequencies of several GHz. In both cases, NV centers can be positioned at increased distances from the closest surface to protect their precious properties [13].

If inhomogeneous broadening of the NV zero-phonon line cannot be reduced, a possible way to bring our resonator to its quantum ground state would be to replace the NV centers in our devices with negatively charged Silicon-Vacancy (SiV) centers [173–175]. The SiV center has recently gained increased attention as an optically accessible single spin system, which can be coherently controlled [176–178]. While spin coherence times T_2^* reside in the \sim ns range even at $T = 5$ K [179, 180], the SiV zero-phonon line shows almost no spectral diffusion due to the defect center's intrinsic symmetry [181, 182]. As its orbital response to strain, which lies in the \sim PHz/strain range [183, 184], is comparable to the NV orbital-strain coupling [105], the SiV is a promising candidate for cooling diamond mechanical resonators to their motional ground state.

In parallel to studying spectral diffusion and decreasing resonator dimensions, we will pursue another very interesting avenue on our recently installed 4 K confocal microscope. Despite its important role for NV spin physics, the S=0 ground state

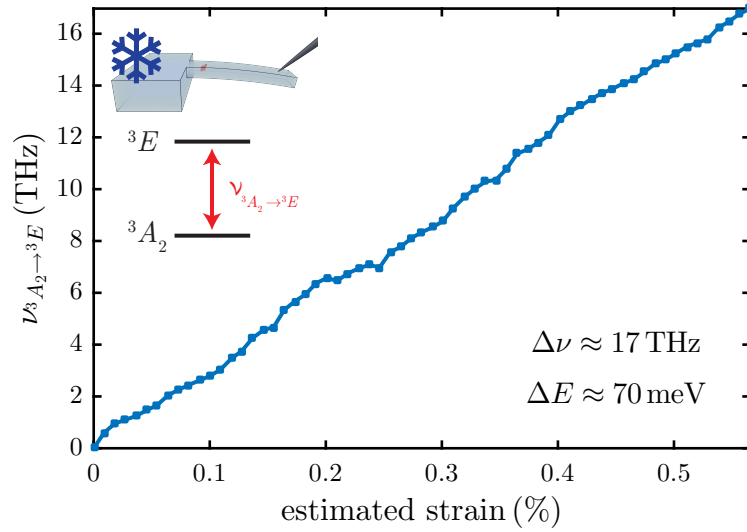


Figure 7.1.: Strain-induced shifts of the S=1 excited state levels, measured via static bending of our hybrid system at $T = 10$ K. Due to the strong orbital-strain coupling, strain changes transition frequencies $\nu_{^3A_2 \rightarrow ^3E}$ by several THz, corresponding to energy shifts of more than 70 meV. We hope to use the strong influence of strain coupling to study the optical properties of NV centers and determine the energetic position of the S=0 ground state relative to the S=1 ground and excited state levels.

is not yet fully understood. Notably, its exact energetic position with respect to the triplet ground and excited state manifolds is unknown. A recent study estimated the energy difference Δ between the $|A_1\rangle$ level of the S=1 excited state and the $|^1A_1\rangle$ level of the singlet ground state to be either around $\Delta \approx 40$ meV or $\Delta \approx 340 - 400$ meV [69]. The NV's strong response to strain might offer a possible approach to address this open question. Preliminary data taken on our 4 K confocal microscope demonstrates strain-induced shifts of the 3E states of several tens of meV (Fig. 7.1), which are comparable to the predicted Δ , and should therefore significantly influence the NV's optical properties, such as spin-dependent decay and intersystem crossing rates [67, 69, 185]. We plan to study these properties under the influence of strain and hope to extract a reliable value for Δ . Corresponding experiments are currently in preparation and should yield first results in the near future.

A. Appendix

A.1. Polarization dependence of microwave spin driving

We stated in section 2.3.2 that due to selection rules the $|0\rangle \rightarrow | + 1\rangle$ transition can be excited with right-circular polarized light while the $|0\rangle \rightarrow | - 1\rangle$ transition can be driven with left-circular polarized light. To derive this we mainly follow the argument given in the supplementary material of [137]. Let us consider a purely transverse AC magnetic field ($B_z = 0$) of arbitrary polarization, parametrized by amplitudes $B_{x,y}$ and phase ϕ . We can then write down the Hamiltonian describing the interaction of the NV S=1 ground state with the magnetic field as

$$\hat{H}_{\text{tot}}/\hbar = D_{\text{gs}}\hat{S}_z^2 + \gamma_{\text{NV}} \left(B_x \cos(\omega_{\text{MW}}t)\hat{S}_x + B_y \cos(\omega_{\text{MW}}t + \phi)\hat{S}_y \right) \quad (\text{A.1})$$

where the S=1 spin matrices are

$$\hat{S}_x = \frac{1}{\sqrt{2}} \begin{pmatrix} 0 & 1 & 0 \\ 1 & 0 & 1 \\ 0 & 1 & 0 \end{pmatrix} \quad \hat{S}_y = \frac{-i}{\sqrt{2}} \begin{pmatrix} 0 & 1 & 0 \\ -1 & 0 & 1 \\ 0 & -1 & 0 \end{pmatrix} \quad (\text{A.2})$$

and we omitted the hyperfine terms for clarity. For further simplification we go into the MW field rotating frame using the transformation [117, 186]

$$\hat{H}_{\text{tot}}^{\text{rot}} = \hat{U}\hat{H}_{\text{int}}\hat{U}^{-1} + i\frac{d\hat{U}}{dt}\hat{U}^{-1} \quad (\text{A.3})$$

with

$$\hat{A}/\hbar = \begin{pmatrix} \omega_{\text{MW}} & 0 & 0 \\ 0 & 0 & 0 \\ 0 & 0 & \omega_{\text{MW}} \end{pmatrix} \quad (\text{A.4})$$

and $\hat{U} = \exp(i\hat{A}t)$. With $\Omega_{x,y}/2\pi = \gamma_{\text{NV}}B_{x,y}$, setting $B_x = B_y$ and thus $\Omega_{\text{MW}} = \Omega_x = \Omega_y$ as well as resonant driving ($2\pi D_{\text{gs}} - \omega_{\text{MW}} = 0$) we obtain

$$\hat{H}_{\text{tot}}^{\text{rot}}/\hbar = \frac{\Omega_{\text{MW}}}{\sqrt{2}} \begin{pmatrix} 0 & \epsilon_- & 0 \\ \epsilon_-^* & 0 & \epsilon_+ \\ 0 & \epsilon_+^* & 0 \end{pmatrix} + \frac{\Omega_{\text{MW}}}{\sqrt{2}} \begin{pmatrix} 0 & \epsilon_+ e^{i2\omega_{\text{MW}}t} & 0 \\ \epsilon_+^* e^{-i2\omega_{\text{MW}}t} & 0 & \epsilon_- e^{-i2\omega_{\text{MW}}t} \\ 0 & \epsilon_-^* e^{i2\omega_{\text{MW}}t} & 0 \end{pmatrix} \quad (\text{A.5})$$

with $\epsilon_{\pm} = (1 - ie^{\pm i\phi})/2$ denoting the polarization of the applied magnetic field. For weak driving, such that $\Omega_{\text{MW}} \ll \omega_{\text{MW}}, 2\pi D_{\text{gs}}$, we can use the rotating wave approximation, i.e. assume that the fast terms $e^{\pm 2i\omega_{\text{MW}}t}$ oscillate many times during a full rotation of the spin and thus average to 0, to rewrite (A.5) and obtain

$$\hat{H}_{\text{tot}}^{\text{RWA}}/\hbar = \frac{\Omega_{\text{MW}}}{\sqrt{2}} \begin{pmatrix} 0 & \epsilon_- & 0 \\ \epsilon_-^* & 0 & \epsilon_+ \\ 0 & \epsilon_+^* & 0 \end{pmatrix}. \quad (\text{A.6})$$

We can now easily see that right-circularly polarized magnetic fields ($\phi = -\pi/2$ and thus $\epsilon_+ = 0, \epsilon_- = 1$) drives the $|0\rangle \rightarrow |-1\rangle$ transition, while left-circularly polarized magnetic fields ($\phi = +\pi/2$ and thus $\epsilon_+ = 1, \epsilon_- = 0$) addresses the $|0\rangle \rightarrow |+1\rangle$ transition. Note that this statement only holds for weak driving as for strong driving the counter-rotating terms of opposite polarization cannot be neglected.

A.2. Influence of NV coordinate system on spin-strain coupling Hamiltonian

As described in the main text, Hughes and Runciman work with a defect coordinate system where $\mathbf{e}_x \parallel [\bar{1}10]$, $\mathbf{e}_y \parallel [\bar{1}\bar{1}2]$ and $\mathbf{e}_z \parallel [111]$ and derive the stress-coupling Hamiltonian

$$\hat{\mathbf{H}}'_{\sigma,XYZ}/h = \begin{pmatrix} 0 & 0 & 0 \\ 0 & M'_{\sigma,z} - M'_{\sigma,x} & M'_{\sigma,y} \\ 0 & M'_{\sigma,y} & M'_{\sigma,z} + M'_{\sigma,x} \end{pmatrix} \quad (\text{A.7})$$

written in the $\{|A\rangle, |E_x\rangle, |E_y\rangle\}$ basis. Doherty *et al.* however define the NV x axis to be contained by one of the mirror planes (a possible NV coordinate system would be $\mathbf{e}_x \parallel [11\bar{2}]$, $\mathbf{e}_y \parallel [\bar{1}10]$ and $\mathbf{e}_z \parallel [111]$). For this definition the coupling Hamiltonian is

$$\hat{\mathbf{H}}^\sigma_{\text{gs}}/h = \begin{pmatrix} 0 & 0 & 0 \\ 0 & M^{\text{gs}}_{\sigma,z} + M^{\text{gs}}_{\sigma,x} & -M^{\text{gs}}_{\sigma,y} \\ 0 & -M^{\text{gs}}_{\sigma,y} & M^{\text{gs}}_{\sigma,z} - M^{\text{gs}}_{\sigma,x} \end{pmatrix} \quad (\text{A.8})$$

where the transverse level shifts have opposite signs.

The two coordinate systems presented above differ by a rotation of $\pi/2$ about the quantization axis. The rotation $\hat{\mathbf{R}}^s_{\mathbf{e}}(\theta)$ of a tensor in spin-space by an angle θ about axis \mathbf{e} is described by

$$\hat{\mathbf{R}}^s_{\mathbf{e}}(\theta) = \exp(-i\hat{\mathbf{J}}_{\mathbf{e}}\theta) \quad (\text{A.9})$$

where $\mathbf{J}_{\mathbf{e}}$ is the creator of rotation about axis \mathbf{e} . We now rotate the NV stress Hamiltonian from (A.8) about the spin quantization axis by performing the rotation

$$\begin{aligned} \hat{\mathbf{H}}^\sigma_{\text{gs,rot}} &= \hat{\mathbf{R}}^s_z(\theta)\hat{\mathbf{H}}^\sigma_{\text{gs}}\hat{\mathbf{R}}^s_z(\theta)^\dagger \\ &= \exp(-i\hat{\mathbf{S}}_z\theta)\hat{\mathbf{H}}^\sigma_{\text{gs}}\exp(i\hat{\mathbf{S}}_z\theta). \end{aligned} \quad (\text{A.10})$$

and obtain for $\theta = \pi/2$

$$\hat{\mathbf{H}}^\sigma_{\text{gs,rot}}/h = \begin{pmatrix} 0 & 0 & 0 \\ 0 & M^{\text{gs}}_{\sigma,z} - M^{\text{gs}}_{\sigma,x} & M^{\text{gs}}_{\sigma,y} \\ 0 & M^{\text{gs}}_{\sigma,y} & M^{\text{gs}}_{\sigma,z} + M^{\text{gs}}_{\sigma,x} \end{pmatrix} \quad (\text{A.11})$$

which is equal to (A.7).

Table A.1.: Overview of NV orientations (defined in analogy to [111], i.e. such that the y axis is contained in a mirror plane). The given rotations align NV1 to NV2-4.

	e_x	e_y	e_z	NV1 \rightarrow NV1-4
NV1	$[\bar{1}10]$	$[\bar{1}\bar{1}2]$	$[111]$	$\mathbf{1}$
NV2	$[1\bar{1}0]$	$[112]$	$[\bar{1}\bar{1}\bar{1}]$	$\mathbf{R}_{[001]}(\pi)$
NV3	$[110]$	$[1\bar{1}\bar{2}]$	$[\bar{1}\bar{1}\bar{1}]$	$\mathbf{R}_{[110]}(\pi)\mathbf{R}_{[001]}(-\pi/2)$
NV4	$[\bar{1}\bar{1}0]$	$[\bar{1}\bar{1}\bar{2}]$	$[1\bar{1}\bar{1}]$	$\mathbf{R}_{[110]}(\pi)\mathbf{R}_{[001]}(\pi/2)$

A.3. Stress and strain coupling: How to include different NV orientations

Stress coupling

As stated in the main text, the formalism developed by Hughes and Runciman describes stress-coupling to a single defect orientation. Due to the diamond lattice structure there are however four NV orientations, which we label NV1-NV4 in the following, that are relevant for our experiment. To include these we are going to keep the defect orientation fixed and rotate the stress tensor. This approach requires defining the four NV orientations and the corresponding rotations that transform NV1 into NV2-4. Both are given in Tab. A.1. The given $\mathbf{R}_{\mathbf{p}}(\theta)$ describe three-dimensional rotations by angles θ about specific axes indicated by the unit vector $\mathbf{p} = \{p_1, p_2, p_3\}^T$. They can be calculated using the relation [187]

$$\mathbf{R}_{\mathbf{p}}(\theta) = \mathbf{1} + \sin \theta \mathbf{P} + (1 - \cos \theta) \mathbf{P}^2 \quad (\text{A.12})$$

where

$$\mathbf{P} = \begin{pmatrix} 0 & -p_3 & p_2 \\ p_3 & 0 & -p_1 \\ -p_2 & p_1 & 0 \end{pmatrix}. \quad (\text{A.13})$$

Note that \mathbf{p} always refers to the original, unrotated coordinate system and θ is positive for a clockwise rotation observed along the axis of rotation \mathbf{p} .

Rotating a vector while keeping the coordinate system fixed is often referred to as an *active transformation*. However, we are going to keep NV1 fixed and rotate the stress tensor, i.e. the crystal coordinate system, around it. We therefore need to perform a *passive transformation* where the coordinate system is rotated while the vector remains unchanged. Passive transformations require working with the inverse rotation matrix $(\mathbf{R}_{\mathbf{p}}(\theta))^{-1}$ where $\mathbf{R}_{\mathbf{p}}(\theta)$ denotes an active transformation. As the rotations in Tab. A.1 are active transformations we use the relation

$$\sigma_{XYZ}^k = (\mathbf{R}_k)^{-1} \sigma_{XYZ}^{\text{NV1}} ((\mathbf{R}_k)^{-1})^T \quad (\text{A.14})$$

to rotate the stress tensor $\sigma_{XYZ}^{\text{NV1}}$ such that it describes the reaction of NV2-4, denoted by the index k , to stress along a certain direction. Let us for example consider NV orientations NV1 and NV2. For NV1 we use the standard

stress tensor from (2.37) of the main text. By performing the rotation $\boldsymbol{\sigma}_{XYZ}^{\text{NV2}} = (\mathbf{R}_{[001]}(\pi))^{-1} \boldsymbol{\sigma}_{XYZ}^{\text{NV1}} ((\mathbf{R}_{[001]}(\pi))^{-1})^T$ we obtain

$$\boldsymbol{\sigma}_{XYZ}^{\text{NV2}} = \begin{pmatrix} \sigma_{XX} & \sigma_{XY} & -\sigma_{XZ} \\ \sigma_{YX} & \sigma_{YY} & -\sigma_{YZ} \\ -\sigma_{ZX} & -\sigma_{ZY} & \sigma_{ZZ} \end{pmatrix}, \quad (\text{A.15})$$

from which follows

$$M_{\sigma,x}^{\text{NV2},'} = B(2\sigma_{ZZ} - \sigma_{XX} - \sigma_{YY}) + C(2\sigma_{XY} + \sigma_{YZ} + \sigma_{XZ}) \quad (\text{A.16a})$$

$$M_{\sigma,y}^{\text{NV2},'} = \sqrt{3}B(\sigma_{XX} - \sigma_{YY}) + \sqrt{3}C(-\sigma_{YZ} + \sigma_{XZ}) \quad (\text{A.16b})$$

$$M_{\sigma,z}^{\text{NV2},'} = A_1(\sigma_{XX} + \sigma_{YY} + \sigma_{ZZ}) + 2A_2(-\sigma_{YZ} - \sigma_{XZ} + \sigma_{XY}). \quad (\text{A.16c})$$

The NV2 level shifts for stress along the [100], [110] and [111] are

$$\Delta_{\pm}^{[100]}/P = A_1 \pm 2B \quad (\text{A.17a})$$

$$\Delta_{\pm}^{[110]}/P = A_1 + A_2 \pm (C - B) \quad (\text{A.17b})$$

$$\Delta_{\pm}^{[111]}/P = A_1 - \frac{2}{3}A_2 \pm \frac{4}{3}C. \quad (\text{A.17c})$$

In analogy we obtain similar expressions for NV3

$$M_{\sigma,x}^{\text{NV3},'} = B(2\sigma_{ZZ} - \sigma_{XX} - \sigma_{YY}) + C(-2\sigma_{XY} + \sigma_{YZ} - \sigma_{XZ}) \quad (\text{A.18a})$$

$$M_{\sigma,y}^{\text{NV3},'} = \sqrt{3}B(\sigma_{XX} - \sigma_{YY}) + \sqrt{3}C(-\sigma_{YZ} - \sigma_{XZ}) \quad (\text{A.18b})$$

$$M_{\sigma,z}^{\text{NV3},'} = A_1(\sigma_{XX} + \sigma_{YY} + \sigma_{ZZ}) + 2A_2(-\sigma_{YZ} + \sigma_{XZ} - \sigma_{XY}) \quad (\text{A.18c})$$

$$\Delta_{\pm}^{[100]}/P = A_1 \pm 2B \quad (\text{A.19a})$$

$$\Delta_{\pm}^{[110]}/P = A_1 - A_2 \pm (-B - C) \quad (\text{A.19b})$$

$$\Delta_{\pm}^{[111]}/P = A_1 - \frac{2}{3}A_2 \pm \frac{4}{3}C \quad (\text{A.19c})$$

and NV4

$$M_{\sigma,x}^{\text{NV4},'} = B(2\sigma_{ZZ} - \sigma_{XX} - \sigma_{YY}) + C(-2\sigma_{XY} - \sigma_{YZ} + \sigma_{XZ}) \quad (\text{A.20a})$$

$$M_{\sigma,y}^{\text{NV4},'} = \sqrt{3}B(\sigma_{XX} - \sigma_{YY}) + \sqrt{3}C(\sigma_{YZ} + \sigma_{XZ}) \quad (\text{A.20b})$$

$$M_{\sigma,z}^{\text{NV4},'} = A_1(\sigma_{XX} + \sigma_{YY} + \sigma_{ZZ}) + 2A_2(\sigma_{YZ} - \sigma_{XZ} - \sigma_{XY}) \quad (\text{A.20c})$$

$$\Delta_{\pm}^{[100]}/P = A_1 \pm 2B \quad (\text{A.21a})$$

$$\Delta_{\pm}^{[110]}/P = A_1 - A_2 \pm (-B - C) \quad (\text{A.21b})$$

$$\Delta_{\pm}^{[111]}/P = A_1 - \frac{2}{3}A_2 \pm \frac{4}{3}C. \quad (\text{A.21c})$$

The results are summarized and commented in the main text (see Tab. 2.1).

Strain coupling

As explained in the main text we find the strain-induced level shifts $M'_{\epsilon,i}$ by substituting the stress tensor components σ_{ij} with $i, j \in \{X, Y, Z\}$ with strain tensor components ϵ_{ij} with $i, j \in \{x, y, z\}$ calculated using

$$\tilde{\sigma}_{XYZ} = \tilde{\mathbf{C}}_{XYZ} \tilde{\mathbf{K}}^T \tilde{\epsilon}_{xyz}. \quad (\text{A.22})$$

This expression can be derived as follows:

$$\tilde{\sigma}_{xyz} = \tilde{\mathbf{C}}_{xyz} \tilde{\epsilon}_{xyz} \quad (\text{A.23a})$$

$$\tilde{\sigma}_{xyz} = \mathbf{K} \tilde{\mathbf{C}}_{XYZ} \mathbf{K}^T \tilde{\epsilon}_{xyz} \quad (\text{A.23b})$$

$$\tilde{\sigma}_{XYZ} = \tilde{\mathbf{K}}^{-1} \tilde{\mathbf{K}} \tilde{\mathbf{C}}_{XYZ} \tilde{\mathbf{K}}^T \tilde{\epsilon}_{xyz} \quad (\text{A.23c})$$

$$\tilde{\sigma}_{XYZ} = \tilde{\mathbf{C}}_{XYZ} \tilde{\mathbf{K}}^T \tilde{\epsilon}_{xyz} \quad (\text{A.23d})$$

where we make use of the relations $\tilde{\sigma}_{xyz} = \tilde{\mathbf{K}} \tilde{\sigma}_{XYZ}$, $\tilde{\mathbf{C}}_{xyz} = \tilde{\mathbf{K}} \tilde{\mathbf{C}}_{XYZ} \tilde{\mathbf{K}}^T$ and $\tilde{\mathbf{K}}^{-1} \tilde{\mathbf{K}} = \mathbf{1}$. $\tilde{\mathbf{K}}$ describes the coordinate system transformation from $XYZ \rightarrow xyz$ with xyz being defined for NV1 (see Tab. A.1) and can be written as

$$\tilde{\mathbf{K}} = \left(\tilde{\mathbf{R}}_{[\bar{1}10]}(\alpha_{\text{NV}}) \tilde{\mathbf{R}}_{[001]}(3\pi/4) \right)^{-1}. \quad (\text{A.24})$$

As we have to work within the Voigt notation, the $\tilde{\mathbf{R}}_p(\theta)$ are 6×6 matrices obtained with

$$\tilde{\mathbf{R}}_p(\theta) = \tilde{\mathbf{1}} + \sin \theta \tilde{\mathbf{P}} + (1 - \cos \theta) \tilde{\mathbf{P}}^2 + \frac{1}{3} \sin \theta (1 - \cos \theta) (\tilde{\mathbf{P}} + \tilde{\mathbf{P}}^3) + \frac{1}{6} (1 - \cos \theta)^2 (\tilde{\mathbf{P}}^2 + \tilde{\mathbf{P}}^4) \quad (\text{A.25})$$

where

$$\tilde{\mathbf{P}} = \begin{pmatrix} 0 & 0 & 0 & 0 & \sqrt{2}p_2 & -\sqrt{2}p_3 \\ 0 & 0 & 0 & -\sqrt{2}p_1 & 0 & \sqrt{2}p_3 \\ 0 & 0 & 0 & \sqrt{2}p_1 & -\sqrt{2}p_2 & 0 \\ 0 & \sqrt{2}p_1 & -\sqrt{2}p_1 & 0 & p_3 & -p_2 \\ -\sqrt{2}p_2 & 0 & \sqrt{2}p_2 & -p_3 & 0 & p_1 \\ \sqrt{2}p_3 & -\sqrt{2}p_3 & 0 & p_2 & -p_1 & 0 \end{pmatrix} \quad (\text{A.26})$$

represents the rotation axis denoted by the unit vector $\mathbf{p} = \{p_1, p_2, p_3\}$ [187].

We are now going to discuss the influence of the chosen NV coordinate system on the expressions for $M'_{\epsilon,i}$ and the corresponding level shifts. Obviously, the definition of different NV coordinate system should not change the resulting level shifts as long as the quantization axes point into the same direction. To investigate this question let us consider the NV coordinate system from NV1 where $\mathbf{e}_x \parallel [\bar{1}10]$, $\mathbf{e}_y \parallel [\bar{1}\bar{1}2]$ and $\mathbf{e}_z \parallel [111]$. As this NV orientation is used by Hughes and Runciman, we will for now call it NVHughes [111]. Barson *et al.*, who quantified the stress-coupling constants A_1 , A_2 , B and C for the S=1 ground state, however employ an NV orientation which we will call NVBarson where $\mathbf{e}_x \parallel [\bar{1}\bar{1}2]$, $\mathbf{e}_y \parallel [1\bar{1}0]$ and $\mathbf{e}_z \parallel [111]$. Obviously, both orientations use the same quantization axis (we therefore expect identical level shifts) but the x and y axes are rotated by $\pi/2$ about the z axis.

The calculated $M'_{\epsilon,i}{}^{\text{H/B}}$ for both NV orientations are shown below ($\tilde{\mathbf{K}}_{\text{H}} = \left(\tilde{\mathbf{R}}_{[\bar{1}10]}(\alpha_{\text{NV}}) \tilde{\mathbf{R}}_{[001]}(3\pi/4) \right)^{-1}$ and $\tilde{\mathbf{K}}_{\text{B}} = \left(\tilde{\mathbf{R}}_{[\bar{1}10]}(\alpha_{\text{NV}}) \tilde{\mathbf{R}}_{[001]}(5\pi/4) \right)^{-1}$):

$$M_{\epsilon,x}^{\text{H}} = b(\epsilon_{xx}^{\text{H}} - \epsilon_{yy}^{\text{H}}) + 2c\epsilon_{yz}^{\text{H}} \quad (\text{A.27a})$$

$$M_{\epsilon,y}^{\text{H}} = -2b\epsilon_{xy}^{\text{H}} - 2c\epsilon_{xz}^{\text{H}} \quad (\text{A.27b})$$

$$M_{\epsilon,z}^{\text{H}} = a_1\epsilon_{zz}^{\text{H}} + a_2(\epsilon_{xx}^{\text{H}} + \epsilon_{yy}^{\text{H}}) \quad (\text{A.27c})$$

$$M_{\epsilon,x}^{\text{B}} = -b(\epsilon_{xx}^{\text{B}} - \epsilon_{yy}^{\text{B}}) + 2c\epsilon_{xz}^{\text{B}} \quad (\text{A.28a})$$

$$M_{\epsilon,y}^{\text{B}} = 2b\epsilon_{xy}^{\text{B}} + 2c\epsilon_{yz}^{\text{B}} \quad (\text{A.28b})$$

$$M_{\epsilon,z}^{\text{B}} = a_1\epsilon_{zz}^{\text{B}} + a_2(\epsilon_{xx}^{\text{B}} + \epsilon_{yy}^{\text{B}}). \quad (\text{A.28c})$$

The corresponding level shifts are given by

$$\Delta_{\pm}^{\text{H}}/\epsilon = [a_1\epsilon_{zz}^{\text{H}} + a_2(\epsilon_{xx}^{\text{H}} + \epsilon_{yy}^{\text{H}})] \quad (\text{A.29})$$

$$\pm \left[b^2(\epsilon_{xx}^{\text{H}} - \epsilon_{yy}^{\text{H}})^2 + 4bc\epsilon_{yz}^{\text{H}}(\epsilon_{xx}^{\text{H}} - \epsilon_{yy}^{\text{H}}) + 4c^2\epsilon_{yz}^{\text{H}2} + 4b^2\epsilon_{xy}^{\text{H}2} + 8bc\epsilon_{xy}^{\text{H}}\epsilon_{xz}^{\text{H}} + 4c^2\epsilon_{xz}^{\text{H}2} \right]^{1/2}$$

and

$$\Delta_{\pm}^{\text{B}}/\epsilon = [a_1\epsilon_{zz}^{\text{B}} + a_2(\epsilon_{xx}^{\text{B}} + \epsilon_{yy}^{\text{B}})] \quad (\text{A.30})$$

$$\pm \left[b^2(\epsilon_{xx}^{\text{B}} - \epsilon_{yy}^{\text{B}})^2 - 4bc\epsilon_{xz}^{\text{B}}(\epsilon_{xx}^{\text{B}} - \epsilon_{yy}^{\text{B}}) + 4c^2\epsilon_{xz}^{\text{B}2} + 4b^2\epsilon_{xy}^{\text{B}2} + 8bc\epsilon_{xy}^{\text{B}}\epsilon_{yz}^{\text{B}} + 4c^2\epsilon_{yz}^{\text{B}2} \right]^{1/2}$$

and obviously differ under the assumption $\epsilon_{ij}^{\text{H}} = \epsilon_{ij}^{\text{B}}$. However, the two strain tensors are *not* the same as they originate from the same stress tensor but were obtained using a different coordinate transformation. Comparing $\tilde{\epsilon}_{xyz}^{\text{B}}$ and $\tilde{\epsilon}_{xyz}^{\text{H}}$ when expressed in terms of the original stress tensor we find

$$\begin{pmatrix} \epsilon_{xx}^{\text{B}} \\ \epsilon_{yy}^{\text{B}} \\ \epsilon_{zz}^{\text{B}} \\ \epsilon_{yz}^{\text{B}} \\ \epsilon_{xz}^{\text{B}} \\ \epsilon_{xy}^{\text{B}} \end{pmatrix} = \begin{pmatrix} \epsilon_{yy}^{\text{H}} \\ \epsilon_{xx}^{\text{H}} \\ \epsilon_{zz}^{\text{H}} \\ -\epsilon_{xz}^{\text{H}} \\ \epsilon_{yz}^{\text{H}} \\ -\epsilon_{xy}^{\text{H}} \end{pmatrix} \quad (\text{A.31})$$

under which $\Delta_{\pm}^{\text{Hughes}} = \Delta_{\pm}^{\text{Barson}}$ is fulfilled. We therefore conclude that the orientation of the x and y axes for a given z axis does not matter as long as one derives the strain tensor in the NV coordinate system appropriately, i.e. with the correct rotation from the original stress tensor defined in the crystal coordinate system.

Finally, to account for all the remaining three NV orientations we write σ_{XYZ} in the corresponding coordinate systems using the already familiar rotation

$$\tilde{\sigma}_{XYZ}^k = \tilde{\mathbf{C}}_{XYZ} \tilde{\mathbf{K}}_k^T \tilde{\epsilon}_{xyz} \quad (\text{A.32})$$

with $\tilde{\mathbf{K}}_k$ denoting the transformation of XYZ into the coordinate system of NV2-NV4, which are given by

$$\tilde{\mathbf{K}}_{\text{NV2}} = \left(\tilde{\mathbf{R}}_{[001]}(\pi) \tilde{\mathbf{R}}_{[\bar{1}10]}(\alpha_{\text{NV}}) \tilde{\mathbf{R}}_{[001]}(3\pi/2) \right)^{-1} \quad (\text{A.33a})$$

$$\tilde{\mathbf{K}}_{\text{NV3}} = \left(\tilde{\mathbf{R}}_{[110]}(\pi) \tilde{\mathbf{R}}_{[001]}(-\pi/2) \tilde{\mathbf{R}}_{[\bar{1}10]}(\alpha_{\text{NV}}) \tilde{\mathbf{R}}_{[001]}(3\pi/2) \right)^{-1} \quad (\text{A.33b})$$

$$\tilde{\mathbf{K}}_{\text{NV4}} = \left(\tilde{\mathbf{R}}_{[110]}(\pi) \tilde{\mathbf{R}}_{[001]}(\pi/2) \tilde{\mathbf{R}}_{[\bar{1}10]}(\alpha_{\text{NV}}) \tilde{\mathbf{R}}_{[001]}(3\pi/2) \right)^{-1}. \quad (\text{A.33c})$$

The resulting level shifts for all NV orientations are summarized in the main text in Tab. 2.2.

A.4. Notes on the harmonic oscillator

The quality factor Q without external driving

The quality factor of an harmonic oscillator compares the energy $E(t)$ stored in the oscillator with the energy $\Delta E = E(t) - E(t + T)$ that is lost during one full oscillation period $T = 2\pi/\omega_{\text{eff}}$. We can therefore write

$$Q = 2\pi \frac{E(t)}{\Delta E} = 2\pi \frac{E(t)}{E(t) - E(t + T)} \quad (\text{A.34})$$

where the stored energy at time t is given by the sum of kinetic and potential energy, thus

$$E(t) = \frac{1}{2} m_{\text{eff}} \dot{u}(t)^2 + \frac{m_{\text{eff}} \omega_{\text{m}}}{2} u(t)^2. \quad (\text{A.35})$$

Under the assumption of weak damping, i.e. $\Gamma_{\text{m}} \ll \omega_{\text{m}}$, we can express $u(t) = A \cos(\omega_{\text{eff}} t) e^{-\Gamma_{\text{m}} t}$ and obtain

$$E(t) = \frac{A^2 m_{\text{eff}} \omega_{\text{m}}^2}{2} e^{-2\Gamma_{\text{m}} t} = E_0 e^{-2\Gamma_{\text{m}} t} \quad (\text{A.36})$$

for the time-evolution of the stored energy. We then calculate the lost energy per cycle $\Delta E = \int_t^{t+T} \dot{E} dt'$ and find

$$\Delta E = E_0 e^{-2\Gamma_{\text{m}} t} (1 - e^{-4\pi\Gamma_{\text{m}}/\omega_{\text{eff}}}). \quad (\text{A.37})$$

For weak damping $(1 - e^{-4\pi\Gamma_{\text{m}}/\omega_{\text{eff}}}) \approx 4\pi\Gamma_{\text{m}}/\omega_{\text{eff}}$ and the Q factor is given by

$$Q = \frac{\omega_{\text{eff}}}{2\Gamma_{\text{m}}} \approx \frac{\omega_{\text{m}}}{2\Gamma_{\text{m}}}. \quad (\text{A.38})$$

Solution for external driving

The solution of a driven oscillator is of the form

$$\tilde{u}(t) = \tilde{u}_0(t) + \tilde{u}_{\text{F}}(t) \quad (\text{A.39})$$

where $\tilde{u}_0(t) = A \cos(\omega_{\text{eff}} t) e^{-\Gamma_{\text{m}} t}$ is the homogeneous solution and describes the time evolution of the resonator without external driving and weak damping. $\tilde{u}_{\text{F}}(t)$

denotes the inhomogeneous solution due to external driving. Choosing the ansatz $\tilde{u}_F(t) = D \cos(\omega_d t - \phi)$ we can use (2.84) from the main text and obtain

$$D(\omega_m^2 - \omega_d^2) \cos(\omega_d t - \phi) - D2\Gamma_m \omega_d \sin(\omega_d t - \phi) = \tilde{F} \cos(\omega_d t) \quad (\text{A.40})$$

where we employed $\ddot{u}_0(t) + 2\Gamma_m \dot{u}_0(t) + \omega_m^2 u_0(t) = 0$ due to (2.81) from the main text.

To find expressions for D and ϕ we remember the trigonometric relations

$$\cos(\omega_d t - \phi) = \cos(\omega_d t) \cos \phi + \sin(\omega_d t) \sin \phi \quad (\text{A.41})$$

and

$$\sin(\omega_d t - \phi) = \sin(\omega_d t) \cos \phi - \cos(\omega_d t) \sin \phi \quad (\text{A.42})$$

and rewrite (A.40), which becomes

$$\alpha \cos \omega_d t - \beta \sin \omega_d t = 0 \quad (\text{A.43})$$

with

$$\alpha = -\tilde{F} + D((\omega_m^2 - \omega_d^2) \cos \phi + 2\Gamma_m \omega_d \sin \phi) \quad (\text{A.44})$$

$$\beta = D((\omega_m^2 - \omega_d^2) \sin \phi - 2\Gamma_m \omega_d \cos \phi). \quad (\text{A.45})$$

Eq. (A.41) can only be fulfilled for $\alpha = \beta = 0$. It follows from $\beta = 0$ that

$$\phi = \arctan\left(\frac{2\Gamma_m \omega_d}{\omega_m^2 - \omega_d^2}\right) \quad (\text{A.46})$$

which, together with the requirement $\alpha = 0$, we use to find

$$D = \frac{\tilde{F}}{\sqrt{(\omega_m^2 - \omega_d^2)^2 + (2\Gamma_m \omega_d)^2}} \quad (\text{A.47})$$

as shown in the expression for the inhomogeneous solution in (2.86) of the main text.

The quality factor Q for external driving

In contrast to the undriven oscillator, where the system's energy $E(t)$ decays over time, no obvious decay takes place in the steady-state of the driven harmonic oscillator. While the system is still subject to dissipation, the external drive provides the dissipated energy and prevents the oscillations from being damped. The mean energy stored in the system is thus constant and is given by

$$\langle E \rangle = \frac{1}{4} m_{\text{eff}} D^2 (\omega_m^2 + \omega_d^2) \quad (\text{A.48})$$

where we used $\langle \sin^2(\omega_d t) \rangle = \langle \cos^2(\omega_d t) \rangle = 1/2$. The dissipated energy E_{diss} per oscillation cycle is

$$E_{\text{diss}} = m_{\text{eff}} 2\Gamma_m \int_0^{T=2\pi/\omega_d} \dot{u}_F^2 dt = \frac{2\pi}{\omega_d} m_{\text{eff}} \Gamma_m \omega_d^2 D^2. \quad (\text{A.49})$$

For $\omega_d = \omega_m$, the Q factor can then be written as

$$Q = 2\pi \frac{\langle E \rangle}{E_{\text{diss}}} = \frac{\omega_m}{2\Gamma_m}. \quad (\text{A.50})$$

From an experimental point of view it is desirable to link the quality factor Q to the resonance curve of $D(\omega_d)$. To that end we write

$$D(\omega_d) = \frac{\tilde{F}}{\sqrt{(\omega_m - \omega_d)^2 (\omega_m + \omega_d)^2 + (2\Gamma_m \omega_d)^2}} \quad (\text{A.51})$$

and examine the oscillator's amplitude when driven close to resonance, i.e. $\omega_d = \omega_{\text{res}}$, where the oscillation amplitude $D_{\text{max}} = D(\omega_{\text{res}})$ is maximized. For weak damping $\omega_{\text{res}} = \omega_m$ and we can simplify (A.51) to

$$D(\omega_d) = \frac{\tilde{F}}{2\omega_m \sqrt{(\omega_m - \omega_d)^2 + \Gamma_m^2}}. \quad (\text{A.52})$$

If we define its width $\Delta\omega_d$ to be the frequency difference between the points where $D_{\text{max}}/\sqrt{2}$ we find that $\Delta\omega_d = 2\Gamma_m$. The Q factor can then be expressed by

$$Q = \frac{\omega_m}{\Delta\omega_d}. \quad (\text{A.53})$$

Note however that $\Delta\omega_d$ is not the full width at half maximum of the distribution $D(\omega_d)$, but $\Delta\omega_d = \Delta\omega_d^{\text{FWHM}}/\sqrt{3}$.

A.5. Characterizing spin-strain coupling in the NV S=1 ground state

A.5.1. Simplified approach from Teissier et al. [1]

Spin-strain coupling in the S=1 NV ground state is described by the Hamiltonian (2.32)

$$\hat{H}_{\text{gs}}^\epsilon/h = \underbrace{M_{\epsilon,z}^{\text{gs}} \hat{S}_z^2}_{\hat{H}_{\text{gs}}^{\epsilon,\parallel}} + \underbrace{M_{\epsilon,x}^{\text{gs}} (\hat{S}_y^2 - \hat{S}_x^2) + M_{\epsilon,y}^{\text{gs}} (\hat{S}_x \hat{S}_y + \hat{S}_y \hat{S}_x)}_{\hat{H}_{\text{gs}}^{\epsilon,\perp}} \quad (\text{A.54})$$

where $M_{\epsilon,i}^{\text{gs}}$ with $i = x, y, z$ denote the strain-induced level shifts. In [1] we neglected the presence of shear strain components and the Poisson effect, i.e. we approximated strain as a vector $\boldsymbol{\epsilon} = \{\epsilon_x, \epsilon_y, \epsilon_z\}$, and expressed

$$M_{\epsilon,x}^{\text{gs}} = d_{\perp}^{\text{gs}} \epsilon_x \quad (\text{A.55a})$$

$$M_{\epsilon,y}^{\text{gs}} = d_{\perp}^{\text{gs}} \epsilon_y \quad (\text{A.55b})$$

$$M_{\epsilon,z}^{\text{gs}} = d_{\parallel}^{\text{gs}} \epsilon_z \quad (\text{A.55c})$$

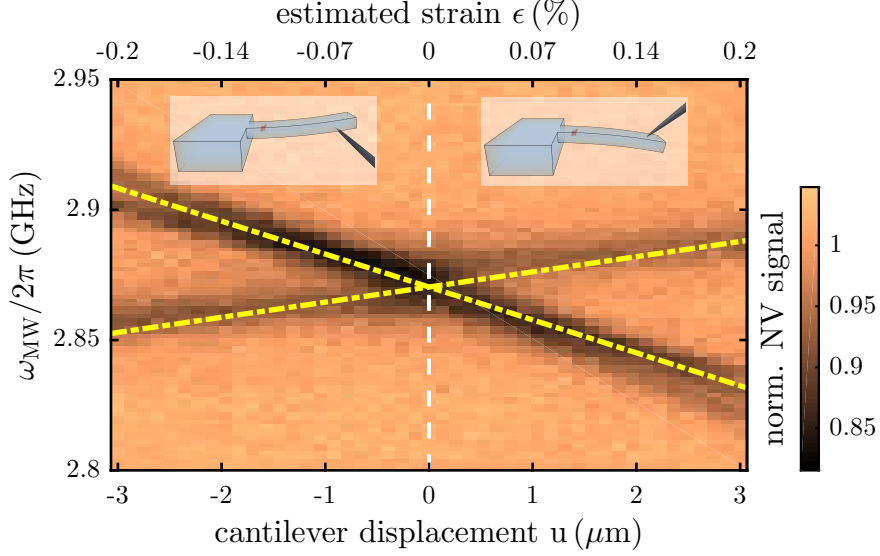


Figure A.1.: Strain-induced splitting of the $S=1$ ground state spin sublevels, monitored via CW ESR measurements, as a function of cantilever displacement u . Positive and negative u describe tensile and compressive strain at the NV's location. Yellow dashed lines represent a fit to (A.56), used to quantify strain coupling constants $d_{\perp,\parallel}^{\text{gs}}$.

as products of strain amplitudes and strain coupling constants $d_{\perp,\parallel}^{\text{gs}}$. The relative spin-sublevel shifts in the NV $S=1$ ground state are then given by (compare (2.34))

$$\Delta_{\pm} = d_{\parallel}^{\text{gs}} \epsilon_z \pm d_{\perp}^{\text{gs}} \sqrt{\epsilon_x^2 + \epsilon_y^2}. \quad (\text{A.56})$$

To quantify $d_{\perp,\parallel}^{\text{gs}}$ we applied variable degrees of tensile and compressive strain to an NV center located close to the clamping-point of a cantilever with $t = 1 \mu\text{m}$ and $l = 47 \mu\text{m}$ by controlled static bending.¹ We measured the effect of this strain on the NV by performing CW ESR measurements as a function of the displacement u (Fig. A.1). The zero-strain ESR line (white dashed line) splits with increasing cantilever displacement as a result of transverse strain. Additionally, a weak center-of-mass shift of the two resulting ESR lines is caused by longitudinal coupling. We fit the observed ESR line shifts to (A.56) (yellow dashed lines in Fig. A.1) and obtained strain-coupling constants

$$d_{\parallel} = (-6.2 \pm 0.5) \text{ GHz/strain} \quad (\text{A.57a})$$

$$d_{\perp} = (16.6 \pm 0.5) \text{ GHz/strain} \quad (\text{A.57b})$$

where errors denote 95 % confidence intervals of our fits.²

For the fit, we assumed that the induced strain-field is unidirectional (i.e. we not only neglected shear terms but also the Poisson effect) and points along the direction

¹Due to the chosen sign convention positive displacement u corresponds to the cantilever being bent downwards, i.e. along $-\mathbf{e}_z$, and creates tensile strain at the position of the NV.

²Similar values were reported by [42], where shear strain components were neglected as well but the Poisson effect was accounted for.

of the cantilever (i.e. along [110]). Near the clamping-point ($x = 0$) and close to the top surface ($z = t/2$) of our cantilever we find strain of amplitude (compare (2.69))

$$\epsilon_{[110]} = \frac{3}{2} \frac{t}{l^2} u = \alpha_\epsilon^{[110]} u \quad (\text{A.58})$$

with $\alpha_\epsilon^{[110]} = 6.8 \times 10^{-4} \mu\text{m}^{-1}$ as $t = 1 \mu\text{m}$ and $l = 47 \mu\text{m}$. For a [110] beam the four NV orientations NV1-4 separate into two families of NV centers, in the following referred to as NVA and NVB, which differ in their response to strain (see Tab.2.1). Family NVA includes NV1 and NV2 and is subject to transverse and longitudinal strain with $\epsilon_z = \sqrt{2/3}\epsilon_{[110]}$ and $\sqrt{\epsilon_x^2 + \epsilon_y^2} = 1/\sqrt{3}\epsilon_{[110]}$. In contrast, family NVB (representing NV orientations NV3 and NV4) experiences only transverse strain, hence ϵ_z vanishes and $\sqrt{\epsilon_x^2 + \epsilon_y^2} = \epsilon_{[110]}$. As the NV measured here clearly shows features of both strain components, we assigned it to family NVA and used the corresponding relations for fitting.

A.5.2. Characterizing spin-strain coupling - bending experiments

In Chap. 3 we performed cantilever bending experiments to extract the spin-stress and spin-strain coupling constants A_1, A_2, B, C and a_1, a_2, b, c , respectively. To that end we investigated three NV centers of family NVA, and three NV centers of family NVB. For each NV, we extracted level shifts $\Delta_{\parallel}^{\text{A,B}}$ and splittings $\Delta_{\perp}^{\text{A,B}}$ (see Fig. A.2) and averaging over all results finally yields mean values for stress-coupling parameters A_1, A_2, B, C . These can then be converted into strain-coupling parameters a_1, a_2, b, c via the relation (2.55). As one can clearly recognize, all three NVA NV centers reacted similarly to stress, i.e. $\Delta_{\parallel}^{\text{A}}$ and $\Delta_{\perp}^{\text{A}}$ were comparable, and we found

$$\bar{\Delta}_{\parallel}^{\text{A}} = (-10.9 \pm 2.4) \text{ MHz GPa} \quad (\text{A.59a})$$

$$\bar{\Delta}_{\perp}^{\text{A}} = (26.6 \pm 3.0) \text{ MHz GPa} \quad (\text{A.59b})$$

by averaging over the three individual results (the error bars denote 68% confidence intervals). In contrast, the two characterized NVs from family NVB showed a significant difference in their response to stress, and we found

$$\bar{\Delta}_{\parallel}^{\text{B}} = (-38.5 \pm 13.4) \text{ MHz GPa} \quad (\text{A.60a})$$

$$\bar{\Delta}_{\perp}^{\text{B}} = (-1.7 \pm 2.4) \text{ MHz GPa.} \quad (\text{A.60b})$$

The observed discrepancy in behavior is most likely caused by different environmental stress fields due to, for example, surface roughness or the proximity of cantilever edges. The significant uncertainties in family NVB result in the large error bars of coupling constants (see Chap. 3). Improving the statistics, i.e. increasing the number of measured NV centers, should dramatically reduce the uncertainty and thus strengthen our analysis.

A.6. Frequency modulation with external driving

At several occasions throughout the main text we make use of the concept of frequency modulation and describe the emerging sidebands with Bessel functions of the first kind and n -th order. Here we give a brief derivation based on [75, 188].

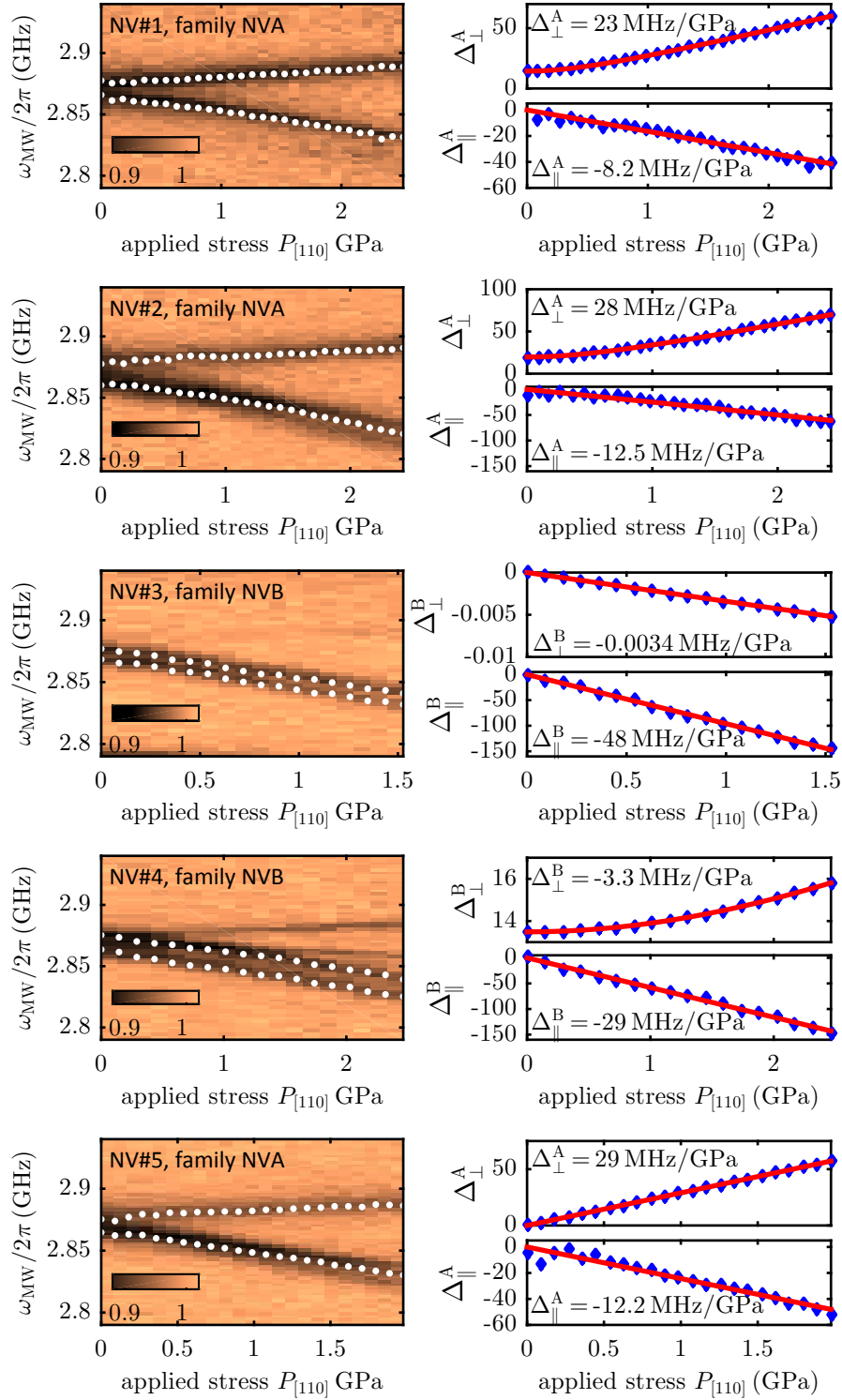


Figure A.2.: Reactions of different NV centers to stress induced by cantilever bending. While the three NVs from family NVA show comparable shifts and splittings, the two NVs from family NVB react quite differently to strain, causing large uncertainties in the stress-coupling constants (see text). $\Delta_{\parallel,\perp}^{A,B}$ are given in units of MHz/GPa.

Assume a carrier signal $x_c(t) = A_c \cos(\omega_c t)$ with amplitude A_c and angular frequency ω_c , whose frequency is modulated by a modulation signal x_m of arbitrary form. The resulting signal $y(t)$ is then given by

$$y(t) = A_c \cos\left(\int_0^t \omega(\tau) d\tau\right) \quad (\text{A.61})$$

where $\omega(\tau)$ describes the instantaneous frequency of the oscillator at time τ . One can show that

$$\begin{aligned} y(t) &= A_c \cos\left(\int_0^t (\omega_c + K_m x_m(\tau)) d\tau\right) \\ &= A_c \cos\left(\omega_c t + K_m \int_0^t x_m(\tau) d\tau\right) \end{aligned} \quad (\text{A.62})$$

where K_m converts the external modulation signal's amplitude into a frequency shift.

In our experiments we in general work with single-tone modulation signals and can thus assume $x_m(t) = A_m \cos(\omega_m t)$. Under this assumption we can then express $y(t)$ as

$$y(t) = A_c \cos\left(\omega_c t + \frac{K_m A_m}{\omega_m} \sin(\omega_m t)\right) \quad (\text{A.63})$$

where the quantity $m = K_m A_m / \omega_m$ is usually referred to as the modulation depth or index. The quantity $\omega_\Delta = K_m A_m$ denotes the maximum induced frequency shift. In the case of the NV center, this can for instance be $\omega_\Delta = \gamma_{\text{NV}} B_z$ for driving with a longitudinal AC magnetic field (see Sec. 2.3) or level shifts $\omega_\Delta = M_{\sigma,z}$ induced by AC stress (see Sec. 3.2.2).

Eq. (A.63) can be further simplified and expressed in terms of Bessel functions. The modulated signal becomes

$$y(t) = A_c \sum_{k=-\infty}^{\infty} J_k(m) \cos(\omega_c t + k\omega_m t) \quad (\text{A.64})$$

where $J_k(m)$ are Bessel functions of first kind and k -th order and denote the k -th sideband. The spectrum of our modulated signal thus contains the central carrier frequency as well as sidebands at frequencies $\omega_c \pm \omega_m, \omega_c \pm 2\omega_m, \omega_c \pm 3\omega_m, \dots$. For constant modulation index m , the amplitude of the appearing sidebands decreases as k increases (Fig. A.3).

A.7. Single phonon coupling strength and mechanical Rabi frequency

In the main text we often refer to longitudinal and transverse single phonon coupling strength $g_0^{\parallel,\perp}$. In the following we present the underlying motivation for this distinction.

We know that the stress-coupling Hamiltonian for the S=1 ground state is given by (see (3.4))

$$\hat{H}_{\text{gs}}^\sigma / h = M_{\sigma,z}^{\text{gs}} \hat{S}_z^2 + M_{\sigma,x}^{\text{gs}} (\hat{S}_y^2 - \hat{S}_x^2) + M_{\sigma,y}^{\text{gs}} (\hat{S}_x \hat{S}_y + \hat{S}_y \hat{S}_x) \quad (\text{A.65})$$

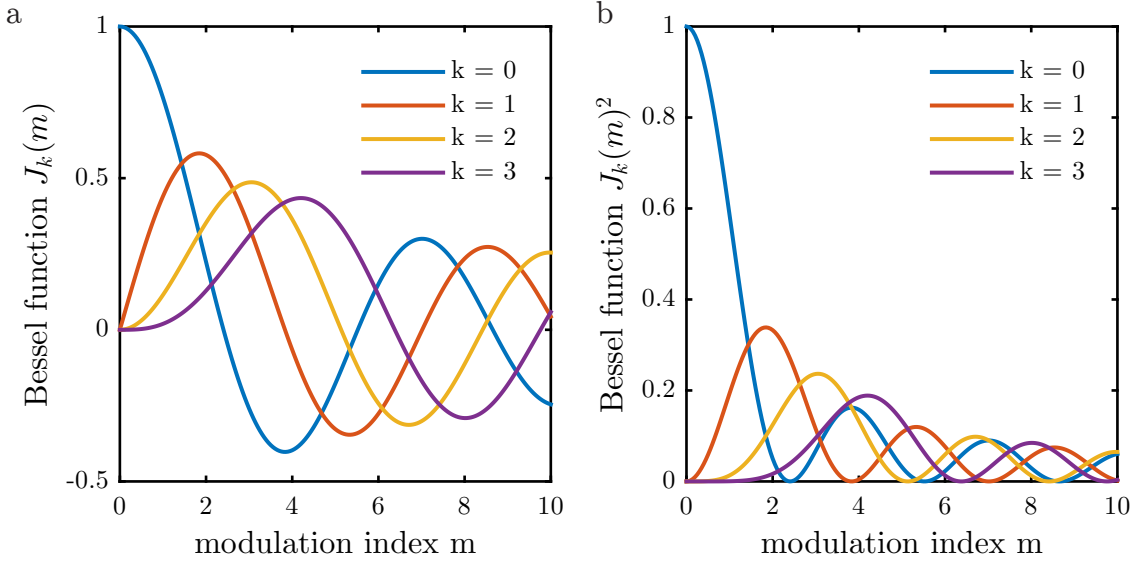


Figure A.3.: Bessel function $J_k(m)$ of k -th order and first kind as a function of modulation index m . a) $J_k(m)$. b) $J_k(m)^2$. With increasing modulation index higher order Bessel functions increase in amplitude and sidebands appear when a signal is frequency modulated.

where $M_{\sigma,i}^{\text{gs}}$ with $i = x, y, z$ denote the stress-induced level shifts. Using the relations $\hat{\mathbf{S}}_{\pm} = \hat{\mathbf{S}}_x \pm i\hat{\mathbf{S}}_y$ we can rewrite (A.65) and obtain

$$\hat{\mathbf{H}}_{\text{gs}}^{\sigma}/h = M_{\sigma,z}^{\text{gs}}\hat{\mathbf{S}}_z^2 - \frac{1}{2} \left[M_{\sigma,x}^{\text{gs}}(\hat{\mathbf{S}}_+^2 + \hat{\mathbf{S}}_-^2) + iM_{\sigma,y}^{\text{gs}}(\hat{\mathbf{S}}_+^2 - \hat{\mathbf{S}}_-^2) \right]. \quad (\text{A.66})$$

By introducing the transverse stress amplitude $M_{\sigma,\perp}^{\text{gs}} = \sqrt{(M_{\sigma,x}^{\text{gs}})^2 + (M_{\sigma,y}^{\text{gs}})^2}$ we can further simplify (A.66) and find

$$\hat{\mathbf{H}}_{\text{gs}}^{\sigma}/h = M_{\sigma,z}^{\text{gs}}\hat{\mathbf{S}}_z^2 - \frac{M_{\sigma,\perp}^{\text{gs}}}{2} (e^{i\varphi}\hat{\mathbf{S}}_+^2 + e^{-i\varphi}\hat{\mathbf{S}}_-^2) \quad (\text{A.67})$$

with $\tan \varphi = M_{\sigma,y}^{\text{gs}}/M_{\sigma,x}^{\text{gs}}$.

To define the corresponding single phonon coupling strengths $g_0^{\parallel,\perp}$ we introduce the position operator $\hat{x} = \Delta x_{\text{zpm}} (\hat{a} + \hat{a}^{\dagger})$ (see Subsec. 2.6.1) and find

$$\begin{aligned} \hat{\mathbf{H}}_{\text{gs}}^{\sigma}/h &= \underbrace{\alpha_z^{\sigma} \Delta x_{\text{zpm}}}_{g_0^{\parallel}/2\pi} (\hat{a} + \hat{a}^{\dagger}) \hat{\mathbf{S}}_z^2 - \underbrace{\frac{\alpha_{\perp}^{\sigma} \Delta x_{\text{zpm}}}{2}}_{g_0^{\perp}/2\pi} (\hat{a} + \hat{a}^{\dagger}) (e^{i\varphi}\hat{\mathbf{S}}_+^2 + e^{-i\varphi}\hat{\mathbf{S}}_-^2) \\ &= \frac{g_0^{\parallel}}{2\pi} (\hat{a} + \hat{a}^{\dagger}) \hat{\mathbf{S}}_z^2 - \frac{g_0^{\perp}}{2\pi} (\hat{a} + \hat{a}^{\dagger}) (e^{i\varphi}\hat{\mathbf{S}}_+^2 + e^{-i\varphi}\hat{\mathbf{S}}_-^2) \end{aligned} \quad (\text{A.68})$$

where $\alpha_{z,\perp}^{\sigma}$ describes the induced level shifts by longitudinal and transverse coupling. To illustrate the difference between g_0^{\parallel} and g_0^{\perp} , let us consider our typical experimental scenario where a shallow implanted NV center of family NVA is embedded in a cantilever aligned to the [110] direction. As seen in (3.7) and (3.9),

$$\alpha_z^{\sigma} = |A_1 + A_2|P_{\text{max}} = P_{\text{max}} \cdot 5.5 \text{ MHz/GPa} \quad (\text{A.69a})$$

$$\alpha_{\perp}^{\sigma} = |C - B|P_{\text{max}} = P_{\text{max}} \cdot 13.3 \text{ MHz/GPa} \quad (\text{A.69b})$$

with $P_{\max} = \frac{3}{2} \frac{t}{l^2} E$ denoting the introduced maximum stress per cantilever displacement. With the definitions for transverse and longitudinal coupling strength from above, and using the measured stress-spin coupling constants from (3.12), we can then write

$$g_0^{\parallel}/2\pi = \alpha_z^{\sigma} \Delta x_{\text{zpm}} = \Delta x_{\text{zpm}} P_{\max} \cdot 5.5 \text{ MHz/GPa} \quad (\text{A.70a})$$

$$g_0^{\perp}/2\pi = \frac{\alpha_{\perp}^{\sigma} \Delta x_{\text{zpm}}}{2} = \frac{\Delta x_{\text{zpm}}}{2} P_{\max} \cdot 13.3 \text{ MHz/GPa} \quad (\text{A.70b})$$

and thus find $g_0^{\parallel} \approx 0.83 g_0^{\perp}$ for NV centers of family NVA that are subject to stress along the [110] direction.

When working with AC stress we usually describe the stress-spin coupling in terms of the mechanical Rabi frequency $\Omega_m^{\parallel, \perp}$. To establish a connection to the coupling strengths $g_0^{\parallel, \perp}$ we describe the driven cantilever by a harmonic oscillator occupying a coherent state $|\alpha\rangle = e^{-|\alpha|^2/2} \sum_n \frac{\alpha^n}{\sqrt{n!}} |n\rangle$ with phonon number eigenstates $|n\rangle$ and dimensionless amplitude α , which we here assume to be real for simplicity. The time-dependent wave-function for the non-stationary state $|\alpha\rangle$ is then $|\alpha(t)\rangle = e^{-i\hat{H}_{\text{ho}}t/\hbar} |\alpha\rangle$, where \hat{H}_{ho} is the Hamiltonian of a harmonic oscillator, i.e. $\hat{H}_{\text{ho}} = \frac{\hat{p}^2}{2m_{\text{eff}}} + \frac{m_{\text{eff}}\omega_m^2}{2} \hat{x}^2$, with position and momentum operators \hat{p} and \hat{x} , respectively. The expectation value for the excitation amplitude of the oscillator in a coherent state is $x(t) = \langle \alpha(t) | \hat{x} | \alpha(t) \rangle = 2\Delta x_{\text{zpm}} |\alpha| \cos(\omega_m t) \equiv \tilde{u}_{\max} \cos(\omega_m t)$, where we defined the oscillator's peak amplitude $\tilde{u}_{\max} = 2\Delta x_{\text{zpm}} |\alpha|$. Correspondingly, the expectation value for $\hat{H}_{\text{gs}}^{\sigma}$ from (A.68) yields

$$\begin{aligned} \langle \alpha(t) | \hat{H}_{\text{gs}}^{\sigma} | \alpha(t) \rangle / \hbar &= g_0^{\parallel} \frac{x(t)}{\Delta x_{\text{zpm}}} \hat{S}_z^2 - g_0^{\perp} \frac{x(t)}{\Delta x_{\text{zpm}}} (e^{i\varphi} \hat{S}_+^2 + e^{-i\varphi} \hat{S}_-^2) \\ &= \frac{g_0^{\parallel} \tilde{u}_{\max}}{\Delta x_{\text{zpm}}} \cos(\omega_m t) \hat{S}_z^2 - \frac{g_0^{\perp} \tilde{u}_{\max}}{\Delta x_{\text{zpm}}} \cos(\omega_m t) (e^{i\varphi} \hat{S}_+^2 + e^{-i\varphi} \hat{S}_-^2) \\ &= \Omega_m^{\parallel} \cos(\omega_m t) \hat{S}_z^2 - \Omega_m^{\perp} \cos(\omega_m t) (e^{i\varphi} \hat{S}_+^2 + e^{-i\varphi} \hat{S}_-^2) \end{aligned} \quad (\text{A.71})$$

with longitudinal and transverse mechanical Rabi frequencies $\Omega_m^{\parallel, \perp} = g_0^{\parallel, \perp} \frac{\tilde{u}_{\max}}{\Delta x_{\text{zpm}}}$.

A.8. Strong mechanical driving: crossings and anti-crossings

To explain the series of crossings and anti-crossings we observed in our strong mechanical driving experiments (see Chap. 5), we essentially follow the treatment of dressed atoms in [133]. We consider a two-level system spanned by the sublevels $|-1, m_I\rangle$ and $|+1, m_I\rangle$ that are separated by the energy $\omega_{1,-1}^{m_I}$. In the presence of our strain field $|N\rangle$, where N denotes the number of phonons with energy $\hbar\omega_m$ in the considered mode, the eigenstates $|\pm 1, N\rangle$ of our system have energies

$$E_{\pm 1, N} = \pm \hbar \frac{\omega_{1,-1}^{m_I}}{2} + N \hbar \omega_m \quad (\text{A.72})$$

if two-level system and strain field do not interact (note that we omitted the nuclear spin quantum number for clarity). The energy diagram, as a function of splitting

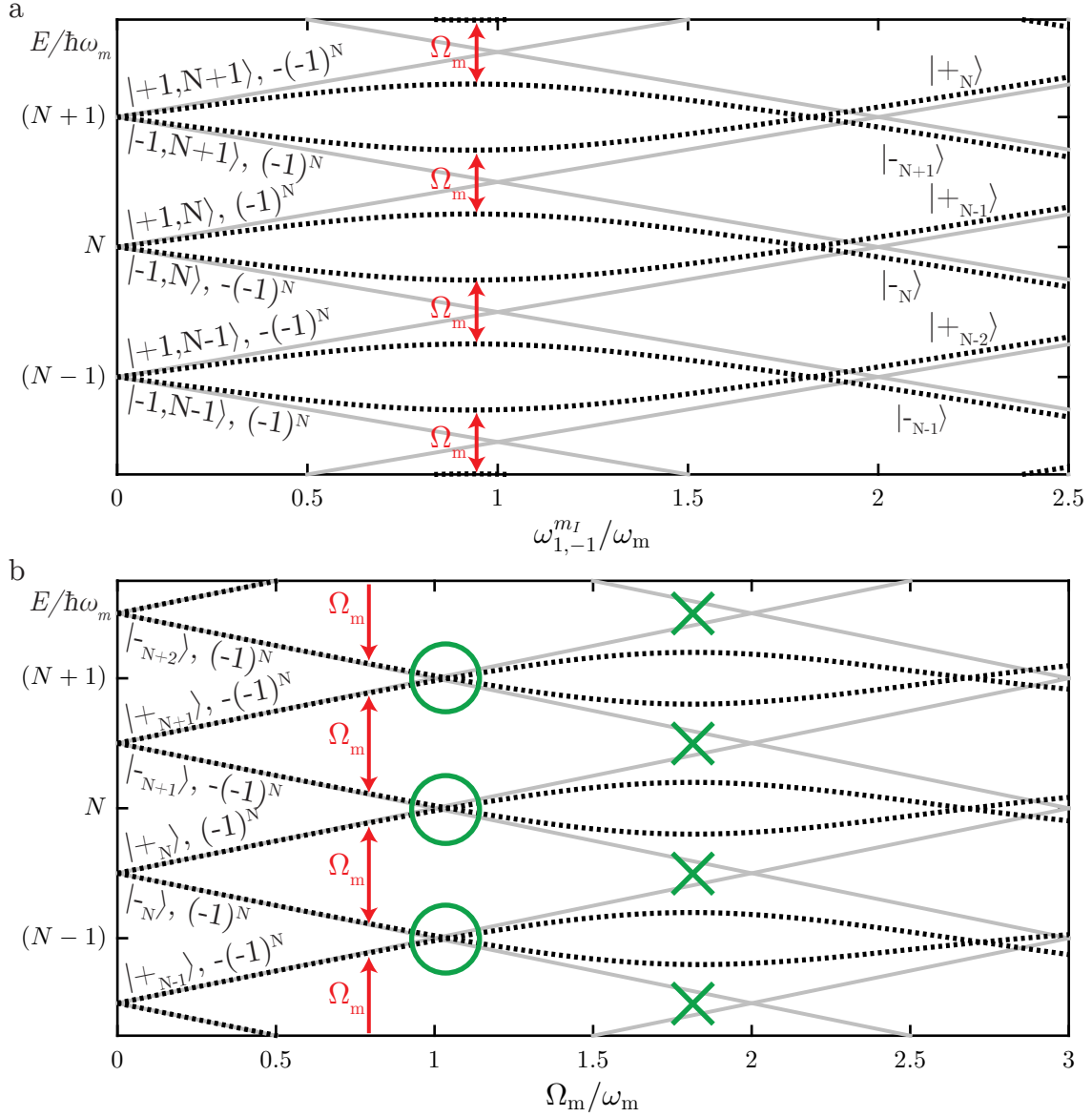


Figure A.4.: Explanation of observed crossings and anti-crossings in our strong driving experiments. a) Without strain coupling, the energy diagram of $|\pm 1, N\rangle$ features an infinite number of eigenstates whose energy splittings evolve linearly with $\omega_{1,-1}^{m_I}$ (silver lines). Strain coupling introduces anti-crossings of previously uncoupled states with equal $\eta(m_s, N)$. b) In our strong driving experiment, we apply a magnetic field B_z to set $\omega_{1,-1}^{m_I} = \omega_m$ and ramp the mechanical driving strength Ω_m . From the rotating wave approximation we expect the dressed state energies to evolve linearly with coupling strength (indicated by the silver lines). However, for $\Omega_m > \omega_m$ the rotating wave approximation breaks down and we observe anti-crossings (crossings) at $\Omega_m = q\omega_m$ with q an even (odd) integer of dressed states with equal $\tilde{\eta}(\tilde{m}_s, \tilde{N})$. In both panels, emerging eigenstates are labeled with electronic spin quantum number, phonon number, and the corresponding value for $\eta(m_s, N)$ (in a) and $\tilde{\eta}(\tilde{m}_s, \tilde{N})$ (in b; see text for further explanation).

$\omega_{1,-1}^{m_I}$ between the two spin sublevels, appears as an infinite number of straight lines with slope $\pm 1/2$ and ordinates $N\hbar\omega_m$ at $\omega_{1,-1}^{m_I} = 0$ (see silver lines in Fig. A.4a).

The interaction of our transverse strain field with the two-level system is described by the Hamiltonian (see (5.1) from the main text)

$$\hat{H}_{\text{gs}}^\perp/\hbar = -g_0^\perp (\hat{a} + \hat{a}^\dagger) \left(\hat{S}_+^2 + \hat{S}_-^2 \right) \quad (\text{A.73})$$

and changes N by ± 1 and m_s by ± 2 . For $\omega_{1,-1}^{m_I} = \omega_m$ we therefore observe anti-crossings of the involved states' energies, for example $|-1, N\rangle$ and $|+1, N+1\rangle$, as they differ by $\Delta N = 1$ and $\Delta m_s = 2$ (see black dotted lines in Fig. A.4a). These lines thus represent the emerging dressed states

$$|+_N\rangle = \sin\theta |-1, N+1\rangle + \cos\theta |+1, N\rangle \quad (\text{A.74a})$$

$$|-_N\rangle = \cos\theta |-1, N+1\rangle - \sin\theta |+1, N\rangle \quad (\text{A.74b})$$

with $\tan(2\theta) = -\Omega_m / (\omega_m - \omega_{1,-1}^{m_I})$. Note that for resonant driving with $\omega_m = \omega_{1,-1}^{m_I}$, $\theta = \pi/4$ and $|\pm_N\rangle = 1/\sqrt{2}(|-1, N+1\rangle + |+1, N\rangle)$. However when we further increase the splitting of our two-level system such that for example $\omega_{1,-1}^{m_I} = 2\omega_m$ the dressed states cross, indicating no coupling. This is simply because the involved states, for example $|-_N\rangle \approx |-1, N+1\rangle$ and $|+_N\rangle \approx |+1, N-1\rangle$, differ by two phonons.

To check whether states cross or anti-cross it is convenient to introduce the quantum number

$$\eta(m_s, N) = (-1)^{m_s/2+N-1/2} \quad (\text{A.75})$$

defined in analogy to [133]. $\eta(m_s, N)$ takes values of -1 and $+1$, i.e. it separates the existing states into two subspaces. Only states from the same subspace, i.e. with equal $\eta(m_s, N)$, anti-cross while states with unequal $\eta(m_s, N)$ cross. Note that m_s and N are defined with respect to the uncoupled eigenstates $|m_s, N\rangle$. To illustrate the role of $\eta(m_s, N)$, we first consider the states $|+1, N\rangle$ with $\eta(1, N) = (-1)^N$ and $|-1, N+1\rangle$ with $\eta(-1, N+1) = (-1)^N$. As the two states belong to the same subspace with respect to η , transverse strain should induce a non-zero coupling between them. This statement can be checked by calculating the coupling matrix element $\langle -1, N+1 | \hat{H}_{\text{gs}}^\perp | +1, N \rangle = -\hbar g_0^\perp$, which is non-zero. In contrast, if two states differ in η , such as $|+1, N-1\rangle$ with $\eta(1, N-1) = -(-1)^N$ and $|-1, N+1\rangle$ with $\eta(-1, N+1) = (-1)^N$, no coupling between these states exists.

To demonstrate strong mechanical spin driving in our experiment, we applied a magnetic field B_z such that $\omega_{1,-1}^{m_I} = \omega_m$ and increased the mechanical Rabi frequency Ω_m . From the rotating wave approximation we expect the emerging dressed state energies to increase and decrease linearly with Ω_m (silver lines in Fig. A.4b) and specifically no interactions between the dressed states to occur. However, for $\Omega_m > \omega_m$, the driving strength Ω_m exceeds the initial spin-splitting $\omega_{1,-1}^{m_I}$ and the rotating wave approximation breaks down. As result, we observe a series of anti-crossings and crossings. Anti-crossings (crossings) appear at $\Omega_m = q\omega_m$ with q an even (odd) integer (see green circles and crosses in Fig. A.4b). In analogy to what is presented above, we can check whether dressed states cross or anti-cross by introducing the quantum number $\tilde{\eta}(\tilde{m}_s, \tilde{N})$ with

$$\tilde{\eta}(\tilde{m}_s, \tilde{N}) = (-1)^{\tilde{m}_s + \tilde{N} - 1} \quad (\text{A.76})$$

where \tilde{m}_s and \tilde{N} are defined with respect to the dressed states $|\pm_N\rangle$. For example, $|-_N\rangle$ with $\tilde{m}_s = -1$ and $\tilde{N} = N$ is characterized by $\tilde{\eta}(\tilde{m}_s, \tilde{N}) = (-1)^N$. As demonstrated above, one can verify that only dressed states with equal $\tilde{\eta}(\tilde{m}_s, \tilde{N})$ couple and form avoided crossings.

A second look at Fig. A.4 reveals that crossings and anti-crossings occur slightly shifted from the predicted value of $\omega_{1,-1}^{m_I}$ and ω_m , respectively. This shift is called the Bloch-Siegert shift [146] and is related to the counter rotating terms of our coupling Hamiltonian. In the rotating wave approximation, these terms are neglected and the Bloch-Siegert shift is not accounted for. If one however includes the counter rotating terms in the calculation, one finds that they effectively dress the two-level system and slightly alter its energy splitting. As a consequence the (anti-)crossings are shifted. In [80], L. Allen and J.H. Eberly give a detailed derivation of the Bloch-Siegert shift and the interested reader is referred to their book for further information.

A.9. Phase-dependent spin dynamics

A.9.1. Closed-contour Hamiltonian and time evolution

In this section we derive Hamiltonian (6.1) from Chap. 6. The NV's S=1 ground state, driven by two MW fields and one strain field, is described by the Hamiltonian

$$\hat{H}_{cc}^{\text{lf}}/\hbar = \begin{pmatrix} \omega_{|-1\rangle} & \Omega_1 \cos(\omega_1 t + \phi_1) & \Omega_3 \cos(\omega_3 t + \phi_3) \\ \Omega_1 \cos(\omega_1 t + \phi_1) & \omega_{|0\rangle} & \Omega_2 \cos(\omega_2 t + \phi_2) \\ \Omega_3 \cos(\omega_3 t + \phi_3) & \Omega_2 \cos(\omega_2 t + \phi_2) & \omega_{|+1\rangle} \end{pmatrix} \quad (\text{A.77})$$

written in the $\{|-1\rangle, |0\rangle, |+1\rangle\}$ basis and expressed in the lab frame. Ω_k , ω_k and ϕ_k with $k = 1, 2, 3$ denote driving field amplitudes, frequencies and phases, respectively. $\hbar\omega_{|i\rangle}$ with $i = 0, \pm 1$ are the energies of the three spin sublevels.

We transform \hat{H}_{cc}^{lf} into the interaction picture by performing the unitary transformation [117, 186]

$$\hat{H}_{cc}^{\text{rf}} = \hat{T} \hat{H}_{cc}^{\text{lf}} \hat{T}^{-1} + i \frac{d\hat{T}}{dt} \hat{T}^{-1} \quad (\text{A.78})$$

with the unitary rotation operator

$$\hat{T} = e^{i(\omega_1 t + \phi_1)|-1\rangle\langle -1|} \cdot e^{i(\omega_2 t + \phi_2)|+1\rangle\langle +1|}. \quad (\text{A.79})$$

By choosing $\hbar\omega_{|0\rangle} = 0$ and neglecting fast rotating terms, we find

$$\hat{H}_{cc}^{\text{rf}}/\hbar = \frac{1}{2} \begin{pmatrix} 2(\omega_{|-1\rangle} - \omega_1) & \Omega_1 & \Omega_3 e^{i(\Phi + \Delta t)} \\ \Omega_1 & 0 & \Omega_2 \\ \Omega_3 e^{-i(\Phi + \Delta t)} & \Omega_2 & 2(\omega_{|+1\rangle} - \omega_2) \end{pmatrix} \quad (\text{A.80})$$

where the global phase $\Phi = \phi_1 + \phi_3 - \phi_2$ and $\Delta = \omega_1 + \omega_3 - \omega_2$. It becomes clear that \hat{H}_{cc}^{rf} is time-independent only for $\Delta = 0$. Consequently, for $\Delta = 0$, equal driving strengths $\Omega_1 = \Omega_2 = \Omega_3 = \Omega$, and detunings $\delta_1 = \omega_{|-1\rangle} - \omega_1$ and $\delta_2 = \omega_{|+1\rangle} - \omega_2$, we obtain

$$\hat{H}_{cc}^{\text{rf}}/\hbar = \frac{1}{2} \begin{pmatrix} 2\delta_1 & \Omega & \Omega e^{i\Phi} \\ \Omega & 0 & \Omega \\ \Omega e^{-i\Phi} & \Omega & 2\delta_2 \end{pmatrix} \quad (\text{A.81})$$

as given in (6.1) of Chap. 6. The corresponding eigenstates and -energies for resonant driving are then found to be

$$|\Psi_k\rangle = \frac{1}{\sqrt{3}} \left(e^{i\frac{\Phi+k4\pi}{3}}, 1, e^{-i\frac{\Phi-k2\pi}{3}} \right) \quad (\text{A.82})$$

$$E_k/\hbar = \Omega \cos\left(\frac{\Phi - k2\pi}{3}\right) \quad (\text{A.83})$$

where $k \in \{-1, 0, 1\}$.

In Chap. 6, we study the time evolution of the population $P_{|0\rangle}(\tau)$ in spin sublevel $|0\rangle$. In the corresponding experiments we initialize the NV in $|0\rangle$ with a green laser pulse. The following abrupt onset of the three driving fields creates the closed-contour interaction and we express

$$|0\rangle = |\Psi(\tau=0)\rangle = (|\Psi_{-1}\rangle + |\Psi_0\rangle + |\Psi_{+1}\rangle)/\sqrt{3} \quad (\text{A.84})$$

as a linear combination of the system's eigenstates $|\Psi_k\rangle$. After a certain evolution time τ the system is in the state

$$\begin{aligned} |\Psi(\tau)\rangle &= e^{-i\hat{\mathbf{H}}_{cc}^{\text{rf}}\tau/\hbar} |\Psi(\tau=0)\rangle \\ &= (e^{-iE_0\tau/\hbar} |\Psi_0\rangle + e^{-iE_{+1}\tau/\hbar} |\Psi_{+1}\rangle + e^{-iE_{-1}\tau/\hbar} |\Psi_{-1}\rangle) / \sqrt{3} \end{aligned} \quad (\text{A.85})$$

where $\hat{\mathbf{U}} = e^{-i\hat{\mathbf{H}}_{cc}^{\text{rf}}\tau/\hbar}$ is the unitary time evolution operator. The final green pulse projects $|\Psi(\tau)\rangle$ back on $|0\rangle$ and we determine

$$\begin{aligned} P_{|0\rangle}(\tau) &= |\langle 0|\Psi(\tau)\rangle|^2 \\ &= \frac{1}{3} + \frac{2}{9} [\cos(2\pi\Delta_{-1,0}\tau) + \cos(2\pi\Delta_{+1,0}\tau) + \cos(2\pi\Delta_{+1,-1}\tau)] \end{aligned} \quad (\text{A.86})$$

with $\Delta_{+1,-1} = (E_{+1} - E_{-1})/\hbar$, $\Delta_{-1,0} = (E_{-1} - E_0)/\hbar$ and $\Delta_{+1,0} = (E_{+1} - E_0)/\hbar$. $P_{|0\rangle}(\tau)$ therefore exhibits beat frequencies due to the presence of three frequency components $\Delta_{i,j}$ that correspond to the differences of eigenenergies E_k . At $\Phi = 0, \pm\pi$,

$$P_{|0\rangle}^{0,\pm\pi}(\tau) = \frac{1}{9} \left[5 + 4 \cos\left(\frac{3\Omega}{2}\tau\right) \right] \quad (\text{A.87})$$

and spin population oscillates between $|0\rangle$ and an equal superposition of $|\pm 1\rangle$ at a period $T_{0,\pm\pi} = 4\pi/3\Omega$. Eq. (A.87) also demonstrates that $P_{|0\rangle}^{0,\pm\pi}(\tau) \neq 0$ for all times τ . At $\Phi = \pm\pi/2$, however,

$$P_{|0\rangle}^{\pm\pi/2}(\tau) = \frac{1}{9} \left[3 + 4 \cos\left(\frac{\sqrt{3}\Omega}{2}\tau\right) + 2 \cos(\sqrt{3}\Omega\tau) \right] \quad (\text{A.88})$$

and $P_{|0\rangle}^{\pm\pi/2}(\tau)$ is maximized every $T_{\pm\pi/2} = 4\pi/\sqrt{3}\Omega$ (the values for $T_{\pm\pi/2}$ and $T_{0,\pm\pi}$ are stated in the main text of Chap. 6).

If we however initialize the system at $\tau = 0$ not in a superposition of $|\Psi_k\rangle$, but in a single eigenstate (for example $|\Psi_{+1}\rangle$ at $\Phi = +\pi/2$), our system will be in the state

$$\begin{aligned} |\Psi(\tau)\rangle &= e^{-i\hat{\mathbf{H}}_{cc}^{\text{rf}}\tau/\hbar} |\Psi(0)\rangle \\ &= e^{-iE_k\tau/\hbar} |\Psi_k\rangle \end{aligned} \quad (\text{A.89})$$

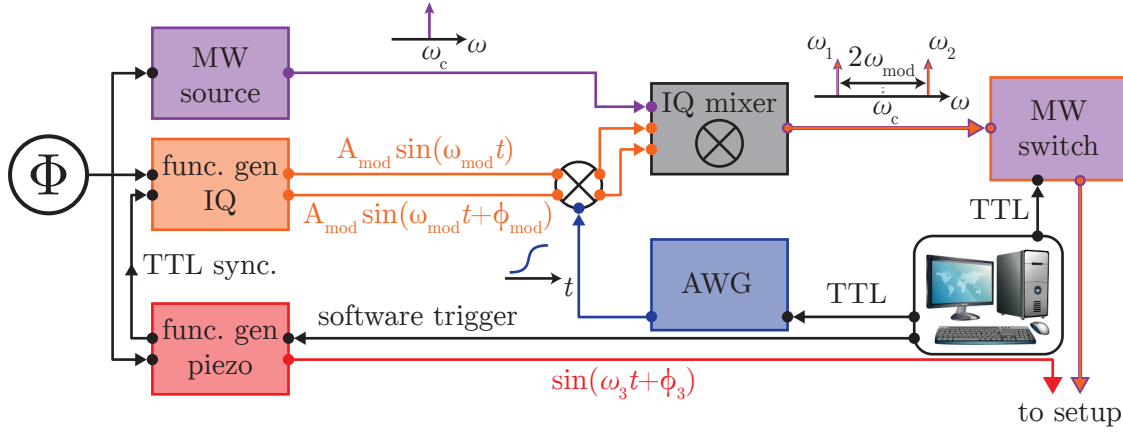


Figure A.5.: Creation of driving fields for closed-contour interaction. The two MW tones with frequencies $\omega_{1,2} = \omega_c \pm \omega_{\text{mod}}$ are created through frequency modulating a carrier signal of frequency ω_c at frequency $\omega_{\text{mod}} = \omega_3/2$. Phase-locking of the three driving fields is achieved via pulsed output synchronization and locking of MW source, IQ and piezo function generators to the same 10 MHz reference signal. An arbitrary waveform generator is used to modify the amplitude of our MW amplitudes for adiabatic state preparation.

after time τ and the measured NV emission

$$P_{|0\rangle}(\tau) = |\langle 0 | \Psi(\tau) \rangle|^2 = \frac{1}{3} \quad (\text{A.90})$$

is time-independent. The absence of oscillation fringes in $P_{|0\rangle}(\tau)$ thus serves as a measure to determine the state preparation fidelity.

A.9.2. Creation of phase-locked driving fields

We create the two MW tones used to drive the $|0\rangle \leftrightarrow |\pm 1\rangle$ transitions by frequency modulating a carrier signal S_c at frequency ω_c and amplitude A_c with two time-dependent modulation signals

$$S_{\text{mod,I}}(t) = A_{\text{mod}} \sin(\omega_{\text{mod}} t + \phi_{\text{mod}}) \quad (\text{A.91})$$

and

$$S_{\text{mod,Q}}(t) = A_{\text{mod}} \sin(\omega_{\text{mod}} t) \quad (\text{A.92})$$

of equal, but constant amplitudes A_{mod} . These signals are mixed to the carrier signal as I and Q modulation inputs, and we obtain the output signal

$$\begin{aligned} S_{\text{out}}(t) &= S_{\text{mod,I}}(t) \text{Re}(S_c) + S_{\text{mod,Q}}(t) \text{Im}(S_c) \\ &= A_c A_{\text{mod}} \left[\sin\left(\frac{\phi_{\text{mod}} - \pi/2}{2}\right) \cdot \cos\left((\omega_c + \omega_{\text{mod}})t + \frac{\pi/2 + \phi_{\text{mod}}}{2}\right) \right] \\ &\quad + A_c A_{\text{mod}} \left[\sin\left(\frac{\phi_{\text{mod}} + \pi/2}{2}\right) \cdot \cos\left((\omega_c - \omega_{\text{mod}})t + \frac{\pi/2 - \phi_{\text{mod}}}{2}\right) \right], \end{aligned} \quad (\text{A.93})$$

which consists of two MW tones separated by $2\omega_{\text{mod}}$ and symmetrically located around ω_c . The relative phase ϕ_{mod} of the two modulation signals allows for modifying the amplitude of the two MW tones. This is usually necessary to establish the condition $\Omega_1 = \Omega_2$, as our MW antenna does not deliver a fully linearly polarized MW field to the NV center. For our adiabatic state preparation experiments we additionally employ an arbitrary waveform generator (Tektronix, AWG5014C) and a homebuilt multiplier to modify the amplitude of our MW driving tones, i.e. we convert $A_{\text{mod}} \rightarrow A_{\text{mod}}(t)$.

As demonstrated above, we can only define a time-independent global phase Φ if the closed-contour condition $\omega_1 + \omega_3 = \omega_2$ is fulfilled. To ensure that this is always the case we choose $\omega_c/2\pi = D_{\text{gs}}$ and $\omega_{\text{mod}} = \omega_3/2$ with ω_3 being the eigenfrequency of our mechanical resonator. The global phase $\Phi = \phi_1 + \phi_3 - \phi_2$ becomes

$$\Phi = \phi_3 - (\phi_{\text{mod}} + \pi) \quad (\text{A.94})$$

under such conditions and for $0 \leq \phi_{\text{mod}} < \pi/2$. It can therefore be controlled by changing the individual phase ϕ_3 of the sinusoidal signal that drives the mechanical actuation of our diamond resonator.

To create the phase-locked driving fields experimentally, we connect the MW generator (Stanford Research Systems, SRS384), the function generator driving the piezo for mechanical actuation (Keysight, 33522A) and the function generator that supplies the IQ modulation signals (Keysight, 33622B) to the same 10 MHz reference signal. To set the global phase to a reproducible value, the output of the piezo function generator is triggered via a software command. Upon receiving the software trigger, it emits another trigger pulse which starts the output of our IQ modulation function generator (Fig. A.5). During our experiment mechanical actuation of our resonator is always active and MW pulses are created by employing a MW switch (MiniCircuits, ZASWA-2-50DR+) with a rise-time of 2 ns, controlled via digital pulses from our fast pulse generator card.

A.9.3. Analysis of environmental noise sources

A.9.3.1. Overview of existing noise sources

Modeling the observed spin dynamics under closed-contour interaction and the dependence of Rabi decay time T_{decay} on driving phase Φ is significantly affected by the presence of several noise sources in our experiment. Most importantly, our measurements are influenced by fluctuations in

- the environmental magnetic field, caused for example by nearby nuclear ^{14}N or ^{13}C spins and characterized by the NV's inhomogeneous coherence time T_2^*
- the amplitudes of our MW driving fields $\Omega_{1,2}$ (in the following referred to as Ω_{MW}), caused by technical noise in the MW circuit
- the AC strain driving strength Ω_3 (labeled with Ω_{m}), originating from technical noise in the piezo driving signal
- the zero-field splitting D_{gs} , caused by variations in temperature or environmental strain or electric fields.

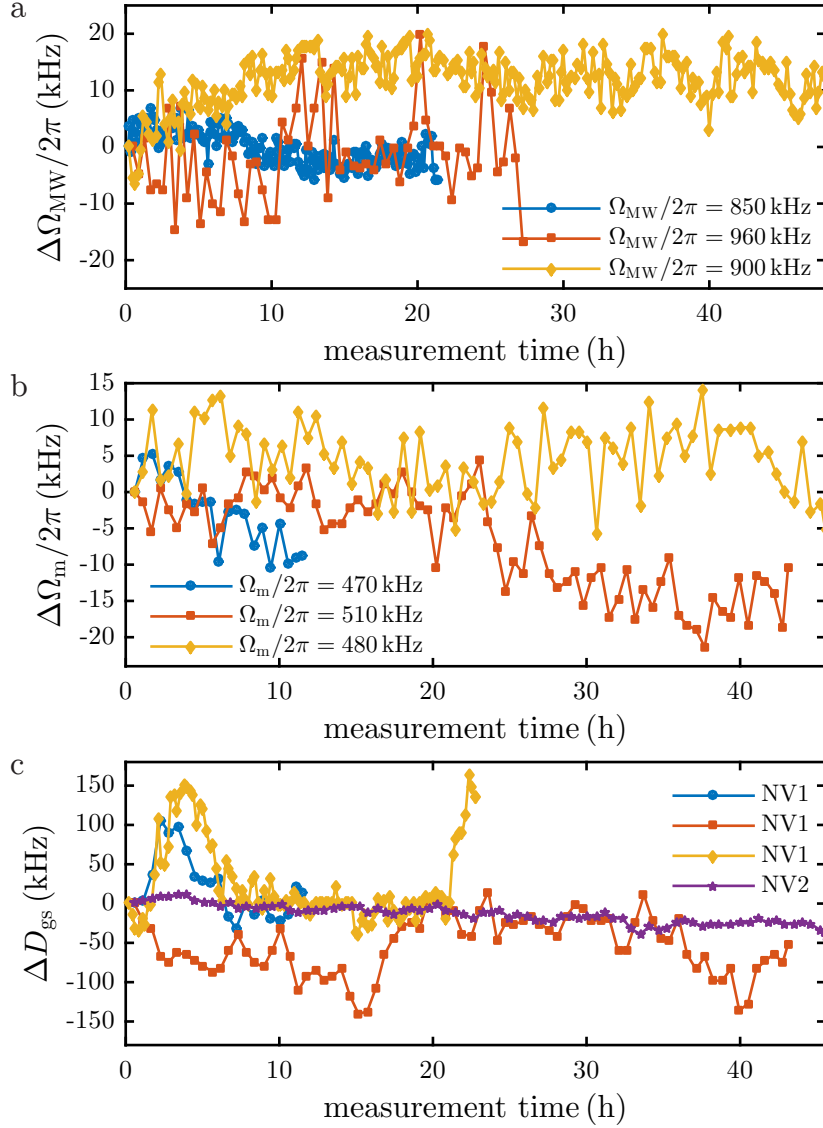


Figure A.6.: Existing fluctuations in our closed-contour interaction scheme. a) Typical fluctuations in our MW driving fields, measured for three different driving strengths $\Omega_{\text{MW}}/2\pi = \{850, 900, 960\}$ kHz (blue, yellow and red curve, respectively) on NVA by performing Rabi oscillation measurements on the $|0\rangle \leftrightarrow |-1\rangle$ transition. b) Typical fluctuations in our AC strain field, measured for three different driving strengths $\Omega_{\text{m}}/2\pi = \{470, 480, 510\}$ kHz (blue, yellow and red curve, respectively) on NVA via the Autler-Townes splitting of the $|+1, +1\rangle$ hyperfine level. c) Fluctuations of the zero-field splitting D_{gs} of different NV centers (three measurements on NVA: blue, yellow and red curve; one measurement on NVB, purple curve) used throughout our quantum interference measurements.

Other noise sources, for example frequency noise of the driving fields, are neglected in the following as we could not find any experimental evidence for their relevance.

To characterize the existing fluctuations in driving field amplitudes and zero-field splitting we performed long-time measurements, using the NV center as a probe (Fig. A.6). Low frequency drifts in Ω_{MW} were analyzed by performing Rabi oscillation measurements on a single hyperfine transition. Similarly, slow fluctuations in Ω_{m} and D_{gs} were investigated via the amplitude of strain-induced Autler-Townes splittings (compare Chap. 5) and ESR transition frequencies, respectively. We found relative driving amplitude fluctuations of $\sigma_{\text{MW}}/\Omega_{\text{MW}} = 0.5\%$ and $\sigma_{\text{m}}/\Omega_{\text{m}} = 0.7\%$ within a bandwidth of ≈ 2 mHz, with σ being the corresponding standard deviations, assuming Gaussian distributions. Additionally, these fluctuations are accompanied by even slower amplitude drifts of $\delta'_{\Omega_{\text{m}}}/\Omega_{\text{m}} \approx \pm 1\%$ and $\delta'_{\Omega_{\text{MW}}}/\Omega_{\text{MW}} \approx \pm 1.5\%$ for strain and MW driving, respectively, which happen on timescales of several hours. In contrast, changes in the zero-field splitting $\delta_{D_{\text{gs}}}/2\pi$ are characterized solely by slow drifts, with drift amplitudes varying between a few and several tens of kHz. The inhomogeneous coherence time T_2^* was measured as explained in Chap. 4 and 5. The data presented in Chap. 6 was taken on an NV with $T_2^* = (2.1 \pm 0.1) \mu\text{s}$. Magnetic noise is thus characterized by a Gaussian distribution with width $\sigma_{T_2^*}/2\pi = 1/\sqrt{2}\pi T_2^* = 107$ kHz [134] and is the strongest noise source in our experimental setting.

In our experiments presented in Chap. 6, we worked with $\Omega_{\text{MW}}/2\pi = \Omega_{\text{m}}/2\pi = 500$ kHz. Absolute driving field fluctuations $\delta_{\Omega_{\text{MW}}}$ and $\delta_{\Omega_{\text{m}}}$, characterized by standard deviations $\sigma_{\text{MW}}/2\pi = 2.5$ kHz and $\sigma_{\text{m}}/2\pi = 3.5$ kHz, as well as slow amplitude drifts $\delta'_{\Omega_{\text{m}}}/2\pi \approx \pm 5$ kHz and $\delta'_{\Omega_{\text{MW}}}/2\pi \approx \pm 7.5$ kHz, accompany fluctuations in the Zeeman splitting ($\sigma_{T_2^*}/2\pi = 107$ kHz) and zero-field splitting ($\delta_{D_{\text{gs}}}/2\pi \lesssim 100$ kHz). In our simulations, we neglect slow driving field amplitude fluctuations $\delta'_{\Omega_{\text{MW}}}$ and $\delta'_{\Omega_{\text{m}}}$ when modeling the influence of existing noise sources for reasons of simplicity, but consider faster driving amplitude fluctuations $\delta_{\Omega_{\text{MW}}}$ and $\delta_{\Omega_{\text{m}}}$.

A.9.3.2. Modeling existing noise sources

To simulate our experimental results from Chap. 6, i.e. the influence of noise on the observed spin dynamics, we solve the time-dependent Schrödinger equation

$$i\hbar \frac{d}{dt} |\Psi(\tau)\rangle = \hat{\mathbf{H}}_{\text{cc}}^{\text{rf}}(\Phi) |\Psi(\tau)\rangle \quad (\text{A.95})$$

for $|\Psi(\tau = 0)\rangle = |0\rangle = (|\Psi_{-1}\rangle + |\Psi_0\rangle + |\Psi_{+1}\rangle)/\sqrt{3}$ (see (A.84)) and for varying Φ , which we sample at n_{phs} points. This approach not only allows modeling the time evolution of the NV spin populations $P_{|m_s\rangle}(\tau) = |\langle m_s | \Psi(\tau) \rangle|^2$ with $m_s = 0, \pm 1$ and their dependence on global phase Φ (see Fig. 6.2 in Chap. 6). By Fourier-transforming $P_{|0\rangle}(\tau)$, we can also compare the modeled spin precession frequency spectrum with our measurements (Fig. 6.3). Fitting $P_{|0\rangle}(\tau)$ with a sum of three exponentially decaying sinusoids (see (6.7)) finally yields a modeled prediction for the phase-dependence of Rabi decay times T_{decay} (Fig. 6.4).

To include driving field fluctuations in our simulations, we set

$$\Omega_{1,2} = \Omega + \delta_{\Omega_{\text{MW}}} \quad (\text{A.96a})$$

$$\Omega_3 = \Omega + \delta_{\Omega_{\text{m}}} \quad (\text{A.96b})$$

where $\Omega/2\pi = 500$ kHz denotes the applied Rabi frequency and $\delta_{\Omega_{\text{MW}}}$ and $\delta_{\Omega_{\text{m}}}$ describe Gaussian fluctuations, taken from a normal distribution with zero mean and standard deviations $\sigma_{\text{MW}}/2\pi = 2.5$ kHz and $\sigma_{\text{m}}/2\pi = 3.5$ kHz, respectively. Magnetic and zero-field splitting fluctuations are included by setting

$$\delta_1 = \delta_{D_{\text{gs}}} + \delta_{T_2^*} \quad (\text{A.97a})$$

$$\delta_2 = \delta_{D_{\text{gs}}} - \delta_{T_2^*} \quad (\text{A.97b})$$

in $\hat{\mathbf{H}}_{\text{cc}}^{\text{rf}}$. Variations $\delta_{D_{\text{gs}}}$ in D_{gs} appear as simultaneous shifts of detunings $\delta_{1,2}$ while magnetic fluctuations $\delta_{T_2^*}$ induce an opposite change. $\delta_{D_{\text{gs}}}$ can in principle be modeled by a random walk approach, but for our simulations presented in the following we usually set it manually. $\delta_{T_2^*}$ is taken from a normal distribution with zero mean and standard deviation $\sigma_{T_2^*}/2\pi = 107$ kHz (see above).

When solving the time-dependent Schrödinger equation, we update $\delta_{T_2^*}$, $\delta_{\Omega_{\text{MW}}}$ and $\delta_{\Omega_{\text{m}}}$ every step along Φ , i.e. n_{phs} times per complete phase sweep. In contrast, $\delta_{D_{\text{gs}}}$ is changed at a much smaller rate, because the zero-field splitting changes on timescales of several hours. Please refer to the provided plots of $\delta_{D_{\text{gs}}}(\Phi)$ (see Fig. A.9). The presented procedure is repeated n_{avg} times and averaging over all solutions yields mean values for $|\Psi(\tau)\rangle$ and E_k with $k = 0, \pm 1$. Note that this approach limits us to low frequency fluctuations with a bandwidth of $1/\tau_{\text{max}} \approx 15$ kHz, as the experimental environment is kept constant as long as the global phase Φ remains unchanged ($\tau_{\text{max}} \approx 60 \mu\text{s}$ the maximum evolution time for which $|\Psi(\tau)\rangle$ is calculated). The excellent agreement between simulations and experiment (see Sec. A.9.3.3) and its simplicity justify our approach.

A.9.3.3. Comparing simulation and experiment

In Fig. A.7 and Fig. A.8, we compare our experimental data presented in Chap. 6 and our modeled results, which we obtained as described above (note that no fluctuations in the zero-field splitting D_{gs} are included unless stated otherwise). In the time domain (Fig. A.7), we observe excellent agreement between experimental data and our model. Yet a few differences do exist. First, the measured interference pattern of $P_{|0\rangle}(\tau)$ in Fig. A.7a is characterized by a slightly lower oscillation contrast compared to its simulated counterpart in Fig. A.7d. We assign this difference to the limited signal-to-noise ratio of our experimental data due to finite integration time. Also, slow fluctuations in driving fields and zero-field splitting have been neglected in our simulation. Second, the experimentally obtained $P_{|\pm 1\rangle}(\tau)$ in Fig. A.7b are characterized by slightly smaller oscillation amplitudes than predicted by our simulations. The simplified noise environment in our model is partly responsible for this discrepancy. However, the finite Q factors of our mechanical resonators have significant influence as well. They lead to a long mechanical response time, which prevents us from switching off the strain field fast enough while the weak microwave swap-pulse is applied to readout spin populations $P_{|\pm 1\rangle}$). Finally, we want to point out that the linecuts for $\Phi = 0$ in Fig. A.7b have not been taken exactly at $\Phi = 0$, but slightly offset at $\Phi \approx +2^\circ$. As a consequence, $P_{|\pm 1\rangle}$ are not degenerate.

Regarding the precession frequencies of the driven NV spin (Fig. A.8a+c), we again find remarkable agreement between experiment and model. However, our data in Fig. A.8a feature avoided crossings of different amplitudes (~ 20 kHz at

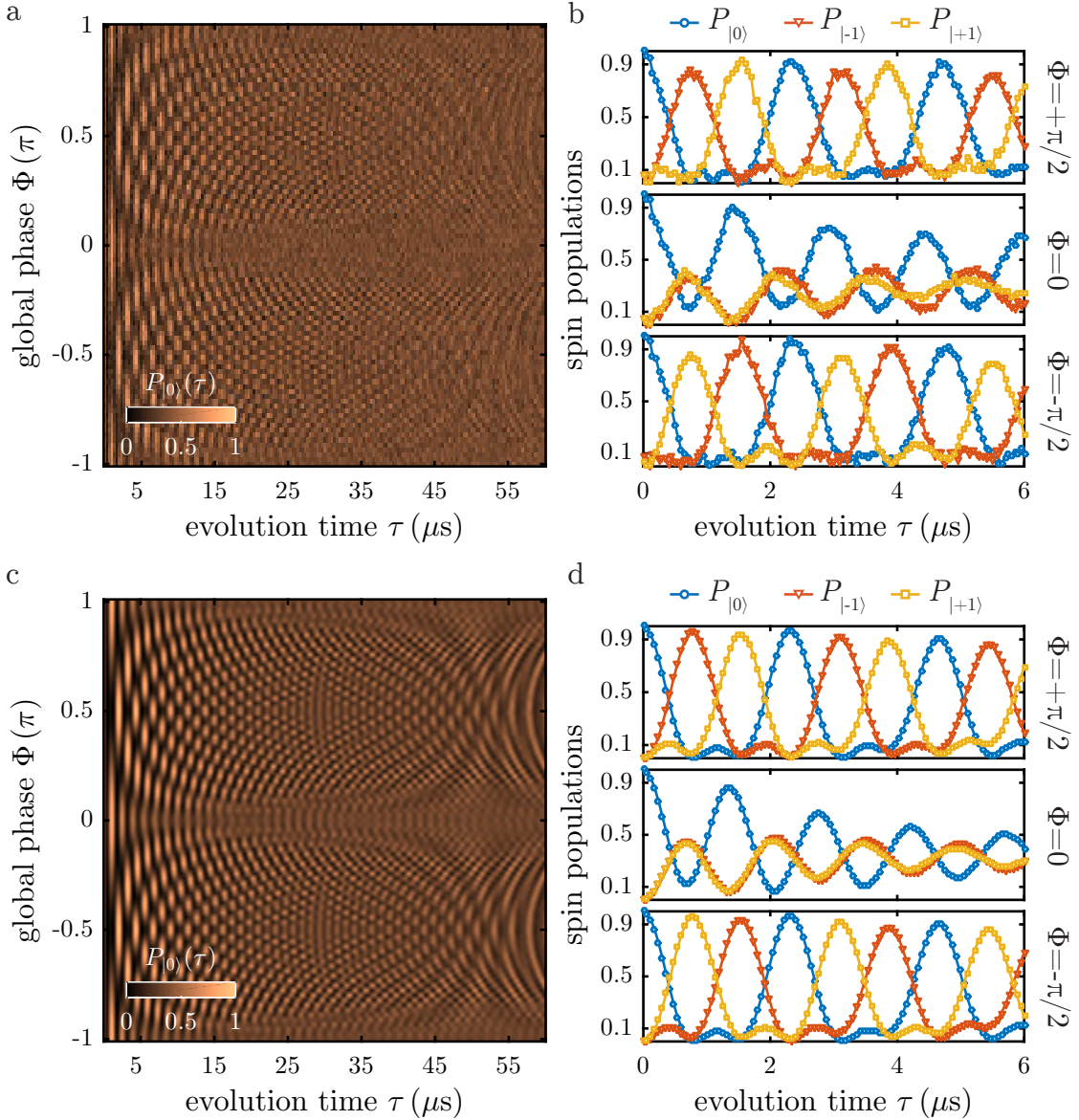


Figure A.7.: Closed-contour spin dynamics controlled by global phase Φ – a comparison between experiment (panels a+b) and our model (panels c+d). In general, we observe excellent agreement between experimental data and simulations in the time domain. The measured time evolution of $P_{|0\rangle}(\tau)$ in panel a is, however, characterized by a lower signal-to-noise ratio compared to its simulated counterpart in panel d, as the experimental integration time was limited. Furthermore, the experimentally obtained $P_{|\pm 1\rangle}(\tau)$ in panel b are characterized by smaller oscillation amplitudes than predicted by our simulations. This is caused by the finite Q factors of our mechanical resonators, leading to a long response time and preventing us from switching off the strain field while the weak microwave swap-pulse is applied to readout spin populations $P_{|\pm 1\rangle}$. Finally, we want to point out that the linecuts for $\Phi = 0$ in panel b have not been taken exactly at $\Phi = 0$, but slightly offset at $\Phi \approx +2^\circ$, causing the observed small mismatch in oscillation frequencies, weaker damping and the non-degeneracy of $P_{|\pm 1\rangle}$.

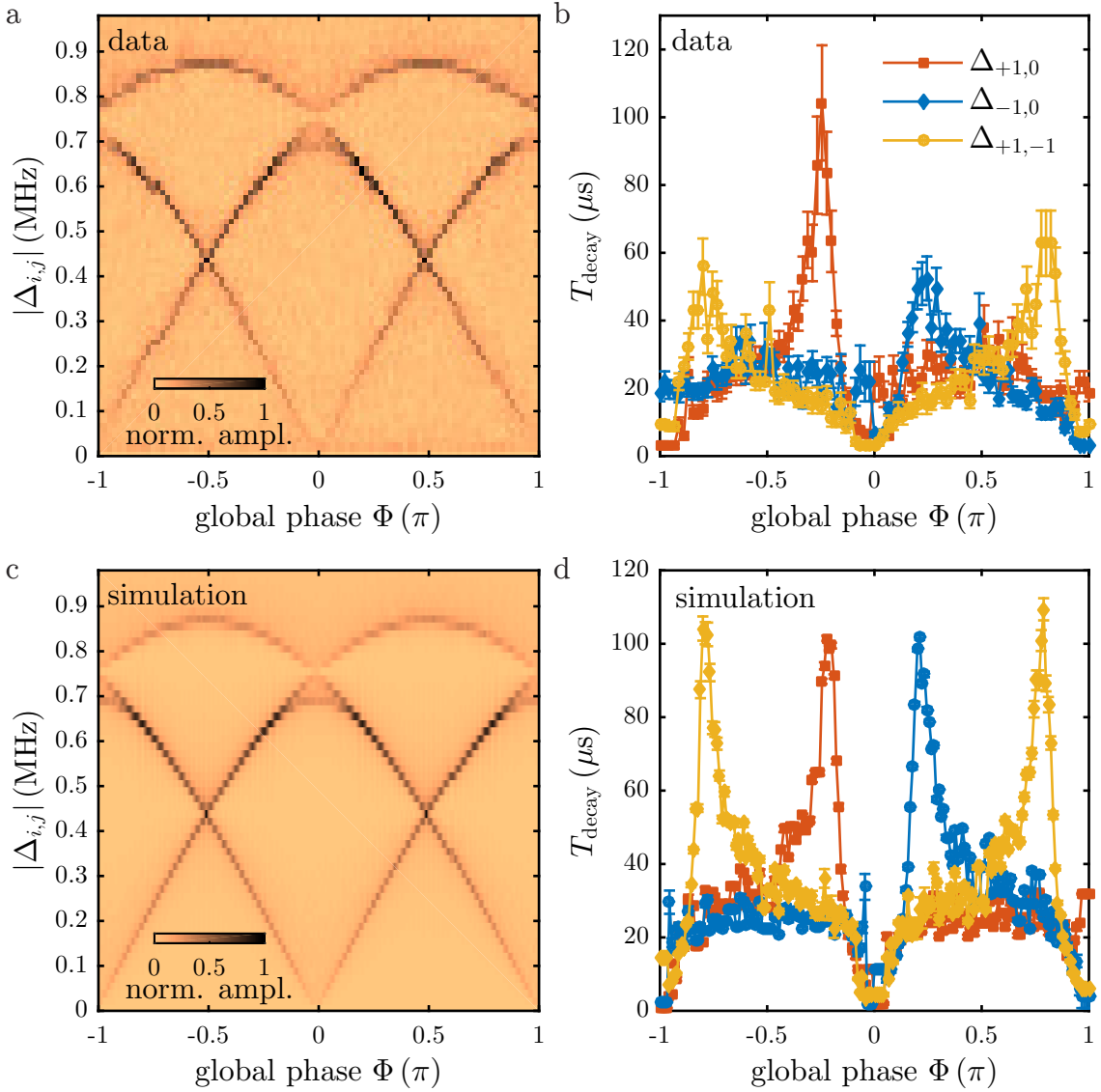


Figure A.8.: Spin precession frequencies and corresponding decay times under closed-contour interaction as measured experimentally (a+b) and obtained from simulations (c+d). Regarding the spin precession frequency spectra, we find great agreement between experiment and model. However, our data in panel a feature avoided crossings of different sizes at $\Phi = 0, \pm 1$ and $|\Delta_{i,j}| \approx 750$ kHz. In the simulated counterpart, (panel c) these are indistinguishable. In contrast, the Rabi decay time spectra in panels b and d are substantially different. While the modeled behavior of T_{decay} features four, equally long living frequency components at $\Phi = \pm\pi/4, \pm 3\pi/4$, the experimentally measured dependence of T_{decay} on Φ is strongly asymmetric. This difference is caused by slow fluctuations, most likely in the zero-field splitting D_{gs} (see text.). Error bars denote 95 % fit confidence intervals.

$\Phi = 0$; ~ 100 kHz at $\Phi = \pm\pi$). In the simulated precession frequency spectrum (Fig. A.8c), these are however of equal size. As we will see later (see Fig. A.9), we assign this mismatch to slow fluctuations in the zero-field splitting D_{gs} . In contrast to the excellent agreement in Fig. A.8a+c, the Rabi decay time spectra in Fig. A.8b+d are substantially different. The modeled phase dependence of T_{decay} features four, equally long living frequency components with maximum decay times of $T_{\text{decay}} \approx 105 \mu\text{s}$ at $\Phi = \pm\pi/4, \pm 3\pi/4$. In our experimental data, T_{decay} is strongly asymmetric. Again, this difference is caused by slow fluctuations, most likely in the zero-field splitting D_{gs} .

To investigate the influence of zero-field splitting variations, represented by detunings δD_{gs} in our model (see (A.97)), on spin precession frequency spectra and Rabi decay time T_{decay} , we repeated our simulations with the same noise environment, but non-zero detunings δD_{gs} , and extracted precession frequencies $\Delta_{i,j}$ and Rabi decay times T_{decay} as described above. The results are shown in Fig. A.9 and indicate the following:

- A fixed $\delta D_{\text{gs}}/2\pi = -100$ kHz (Fig. A.9a) increases avoided crossings and induces a strong asymmetry in $T_{\text{decay}}(\Phi)$. Specifically, the frequency components $\Delta_{+1,-1}$ at $\Phi \approx \pm 3\pi/4$ decay with $T_{\text{decay}} \approx 120 \mu\text{s}$, and therefore decohere much slower than the $\Delta_{\pm 1,0}$ components, located at $\Phi \approx \pm\pi/4$, which are characterized by $T_{\text{decay}} \approx 65 \mu\text{s}$.
- Decreasing D_{gs} , i.e. setting $\delta D_{\text{gs}}/2\pi = +100$ kHz, also increases avoided crossings in the spin precession frequency spectrum. Inverting the detuning's polarity, however, also inverses its effect on $T_{\text{decay}}(\Phi)$. Now, the $\Delta_{\pm 1,0}$ components decay with $T_{\text{decay}} \approx 120 \mu\text{s}$ and the frequency components $\Delta_{+1,-1}$ disappear on timescales $T_{\text{decay}} \approx 65 \mu\text{s}$,

By varying δD_{gs} with Φ (see inset to Fig. A.9c) while solving the time-dependent Schrödinger equation, we can qualitatively reproduce the experimentally determined phase dependence of T_{decay} very well (compare Fig. A.9c and Fig. A.8b). The employed variations in zero-field splitting D_{gs} of $\delta D_{\text{gs}}/2\pi \approx \pm 100$ kHz are in good agreement with the experimentally determined fluctuations (see Fig. A.6c), and are most likely caused by environmental temperature fluctuations [189]. Note, however, that we did not measure how D_{gs} actually evolved during data acquisition. We attribute the remaining mismatch between experiment and theory to our lack of knowledge over the noise environment, especially slow fluctuations in driving field amplitudes and zero-field splitting, during the measurement. The results from Fig. A.9c, even though they almost quantitatively confirm our experimental data, should therefore be considered as a proof of principle to demonstrate that our experimental results lie within the framework of our closed-interaction system.

As discussed, our simulations indicate that slow fluctuations are responsible for the observed asymmetry in T_{decay} . We can support this statement by further analysis of our experimental data. Typically, $P_{|0\rangle}(\tau, \Phi)$ (see for example Fig. 6.2a) is obtained by averaging over several complete phase sweeps. In Fig. A.10 we plot $P_{|0\rangle}(\tau)$ (left), spin precession frequencies $\Delta_{i,j}$ (middle) and the root-mean square (RMS) of $P_{|0\rangle}(\tau)$ for $\tau \in [50, 60] \mu\text{s}$ (right) versus Φ for four of these phase sweeps (note that the data set used here is not the one from Chap. 6, but was recorded under similar conditions).

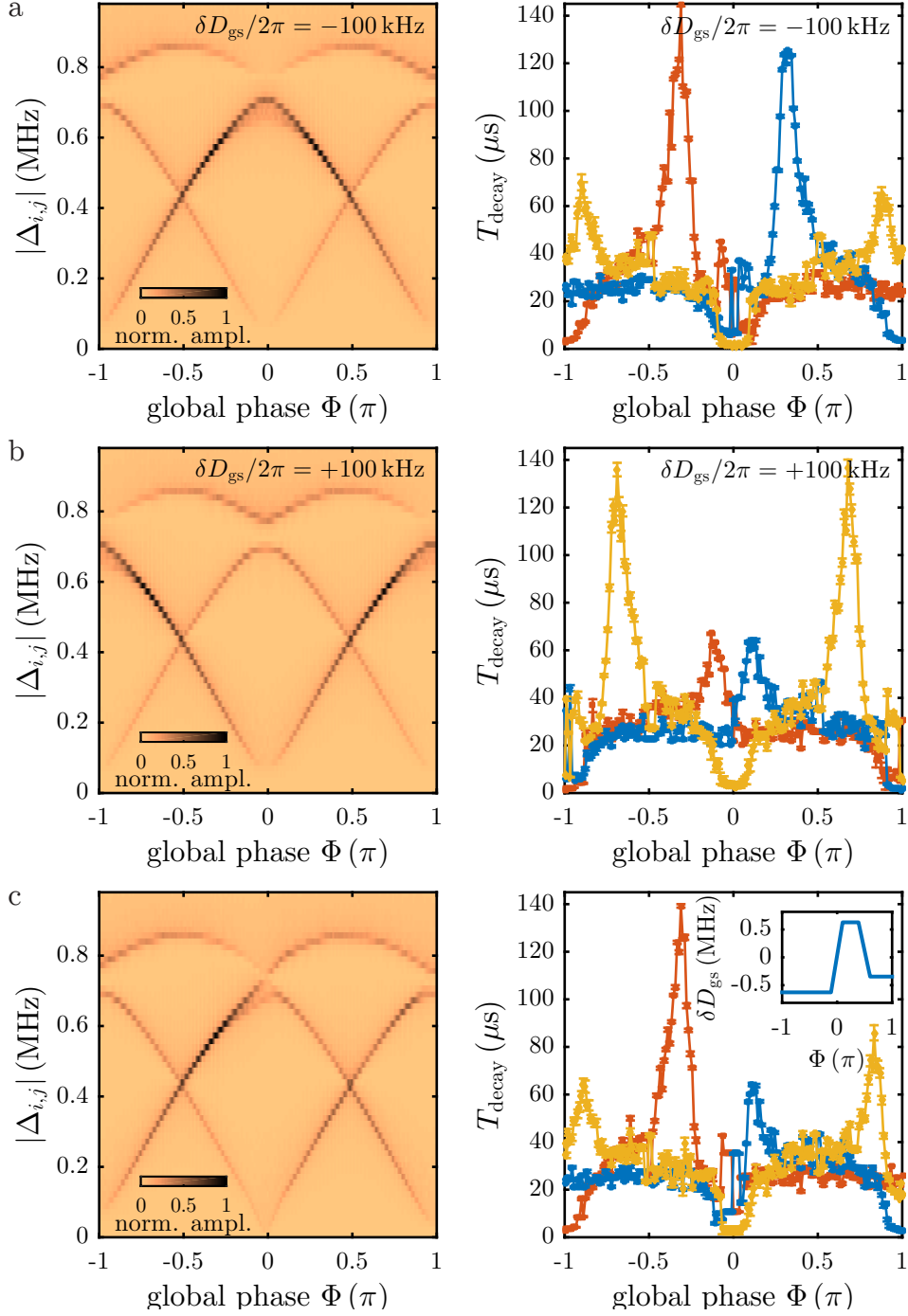


Figure A.9.: Influence of zero-field splitting variations on spin precession frequencies (left) and Rabi decay times (right). a+b) A constant detuning δD_{gs} causes a strong asymmetry in the phase dependence of T_{decay} . When $\delta D_{gs} > 0$, the $\Delta_{+1,-1}$ components at $\Phi \approx \pm 3\pi/4$ decay much slower than the $\Delta_{\pm 1,0}$ components, located at $\Phi \approx \pm\pi/4$. For $\delta D_{gs} < 0$, this effect is reversed. c) Varying δD_{gs} with global phase Φ (see inset), allows reproducing the experimentally determined behavior from Fig. A.8b.

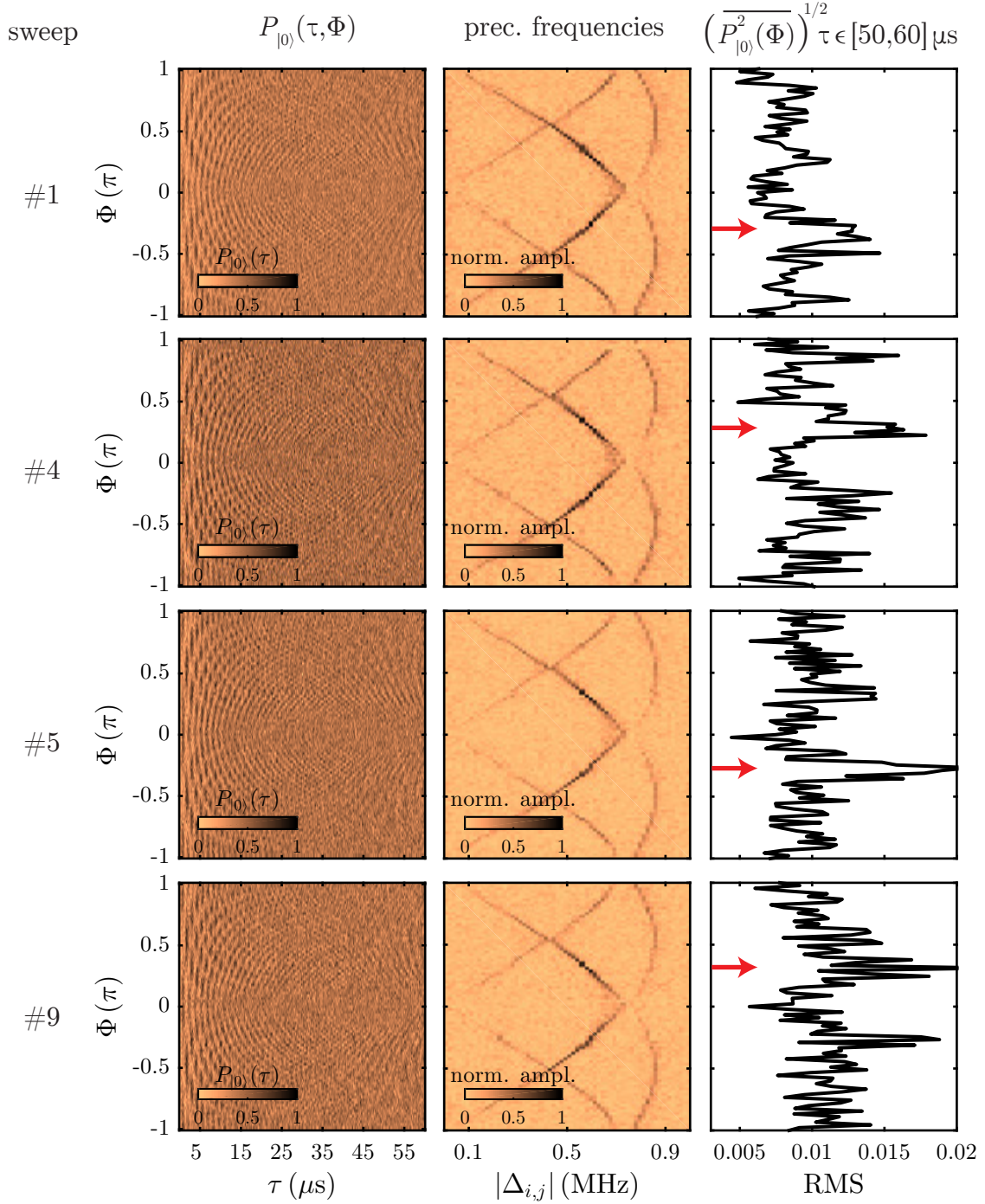


Figure A.10.: Time evolution of our experimental data. When investigating the time evolution of our closed-contour interaction scheme we essentially average over individually taken phase sweeps. Spin dynamics $P_{|0\rangle}(\tau, \Phi)$ (left), precession frequencies $\Delta_{i,j}$ (middle) and the root-mean square of $P_{|0\rangle}(\tau)$ for $\tau \in [50, 60] \mu\text{s}$ are shown here for four such sweeps. RMS maxima, indicating weak damping and marked by red arrows, change position with measurement time and thus hint at the presence of slowly evolving fluctuations.

The root-mean square of $P_{|0\rangle}(\tau)$ serves as a measure for the corresponding decay time T_{decay} , which could not be extracted by fitting due to the limited signal-to-noise ratio of the experimental data. Whenever the RMS of $P_{|0\rangle}(\tau)$ is large, the decay time is long. One can see that the individual RMS spectra show different behaviors with respect to Φ , i.e. the observable maxima differ in amplitude and slightly in position. This behavior is very similar to the influence of fluctuations in zero-field splitting D_{gs} (see discussion above) and thus confirms the presence of slow experimental fluctuations.

A.10. Strain- and stress-coupling Hamiltonians for NV orientations NV1-NV4

In this section, we present the Mathematica file that was used to calculate the stress- and strain tensors for all for NV orientations (see Sec. 2.4).

1. Calculate stress tensor for different stress directions

```
ClearAll["Global`*"] (*clearing all variables*)
```

Crystal coordinate system XYZ

```
X = {1, 0, 0};
Y = {0, 1, 0};
Z = {0, 0, 1};
```

Calculate stress tensor coordinates for an arbitrary stress direction

```
(*P denotes the applied amount of stress.*)
```

```
StressDir = {1, 1, 1};
σXX = P * Cos[VectorAngle[StressDir, X]] * Cos[VectorAngle[StressDir, X]];
σXY = P * Cos[VectorAngle[StressDir, X]] * Cos[VectorAngle[StressDir, Y]];
σXZ = P * Cos[VectorAngle[StressDir, X]] * Cos[VectorAngle[StressDir, Z]];
σYY = P * Cos[VectorAngle[StressDir, Y]] * Cos[VectorAngle[StressDir, Y]];
σYZ = P * Cos[VectorAngle[StressDir, Y]] * Cos[VectorAngle[StressDir, Z]];
σZZ = P * Cos[VectorAngle[StressDir, Z]] * Cos[VectorAngle[StressDir, Z]];
σXYZTensor = {{σXX, σXY, σXZ}, {σXY, σYY, σYZ}, {σXZ, σYZ, σZZ}} // MatrixForm
```

$$\begin{pmatrix} \sigma_{XX} & \sigma_{XY} & \sigma_{XZ} \\ \sigma_{XY} & \sigma_{YY} & \sigma_{YZ} \\ \sigma_{XZ} & \sigma_{YZ} & \sigma_{ZZ} \end{pmatrix}$$

Stress tensors for some predefined stress directions

```
σ100vec = {σx → 1, σy → 0, σz → 0};
σ110vec = {σx → 1, σy → 1, σz → 0};
σm110vec = {σx → -1, σy → 1, σz → 0};
σm1m10vec = {σx → -1, σy → -1, σz → 0};
σ1m10vec = {σx → 1, σy → -1, σz → 0};
σ111vec = {σx → 1, σy → 1, σz → 1};
```

2 | *StrainStressCoupling_Complete_forthesis.nb*

```
σ110 = {{σXX, σXY, σXZ}, {σXY, σYY, σYZ}, {σXZ, σYZ, σZZ}} /. σ110vec
σm110 = {{σXX, σXY, σXZ}, {σXY, σYY, σYZ}, {σXZ, σYZ, σZZ}} /. σm110vec
σ1m10 = {{σXX, σXY, σXZ}, {σXY, σYY, σYZ}, {σXZ, σYZ, σZZ}} /. σ1m10vec
σ1m10 = {{σXX, σXY, σXZ}, {σXY, σYY, σYZ}, {σXZ, σYZ, σZZ}} /. σ1m10vec
```

```
{{P/2, P/2, 0}, {P/2, P/2, 0}, {0, 0, 0}}
```

```
{{P/2, -P/2, 0}, {-P/2, P/2, 0}, {0, 0, 0}}
```

```
{{P/2, P/2, 0}, {P/2, P/2, 0}, {0, 0, 0}}
```

```
{{P/2, -P/2, 0}, {-P/2, P/2, 0}, {0, 0, 0}}
```

2. Stress- and strain-induced level shifts for all four NV orientations

- To include all four NV orientations, we keep the NV orientation fixed and rotate the crystal coordinate system. Essentially, we rotate the stress tensor using a passive transformation.
- The formalism here employs an NV center, whose coordinate system xyz is defined such that the y axis is contained by one of the three mirror planes.

```
ClearAll["Global`*"] (*clearing all variables*)
```

2.1 Defining NV orientations

Here we determine possible orientations of the four NV directions in a [001]-oriented diamond. As stated above, the NV coordinate systems xyz are defined such that the y axis is contained by one of the three mirror planes.

Schematic NV center

```

radiuslattice = 0.0025;
radiusatoms = 0.04;
lengthlatticecoordsys = 0.6;
box = {Line[{{0, 0, 0}, {1, 0, 0}, {1, 1, 0}, {0, 1, 0}, {0, 0, 0}, {0, 0, 1},
           {1, 0, 1}, {1, 1, 1}, {0, 1, 1}, {0, 0, 1}], Line[{{0, 1, 0}, {0, 1, 1}],
       Line[{{1, 1, 0}, {1, 1, 1}], Line[{{1, 0, 0}, {1, 0, 1}]}];
Nitrogen = Sphere[{0, 0, 0}, radiusatoms];
Vacancy = Sphere[0.5 * {1, 1, 1}, radiusatoms];
Carbons = {Sphere[{1, 1, 0}, radiusatoms],
           Sphere[{0, 1, 1}, radiusatoms], Sphere[{1, 0, 1}, radiusatoms]};
NNNconnection = {Cylinder[{{0, 0, 0}, {0.5, 0.5, 0.5}}, radiuslattice],
                 Cylinder[{{0.5, 0.5, 0.5}, {1, 0, 1}}, radiuslattice],
                 Cylinder[{{0.5, 0.5, 0.5}, {0, 1, 1}}, radiuslattice],
                 Cylinder[{{0.5, 0.5, 0.5}, {1, 1, 0}}, radiuslattice]};
planeCarbons = Polygon[{{1, 1, 0}, {0, 1, 1}, {1, 0, 1}}];
LatticeCoordSys = {Arrow[{{0, 0, 0}, 1 * lengthlatticecoordsys * {1, 0, 0}},
                    Arrow[{{0, 0, 0}, lengthlatticecoordsys * {0, 1, 0}},
                    Arrow[{{0, 0, 0}, lengthlatticecoordsys * {0, 0, 1}]}];

```

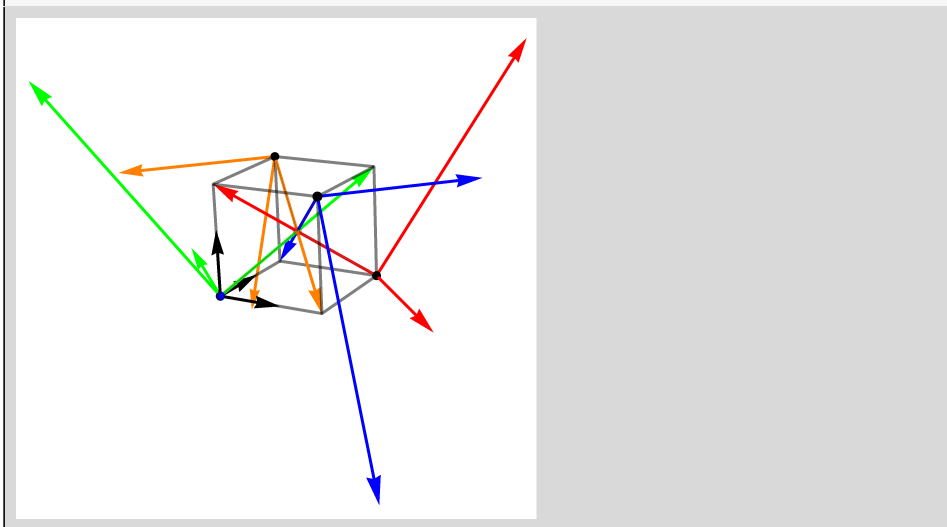
4 | *StrainStressCoupling_Complete_forthesis.nb*

Orientations of NV1 - 4 (as defined by Hughes1967, the y axis lies in a mirror plane of the defect)

```
start1 = {0, 0, 0};
NV1x = {-1, 1, 0};
NV1y = {-1, -1, 2};
NV1z = {1, 1, 1};
NVCoordSys1 = {Arrow[{start1, start1 + NV1x}],
  Arrow[{start1, start1 + NV1y}], Arrow[{start1, start1 + NV1z}]};
start2 = {1, 1, 0};
NV2x = {1, -1, 0};
NV2y = {1, 1, 2};
NV2z = {-1, -1, 1};
NVCoordSys2 = {Arrow[{start2, start2 + NV2x}],
  Arrow[{start2, start2 + NV2y}], Arrow[{start2, start2 + NV2z}]};
start3 = {1, 0, 1};
NV3x = {1, 1, 0};
NV3y = {1, -1, -2};
NV3z = {-1, 1, -1};
NVCoordSys3 = {Arrow[{start3, start3 + NV3x}],
  Arrow[{start3, start3 + NV3y}], Arrow[{start3, start3 + NV3z}]};
start4 = {0, 1, 1};
NV4x = {-1, -1, 0};
NV4y = {-1, 1, -2};
NV4z = {1, -1, -1};
NVCoordSys4 = {Arrow[{start4, start4 + NV4x}],
  Arrow[{start4, start4 + NV4y}], Arrow[{start4, start4 + NV4z}]};
```

Graphical representation of coordinate systems

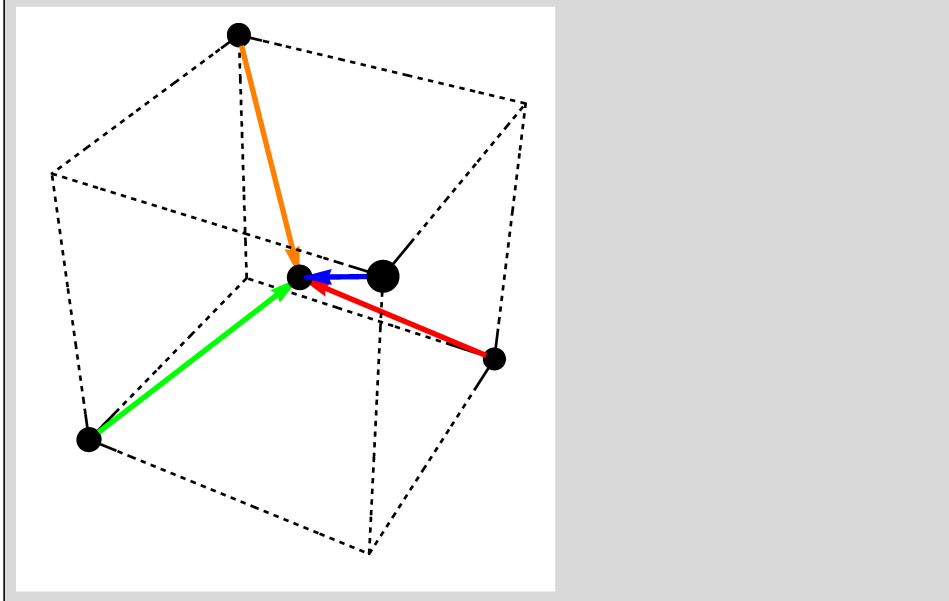
```
graph = Graphics3D[{Blue, Nitrogen, Red, Opacity[0.2], Vacancy, Black,  
  Opacity[1], Carbons, EdgeForm[], Gray, NNNconncetion, Opacity[1],  
  Black, Thick, LatticeCoordSys, Opacity[1], Thick, Green, NVCoordSys1,  
  Thick, Red, NVCoordSys2, Thick, Blue, NVCoordSys3, Thick, Orange,  
  NVCoordSys4, Opacity[0.5], Black, box}, Boxed -> False, Background -> White]
```



6 | *StrainStressCoupling_Complete_forthesis.nb*

Graphical representation of coordinate systems showing only the quantization axis

```
graph = Graphics3D[{Black, Nitrogen, Black, Vacancy, Black, Opacity[1], Carbons,
  EdgeForm[], Opacity[0], Gray, NNNconnection, Opacity[1], Thickness[0.01],
  Green, Arrowheads[0.05], Arrow[{start1, start1 + 0.5 * NV1z}], Red,
  Arrow[{start2, start2 + 0.5 * NV2z}], Blue, Arrow[{start3, start3 + 0.5 * NV3z}],
  Orange, Arrow[{start4, start4 + 0.5 * NV4z}], Thickness[0.005], Opacity[1],
  Black, Dashing[0.01], box}, Boxed -> False, Background -> White]
```



2.2 Defining rotation matrices for NV1 to NV2-4

The index denotes the vector about which the rotation is performed. An active rotation is a rotation of a vector in a fixed coordinate system. A rotation is positive if performed clockwise (observed along the rotation vector).

General definitions of rotation matrices (in 3x3 form)

```

Rx[xdeg_] := RotationMatrix[xdeg / 180 *  $\pi$ , {1, 0, 0}]
Ry[ydeg_] := RotationMatrix[ydeg / 180 *  $\pi$ , {0, 1, 0}]
Rz[zdeg_] := RotationMatrix[zdeg / 180 *  $\pi$ , {0, 0, 1}]
Rmlp10[deg_] := RotationMatrix[deg / 180 *  $\pi$ , {-1, 1, 0}]
Rp1p10[deg_] := RotationMatrix[deg / 180 *  $\pi$ , {1, 1, 0}]
R111[deg_] := RotationMatrix[deg / 180 *  $\pi$ , {1, 1, 1}]
Rpar111[vec_] := RotationMatrix[{vec, {1, 1, 1}}]

```

Active rotation NV1 to NV2: Rot12 = Rz[180]

```

Rot12 = Rz[180];
NV2x12 = Rot12.NV1x
NV2y12 = Rot12.NV1y
NV2z12 = Rot12.NV1z

```

```
{1, -1, 0}
```

```
{1, 1, 2}
```

```
{-1, -1, 1}
```

Active rotation NV1 to NV3: Rot13 = Rp1p10[180].Rz[-90]

```

Rot13 = Rp1p10[180].Rz[-90];
NV3x13 = Rot13.NV1x
NV3y13 = Rot13.NV1y
NV3z13 = Rot13.NV1z

```

```
{1, 1, 0}
```

```
{1, -1, -2}
```

```
{-1, 1, -1}
```

8 | *StrainStressCoupling_Complete_forthesis.nb*

Active rotation NV1 to NV4: $\text{Rot14} = \text{Rp1p10}[180].\text{Rz}[90]$

```
Rot14 = Rp1p10[180].Rz[90];
NV4x14 = Rot14.NV1x
NV4y14 = Rot14.NV1y
NV4z14 = Rot14.NV1z
```

```
{-1, -1, 0}
```

```
{-1, 1, -2}
```

```
{1, -1, -1}
```

2.3 Stress-induced level shifts M_x , M_y and M_z for all four NV orientations NV1-4 (defined in crystal coordinates XYZ)

Define stress tensor in crystal coordinates XYZ with X||[100], Y||[010] and Z||[001]

```
 $\sigma_{XYZ} = \{\{\sigma_{XX}, \sigma_{XY}, \sigma_{XZ}\}, \{\sigma_{YX}, \sigma_{YY}, \sigma_{YZ}\}, \{\sigma_{ZX}, \sigma_{ZY}, \sigma_{ZZ}\}\};$ 
 $\epsilon_{XYZ} = \{\{\epsilon_{XX}, \epsilon_{XY}, \epsilon_{XZ}\}, \{\epsilon_{YX}, \epsilon_{YY}, \epsilon_{YZ}\}, \{\epsilon_{ZX}, \epsilon_{ZY}, \epsilon_{ZZ}\}\};$ 
```

Rotate stress tensors to describe effect on NV1 (nothing changes, as the level shifts are defined for this orientation and given in Hughes1967)

```

σXYZNV1 = σXYZ;
MxNV1 = B * (2 * σXYZNV1[[3, 3]] - σXYZNV1[[1, 1]] - σXYZNV1[[2, 2]]) +
  C * (2 * σXYZNV1[[1, 2]] - σXYZNV1[[2, 3]] - σXYZNV1[[1, 3]]);
MyNV1 = Sqrt[3] * B * (σXYZNV1[[1, 1]] - σXYZNV1[[2, 2]]) +
  Sqrt[3] * C * (σXYZNV1[[2, 3]] - σXYZNV1[[1, 3]]);
MzNV1 = A1 * (σXYZNV1[[1, 1]] + σXYZNV1[[2, 2]] + σXYZNV1[[3, 3]]) +
  2 * A2 * (σXYZNV1[[2, 3]] + σXYZNV1[[1, 3]] + σXYZNV1[[1, 2]]);
MatrixForm[σXYZNV1]
MatrixForm[{MxNV1, MyNV1, MzNV1}]

```

$$\begin{pmatrix} \sigma_{XX} & \sigma_{XY} & \sigma_{XZ} \\ \sigma_{YX} & \sigma_{YY} & \sigma_{YZ} \\ \sigma_{ZX} & \sigma_{ZY} & \sigma_{ZZ} \end{pmatrix}$$

$$\begin{pmatrix} C (2 \sigma_{XY} - \sigma_{XZ} - \sigma_{YZ}) + B (-\sigma_{XX} - \sigma_{YY} + 2 \sigma_{ZZ}) \\ \sqrt{3} B (\sigma_{XX} - \sigma_{YY}) + \sqrt{3} C (-\sigma_{XZ} + \sigma_{YZ}) \\ 2 A_2 (\sigma_{XY} + \sigma_{XZ} + \sigma_{YZ}) + A_1 (\sigma_{XX} + \sigma_{YY} + \sigma_{ZZ}) \end{pmatrix}$$

Rotate stress tensors to describe NV2

```

σXYZNV2 = Inverse[Rot12].σXYZ.Transpose[Inverse[Rot12]];
MxNV2 = B * (2 * σXYZNV2[[3, 3]] - σXYZNV2[[1, 1]] - σXYZNV2[[2, 2]]) +
  C * (2 * σXYZNV2[[1, 2]] - σXYZNV2[[2, 3]] - σXYZNV2[[1, 3]]);
MyNV2 = Sqrt[3] * B * (σXYZNV2[[1, 1]] - σXYZNV2[[2, 2]]) +
  Sqrt[3] * C * (σXYZNV2[[2, 3]] - σXYZNV2[[1, 3]]);
MzNV2 = A1 * (σXYZNV2[[1, 1]] + σXYZNV2[[2, 2]] + σXYZNV2[[3, 3]]) +
  2 * A2 * (σXYZNV2[[2, 3]] + σXYZNV2[[1, 3]] + σXYZNV2[[1, 2]]);
MatrixForm[σXYZNV2]
MatrixForm[{MxNV2, MyNV2, MzNV2}]

```

$$\begin{pmatrix} \sigma_{XX} & \sigma_{XY} & -\sigma_{XZ} \\ \sigma_{YX} & \sigma_{YY} & -\sigma_{YZ} \\ -\sigma_{ZX} & -\sigma_{ZY} & \sigma_{ZZ} \end{pmatrix}$$

$$\begin{pmatrix} C (2 \sigma_{XY} + \sigma_{XZ} + \sigma_{YZ}) + B (-\sigma_{XX} - \sigma_{YY} + 2 \sigma_{ZZ}) \\ \sqrt{3} B (\sigma_{XX} - \sigma_{YY}) + \sqrt{3} C (\sigma_{XZ} - \sigma_{YZ}) \\ 2 A_2 (\sigma_{XY} - \sigma_{XZ} - \sigma_{YZ}) + A_1 (\sigma_{XX} + \sigma_{YY} + \sigma_{ZZ}) \end{pmatrix}$$

Rotate stress tensors to describe NV3

```

σXYZNV3 = Inverse[Rot13].σXYZ.Transpose[Inverse[Rot13]];
MxNV3 = B * (2 * σXYZNV3[[3, 3]] - σXYZNV3[[1, 1]] - σXYZNV3[[2, 2]]) +
  C * (2 * σXYZNV3[[1, 2]] - σXYZNV3[[2, 3]] - σXYZNV3[[1, 3]]);
MyNV3 = Sqrt[3] * B * (σXYZNV3[[1, 1]] - σXYZNV3[[2, 2]]) +
  Sqrt[3] * C * (σXYZNV3[[2, 3]] - σXYZNV3[[1, 3]]);
MzNV3 = A1 * (σXYZNV3[[1, 1]] + σXYZNV3[[2, 2]] + σXYZNV3[[3, 3]]) +
  2 * A2 * (σXYZNV3[[2, 3]] + σXYZNV3[[1, 3]] + σXYZNV3[[1, 2]]);
MatrixForm[σXYZNV3]
MatrixForm[{MxNV3, MyNV3, MzNV3}]

```

$$\begin{pmatrix} \sigma_{XX} & -\sigma_{XY} & \sigma_{XZ} \\ -\sigma_{YX} & \sigma_{YY} & -\sigma_{YZ} \\ \sigma_{ZX} & -\sigma_{ZY} & \sigma_{ZZ} \end{pmatrix}$$

$$\begin{pmatrix} C(-2\sigma_{XY} - \sigma_{XZ} + \sigma_{YZ}) + B(-\sigma_{XX} - \sigma_{YY} + 2\sigma_{ZZ}) \\ \sqrt{3} B(\sigma_{XX} - \sigma_{YY}) + \sqrt{3} C(-\sigma_{XZ} - \sigma_{YZ}) \\ 2A2(-\sigma_{XY} + \sigma_{XZ} - \sigma_{YZ}) + A1(\sigma_{XX} + \sigma_{YY} + \sigma_{ZZ}) \end{pmatrix}$$

Rotate stress tensors to describe NV4

```

σXYZNV4 = Inverse[Rot14].σXYZ.Transpose[Inverse[Rot14]];
MxNV4 = B * (2 * σXYZNV4[[3, 3]] - σXYZNV4[[1, 1]] - σXYZNV4[[2, 2]]) +
  C * (2 * σXYZNV4[[1, 2]] - σXYZNV4[[2, 3]] - σXYZNV4[[1, 3]]);
MyNV4 = Sqrt[3] * B * (σXYZNV4[[1, 1]] - σXYZNV4[[2, 2]]) +
  Sqrt[3] * C * (σXYZNV4[[2, 3]] - σXYZNV4[[1, 3]]);
MzNV4 = A1 * (σXYZNV4[[1, 1]] + σXYZNV4[[2, 2]] + σXYZNV4[[3, 3]]) +
  2 * A2 * (σXYZNV4[[2, 3]] + σXYZNV4[[1, 3]] + σXYZNV4[[1, 2]]);
MatrixForm[σXYZNV4]
MatrixForm[{MxNV4, MyNV4, MzNV4}]

```

$$\begin{pmatrix} \sigma_{XX} & -\sigma_{XY} & -\sigma_{XZ} \\ -\sigma_{YX} & \sigma_{YY} & \sigma_{YZ} \\ -\sigma_{ZX} & \sigma_{ZY} & \sigma_{ZZ} \end{pmatrix}$$

$$\begin{pmatrix} C(-2\sigma_{XY} + \sigma_{XZ} - \sigma_{YZ}) + B(-\sigma_{XX} - \sigma_{YY} + 2\sigma_{ZZ}) \\ \sqrt{3} B(\sigma_{XX} - \sigma_{YY}) + \sqrt{3} C(\sigma_{XZ} + \sigma_{YZ}) \\ 2A2(-\sigma_{XY} - \sigma_{XZ} + \sigma_{YZ}) + A1(\sigma_{XX} + \sigma_{YY} + \sigma_{ZZ}) \end{pmatrix}$$

Check whether calculations of above are correct

Definition of stress tensors for stress along main directions

The stress tensors can be obtained by executing section "Calculate stress tensor for different stress directions"

```

fixedpar100 = {σXX → 1, σXY → 0, σXZ → 0,
  σYX → 0, σYY → 0, σYZ → 0, σZX → 0, σZY → 0, σZZ → 0};
fixedpar110 = {σXX → 0.5, σXY → 0.5, σXZ → 0, σYX → 0.5,
  σYY → 0.5, σYZ → 0, σZX → 0, σZY → 0, σZZ → 0};
fixedpar111 = {σXX → 0.5, σXY → -0.5, σXZ → 0, σYX → -0.5,
  σYY → 0.5, σYZ → 0, σZX → 0, σZY → 0, σZZ → 0};
fixedpar111 = {σXX → 1/3, σXY → 1/3, σXZ → 1/3, σYX → 1/3,
  σYY → 1/3, σYZ → 1/3, σZX → 1/3, σZY → 1/3, σZZ → 1/3};

```

Calculate M_x , M_y and M_z of NV1-4 for stresses along [100], [110] and [111]

[100]: NV1-4 show identical reaction

[110]: NVs split into two families with identical reaction. NVA = NV1 and NV2. NVB = NV3 and NV4.

[111]: NV1 has a different reaction to stress than NV2-4

```

M100 = {{MxNV1, MyNV1, MzNV1}, {MxNV2, MyNV2, MzNV2}, {MxNV3, MyNV3, MzNV3},
  {MxNV4, MyNV4, MzNV4}} /. fixedpar100 // FullSimplify // TableForm
M110 = {{MxNV1, MyNV1, MzNV1}, {MxNV2, MyNV2, MzNV2}, {MxNV3, MyNV3, MzNV3},
  {MxNV4, MyNV4, MzNV4}} /. fixedpar110 // FullSimplify // TableForm
M111 = {{MxNV1, MyNV1, MzNV1}, {MxNV2, MyNV2, MzNV2}, {MxNV3, MyNV3, MzNV3},
  {MxNV4, MyNV4, MzNV4}} /. fixedpar111 // FullSimplify // TableForm

```

```

-B      √3 B      A1
-B      √3 B      A1
-B      √3 B      A1
-B      √3 B      A1

```

```

-1. B + 1. C      0.      1. A1 + 1. A2
-1. B + 1. C      0.      1. A1 + 1. A2
-1. B - 1. C      0.      1. A1 - 1. A2
-1. B - 1. C      0.      1. A1 - 1. A2

```

```

0      0      A1 + 2 A2
4 C    0      A1 - 2 A2
  3
- 2 C   - 2 C   A1 - 2 A2
  3      √3
- 2 C    2 C   A1 - 2 A2
  3      √3

```

Calculate level shifts $\Delta = M_z \pm \sqrt{M_x^2 + M_y^2}$ of NV1-4 for stresses along [100], [110] and [111]

<pre> comp100 = {{Sqrt[MxNV1^2 + MyNV1^2], MzNV1}, {Sqrt[MxNV2^2 + MyNV2^2], MzNV2}, {Sqrt[MxNV3^2 + MyNV3^2], MzNV3}, {Sqrt[MxNV4^2 + MyNV4^2], MzNV4}} /. fixedpar100 // FullSimplify // TableForm comp110 = {{Sqrt[MxNV1^2 + MyNV1^2], MzNV1}, {Sqrt[MxNV2^2 + MyNV2^2], MzNV2}, {Sqrt[MxNV3^2 + MyNV3^2], MzNV3}, {Sqrt[MxNV4^2 + MyNV4^2], MzNV4}} /. fixedpar110 // TableForm compm110 = {{Sqrt[MxNV1^2 + MyNV1^2], MzNV1}, {Sqrt[MxNV2^2 + MyNV2^2], MzNV2}, {Sqrt[MxNV3^2 + MyNV3^2], MzNV3}, {Sqrt[MxNV4^2 + MyNV4^2], MzNV4}} /. fixedparm110 // FullSimplify // TableForm comp111 = {{Sqrt[MxNV1^2 + MyNV1^2], MzNV1}, {Sqrt[MxNV2^2 + MyNV2^2], MzNV2}, {Sqrt[MxNV3^2 + MyNV3^2], MzNV3}, {Sqrt[MxNV4^2 + MyNV4^2], MzNV4}} /. fixedpar111 // FullSimplify // TableForm </pre>	
$2\sqrt{B^2}$	A1
$\sqrt{0. + (-1. B + 1. C)^2}$	1. A1 + 1. A2
$\sqrt{0. + (-1. B + 1. C)^2}$	1. A1 + 1. A2
$\sqrt{0. + (-1. b - 1. c)^2}$	1. a1 - 1. a2
$\sqrt{0. + (-1. b - 1. c)^2}$	1. a1 - 1. a2
$\sqrt{(1. B + 1. C)^2}$	1. A1 - 1. A2
$\sqrt{(1. B + 1. C)^2}$	1. A1 - 1. A2
$\sqrt{(1. b - 1. c)^2}$	1. a1 + 1. a2
$\sqrt{(1. b - 1. c)^2}$	1. a1 + 1. a2
0	A1 + 2 A2
$\frac{4\sqrt{c^2}}{3}$	A1 - $\frac{2A2}{3}$
$\frac{4\sqrt{c^2}}{3}$	a1 - $\frac{2a2}{3}$
$\frac{4\sqrt{c^2}}{3}$	a1 - $\frac{2a2}{3}$

2.4 Strain-induced level shifts M_x , M_y and M_z for all four NV orientations NV1-4 (defined in NV coordinates xyz)

Approach :

- 1) Convert σ_{XYZ} into ϵ_{XYZ}
- 2) Convert ϵ_{XYZ} into ϵ_{xyz} for NV1-4
- 3) Use expressions for $M_x\epsilon$, $M_y\epsilon$, $M_z\epsilon$ from Ludlow1968 and insert ϵ_{xyz} for NV1-4.

Note: setting $\gamma=1$ yields strain tensors used in Lee2016

```
ClearAll["Global`*"] (*clearing all variables*)
```

Definition of rotations

```
CXYZ = {{C11, C12, C12, 0, 0, 0}, {C12, C11, C12, 0, 0, 0}, {C12, C12, C11, 0, 0, 0},
        {0, 0, 0, C44, 0, 0}, {0, 0, 0, 0, C44, 0}, {0, 0, 0, 0, 0, C44}};

(*rotation matrices in 3x3 form*)
Rx[xdeg_] := RotationMatrix[xdeg / 180 *  $\pi$ , {1, 0, 0}]
Ry[ydeg_] := RotationMatrix[ydeg / 180 *  $\pi$ , {0, 1, 0}]
Rz[zdeg_] := RotationMatrix[zdeg / 180 *  $\pi$ , {0, 0, 1}]
Rmlp10[deg_] := RotationMatrix[deg / 180 *  $\pi$ , {-1, 1, 0}]
Rp1p10[deg_] := RotationMatrix[deg / 180 *  $\pi$ , {1, 1, 0}]
R111[deg_] := RotationMatrix[deg / 180 *  $\pi$ , {1, 1, 1}]
Rpar111[vec_] := RotationMatrix[{vec, {1, 1, 1}}]

(*Rotations NV1 to NV2-4*)
Rot12 = Rz[180];
Rot13 = Rp1p10[180].Rz[-90];
Rot14 = Rp1p10[180].Rz[90];
```

Find expression for strain tensor ϵ_{XYZ} for the four different NV orientations when starting from σ_{XYZ}

Convert σ_{XYZ} into ϵ_{XYZ}

```

σXYZ6x6 = {σXX, σYY, σZZ, σYZ, σXZ, σXY};
εXYZ6x6calc = Inverse[CXYZ].σXYZ6x6 // FullSimplify;
MatrixForm[εXYZ6x6calc]
εXYZcalc = {{εXYZ6x6calc[[1]], εXYZ6x6calc[[6]], εXYZ6x6calc[[5]]},
             {εXYZ6x6calc[[6]], εXYZ6x6calc[[2]], εXYZ6x6calc[[4]]},
             {εXYZ6x6calc[[5]], εXYZ6x6calc[[4]], εXYZ6x6calc[[3]]}};
MatrixForm[εXYZcalc]

```

$$\begin{pmatrix} \frac{C11 \sigma_{XX} + C12 (\sigma_{XX} - \sigma_{YY} - \sigma_{ZZ})}{C11^2 + C11 C12 - 2 C12^2} \\ \frac{C11 \sigma_{YY} - C12 (\sigma_{XX} - \sigma_{YY} + \sigma_{ZZ})}{(C11 - C12) (C11 + 2 C12)} \\ \frac{-C12 (\sigma_{XX} + \sigma_{YY}) + (C11 + C12) \sigma_{ZZ}}{(C11 - C12) (C11 + 2 C12)} \\ \frac{\sigma_{YZ}}{C44} \\ \frac{\sigma_{XZ}}{C44} \\ \frac{\sigma_{XY}}{C44} \end{pmatrix}$$

$$\begin{pmatrix} \frac{C11 \sigma_{XX} + C12 (\sigma_{XX} - \sigma_{YY} - \sigma_{ZZ})}{C11^2 + C11 C12 - 2 C12^2} & \frac{\sigma_{XY}}{C44} & \frac{\sigma_{XZ}}{C44} \\ \frac{\sigma_{XY}}{C44} & \frac{C11 \sigma_{YY} - C12 (\sigma_{XX} - \sigma_{YY} + \sigma_{ZZ})}{(C11 - C12) (C11 + 2 C12)} & \frac{\sigma_{YZ}}{C44} \\ \frac{\sigma_{XZ}}{C44} & \frac{\sigma_{YZ}}{C44} & \frac{-C12 (\sigma_{XX} + \sigma_{YY}) + (C11 + C12) \sigma_{ZZ}}{(C11 - C12) (C11 + 2 C12)} \end{pmatrix}$$

Rotation of ϵ_{XYZ} into ϵ_{xyz} of NV1; calculate $M_{\epsilon NV1}$, $M_{\gamma NV1}$ and $M_{z \epsilon NV1}$

```

KHughes = Rmlp10[ArcCos[1 / Sqrt[3]] /  $\pi$  * 180].Rz[135];
RotNV1e = Inverse[KHughes];
exzyNV1calc = RotNV1e.eXYZcalc.Transpose[RotNV1e] // FullSimplify;
M $\epsilon$ NV1calc = b (exzyNV1calc[[1, 1]] - exzyNV1calc[[2, 2]]) + 2 c exzyNV1calc[[2, 3]]
M $\gamma$ NV1calc = -2 b exzyNV1calc[[1, 2]] - 2 c exzyNV1calc[[1, 3]]
Mz $\epsilon$ NV1calc =
  a1 exzyNV1calc[[3, 3]] + a2 (exzyNV1calc[[1, 1]] + exzyNV1calc[[2, 2]])

```

$$\begin{aligned}
& - \frac{\sqrt{2} c ((C11 - C12) (2 \sigma_{XY} - \sigma_{XZ} - \sigma_{YZ}) + C44 (\sigma_{XX} + \sigma_{YY} - 2 \sigma_{ZZ}))}{3 (C11 - C12) C44} + \\
& b \left(\frac{C11 C44 \sigma_{XX} - 2 C11^2 \sigma_{XY} - 2 C11 C12 \sigma_{XY} + 4 C12^2 \sigma_{XY} + C11 C44 \sigma_{YY} - 2 C12 C44 \sigma_{ZZ}}{2 C11^2 C44 + 2 C11 C12 C44 - 4 C12^2 C44} - \right. \\
& \quad (2 C11^2 (\sigma_{XY} - 2 (\sigma_{XZ} + \sigma_{YZ})) + \\
& \quad \quad 2 C12 (-2 C12 (\sigma_{XY} - 2 (\sigma_{XZ} + \sigma_{YZ})) + C44 (-2 (\sigma_{XX} + \sigma_{YY}) + \sigma_{ZZ})) + \\
& \quad \quad \left. C11 (2 C12 (\sigma_{XY} - 2 (\sigma_{XZ} + \sigma_{YZ})) + C44 (\sigma_{XX} + \sigma_{YY} + 4 \sigma_{ZZ}))) \right) / \\
& \quad (6 (C11 - C12) (C11 + 2 C12) C44)
\end{aligned}$$

$$- \frac{\sqrt{\frac{2}{3}} c (C44 (-\sigma_{XX} + \sigma_{YY}) - (C11 - C12) (\sigma_{XZ} - \sigma_{YZ}))}{(C11 - C12) C44} - b \left(\frac{\sigma_{XX} - \sigma_{YY}}{C11 - C12} - \frac{2 (\sigma_{XZ} - \sigma_{YZ})}{C44} \right) \sqrt{3}$$

$$\begin{aligned}
& a1 \frac{(2 (C11 + 2 C12) (\sigma_{XY} + \sigma_{XZ} + \sigma_{YZ}) + C44 (\sigma_{XX} + \sigma_{YY} + \sigma_{ZZ}))}{3 (C11 + 2 C12) C44} + \\
& a2 \left(\frac{C11 C44 \sigma_{XX} - 2 C11^2 \sigma_{XY} - 2 C11 C12 \sigma_{XY} + 4 C12^2 \sigma_{XY} + C11 C44 \sigma_{YY} - 2 C12 C44 \sigma_{ZZ}}{2 C11^2 C44 + 2 C11 C12 C44 - 4 C12^2 C44} + \right. \\
& \quad (2 C11^2 (\sigma_{XY} - 2 (\sigma_{XZ} + \sigma_{YZ})) + \\
& \quad \quad 2 C12 (-2 C12 (\sigma_{XY} - 2 (\sigma_{XZ} + \sigma_{YZ})) + C44 (-2 (\sigma_{XX} + \sigma_{YY}) + \sigma_{ZZ})) + \\
& \quad \quad \left. C11 (2 C12 (\sigma_{XY} - 2 (\sigma_{XZ} + \sigma_{YZ})) + C44 (\sigma_{XX} + \sigma_{YY} + 4 \sigma_{ZZ}))) \right) / \\
& \quad (6 (C11 - C12) (C11 + 2 C12) C44)
\end{aligned}$$

Rotation of ϵ_{XYZ} into ϵ_{xyz} of NV2; calculate $M_{\epsilon NV2}$, $M_{y\epsilon NV2}$ and $M_{z\epsilon NV2}$

```

RotNV2e = Inverse[Rot12.KHughes];
exzyNV2calc = RotNV2e.eXYZcalc.Transpose[RotNV2e] // FullSimplify;
M $\epsilon$ NV2calc = b (exzyNV2calc[[1, 1]] - exzyNV2calc[[2, 2]]) + 2 c exzyNV2calc[[2, 3]]
My $\epsilon$ NV2calc = -2 b exzyNV2calc[[1, 2]] - 2 c exzyNV2calc[[1, 3]]
Mz $\epsilon$ NV2calc =
a1 exzyNV2calc[[3, 3]] + a2 (exzyNV2calc[[1, 1]] + exzyNV2calc[[2, 2]])

```

$$\begin{aligned}
& - \frac{\sqrt{2} c ((C11 - C12) (2 \sigma_{XY} + \sigma_{XZ} + \sigma_{YZ}) + C44 (\sigma_{XX} + \sigma_{YY} - 2 \sigma_{ZZ}))}{3 (C11 - C12) C44} + \\
& b \left(\frac{C11 C44 \sigma_{XX} - 2 C11^2 \sigma_{XY} - 2 C11 C12 \sigma_{XY} + 4 C12^2 \sigma_{XY} + C11 C44 \sigma_{YY} - 2 C12 C44 \sigma_{ZZ}}{2 C11^2 C44 + 2 C11 C12 C44 - 4 C12^2 C44} - \right. \\
& \left. \frac{(2 C11^2 (\sigma_{XY} + 2 (\sigma_{XZ} + \sigma_{YZ})) - 4 C12 (C44 (\sigma_{XX} + \sigma_{YY}) + C12 (\sigma_{XY} + 2 (\sigma_{XZ} + \sigma_{YZ}))) + 2 C12 C44 \sigma_{ZZ} + C11 (2 C12 (\sigma_{XY} + 2 (\sigma_{XZ} + \sigma_{YZ})) + C44 (\sigma_{XX} + \sigma_{YY} + 4 \sigma_{ZZ})))}{(6 (C11 - C12) (C11 + 2 C12) C44)} \right)
\end{aligned}$$

$$\begin{aligned}
& - \frac{\sqrt{\frac{2}{3}} c (C44 (-\sigma_{XX} + \sigma_{YY}) + (C11 - C12) (\sigma_{XZ} - \sigma_{YZ}))}{(C11 - C12) C44} - \frac{b \left(\frac{\sigma_{XX} - \sigma_{YY}}{C11 - C12} + \frac{2 (\sigma_{XZ} - \sigma_{YZ})}{C44} \right)}{\sqrt{3}}
\end{aligned}$$

$$\begin{aligned}
& \frac{a1 (2 (C11 + 2 C12) (\sigma_{XY} - \sigma_{XZ} - \sigma_{YZ}) + C44 (\sigma_{XX} + \sigma_{YY} + \sigma_{ZZ}))}{3 (C11 + 2 C12) C44} + \\
& a2 \left(\frac{C11 C44 \sigma_{XX} - 2 C11^2 \sigma_{XY} - 2 C11 C12 \sigma_{XY} + 4 C12^2 \sigma_{XY} + C11 C44 \sigma_{YY} - 2 C12 C44 \sigma_{ZZ}}{2 C11^2 C44 + 2 C11 C12 C44 - 4 C12^2 C44} + \right. \\
& \left. \frac{(2 C11^2 (\sigma_{XY} + 2 (\sigma_{XZ} + \sigma_{YZ})) - 4 C12 (C44 (\sigma_{XX} + \sigma_{YY}) + C12 (\sigma_{XY} + 2 (\sigma_{XZ} + \sigma_{YZ}))) + 2 C12 C44 \sigma_{ZZ} + C11 (2 C12 (\sigma_{XY} + 2 (\sigma_{XZ} + \sigma_{YZ})) + C44 (\sigma_{XX} + \sigma_{YY} + 4 \sigma_{ZZ})))}{(6 (C11 - C12) (C11 + 2 C12) C44)} \right)
\end{aligned}$$

Rotation of ϵ_{XYZ} into ϵ_{xyz} of NV3; calculate $M_{\epsilon NV3}$, $My_{\epsilon NV3}$ and $Mz_{\epsilon NV3}$

```

RotNV3e = Inverse[Rot13.KHughes];
exzyNV3calc = RotNV3e.eXYZcalc.Transpose[RotNV3e] // FullSimplify;
Mx $\epsilon$ NV3calc = b (exzyNV3calc[[1, 1]] - exzyNV3calc[[2, 2]]) + 2 c exzyNV3calc[[2, 3]]
My $\epsilon$ NV3calc = -2 b exzyNV3calc[[1, 2]] - 2 c exzyNV3calc[[1, 3]]
Mz $\epsilon$ NV3calc =
  a1 exzyNV3calc[[3, 3]] + a2 (exzyNV3calc[[1, 1]] + exzyNV3calc[[2, 2]])

```

$$\frac{\sqrt{2} c ((C11 - C12) (2 \sigma_{XY} + \sigma_{XZ} - \sigma_{YZ}) - C44 (\sigma_{XX} + \sigma_{YY} - 2 \sigma_{ZZ}))}{3 (C11 - C12) C44} +$$

$$b \left(\frac{2 C11^2 \sigma_{XY} + C11 (2 C12 \sigma_{XY} + C44 (\sigma_{XX} + \sigma_{YY})) - 2 C12 (2 C12 \sigma_{XY} + C44 \sigma_{ZZ})}{2 (C11^2 + C11 C12 - 2 C12^2) C44} - \right.$$

$$\left. \begin{aligned} & (-2 C11^2 (\sigma_{XY} + 2 \sigma_{XZ} - 2 \sigma_{YZ}) + \\ & 2 C12 (2 C12 (\sigma_{XY} + 2 \sigma_{XZ} - 2 \sigma_{YZ}) + C44 (-2 (\sigma_{XX} + \sigma_{YY}) + \sigma_{ZZ})) + \\ & C11 (-2 C12 (\sigma_{XY} + 2 \sigma_{XZ} - 2 \sigma_{YZ}) + C44 (\sigma_{XX} + \sigma_{YY} + 4 \sigma_{ZZ})) \end{aligned} \right) /$$

$$(6 (C11 - C12) (C11 + 2 C12) C44)$$

$$- \frac{\sqrt{\frac{2}{3}} c (C44 (-\sigma_{XX} + \sigma_{YY}) - (C11 - C12) (\sigma_{XZ} + \sigma_{YZ}))}{(C11 - C12) C44} - \frac{b \left(\frac{\sigma_{XX} - \sigma_{YY}}{C11 - C12} - \frac{2 (\sigma_{XZ} + \sigma_{YZ})}{C44} \right)}{\sqrt{3}}$$

$$a1 \frac{(-2 (C11 + 2 C12) (\sigma_{XY} - \sigma_{XZ} + \sigma_{YZ}) + C44 (\sigma_{XX} + \sigma_{YY} + \sigma_{ZZ}))}{3 (C11 + 2 C12) C44} +$$

$$a2 \left(\frac{2 C11^2 \sigma_{XY} + C11 (2 C12 \sigma_{XY} + C44 (\sigma_{XX} + \sigma_{YY})) - 2 C12 (2 C12 \sigma_{XY} + C44 \sigma_{ZZ})}{2 (C11^2 + C11 C12 - 2 C12^2) C44} + \right.$$

$$\left. \begin{aligned} & (-2 C11^2 (\sigma_{XY} + 2 \sigma_{XZ} - 2 \sigma_{YZ}) + \\ & 2 C12 (2 C12 (\sigma_{XY} + 2 \sigma_{XZ} - 2 \sigma_{YZ}) + C44 (-2 (\sigma_{XX} + \sigma_{YY}) + \sigma_{ZZ})) + \\ & C11 (-2 C12 (\sigma_{XY} + 2 \sigma_{XZ} - 2 \sigma_{YZ}) + C44 (\sigma_{XX} + \sigma_{YY} + 4 \sigma_{ZZ})) \end{aligned} \right) /$$

$$(6 (C11 - C12) (C11 + 2 C12) C44)$$

Rotation of ϵ_{XYZ} into ϵ_{xyz} of NV4; calculate $M_{x\epsilon NV4}$, $M_{y\epsilon NV4}$ and $M_{z\epsilon NV4}$

$$\begin{aligned}
 & \text{RotNV4e} = \text{Inverse}[\text{Rot14.KHughes}]; \\
 & \epsilon_{zyNV4calc} = \text{RotNV4e}.\epsilon_{XYZcalc}.\text{Transpose}[\text{RotNV4e}] // \text{FullSimplify}; \\
 & M_{x\epsilon NV4calc} = b (\epsilon_{zyNV4calc}[[1, 1]] - \epsilon_{zyNV4calc}[[2, 2]]) + 2 c \epsilon_{zyNV4calc}[[2, 3]] \\
 & M_{y\epsilon NV4calc} = -2 b \epsilon_{zyNV4calc}[[1, 2]] - 2 c \epsilon_{zyNV4calc}[[1, 3]] \\
 & M_{z\epsilon NV4calc} = \\
 & \quad a1 \epsilon_{zyNV4calc}[[3, 3]] + a2 (\epsilon_{zyNV4calc}[[1, 1]] + \epsilon_{zyNV4calc}[[2, 2]]) \\
 & \frac{\sqrt{2} c ((C11 - C12) (2 \sigma_{XY} - \sigma_{XZ} + \sigma_{YZ}) - C44 (\sigma_{XX} + \sigma_{YY} - 2 \sigma_{ZZ}))}{3 (C11 - C12) C44} + \\
 & b \left(\frac{2 C11^2 \sigma_{XY} + C11 (2 C12 \sigma_{XY} + C44 (\sigma_{XX} + \sigma_{YY})) - 2 C12 (2 C12 \sigma_{XY} + C44 \sigma_{ZZ})}{2 (C11^2 + C11 C12 - 2 C12^2) C44} - \right. \\
 & \quad \left. (-2 C11^2 (\sigma_{XY} - 2 \sigma_{XZ} + 2 \sigma_{YZ}) + \right. \\
 & \quad \left. 2 C12 (2 C12 (\sigma_{XY} - 2 \sigma_{XZ} + 2 \sigma_{YZ}) + C44 (-2 (\sigma_{XX} + \sigma_{YY}) + \sigma_{ZZ})) + \right. \\
 & \quad \left. C11 (-2 C12 (\sigma_{XY} - 2 \sigma_{XZ} + 2 \sigma_{YZ}) + C44 (\sigma_{XX} + \sigma_{YY} + 4 \sigma_{ZZ})) \right) / \\
 & \quad \left. (6 (C11 - C12) (C11 + 2 C12) C44) \right) \\
 & - \frac{\sqrt{\frac{2}{3}} c (C44 (-\sigma_{XX} + \sigma_{YY}) + (C11 - C12) (\sigma_{XZ} + \sigma_{YZ}))}{(C11 - C12) C44} - b \left(\frac{\sigma_{XX} - \sigma_{YY}}{C11 - C12} + \frac{2 (\sigma_{XZ} + \sigma_{YZ})}{C44} \right)}{\sqrt{3}} \\
 & a1 \frac{(-2 (C11 + 2 C12) (\sigma_{XY} + \sigma_{XZ} - \sigma_{YZ}) + C44 (\sigma_{XX} + \sigma_{YY} + \sigma_{ZZ}))}{3 (C11 + 2 C12) C44} + \\
 & a2 \left(\frac{2 C11^2 \sigma_{XY} + C11 (2 C12 \sigma_{XY} + C44 (\sigma_{XX} + \sigma_{YY})) - 2 C12 (2 C12 \sigma_{XY} + C44 \sigma_{ZZ})}{2 (C11^2 + C11 C12 - 2 C12^2) C44} + \right. \\
 & \quad \left. (-2 C11^2 (\sigma_{XY} - 2 \sigma_{XZ} + 2 \sigma_{YZ}) + \right. \\
 & \quad \left. 2 C12 (2 C12 (\sigma_{XY} - 2 \sigma_{XZ} + 2 \sigma_{YZ}) + C44 (-2 (\sigma_{XX} + \sigma_{YY}) + \sigma_{ZZ})) + \right. \\
 & \quad \left. C11 (-2 C12 (\sigma_{XY} - 2 \sigma_{XZ} + 2 \sigma_{YZ}) + C44 (\sigma_{XX} + \sigma_{YY} + 4 \sigma_{ZZ})) \right) / \\
 & \quad \left. (6 (C11 - C12) (C11 + 2 C12) C44) \right)
 \end{aligned}$$

Calculate strain-induced level shifts for NV1-4

Our formalism is based on σ_{XYZ} (see above -- all expressions for M_x , M_y , and M_z depend on stress tensor components). To extract level shifts for certain cantilever directions, we therefore need to use the corresponding stress tensors.

The final results for strain-induced level shifts are given in dependence of stiffness tensor components $C11$, $C12$ and $C44$. The following relations are used to rewrite them:

$$E = (C11 - C12)(C11 + 2 \cdot C12)/(C11 + C12)$$

$$\nu = \frac{C12}{C11} + C12$$

$$(1-\nu) = C11/(C11 + C12)$$

$$\nu = (C11 - C12)/C44$$

```

fixedpar100 =
  {σXX → 1, σXY → 0, σXZ → 0, σYX → 0, σYY → 0, σYZ → 0, σZX → 0, σZY → 0, σZZ → 0};
fixedpar110 = {σXX → 0.5, σXY → 0.5, σXZ → 0, σYX → 0.5,
  σYY → 0.5, σYZ → 0, σZX → 0, σZY → 0, σZZ → 0};
fixedpar111 = {σXX → 1/3, σXY → 1/3, σXZ → 1/3, σYX → 1/3,
  σYY → 1/3, σYZ → 1/3, σZX → 1/3, σZY → 1/3, σZZ → 1/3};

```

```

exzyNV1calc /. fixedpar100 // FullSimplify // MatrixForm
exzyNV1calc /. fixedpar110 // FullSimplify // MatrixForm
exzyNV1calc /. fixedpar111 // FullSimplify // MatrixForm

```

$$\begin{pmatrix} \frac{c11}{2c11^2+2c11c12-4c12^2} & \frac{1}{\sqrt{3}(2c11-2c12)} & -\frac{1}{\sqrt{6}(c11-c12)} \\ \frac{1}{\sqrt{3}(2c11-2c12)} & \frac{c11-4c12}{6(c11^2+c11c12-2c12^2)} & -\frac{1}{3\sqrt{2}(c11-c12)} \\ -\frac{1}{\sqrt{6}(c11-c12)} & -\frac{1}{3\sqrt{2}(c11-c12)} & \frac{1}{3c11+6c12} \end{pmatrix}$$

$$\begin{pmatrix} \frac{0.5c11}{1.c11^2+1.c11c12-2.c12^2} - \frac{0.5}{c44} & 0. & 0. \\ 0. & \frac{0.166667c11-0.666667c12}{1.c11^2+1.c11c12-2.c12^2} + \frac{0.166667}{c44} & -\frac{0.235702}{1.c11-1.c12} - \frac{0.235702}{c44} \\ 0. & -\frac{0.235702}{1.c11-1.c12} - \frac{0.235702}{c44} & \frac{0.333333}{1.c11+2.c12} + \frac{0.333333}{c44} \end{pmatrix}$$

$$\begin{pmatrix} \frac{1}{3} \left(\frac{1}{c11+2c12} - \frac{1}{c44} \right) & 0 & 0 \\ 0 & \frac{1}{3} \left(\frac{1}{c11+2c12} - \frac{1}{c44} \right) & 0 \\ 0 & 0 & \frac{2c11+4c12+c44}{3c11c44+6c12c44} \end{pmatrix}$$

3. Miscellaneous

```
ClearAll["Global`*"] (*clearing all variables*)
```

3.1 Expressing spin-strain coupling Hamiltonians in different basis

spin-orbit basis

```
(*The corrected spin-orbit states are called  $\{\Phi_{1,A1}^{so'}, \Phi_{1,Ex}^{so'}, \Phi_{1,Ey}^{so'}\}$  in Doherty2012  
(PRB85, 205203 (2012)) and  $\{|A1\rangle, |Ex\rangle, |Ey\rangle\}$  in Barson2017*)
```

```
SxSO = ħ {{0, 0, -i}, {0, 0, 0}, {i, 0, 0}};  
SySO = ħ {{0, i, 0}, {-i, 0, 0}, {0, 0, 0}};  
SzSO = ħ {{0, 0, 0}, {0, 0, -i}, {0, i, 0}};  
SzSO.SzSO  
SySO.SySO - SxSO.SxSO // FullSimplify  
SxSO.SySO + SySO.SxSO
```

```
{{0, 0, 0}, {0, ħ2, 0}, {0, 0, ħ2}}
```

```
{{0, 0, 0}, {0, ħ2, 0}, {0, 0, -ħ2}}
```

```
{{0, 0, 0}, {0, 0, -ħ2}, {0, -ħ2, 0}}
```

```
(*The strain Hamiltonian in the ground state +  
therefore takes the following form --> eq. (23) in Doherty2012
```

```
VstrSO =  $\frac{1}{\hbar^2} * (dpar * \sigma_z * SzSO.SzSO +$   
dperp *  $\sigma_x * (SySO.SySO - SxSO.SxSO) + dperp * \sigma_y * (SxSO.SySO + SySO.SxSO)$ );  
MatrixForm[VstrSO] // FullSimplify
```

```

$$\begin{pmatrix} 0 & 0 & 0 \\ 0 & dperp \sigma_x + dpar \sigma_z & -dperp \sigma_y \\ 0 & -dperp \sigma_y & -dperp \sigma_x + dpar \sigma_z \end{pmatrix}$$

```

spin basis

```
(*see for example www.easyspin.org*)

Sx = ħ / Sqrt[2] * {{0, 1, 0}, {1, 0, 1}, {0, 1, 0}};
Sy = -i ħ / Sqrt[2] * {{0, 1, 0}, {-1, 0, 1}, {0, -1, 0}};
Sz = ħ {{1, 0, 0}, {0, 0, 0}, {0, 0, 1}};

(*In this case, the strain Vstr takes the following form in the {|-1>,|0>,|+
1>} basis *)

Vstr =
  1
  ħ² (dpar * oz * Sz.Sz + dperp * ox * (Sy.Sy - Sx.Sx) + dperp * oy * (Sx.Sy + Sy.Sx));
Vstrtemp = 1
          ħ² (Mztemp * Sz.Sz + Mxtemp * (Sx.Sx - Sy.Sy) - Mytemp * (Sx.Sy + Sy.Sx));
MatrixForm[Vstr] // FullSimplify

(
  dpar oz      0 -dperp (ox + i oy)
  0            0      0
 -dperp (ox - i oy) 0      dpar oz
)
```

3.2 Testing rotations - Voigt and standard notation

```
(*Runciman1967 define a fixed NV orientation with z||[111],
x||[-110] and y||[-1-12]. In the SOM of Barson et al. they convert
stress in the crystal basis to strain in the NV basis by performing
the rotations [100]→[-1-12], [010]→[1-10] and [001]→[111].*)
```

define 3x3 rotation

```
Rx[xdeg_] := RotationMatrix[xdeg / 180 * π, {1, 0, 0}]
Ry[ydeg_] := RotationMatrix[ydeg / 180 * π, {0, 1, 0}]
Rz[zdeg_] := RotationMatrix[zdeg / 180 * π, {0, 0, 1}]
Rm1p10[deg_] := RotationMatrix[deg / 180 * π, {-1, 1, 0}]
Rp1p10[deg_] := RotationMatrix[deg / 180 * π, {1, 1, 0}]
R111[deg_] := RotationMatrix[deg / 180 * π, {1, 1, 1}]
Rpar111[vec_] := RotationMatrix[{vec, {1, 1, 1}}]
```

define rotations such that [100] -> [11-2], [010] -> [-110] and [001] -> [111]

Rotation as e.g. in Doherty2012 : Rm1p10[ArcCos[1/Sqrt[3]]/π*180].Rz[45]
 Note that the NV coordinate system is defined such that the x axis is contained by one of the mirror planes

```
unitx = UnitVector[3, 1];
unity = UnitVector[3, 2];
unitz = UnitVector[3, 3];
```

(*this approach starts with a rotation of 135deg about the z-axis,
followed with aligning the [001] direction to [111]*)

```
rot1 = Rpar111[{0, 0, 1}].Rz[45];
rot1vecx = rot1.unitx;
rot1vecy = rot1.unity;
rot1vecz = rot1.unitz;
MatrixForm[{rot1, Sqrt[6] * rot1vecx, Sqrt[2] * rot1vecy, Sqrt[3] * rot1vecz}] //
FullSimplify
```

$$\left(\begin{array}{ccc} \left\{ \frac{1}{\sqrt{6}}, -\frac{1}{\sqrt{2}}, \frac{1}{\sqrt{3}} \right\} & \left\{ \frac{1}{\sqrt{6}}, \frac{1}{\sqrt{2}}, \frac{1}{\sqrt{3}} \right\} & \left\{ -\sqrt{\frac{2}{3}}, 0, \frac{1}{\sqrt{3}} \right\} \\ 1 & 1 & -2 \\ -1 & 1 & 0 \\ 1 & 1 & 1 \end{array} \right)$$

(*the next approach also starts with rotating by 45deg about the z-axis,
but than rotates by about 54.3deg about the [-110] axis,
i.e. the x-axis of the NV center*)

```
rot2 = Rm1p10[ArcCos[1 / Sqrt[3]] / π * 180].Rz[45];
rot2vecx = rot2.unitx;
rot2vecy = rot2.unity;
rot2vecz = rot2.unitz;
MatrixForm[{rot2, Sqrt[6] * rot2vecx, Sqrt[2] * rot2vecy, Sqrt[3] * rot2vecz}] //
FullSimplify
```

$$\left(\begin{array}{ccc} \left\{ \frac{1}{\sqrt{6}}, -\frac{1}{\sqrt{2}}, \frac{1}{\sqrt{3}} \right\} & \left\{ \frac{1}{\sqrt{6}}, \frac{1}{\sqrt{2}}, \frac{1}{\sqrt{3}} \right\} & \left\{ -\sqrt{\frac{2}{3}}, 0, \frac{1}{\sqrt{3}} \right\} \\ 1 & 1 & -2 \\ -1 & 1 & 0 \\ 1 & 1 & 1 \end{array} \right)$$

define rotations such that [100] -> [-1-12], [010] -> [1-10] and [001] -> [111]

Rotation as in Barson2017 : Rm1p10[ArcCos[1/Sqrt[3]]/π*180].Rz[225]

Note that the NV coordinate system is defined such that the x axis is contained by one of the mirror planes, but different to the NV orientation from Doherty2012

24 | *StrainStressCoupling_Complete_forthesis.nb*

```

rot3 = Rpar111[{0, 0, 1}].Rz[225];
rot3vecx = rot3.unitx;
rot3vecy = rot3.unity;
rot3vecz = rot3.unitz;
MatrixForm[{rot3, Sqrt[6] * rot3vecx, Sqrt[2] * rot3vecy, Sqrt[3] * rot3vecz}] //
FullSimplify

```

$$\left(\begin{array}{ccc} \left\{ -\frac{1}{\sqrt{6}}, \frac{1}{\sqrt{2}}, \frac{1}{\sqrt{3}} \right\} & \left\{ -\frac{1}{\sqrt{6}}, -\frac{1}{\sqrt{2}}, \frac{1}{\sqrt{3}} \right\} & \left\{ \sqrt{\frac{2}{3}}, 0, \frac{1}{\sqrt{3}} \right\} \\ -1 & -1 & 2 \\ 1 & -1 & 0 \\ 1 & 1 & 1 \end{array} \right)$$

```

rot4 = Rmlp10[ArcCos[1 / Sqrt[3]] / π * 180].Rz[225];
rot4vecx = rot4.unitx;
rot4vecy = rot4.unity;
rot4vecz = rot4.unitz;
MatrixForm[{rot4, Sqrt[6] * rot4vecx, Sqrt[2] * rot4vecy, Sqrt[3] * rot4vecz}] //
FullSimplify

```

$$\left(\begin{array}{ccc} \left\{ -\frac{1}{\sqrt{6}}, \frac{1}{\sqrt{2}}, \frac{1}{\sqrt{3}} \right\} & \left\{ -\frac{1}{\sqrt{6}}, -\frac{1}{\sqrt{2}}, \frac{1}{\sqrt{3}} \right\} & \left\{ \sqrt{\frac{2}{3}}, 0, \frac{1}{\sqrt{3}} \right\} \\ -1 & -1 & 2 \\ 1 & -1 & 0 \\ 1 & 1 & 1 \end{array} \right)$$

define rotations such that [100] -> [-110], [010] -> [-1-12] and [001] -> [111]

Rotation to match NV orientation from Hughes1967 : Rm1p10[ArcCos[1/Sqrt[3]]/π*180].Rz[135]
 In contrast to the two rotations defined above, here one of the mirror planes contains the y axis!

```

rot5 = Rmlp10[ArcCos[1 / Sqrt[3]] / π * 180].Rz[135];
rot5vecx = rot5.unitx;
rot5vecy = rot5.unity;
rot5vecz = rot5.unitz;
MatrixForm[{rot5, Sqrt[2] * rot5vecx, Sqrt[6] * rot5vecy, Sqrt[3] * rot5vecz}] //
FullSimplify

```

$$\left(\begin{array}{ccc} \left\{ -\frac{1}{\sqrt{2}}, -\frac{1}{\sqrt{6}}, \frac{1}{\sqrt{3}} \right\} & \left\{ \frac{1}{\sqrt{2}}, -\frac{1}{\sqrt{6}}, \frac{1}{\sqrt{3}} \right\} & \left\{ 0, \sqrt{\frac{2}{3}}, \frac{1}{\sqrt{3}} \right\} \\ -1 & 1 & 0 \\ -1 & -1 & 2 \\ 1 & 1 & 1 \end{array} \right)$$

convert 3 x3 rotation matrix into 6 x6 rotation matrix - compare methods
 from Koay2009 and Mehrabadi1995

To convert strain to stress and change the coordinate system from crystal to NV, we need to rotate the strain/stress tensor. These can be expressed in a 6x1 vector in Voigt notation. Consequently, to rotate these we need to define a 6x6 rotation matrix. These two papers which deal with exactly this problem:

- Mehrabadi et al., Int. Journal of Solids and Structures 32, 439 (1995).
- Koay et al., Mechanics of Materials 41, 951 (2009).

Going to use the formalism from Mehrabadi1995.

```
pvec = {p1, p2, p3}; (*unit vector about we rotate*)
P3x3 = {{0, -pvec[[3]], pvec[[2]]},
        {pvec[[3]], 0, -pvec[[1]]}, {-pvec[[2]], pvec[[1]], 0}};
(*skew-symmetric tensor in 3x3 form*)
Rot3x3[deg_] :=
  IdentityMatrix[3] + Sin[deg * π / 180] * P3x3 + (1 - Cos[deg * π / 180]) * P3x3.P3x3;
(*equation (1) from Mehrabadi1995*)
P6x6 = {{0, 0, 0, 0, Sqrt[2] * pvec[[2]], -Sqrt[2] * pvec[[3]]},
        {0, 0, 0, -Sqrt[2] * pvec[[1]], 0, Sqrt[2] * pvec[[3]]},
        {0, 0, 0, Sqrt[2] * pvec[[1]], -Sqrt[2] * pvec[[2]], 0},
        {0, Sqrt[2] * pvec[[1]], -Sqrt[2] * pvec[[1]], 0, pvec[[3]], -pvec[[2]]},
        {-Sqrt[2] * pvec[[2]], 0, Sqrt[2] * pvec[[2]], -pvec[[3]], 0, pvec[[1]]},
        {Sqrt[2] * pvec[[3]], -Sqrt[2] * pvec[[3]], 0, pvec[[2]], -pvec[[1]], 0}};
(*skew-symmetric tensor in 6x6 form,
eq. (5) from Mehrabadi1995*)
Rot6x6[deg_] :=
  IdentityMatrix[6] + Sin[deg * π / 180] * P6x6 + (1 - Cos[deg * π / 180]) * P6x6.P6x6 +
  1 / 3 * Sin[deg * π / 180] * (1 - Cos[deg * π / 180]) * (P6x6 + P6x6.P6x6.P6x6) +
  1 / 6 * (1 - Cos[deg * π / 180]) ^ 2 * (P6x6.P6x6 + P6x6.P6x6.P6x6)
(*rotation matrix as in eq. (4) from Mehrabadi1995*)
```

(*Note that the vector pvec needs to be normalized such that Rot6x6 is still orthogonal*)

```
Transpose[Rot6x6[10]].Rot6x6[10] /.
  {p1 → 2 / Sqrt[6], p2 → 1 / Sqrt[6], p3 → 1 / Sqrt[6]} // N // Chop
{{1., 0, 0, 0, 0, 0}, {0, 1., 0, 0, 0, 0}, {0, 0, 1., 0, 0, 0},
 {0, 0, 0, 1., 0, 0}, {0, 0, 0, 0, 1., 0}, {0, 0, 0, 0, 0, 1.}}
```

rotate strain tensor and strain tensor in Voigt notation and compare to matrix notation

Voigt notation

```
Rz6x6[deg_] := Rot6x6[deg] /. {p1 → 0, p2 → 0, p3 → 1}
(*rotation about the z-axis*)
Rmlp106x6[deg_] := Rot6x6[deg] /. {p1 → -1 / Sqrt[2], p2 → 1 / Sqrt[2], p3 → 0}
(*rotation about the [-110] axis*)
R1116x6[deg_] := Rot6x6[deg] /. {p1 → 1 / Sqrt[3], p2 → 1 / Sqrt[3], p3 → 1 / Sqrt[3]}
(*rotation about the [111] axis*)
```

```
Kvoigt = Rmlp106x6[ArcCos[1 / Sqrt[3]] / π * 180].Rz6x6[45];
```

```
Transpose[Kvoigt].Kvoigt // N // Chop // MatrixForm;
```

```
ovoigt = {σXX, σYY, σZZ, Sqrt[2] * σYZ, Sqrt[2] * σXZ, Sqrt[2] * σXY};
ovoigtrot = Kvoigt.ovoigt;
MatrixForm[ovoigtrot // N // Chop]
```

$$\begin{pmatrix} 0.166667 \sigma_{XX} - 0.57735 \sigma_{XY} + 0.471405 \sigma_{XZ} + 0.5 \sigma_{YY} - 0.816497 \sigma_{YZ} + 0.333333 \sigma_{ZZ} \\ 0.166667 \sigma_{XX} + 0.57735 \sigma_{XY} + 0.471405 \sigma_{XZ} + 0.5 \sigma_{YY} + 0.816497 \sigma_{YZ} + 0.333333 \sigma_{ZZ} \\ 0.666667 \sigma_{XX} - 0.942809 \sigma_{XZ} + 0.333333 \sigma_{ZZ} \\ -0.471405 \sigma_{XX} - 0.816497 \sigma_{XY} - 0.333333 \sigma_{XZ} + 0.57735 \sigma_{YZ} + 0.471405 \sigma_{ZZ} \\ -0.471405 \sigma_{XX} + 0.816497 \sigma_{XY} - 0.333333 \sigma_{XZ} - 0.57735 \sigma_{YZ} + 0.471405 \sigma_{ZZ} \\ 0.235702 \sigma_{XX} + 0.666667 \sigma_{XZ} - 0.707107 \sigma_{YY} + 0.471405 \sigma_{ZZ} \end{pmatrix}$$

Matrix notation

```
K3x3 = Rmlp10[ArcCos[1 / Sqrt[3]] / π * 180].Rz[45];
σ3x3 = {{σXX, σXY, σXZ}, {σYX, σYY, σYZ}, {σZX, σZY, σZZ}};
σ3x3rot =
  K3x3.σ3x3.Transpose[K3x3] /. {σZY → σYZ, σZX → σXZ, σYX → σXY} // N //
  FullSimplify;
MatrixForm[σ3x3rot]
```

$$\begin{pmatrix} 0.166667 \sigma_{XX} - 0.57735 \sigma_{XY} + 0.471405 \sigma_{XZ} + 0.5 \sigma_{YY} - 0.816497 \sigma_{YZ} + 0.333333 \sigma_{ZZ} & & \\ & 0. + 0.166667 \sigma_{XX} + 0.471405 \sigma_{XZ} - 0.5 \sigma_{YY} + 0.333333 \sigma_{ZZ} & 0.1666 \\ -0.333333 \sigma_{XX} + 0.57735 \sigma_{XY} - 0.235702 \sigma_{XZ} - 0.408248 \sigma_{YZ} + 0.333333 \sigma_{ZZ} & & -0 \end{pmatrix}$$

Comparison

```

ovoigtrot[[1]]/σ3x3rot[[1,1]]//N//FullSimplify//Chop
ovoigtrot[[2]]/σ3x3rot[[2,2]]//N//FullSimplify//Chop
ovoigtrot[[3]]/σ3x3rot[[3,3]]//N//FullSimplify//Chop
ovoigtrot[[4]]/Sqrt[2]/σ3x3rot[[2,3]]//N//FullSimplify//Chop
ovoigtrot[[5]]/Sqrt[2]/σ3x3rot[[1,3]]//N//FullSimplify//Chop
ovoigtrot[[6]]/Sqrt[2]/σ3x3rot[[1,2]]//N//FullSimplify//Chop

```

1.

1.

1.

1.

$$\frac{-0.333333 \sigma_{XX} + 0.57735 \sigma_{XY} - 0.235702 \sigma_{XZ} - 0.408248 \sigma_{YZ} + 0.333333 \sigma_{ZZ}}{-0.333333 \sigma_{XX} + 0.57735 \sigma_{XY} - 0.235702 \sigma_{XZ} - 0.408248 \sigma_{YZ} + 0.333333 \sigma_{ZZ}}$$

1.

```

(*When comparing both ways of doing the rotation,
   one finds that both are the same if: a) one assumes  $\sigma_{ij}=\sigma_{ji}$  and b)
   takes into account the additional factor of Sqrt[2] that is
   present in the definition of ovoigt.*)

```

3.3 Converting stress tensor in crystal coordinates XYZ to strain in NV coordinates xyz for three different NV orientations

NV orientation from Barson2017

It is important to know that we are using a `Transpose[Transpose[[Rot]]` expression here. This is because our rotation “KBarson6x6” rotates vectors --> active transformation. We however want to keep the vector fixed and rotate the coordinate system and thus need to work with the inverse of the rotation matrix --> passive transformation.*)

```

CXYZ = {{C11, C12, C12, 0, 0, 0}, {C12, C11, C12, 0, 0, 0}, {C12, C12, C11, 0, 0, 0},
        {0, 0, 0, C44, 0, 0}, {0, 0, 0, 0, C44, 0}, {0, 0, 0, 0, 0, C44}};
(*stiffness tensor for a cubic material, e.g. diamond;
taken from Gross, Festkoerperphysik;*)
MatrixForm[CXYZ]

```

$$\begin{pmatrix} C11 & C12 & C12 & 0 & 0 & 0 \\ C12 & C11 & C12 & 0 & 0 & 0 \\ C12 & C12 & C11 & 0 & 0 & 0 \\ 0 & 0 & 0 & C44 & 0 & 0 \\ 0 & 0 & 0 & 0 & C44 & 0 \\ 0 & 0 & 0 & 0 & 0 & C44 \end{pmatrix}$$

```

exzy6x6 = {exx, eyy, ezz, Sqrt[2] * eyz, Sqrt[2] * exz, Sqrt[2] * exy};
(*in NV coordinate system*)
oXYZ6x6 = {oXX, oYY, oZZ, Sqrt[2] * oYZ, Sqrt[2] * oXZ, Sqrt[2] * oYX};
(*in NV coordinate system*)
KBarson6x6 = Rm1p106x6[ArcCos[1 / Sqrt[3]] / π * 180].Rz6x6[225];
(*rotation from NV coordinate system to cubic coordinate system*)
exyz6x6rotBarson =
  Transpose[KBarson6x6].Inverse[CXYZ].oXYZ6x6 // FullSimplify;
oXYZ6x6rot = CXYZ.Inverse[Transpose[KBarson6x6]].exzy6x6 // FullSimplify;
oXYZ6x6rot2 = CXYZ2.Inverse[Transpose[KBarson6x6]].exzy6x6 // FullSimplify;
(*convert stress in XYZ to strain in xyz, using voigt notation;
MatrixForm[exyz6x6rotBarson];

```

```

Mz = a1 * (oXYZ6x6rot[[1]] + oXYZ6x6rot[[2]] + oXYZ6x6rot[[3]]) +
  2 * a2 * (oXYZ6x6rot[[4]] / Sqrt[2] + oXYZ6x6rot[[5]] / Sqrt[2] +
  oXYZ6x6rot[[6]] / Sqrt[2]) // FullSimplify
Mx = b * (2 * oXYZ6x6rot[[3]] - oXYZ6x6rot[[1]] - oXYZ6x6rot[[2]]) +
  c * (2 * oXYZ6x6rot[[6]] / Sqrt[2] - oXYZ6x6rot[[4]] / Sqrt[2] -
  oXYZ6x6rot[[5]] / Sqrt[2]) // FullSimplify
My = Sqrt[3] * b * (oXYZ6x6rot[[1]] - oXYZ6x6rot[[2]]) + Sqrt[3] * c *
  (oXYZ6x6rot[[4]] / Sqrt[2] - oXYZ6x6rot[[5]] / Sqrt[2]) // FullSimplify

```

$$-a2 C44 (\epsilon_{xx} + \epsilon_{yy} - 2 \epsilon_{zz}) + a1 (C11 + 2 C12) (\epsilon_{xx} + \epsilon_{yy} + \epsilon_{zz})$$

$$c C44 (\epsilon_{xx} - \sqrt{2} \epsilon_{xz} - \epsilon_{yy}) + b (C11 - C12) (\epsilon_{xx} + 2 \sqrt{2} \epsilon_{xz} - \epsilon_{yy})$$

$$-2 b (C11 - C12) (\epsilon_{xy} - \sqrt{2} \epsilon_{yz}) - c C44 (2 \epsilon_{xy} + \sqrt{2} \epsilon_{yz})$$

NV orientation from Hughes1967 (compare to results from Ludlow1968)

```

KHughes6x6 = Rm1p106x6[ArcCos[1 / Sqrt[3]] /  $\pi$  * 180].Rz6x6[135];
 $\sigma$ XZY6x6rotHughes =
  CXYZ.Inverse[Transpose[KHughes6x6]].exzy6x6 // FullSimplify;
MatrixForm[ $\sigma$ XZY6x6rotHughes];

```

```

Mz = a1 * ( $\sigma$ XZY6x6rotHughes[[1]] +  $\sigma$ XZY6x6rotHughes[[2]] +  $\sigma$ XZY6x6rotHughes[[3]]) +
  2 * a2 * ( $\sigma$ XZY6x6rotHughes[[4]] / Sqrt[2] +  $\sigma$ XZY6x6rotHughes[[5]] / Sqrt[2] +
   $\sigma$ XZY6x6rotHughes[[6]] / Sqrt[2]) // FullSimplify
Mx = b * (2 *  $\sigma$ XZY6x6rotHughes[[3]] -  $\sigma$ XZY6x6rotHughes[[1]] -
   $\sigma$ XZY6x6rotHughes[[2]]) +
  c * (2 *  $\sigma$ XZY6x6rotHughes[[6]] / Sqrt[2] -  $\sigma$ XZY6x6rotHughes[[4]] / Sqrt[2] -
   $\sigma$ XZY6x6rotHughes[[5]] / Sqrt[2]) // FullSimplify
My = Sqrt[3] * b * ( $\sigma$ XZY6x6rotHughes[[1]] -  $\sigma$ XZY6x6rotHughes[[2]]) +
  Sqrt[3] * c * ( $\sigma$ XZY6x6rotHughes[[4]] / Sqrt[2] -
   $\sigma$ XZY6x6rotHughes[[5]] / Sqrt[2]) // FullSimplify

```

```
-a2 C44 (exx + eyy - 2 ezz) + a1 (C11 + 2 C12) (exx + eyy + ezz)
```

```
-b (C11 - C12) (exx - eyy - 2  $\sqrt{2}$  eyz) - c C44 (exx - eyy +  $\sqrt{2}$  eyz)
```

```
2 b (C11 - C12) (exy -  $\sqrt{2}$  exz) + c C44 (2 exy +  $\sqrt{2}$  exz)
```

NV orientation from Doherty2012

```

KDoherty6x6 = Rmlp106x6[ArcCos[1 / Sqrt[3]] /  $\pi$  * 180].Rz6x6[45];
 $\sigma$ XZY6x6rot2Doherty =
  CXYZ.Inverse[Transpose[KDoherty6x6]].exyz6x6 // FullSimplify;
exyz6x6rotDoherty = Transpose[KDoherty6x6].Inverse[CXYZ]. $\sigma$ XZY6x6 //
  FullSimplify;
MatrixForm[exyz6x6rotDoherty]
Mz = a1 * ( $\sigma$ XZY6x6rot2Doherty[[1]] +
   $\sigma$ XZY6x6rot2Doherty[[2]] +  $\sigma$ XZY6x6rot2Doherty[[3]]) +
  2 * a2 * ( $\sigma$ XZY6x6rot2Doherty[[4]] / Sqrt[2] +  $\sigma$ XZY6x6rot2Doherty[[5]] / Sqrt[2] +
   $\sigma$ XZY6x6rot2Doherty[[6]] / Sqrt[2]) // FullSimplify
Mx = b * (2 *  $\sigma$ XZY6x6rot2Doherty[[3]] -  $\sigma$ XZY6x6rot2Doherty[[1]]) -
   $\sigma$ XZY6x6rot2Doherty[[2]]) +
  c * (2 *  $\sigma$ XZY6x6rot2Doherty[[6]] / Sqrt[2] -  $\sigma$ XZY6x6rot2Doherty[[4]] / Sqrt[2] -
   $\sigma$ XZY6x6rot2Doherty[[5]] / Sqrt[2]) // FullSimplify
My = Sqrt[3] * b * ( $\sigma$ XZY6x6rot2Doherty[[1]] -  $\sigma$ XZY6x6rot2Doherty[[2]]) +
  Sqrt[3] * c * ( $\sigma$ XZY6x6rot2Doherty[[4]] / Sqrt[2] -
   $\sigma$ XZY6x6rot2Doherty[[5]] / Sqrt[2]) // FullSimplify

```

$$\left(\begin{array}{l} \frac{2 C_{11}^2 (-2 \sigma_{XZ} + \sigma_{YX} - 2 \sigma_{YZ}) + 2 C_{12} (2 C_{12} (2 \sigma_{XZ} - \sigma_{YX} + 2 \sigma_{YZ}) + C_{44} (-2 (\sigma_{XX} + \sigma_{YY}) + \sigma_{ZZ})) + C_{11} (2 C_{12} (-2 \sigma_{XZ} + \sigma_{YX} - 2 \sigma_{YZ}) + C_{44} (\sigma_{XX} + \sigma_{YY} - 2 \sigma_{ZZ}))}{6 (C_{11} - C_{12}) (C_{11} + 2 C_{12}) C_{44}} \\ \frac{C_{11} C_{44} \sigma_{XX} - 2 C_{11}^2 \sigma_{YX} - 2 C_{11} C_{12} \sigma_{YX} + 4 C_{12}^2 \sigma_{YX} + C_{11} C_{44} \sigma_{YY} - 2 C_{12} C_{44} \sigma_{ZZ}}{2 C_{11}^2 C_{44} + 2 C_{11} C_{12} C_{44} - 4 C_{12}^2 C_{44}} \\ \frac{2 (C_{11} + 2 C_{12}) (\sigma_{XZ} + \sigma_{YX} + \sigma_{YZ}) + C_{44} (\sigma_{XX} + \sigma_{YY} + \sigma_{ZZ})}{3 (C_{11} + 2 C_{12}) C_{44}} \\ \frac{C_{44} (-\sigma_{XX} + \sigma_{YY}) - (C_{11} - C_{12}) (\sigma_{XZ} - \sigma_{YZ})}{\sqrt{3} (C_{11} - C_{12}) C_{44}} \\ \frac{-(C_{11} - C_{12}) (\sigma_{XZ} - 2 \sigma_{YX} + \sigma_{YZ}) + C_{44} (\sigma_{XX} + \sigma_{YY} - 2 \sigma_{ZZ})}{3 (C_{11} - C_{12}) C_{44}} \\ \frac{C_{44} (-\sigma_{XX} + \sigma_{YY}) + 2 (C_{11} - C_{12}) (\sigma_{XZ} - \sigma_{YZ})}{\sqrt{6} (C_{11} - C_{12}) C_{44}} \end{array} \right)$$

$$-a_2 C_{44} (\epsilon_{xx} + \epsilon_{yy} - 2 \epsilon_{zz}) + a_1 (C_{11} + 2 C_{12}) (\epsilon_{xx} + \epsilon_{yy} + \epsilon_{zz})$$

$$b (C_{11} - C_{12}) (\epsilon_{xx} - 2 \sqrt{2} \epsilon_{xz} - \epsilon_{yy}) + c C_{44} (\epsilon_{xx} + \sqrt{2} \epsilon_{xz} - \epsilon_{yy})$$

$$c C_{44} (-2 \epsilon_{xy} + \sqrt{2} \epsilon_{yz}) - 2 b (C_{11} - C_{12}) (\epsilon_{xy} + \sqrt{2} \epsilon_{yz})$$

Comparison of strain tensor elements for NVs with same quantization axis, but different x and y axes

```

exyz6x6rotHughes =
Transpose[KHughes6x6].Inverse[CXYZ].σXYZ6x6 // FullSimplify // MatrixForm
exyz6x6rotBarson =
Transpose[KBarson6x6].Inverse[CXYZ].σXYZ6x6 // FullSimplify // MatrixForm

```

$$\left(\begin{array}{c}
\frac{C11 C44 \sigma_{XX} - 2 C11^2 \sigma_{YX} - 2 C11 C12 \sigma_{YX} + 4 C12^2 \sigma_{YX} + C11 C44 \sigma_{YY} - 2 C12 C44 \sigma_{ZZ}}{2 C11^2 C44 + 2 C11 C12 C44 - 4 C12^2 C44} \\
\frac{2 C11^2 (-2 \sigma_{XZ} + \sigma_{YX} - 2 \sigma_{YZ}) + 2 C12 (2 C12 (2 \sigma_{XZ} - \sigma_{YX} + 2 \sigma_{YZ}) + C44 (-2 (\sigma_{XX} + \sigma_{YY}) + \sigma_{ZZ})) + C11 (2 C12 (-2 \sigma_{XZ} + \sigma_{YX} - 2 \sigma_{YZ}) + C44 (\sigma_{XX} + \sigma_{YY} - 2 \sigma_{ZZ}))}{6 (C11 - C12) (C11 + 2 C12) C44} \\
\frac{2 (C11 + 2 C12) (\sigma_{XZ} + \sigma_{YX} + \sigma_{YZ}) + C44 (\sigma_{XX} + \sigma_{YY} + \sigma_{ZZ})}{3 (C11 + 2 C12) C44} \\
\frac{(C11 - C12) (\sigma_{XZ} - 2 \sigma_{YX} + \sigma_{YZ}) - C44 (\sigma_{XX} + \sigma_{YY} - 2 \sigma_{ZZ})}{3 (C11 - C12) C44} \\
\frac{C44 (-\sigma_{XX} + \sigma_{YY}) - (C11 - C12) (\sigma_{XZ} - \sigma_{YZ})}{\sqrt{3} (C11 - C12) C44} \\
\frac{\frac{\sigma_{XX} - \sigma_{YY} - 2 (\sigma_{XZ} - \sigma_{YZ})}{C11 - C12} - \frac{C44}{C44}}{\sqrt{6}}
\end{array} \right)$$

$$\left(\begin{array}{c}
\frac{2 C11^2 (-2 \sigma_{XZ} + \sigma_{YX} - 2 \sigma_{YZ}) + 2 C12 (2 C12 (2 \sigma_{XZ} - \sigma_{YX} + 2 \sigma_{YZ}) + C44 (-2 (\sigma_{XX} + \sigma_{YY}) + \sigma_{ZZ})) + C11 (2 C12 (-2 \sigma_{XZ} + \sigma_{YX} - 2 \sigma_{YZ}) + C44 (\sigma_{XX} + \sigma_{YY} - 2 \sigma_{ZZ}))}{6 (C11 - C12) (C11 + 2 C12) C44} \\
\frac{C11 C44 \sigma_{XX} - 2 C11^2 \sigma_{YX} - 2 C11 C12 \sigma_{YX} + 4 C12^2 \sigma_{YX} + C11 C44 \sigma_{YY} - 2 C12 C44 \sigma_{ZZ}}{2 C11^2 C44 + 2 C11 C12 C44 - 4 C12^2 C44} \\
\frac{2 (C11 + 2 C12) (\sigma_{XZ} + \sigma_{YX} + \sigma_{YZ}) + C44 (\sigma_{XX} + \sigma_{YY} + \sigma_{ZZ})}{3 (C11 + 2 C12) C44} \\
\frac{\frac{\sigma_{XX} - \sigma_{YY} + \sigma_{XZ} - \sigma_{YZ}}{C11 - C12} - \frac{C44}{C44}}{\sqrt{3}} \\
\frac{(C11 - C12) (\sigma_{XZ} - 2 \sigma_{YX} + \sigma_{YZ}) - C44 (\sigma_{XX} + \sigma_{YY} - 2 \sigma_{ZZ})}{3 (C11 - C12) C44} \\
\frac{C44 (-\sigma_{XX} + \sigma_{YY}) + 2 (C11 - C12) (\sigma_{XZ} - \sigma_{YZ})}{\sqrt{6} (C11 - C12) C44}
\end{array} \right)$$

3.4 Rotations in spin-space

```
RotSpin[p_, deg_] := MatrixExp[-i p deg π / (180 ħ)]
```

32 | *StrainStressCoupling_Complete_forthesis.nb*

```
alpha = -90;
RotSpin[Sz, alpha].Vstr.Inverse[RotSpin[Sz, alpha]] // FullSimplify //
MatrixForm
MatrixForm[Vstr] // FullSimplify

RotSpin[SzSO, alpha].VstrSO.Inverse[RotSpin[SzSO, alpha]] // FullSimplify //
MatrixForm
MatrixForm[VstrSO] // FullSimplify
```

$$\begin{pmatrix} \text{dpar } \sigma_z & 0 & -\text{dperp } (\sigma_x + i \sigma_y) \\ 0 & 0 & 0 \\ -\text{dperp } (\sigma_x - i \sigma_y) & 0 & \text{dpar } \sigma_z \end{pmatrix}$$

$$\begin{pmatrix} \text{dpar } \sigma_z & 0 & -\text{dperp } (\sigma_x + i \sigma_y) \\ 0 & 0 & 0 \\ -\text{dperp } (\sigma_x - i \sigma_y) & 0 & \text{dpar } \sigma_z \end{pmatrix}$$

$$\begin{pmatrix} 0 & 0 & 0 \\ 0 & -\text{dperp } \sigma_x + \text{dpar } \sigma_z & \text{dperp } \sigma_y \\ 0 & \text{dperp } \sigma_y & \text{dperp } \sigma_x + \text{dpar } \sigma_z \end{pmatrix}$$

$$\begin{pmatrix} 0 & 0 & 0 \\ 0 & \text{dperp } \sigma_x + \text{dpar } \sigma_z & -\text{dperp } \sigma_y \\ 0 & -\text{dperp } \sigma_y & -\text{dperp } \sigma_x + \text{dpar } \sigma_z \end{pmatrix}$$

B. Bibliography

- [1] J. Teissier, A. Barfuss, P. Appel, E. Neu, and P. Maletinsky, *Strain Coupling of a Nitrogen-Vacancy Center Spin to a Diamond Mechanical Oscillator*, [Physical Review Letters](#) **113**, 020503 (2014).
- [2] D. P. DiVincenzo, *The Physical Implementation of Quantum Computation*, [Fortschritte der Physik](#) **48**, 771 (2000).
- [3] T. D. Ladd, F. Jelezko, R. Laflamme, Y. Nakamura, C. Monroe, and J. L. O'Brien, *Quantum computers*, [Nature](#) **464**, 45 (2010).
- [4] N. Gisin, G. Ribordy, W. Tittel, and H. Zbinden, *Quantum cryptography*, [Review of Modern Physics](#) **74**, 145 (2002).
- [5] C. L. Degen, F. Reinhard, and P. Cappellaro, *Quantum sensing*, [Reviews of Modern Physics](#) **89**, 035002 (2017).
- [6] J. Ma, X. Wang, C. P. Sun, and F. Nori, *Quantum spin squeezing*, [Physics Reports](#) **509**, 89 (2011).
- [7] R. Hanson, L. P. Kouwenhoven, J. R. Petta, S. Tarucha, and L. M. K. Vandersypen, *Spins in few-electron quantum dots*, [Review of Modern Physics](#) **79**, 1217 (2007).
- [8] J. Clarke and F. K. Wilhelm, *Superconducting quantum bits*, [Nature](#) **453**, 1031 (2008).
- [9] F. A. Zwanenburg, A. S. Dzurak, A. Morello, M. Y. Simmons, L. C. L. Hollenberg, G. Klimeck, S. Rogge, S. N. Coppersmith, and M. A. Eriksson, *Silicon quantum electronics*, [Review of Modern Physics](#) **85**, 961 (2013).
- [10] V. Dobrovitski, G. Fuchs, A. Falk, C. Santori, and D. Awschalom, *Quantum Control over Single Spins in Diamond*, [Annual Review of Condensed Matter Physics](#) **4**, 23 (2013).
- [11] R. Schirhagl, K. Chang, M. Loretz, and C. L. Degen, *Nitrogen-Vacancy Centers in Diamond: Nanoscale Sensors for Physics and Biology*, [Annual Review of Physical Chemistry](#) **65**, 83 (2014).
- [12] J. Stajic, *The Future of Quantum Information Processing*, [Science](#) **339**, 1163 (2013).
- [13] D. Lee, K. W. Lee, J. V. Cady, P. Ovartchaiyapong, and A. C. Bleszynski Jayich, *Topical review: spins and mechanics in diamond*, [Journal of Optics](#) **19**, 033001 (2017).

-
- [14] Z.-L. Xiang, S. Ashhab, J. Q. You, and F. Nori, *Hybrid quantum circuits: Superconducting circuits interacting with other quantum systems*, [Reviews of Modern Physics](#) **85**, 623 (2013).
- [15] C. L. Degen, F. Reinhard, and P. Cappellaro, *Quantum sensing*, [Reviews of Modern Physics](#) **89**, 035002 (2017).
- [16] D. Hunger, S. Camerer, T. W. Hänsch, D. König, J. P. Kotthaus, J. Reichel, and P. Treutlein, *Resonant Coupling of a Bose-Einstein Condensate to a Micromechanical Oscillator*, [Physical Review Letters](#) **104**, 143002 (2010).
- [17] A. D. O’Connell, M. Hofheinz, M. Ansmann, R. C. Bialczak, M. Lenander, E. Lucero, M. Neeley, D. Sank, H. Wang, M. Weides, J. Wenner, J. M. Martinis, and A. N. Cleland, *Quantum ground state and single-phonon control of a mechanical resonator*, [Nature](#) **464**, 697 (2010).
- [18] O. Arcizet, V. Jacques, A. Siria, P. Poncharal, P. Vincent, and S. Seidelin, *A single nitrogen-vacancy defect coupled to a nanomechanical oscillator*, [Nature Physics](#) **7**, 879 (2011).
- [19] P. Treutlein, C. Genes, K. Hammerer, M. Poggio, and P. Rabl, *Hybrid Mechanical Systems*, in M. Aspelmeyer, T. J. Kippenberg, and F. Marquardt (editors), *Cavity Optomechanics*, Quantum Science and Technology, pp. 327–351 (Springer Berlin Heidelberg) (2014).
- [20] S. J. M. Habraken, K. Stannigel, M. D. Lukin, P. Zoller, and P. Rabl, *Continuous mode cooling and phonon routers for phononic quantum networks*, [New Journal of Physics](#) **14**, 115004 (2012).
- [21] J. D. Teufel, T. Donner, D. Li, J. W. Harlow, M. S. Allman, K. Cicak, A. J. Sirois, J. D. Whittaker, K. W. Lehnert, and R. W. Simmonds, *Sideband cooling of micromechanical motion to the quantum ground state*, [Nature](#) **475**, 359 (2011).
- [22] J. Chan, T. P. M. Alegre, A. H. Safavi-Naeini, J. T. Hill, A. Krause, S. Groblacher, M. Aspelmeyer, and O. Painter, *Laser cooling of a nanomechanical oscillator into its quantum ground state*, [Nature](#) **478**, 89 (2011).
- [23] M. Underwood, D. Mason, D. Lee, H. Xu, L. Jiang, A. B. Shkarin, K. Børkje, S. M. Girvin, and J. G. E. Harris, *Measurement of the motional sidebands of a nanogram-scale oscillator in the quantum regime*, [Physical Review A](#) **92**, 061801 (2015).
- [24] T. A. Palomaki, J. D. Teufel, R. W. Simmonds, and K. W. Lehnert, *Entangling Mechanical Motion with Microwave Fields*, [Science](#) **342**, 710 (2013).
- [25] E. E. Wollman, C. U. Lei, A. J. Weinstein, J. Suh, A. Kronwald, F. Marquardt, A. A. Clerk, and K. C. Schwab, *Quantum squeezing of motion in a mechanical resonator*, [Science](#) **349**, 952 (2015).

-
- [26] F. Lecocq, J. B. Clark, R. W. Simmonds, J. Aumentado, and J. D. Teufel, *Quantum Nondemolition Measurement of a Nonclassical State of a Massive Object*, [Physical Review X](#) **5**, 041037 (2015).
- [27] U. L. Andersen, J. S. Neergaard-Nielsen, P. van Loock, and A. Furusawa, *Hybrid discrete- and continuous-variable quantum information*, [Nature Physics](#) **11**, 713 (2015).
- [28] M.-A. Lemonde, N. Didier, and A. A. Clerk, *Nonlinear Interaction Effects in a Strongly Driven Optomechanical Cavity*, [Physical Review Letters](#) **111**, 053602 (2013).
- [29] M. Aspelmeyer, T. J. Kippenberg, and F. Marquardt, *Cavity optomechanics*, [Review of Modern Physics](#) **86**, 1391 (2014).
- [30] M.-A. Lemonde, N. Didier, and A. A. Clerk, *Enhanced nonlinear interactions in quantum optomechanics via mechanical amplification*, [Nature Communications](#) **7**, 11338 (2016).
- [31] S. Etaki, M. Poot, I. Mahboob, K. Onomitsu, H. Yamaguchi, and H. S. J. van der Zant, *Motion detection of a micromechanical resonator embedded in a d.c. SQUID*, [Nature Physics](#) **4**, 785 (2008).
- [32] M. D. LaHaye, J. Suh, P. M. Echternach, K. C. Schwab, and M. L. Roukes, *Nanomechanical measurements of a superconducting qubit*, [Nature](#) **459**, 960 (2009).
- [33] J.-M. Pirkkalainen, S. U. Cho, J. Li, G. S. Paraoanu, P. J. Hakonen, and M. A. Sillanpää, *Hybrid circuit cavity quantum electrodynamics with a micromechanical resonator*, [Nature](#) **494**, 211 (2013).
- [34] S. Camerer, M. Korppi, A. Jöckel, D. Hunger, T. W. Hänsch, and P. Treutlein, *Realization of an Optomechanical Interface Between Ultracold Atoms and a Membrane*, [Physical Review Letters](#) **107**, 223001 (2011).
- [35] A. Jöckel, A. Faber, T. Kampschulte, M. Korppi, M. T. Rakher, and P. Treutlein, *Sympathetic cooling of a membrane oscillator in a hybrid mechanical-atomic system*, [Nature Nanotechnology](#) **10**, 55 (2015).
- [36] D. Rugar, R. Budakian, H. J. Mamin, and B. W. Chui, *Single spin detection by magnetic resonance force microscopy*, [Nature](#) **430**, 329 (2004).
- [37] S. Kolkowitz, A. C. Bleszynski Jayich, Q. P. Unterreithmeier, S. D. Bennett, P. Rabl, J. G. E. Harris, and M. D. Lukin, *Coherent Sensing of a Mechanical Resonator with a Single-Spin Qubit*, [Science](#) **335**, 1603 (2012).
- [38] I. Yeo, P.-L. de Assis, A. Gloppe, E. Dupont-Ferrier, P. Verlot, N. Malik, E. Dupuy, J. Claudon, J.-M. Gerard, A. Auffeves, G. Nogués, S. Seidelin, J.-P. Poizat, O. Arcizet, and M. Richard, *Strain-mediated coupling in a quantum dot-mechanical oscillator hybrid system*, [Nature Nanotechnology](#) **9**, 106 (2014).

- [39] M. Montinaro, G. Wüst, M. Munsch, Y. Fontana, E. Russo-Averchi, M. Heiss, A. Fontcuberta i Morral, R. J. Warburton, and M. Poggio, *Quantum Dot Opto-Mechanics in a Fully Self-Assembled Nanowire*, [Nano Letters](#) **14**, 4454 (2014).
- [40] M. Munsch, A. V. Kuhlmann, D. Cadeddu, J.-M. Gérard, J. Claudon, M. Poggio, and R. J. Warburton, *Resonant driving of a single photon emitter embedded in a mechanical oscillator*, [Nature Communications](#) **8**, 76 (2017).
- [41] E. R. MacQuarrie, T. A. Gosavi, N. R. Jungwirth, S. A. Bhave, and G. D. Fuchs, *Mechanical Spin Control of Nitrogen-Vacancy Centers in Diamond*, [Physical Review Letters](#) **111**, 227602 (2013).
- [42] P. Ouartchaiyapong, K. W. Lee, B. A. Myers, and A. C. Bleszynski Jayich, *Dynamic strain-mediated coupling of a single diamond spin to a mechanical resonator*, [Nature Communications](#) **5**, 4429 (2014).
- [43] M. W. Doherty, N. B. Manson, P. Delaney, F. Jelezko, J. Wrachtrup, and L. C. Hollenberg, *The nitrogen-vacancy colour centre in diamond*, [Physics Reports](#) **528**, 1 (2013).
- [44] L. Childress and R. Hanson, *Diamond NV centers for quantum computing and quantum networks*, [MRS Bulletin](#) **38**, 134 (2013).
- [45] P. Ouartchaiyapong, L. M. A. Pascal, B. A. Myers, P. Lauria, and A. C. Bleszynski Jayich, *High quality factor single-crystal diamond mechanical resonators*, [Applied Physics Letters](#) **101**, 163505 (2012).
- [46] Y. Tao and C. Degen, *Facile Fabrication of Single-Crystal-Diamond Nanostructures with Ultrahigh Aspect Ratio*, [Advanced Materials](#) **25**, 3962 (2013).
- [47] Y. Tao, J. M. Boss, B. A. Moores, and C. L. Degen, *Single-crystal diamond nanomechanical resonators with quality factors exceeding one million*, [Nature Communications](#) **5**, 3638 (2014).
- [48] P. Rabl, S. J. Kolkowitz, F. H. L. Koppens, J. G. E. Harris, P. Zoller, and M. D. Lukin, *A quantum spin transducer based on nanoelectromechanical resonator arrays*, [Nature Physics](#) **6**, 602 (2010).
- [49] K. V. Kepesidis, S. D. Bennett, S. Portolan, M. D. Lukin, and P. Rabl, *Phonon cooling and lasing with nitrogen-vacancy centers in diamond*, [Physical Review B](#) **88**, 064105 (2013).
- [50] J. H. N. Loubser and J. A. van Wyk, *Electron spin resonance in the study of diamond*, [Reports on Progress in Physics](#) **41**, 1201 (1978).
- [51] J. R. Maze, A. Gali, E. Togan, Y. Chu, A. Trifonov, E. Kaxiras, and M. D. Lukin, *Properties of nitrogen-vacancy centers in diamond: the group theoretic approach*, [New Journal of Physics](#) **13**, 025025 (2011).
- [52] A. Gali, M. Fyta, and E. Kaxiras, *Ab initio supercell calculations on nitrogen-vacancy center in diamond: Electronic structure and hyperfine tensors*, [Physical Review B](#) **77**, 155206 (2008).

-
- [53] F. Dolde, H. Fedder, M. W. Doherty, T. Nöbauer, F. Rempp, G. Balasubramanian, T. Wolf, F. Reinhard, L. C. L. Hollenberg, F. Jelezko, and J. Wrachtrup, *Electric-field sensing using single diamond spins*, [Nature Physics](#) **7**, 459 (2011).
- [54] K. Fang, V. M. Acosta, C. Santori, Z. Huang, K. M. Itoh, H. Watanabe, S. Shikata, and R. G. Beausoleil, *High-Sensitivity Magnetometry Based on Quantum Beats in Diamond Nitrogen-Vacancy Centers*, [Physical Review Letters](#) **110**, 130802 (2013).
- [55] A. Batalov, V. Jacques, F. Kaiser, P. Siyushev, P. Neumann, L. J. Rogers, R. L. McMurtrie, N. B. Manson, F. Jelezko, and J. Wrachtrup, *Low Temperature Studies of the Excited-State Structure of Negatively Charged Nitrogen-Vacancy Color Centers in Diamond*, [Physical Review Letters](#) **102**, 195506 (2009).
- [56] P. Neumann, R. Kolesov, V. Jacques, J. Beck, J. Tisler, A. Batalov, L. Rogers, N. B. Manson, G. Balasubramanian, F. Jelezko, and J. Wrachtrup, *Excited-state spectroscopy of single NV defects in diamond using optically detected magnetic resonance*, [New Journal of Physics](#) **11**, 013017 (2009).
- [57] G. D. Fuchs, V. V. Dobrovitski, R. Hanson, A. Batra, C. D. Weis, T. Schenkel, and D. D. Awschalom, *Excited-State Spectroscopy Using Single Spin Manipulation in Diamond*, [Physical Review Letters](#) **101**, 117601 (2008).
- [58] P. Tamarat, N. B. Manson, J. P. Harrison, R. L. McMurtrie, A. Nizovtsev, C. Santori, R. G. Beausoleil, P. Neumann, T. Gaebel, F. Jelezko, P. Hemmer, and J. Wrachtrup, *Spin-flip and spin-conserving optical transitions of the nitrogen-vacancy centre in diamond*, [New Journal of Physics](#) **10**, 045004 (2008).
- [59] M. Steiner, P. Neumann, J. Beck, F. Jelezko, and J. Wrachtrup, *Universal enhancement of the optical readout fidelity of single electron spins at nitrogen-vacancy centers in diamond*, [Physical Review B](#) **81**, 035205 (2010).
- [60] P. Maletinsky, S. Hong, M. S. Grinolds, B. Hausmann, M. D. Lukin, R. L. Walsworth, M. Lončar, and A. Yacoby, *A robust scanning diamond sensor for nanoscale imaging with single nitrogen-vacancy centres*, [Nature Nanotechnology](#) **7**, 320 (2012).
- [61] P. Appel, M. Ganzhorn, E. Neu, and P. Maletinsky, *Nanoscale microwave imaging with a single electron spin in diamond*, [New Journal of Physics](#) **17**, 112001 (2015).
- [62] L. Thiel, D. Rohner, M. Ganzhorn, P. Appel, E. Neu, B. Müller, R. Kleiner, D. Koelle, and P. Maletinsky, *Quantitative nanoscale vortex imaging using a cryogenic quantum magnetometer*, [Nature Nanotechnology](#) **11**, 677 (2016).
- [63] M. V. G. Dutt, L. Childress, L. Jiang, E. Togan, J. Maze, F. Jelezko, A. S. Zibrov, P. R. Hemmer, and M. D. Lukin, *Quantum Register Based on Individual Electronic and Nuclear Spin Qubits in Diamond*, [Science](#) **316**, 1312 (2007).

- [64] T. van der Sar, Z. H. Wang, M. S. Blok, H. Bernien, T. H. Taminiau, D. M. Toyli, D. A. Lidar, D. D. Awschalom, R. Hanson, and V. V. Dobrovitski, *Decoherence-protected quantum gates for a hybrid solid-state spin register*, [Nature](#) **484**, 82 (2012).
- [65] B. Hensen, H. Bernien, A. E. Dreau, A. Reiserer, N. Kalb, M. S. Blok, J. Ruitenbergh, R. F. L. Vermeulen, R. N. Schouten, C. Abellan, W. Amaya, V. Pruneri, M. W. Mitchell, M. Markham, D. J. Twitchen, D. Elkouss, S. Wehner, T. H. Taminiau, and R. Hanson, *Loophole-free Bell inequality violation using electron spins separated by 1.3 kilometres*, [Nature](#) **526**, 682 (2015).
- [66] A. Batalov, C. Zierl, T. Gaebel, P. Neumann, I.-Y. Chan, G. Balasubramanian, P. R. Hemmer, F. Jelezko, and J. Wrachtrup, *Temporal Coherence of Photons Emitted by Single Nitrogen-Vacancy Defect Centers in Diamond Using Optical Rabi-Oscillations*, [Physical Review Letters](#) **100**, 077401 (2008).
- [67] L. Robledo, H. Bernien, T. van der Sar, and R. Hanson, *Spin dynamics in the optical cycle of single nitrogen-vacancy centres in diamond*, [New Journal of Physics](#) **13**, 025013 (2011).
- [68] N. B. Manson, J. P. Harrison, and M. J. Sellars, *Nitrogen-vacancy center in diamond: Model of the electronic structure and associated dynamics*, [Physical Review B](#) **74**, 104303 (2006).
- [69] M. L. Goldman, A. Sipahigil, M. W. Doherty, N. Y. Yao, S. D. Bennett, M. Markham, D. J. Twitchen, N. B. Manson, A. Kubanek, and M. D. Lukin, *Phonon-Induced Population Dynamics and Intersystem Crossing in Nitrogen-Vacancy Centers*, [Physical Review Letters](#) **114**, 145502 (2015).
- [70] I. I. Rabi, *Space Quantization in a Gyating Magnetic Field*, [Physical Review](#) **51**, 652 (1937).
- [71] A. Schweiger and G. Jeschke, *Principles of pulse electron paramagnetic resonance* (Oxford University Press) (2005).
- [72] G. Grynberg, A. Aspect, and C. Fabre, *Introduction to Quantum Optics: From the Semi-classical Approach to Quantized Light* (Cambridge University Press) (2010).
- [73] M. Fox, *Quantum Optics: An introduction* (Oxford University Press) (2014).
- [74] C. P. Slichter, *Principles of Magnetic Resonance*, [volume 1 \(Springer-Verlag Berlin Heidelberg\)](#), 3 edition (1990).
- [75] J. M. Chowning, *The Synthesis of Complex Audio Spectra by Means of Frequency Modulation*, [Computer Music Journal](#) **1**, pp. 46 (1977).
- [76] P. Rabl, P. Cappellaro, M. V. G. Dutt, L. Jiang, J. R. Maze, and M. D. Lukin, *Strong magnetic coupling between an electronic spin qubit and a mechanical resonator*, [Physical Review B](#) **79**, 041302 (2009).

-
- [77] S. Hong, M. S. Grinolds, P. Maletinsky, R. L. Walsworth, M. D. Lukin, and A. Yacoby, *Coherent, Mechanical Control of a Single Electronic Spin*, [Nano Letters](#) **12**, 3920 (2012).
- [78] B. Pigeau, S. Rohr, L. Mercier de Lepinay, A. Glippe, V. Jacques, and O. Arcizet, *Observation of a phononic Mollow triplet in a multimode hybrid spin-nanomechanical system*, [Nature Communications](#) **6**, 8603 (2015).
- [79] S. Rohr, E. Dupont-Ferrier, B. Pigeau, P. Verlot, V. Jacques, and O. Arcizet, *Synchronizing the Dynamics of a Single Nitrogen Vacancy Spin Qubit on a Parametrically Coupled Radio-Frequency Field through Microwave Dressing*, [Physical Review Letters](#) **112**, 010502 (2014).
- [80] L. Allen and J. H. Eberly, *Optical Resonance and Two-Level Atoms* (Dover Publications, New York) (1987).
- [81] A. Jarmola, V. M. Acosta, K. Jensen, S. Chemerisov, and D. Budker, *Temperature- and Magnetic-Field-Dependent Longitudinal Spin Relaxation in Nitrogen-Vacancy Ensembles in Diamond*, [Physical Review Letters](#) **108**, 197601 (2012).
- [82] T. Rosskopf, A. Dussaux, K. Ohashi, M. Loretz, R. Schirhagl, H. Watanabe, S. Shikata, K. M. Itoh, and C. L. Degen, *Investigation of Surface Magnetic Noise by Shallow Spins in Diamond*, [Physical Review Letters](#) **112**, 147602 (2014).
- [83] Y. Romach, C. Müller, T. Unden, L. J. Rogers, T. Isoda, K. M. Itoh, M. Markham, A. Stacey, J. Meijer, S. Pezzagna, B. Naydenov, L. P. McGuinness, N. Bar-Gill, and F. Jelezko, *Spectroscopy of Surface-Induced Noise Using Shallow Spins in Diamond*, [Physical Review Letters](#) **114**, 017601 (2015).
- [84] S. Kolkowitz, A. Safira, A. A. High, R. C. Devlin, S. Choi, Q. P. Unterreithmeier, D. Patterson, A. S. Zibrov, V. E. Manucharyan, H. Park, and M. D. Lukin, *Probing Johnson noise and ballistic transport in normal metals with a single-spin qubit*, [Science](#) **347**, 1129 (2015).
- [85] S. Rohr, *Hybrid spin-nanomechanical systems in parametric Interaction*, Ph.D. thesis, Université de Grenoble (2014).
- [86] G. Ithier, E. Collin, P. Joyez, P. J. Meeson, D. Vion, D. Esteve, F. Chiarello, A. Shnirman, Y. Makhlin, J. Schrieffer, and G. Schön, *Decoherence in a superconducting quantum bit circuit*, [Physical Review B](#) **72**, 134519 (2005).
- [87] B. A. Myers, A. Das, M. C. Dartiaillh, K. Ohno, D. D. Awschalom, and A. C. Bleszynski Jayich, *Probing Surface Noise with Depth-Calibrated Spins in Diamond*, [Physical Review Letters](#) **113**, 027602 (2014).
- [88] M. Kim, H. J. Mamin, M. H. Sherwood, K. Ohno, D. D. Awschalom, and D. Rugar, *Decoherence of Near-Surface Nitrogen-Vacancy Centers Due to Electric Field Noise*, [Physical Review Letters](#) **115**, 087602 (2015).

-
- [89] N. Bar-Gill, L. Pham, A. Jarmola, D. Budker, and R. Walsworth, *Solid-state electronic spin coherence time approaching one second*, [Nature Communications](#) **4**, 1743 (2013).
- [90] A. Dréau, M. Lesik, L. Rondin, P. Spinicelli, O. Arcizet, J.-F. Roch, and V. Jacques, *Avoiding power broadening in optically detected magnetic resonance of single NV defects for enhanced dc magnetic field sensitivity*, [Physical Review B](#) **84**, 195204 (2011).
- [91] G. Davies and M. F. Hamer, *Optical Studies of the 1.945 eV Vibronic Band in Diamond*, [Proceedings of the Royal Society of London A: Mathematical, Physical and Engineering Sciences](#) **348**, 285 (1976).
- [92] M. W. Doherty, V. V. Struzhkin, D. A. Simpson, L. P. McGuinness, Y. Meng, A. Stacey, T. J. Karle, R. J. Hemley, N. B. Manson, L. Hollenberg, Lloyd C. and S. Praver, *Electronic Properties and Metrology Applications of the Diamond NV Center under Pressure*, [Physical Review Letters](#) **112**, 047601 (2014).
- [93] L. J. Rogers, S. Armstrong, M. J. Sellars, and N. B. Manson, *Infrared emission of the NV centre in diamond: Zeeman and uniaxial stress studies*, [New Journal of Physics](#) **10**, 103024 (2008).
- [94] L. J. Rogers, M. W. Doherty, M. S. J. Barson, S. Onoda, T. Ohshima, and N. B. Manson, *Singlet levels of the NV centre in diamond*, [New Journal of Physics](#) **17**, 013048 (2015).
- [95] I. Wilson-Rae, P. Zoller, and A. Imamoglu, *Laser Cooling of a Nanomechanical Resonator Mode to its Quantum Ground State*, [Physical Review Letters](#) **92**, 075507 (2004).
- [96] P. Rabl, *Cooling of mechanical motion with a two-level system: The high-temperature regime*, [Physical Review B](#) **82**, 165320 (2010).
- [97] S. Meesala, Y.-I. Sohn, H. A. Atikian, S. Kim, M. J. Burek, J. T. Choy, and M. Lončar, *Enhanced Strain Coupling of Nitrogen-Vacancy Spins to Nanoscale Diamond Cantilevers*, [Physical Review Applied](#) **5**, 034010 (2016).
- [98] E. R. MacQuarrie, M. Otten, S. K. Gray, and G. D. Fuchs, *Cooling a mechanical resonator with nitrogen-vacancy centres using a room temperature excited state spinstrain interaction*, [Nature Communications](#) **8**, 14358 (2017).
- [99] A. Barfuss, J. Teissier, E. Neu, A. Nunnenkamp, and P. Maletinsky, *Strong mechanical driving of a single electron spin*, [Nature Physics](#) **11**, 820 (2015).
- [100] E. R. MacQuarrie, T. A. Gosavi, A. M. Moehle, N. R. Jungwirth, S. A. Bhave, and G. D. Fuchs, *Coherent control of a nitrogen-vacancy center spin ensemble with a diamond mechanical resonator*, [Optica](#) **2**, 233 (2015).
- [101] E. R. MacQuarrie, T. A. Gosavi, S. A. Bhave, and G. D. Fuchs, *Continuous dynamical decoupling of a single diamond nitrogen-vacancy center spin with a mechanical resonator*, [Physical Review B](#) **92**, 224419 (2015).

-
- [102] J. Teissier, A. Barfuss, and P. Maletinsky, *Hybrid continuous dynamical decoupling: a photon-phonon doubly dressed spin*, [Journal of Optics](#) **19**, 044003 (2017).
- [103] M. S. J. Barson, P. Peddibhotla, P. Ovartchaiyapong, K. Ganesan, R. L. Taylor, M. Gebert, Z. Mielens, B. Koslowski, D. A. Simpson, L. P. McGuinness, J. McCallum, S. Prawer, S. Onoda, T. Ohshima, A. C. Bleszynski Jayich, F. Jelezko, N. B. Manson, and M. W. Doherty, *Nanomechanical Sensing Using Spins in Diamond*, [Nano Letters](#) **17**, 1496 (2017).
- [104] F. Grazioso, B. R. Patton, P. Delaney, M. L. Markham, D. J. Twitchen, and J. M. Smith, *Measurement of the full stress tensor in a crystal using photoluminescence from point defects: The example of nitrogen vacancy centers in diamond*, [Applied Physics Letters](#) **103**, 101905 (2013).
- [105] K. W. Lee, D. Lee, P. Ovartchaiyapong, J. Minguzzi, J. R. Maze, and A. C. Bleszynski Jayich, *Strain Coupling of a Mechanical Resonator to a Single Quantum Emitter in Diamond*, [Physical Review Applied](#) **6**, 034005 (2016).
- [106] M. W. Doherty, F. Dolde, H. Fedder, F. Jelezko, J. Wrachtrup, N. B. Manson, and L. C. L. Hollenberg, *Theory of the ground-state spin of the NV center in diamond*, [Physical Review B](#) **85**, 205203 (2012).
- [107] M. W. Doherty, N. B. Manson, P. Delaney, and L. C. L. Hollenberg, *The negatively charged nitrogen-vacancy centre in diamond: the electronic solution*, [New Journal of Physics](#) **13**, 025019 (2011).
- [108] R. Gross and A. Marx, *Festkörperphysik* (De Gruyter Oldenbourg) (2012).
- [109] W. Voigt, *Lehrbuch der Kristallphysik*, ([Vieweg+Teubner Verlag](#)) (1966).
- [110] A. N. Cleland, *Foundations of Nanomechanics - From Solid-State Theory to Device Applications* (Springer-Verlag Berlin Heidelberg) (2003).
- [111] A. E. Hughes and W. A. Runciman, *Uniaxial stress splitting of doubly degenerate states of tetragonal and trigonal centres in cubic crystals*, [Proceedings of the Physical Society](#) **90**, 827 (1967).
- [112] I. K. Ludlow, *Spin-orbit coupling and stress spectra of trigonal colour centres in magnesium oxide*, [Journal of Physics C: Solid State Physics](#) **1**, 1194 (1968).
- [113] R. T. Fenner and J. N. Reddy, *Mechanics of Solids and Structures* (CRS Press Taylor & Francis Group) (2012).
- [114] I. H. Shames and F. A. Cozzarelli, *Elastic and Inelastic Stress Analysis* (Prentice-Hall International, Inc.) (1992).
- [115] B. D. Hauer, C. Doolin, K. S. D. Beach, and J. P. Davis, *A general procedure for thermomechanical calibration of nano/micro-mechanical resonators*, [Annals of Physics](#) **339**, 181 (2013).
- [116] W. Känzig, *Mechanik und Wellenlehre* (vdf Hochschulverlag AG) (1994).

-
- [117] S. Buckle, S. Barnett, P. Knight, M. Lauder, and D. Pegg, *Atomic Interferometers*, [Optica Acta: International Journal of Optics](#) **33**, 1129 (1986).
- [118] S. D. Bennett, N. Y. Yao, J. Otterbach, P. Zoller, P. Rabl, and M. D. Lukin, *Phonon-Induced Spin-Spin Interactions in Diamond Nanostructures: Application to Spin Squeezing*, [Physical Review Letters](#) **110**, 156402 (2013).
- [119] P. Appel, E. Neu, M. Ganzhorn, A. Barfuss, M. Batzer, M. Gratz, A. Tschöpe, and P. Maletinsky, *Fabrication of all diamond scanning probes for nanoscale magnetometry*, [Review of Scientific Instruments](#) **87**, 063703 (2016).
- [120] J. F. Ziegler, J. P. Biersack, and M. D. Ziegler, *SRIM - The Stopping and Range of Ions in Matter*, (2015).
- [121] M. Minsky, *Memoir on inventing the confocal scanning microscope*, [Scanning](#) **10**, 128 (1988).
- [122] A. Gruber, A. Dräbenstedt, C. Tietz, L. Fleury, J. Wrachtrup, and C. v. Borczyskowski, *Scanning Confocal Optical Microscopy and Magnetic Resonance on Single Defect Centers*, [Science](#) **276**, 2012 (1997).
- [123] L. Thiel, *Setup to observe Electron Spin Resonance in Nitrogen Vacancy centers*, Master's thesis, University of Basel (2013).
- [124] R. H. Webb, *Confocal optical microscopy*, [Reports on Progress in Physics](#) **59**, 427 (1996).
- [125] D. Leibfried, R. Blatt, C. Monroe, and D. Wineland, *Quantum dynamics of single trapped ions*, [Reviews of Modern Physics](#) **75**, 281 (2003).
- [126] G. D. Fuchs, V. V. Dobrovitski, D. M. Toyli, F. J. Heremans, and D. D. Awschalom, *Gigahertz Dynamics of a Strongly Driven Single Quantum Spin*, [Science](#) **326**, 1520 (2009).
- [127] N. Bar-Gill, L. Pham, C. Belthangady, D. Le Sage, P. Cappellaro, J. Maze, M. Lukin, A. Yacoby, and R. Walsworth, *Suppression of spin-bath dynamics for improved coherence of multi-spin-qubit systems*, [Nature Communications](#) **3**, 858 (2012).
- [128] F. F. Fanchini, J. E. M. Hornos, and R. d. J. Napolitano, *Continuously decoupling single-qubit operations from a perturbing thermal bath of scalar bosons*, [Physical Review A](#) **75**, 022329 (2007).
- [129] D. A. Golter, T. K. Baldwin, and H. Wang, *Protecting a Solid-State Spin from Decoherence Using Dressed Spin States*, [Physical Review Letter](#) **113**, 237601 (2014).
- [130] G. de Lange, Z. H. Wang, D. Rist, V. V. Dobrovitski, and R. Hanson, *Universal Dynamical Decoupling of a Single Solid-State Spin from a Spin Bath*, [Science](#) **330**, 60 (2010).

-
- [131] J.-M. Cai, B. Naydenov, R. Pfeiffer, L. P. McGuinness, K. D. Jahnke, F. Jelezko, M. B. Plenio, and A. Retzker, *Robust dynamical decoupling with concatenated continuous driving*, [New Journal of Physics](#) **14**, 113023 (2012).
- [132] J. R. Maze, A. Dréau, V. Waselowski, H. Duarte, J.-F. Roch, and V. Jacques, *Free induction decay of single spins in diamond*, [New Journal of Physics](#) **14**, 103041 (2012).
- [133] C. Cohen-Tannoudji, J. Dupont-Roc, and G. Grynberg, *Atom-Photon Interactions: Basic Processes and Applications* (WILEY-VCH Verlag GmbH & KGaA) (2004).
- [134] P. Jamonneau, M. Lesik, J. P. Tetienne, I. Alvizu, L. Mayer, A. Dréau, S. Kosen, J.-F. Roch, S. Pezzagna, J. Meijer, T. Teraji, Y. Kubo, P. Bertet, J. R. Maze, and V. Jacques, *Competition between electric field and magnetic field noise in the decoherence of a single spin in diamond*, [Physical Review B](#) **93**, 024305 (2016).
- [135] S. Nadj-Perge, S. M. Frolov, E. P. A. M. Bakkers, and L. P. Kouwenhoven, *Spin-orbit qubit in a semiconductor nanowire*, [Nature](#) **468**, 1084 (2010).
- [136] W. D. Oliver, Y. Yu, J. C. Lee, K. K. Berggren, L. S. Levitov, and T. P. Orlando, *Mach-Zehnder Interferometry in a Strongly Driven Superconducting Qubit*, [Science](#) **310**, 1653 (2005).
- [137] P. London, P. Balasubramanian, B. Naydenov, L. P. McGuinness, and F. Jelezko, *Strong driving of a single spin using arbitrarily polarized fields*, [Physical Review A](#) **90**, 012302 (2014).
- [138] J. Tuorila, M. Silveri, M. Sillanpää, E. Thuneberg, Y. Makhlin, and P. Hakonen, *Stark Effect and Generalized Bloch-Siegert Shift in a Strongly Driven Two-Level System*, [Physical Review Letters](#) **105**, 257003 (2010).
- [139] M. Silveri, J. Tuorila, M. Kemppainen, and E. Thuneberg, *Probe spectroscopy of quasienergy states*, [Physical Review B](#) **87**, 134505 (2013).
- [140] X. Xu, Z. Wang, C. Duan, P. Huang, P. Wang, Y. Wang, N. Xu, X. Kong, F. Shi, X. Rong, and J. Du, *Coherence-Protected Quantum Gate by Continuous Dynamical Decoupling in Diamond*, [Physical Review Letters](#) **109**, 070502 (2012).
- [141] J. Danon and M. S. Rudner, *Multilevel Interference Resonances in Strongly Driven Three-Level Systems*, [Physical Review Letters](#) **113**, 247002 (2014).
- [142] S. H. Autler and C. H. Townes, *Stark Effect in Rapidly Varying Fields*, [Physical Review](#) **100**, 703 (1955).
- [143] G. Wrigge, I. Gerhardt, J. Hwang, G. Zumofen, and V. Sandoghdar, *Efficient coupling of photons to a single molecule and the observation of its resonance fluorescence*, [Nature Physics](#) **4**, 60 (2008).

- [144] X. Xu, B. Sun, P. R. Berman, D. G. Steel, A. S. Bracker, D. Gammon, and L. J. Sham, *Coherent Optical Spectroscopy of a Strongly Driven Quantum Dot*, [Science](#) **317**, 929 (2007).
- [145] M. Baur, S. Filipp, R. Bianchetti, J. M. Fink, M. Göppl, L. Steffen, P. J. Leek, A. Blais, and A. Wallraff, *Measurement of Autler-Townes and Mollow Transitions in a Strongly Driven Superconducting Qubit*, [Physical Review Letters](#) **102**, 243602 (2009).
- [146] F. Bloch and A. Siegert, *Magnetic Resonance for Nonrotating Fields*, [Physical Review](#) **57**, 522 (1940).
- [147] M. Fleischhauer, A. Imamoglu, and J. P. Marangos, *Electromagnetically induced transparency: Optics in coherent media*, [Review of Modern Physics](#) **77**, 633 (2005).
- [148] H. R. Gray, R. M. Whitley, and C. R. Stroud, *Coherent trapping of atomic populations*, [Optics Letters](#) **3**, 218 (1978).
- [149] E. Arimondo, *V Coherent Population Trapping in Laser Spectroscopy*, [Progress in Optics](#), volume 35, pp. 257 – 354 (Elsevier) (1996).
- [150] B. D. Agap'ev, M. B. Gornyy, B. G. Matisov, and Y. V. Rozhdestvenski, *Coherent population trapping in quantum systems*, [Physics-Uspekhi](#) **36**, 763 (1993).
- [151] D. F. Phillips, A. Fleischhauer, A. Mair, R. L. Walsworth, and M. D. Lukin, *Storage of Light in Atomic Vapor*, [Physical Review Letters](#) **86**, 783 (2001).
- [152] J. Kitching, S. Knappe, M. Vukicevic, L. Hollberg, R. Wynands, and W. Weidmann, *A microwave frequency reference based on VCSEL-driven dark line resonances in Cs vapor*, [IEEE Transactions on Instrumentation and Measurement](#) **49**, 1313 (2000).
- [153] J. Vanier, *Atomic clocks based on coherent population trapping: a review*, [Applied Physics B](#) **81**, 421 (2005).
- [154] K. Bergmann, H. Theuer, and B. W. Shore, *Coherent population transfer among quantum states of atoms and molecules*, [Review of Modern Physics](#) **70**, 1003 (1998).
- [155] K. Bergmann, N. V. Vitanov, and B. W. Shore, *Perspective: Stimulated Raman adiabatic passage: The status after 25 years*, [The Journal of Chemical Physics](#) **142**, 170901 (2015).
- [156] B. W. Shore, *Manipulating Quantum Structures Using Laser Pulses* (Cambridge University Press) (2011).
- [157] D. Kosachiov, B. Matisov, and Y. Rozhdestvensky, *Coherent population trapping: sensitivity of an atomic system to the relative phase of exciting fields*, [Optics Communications](#) **85**, 209 (1991).

-
- [158] D. V. Kosachiov, B. G. Matisov, and Y. V. Rozhdestvensky, *Coherent phenomena in multilevel systems with closed interaction contour*, [Journal of Physics B: Atomic, Molecular and Optical Physics](#) **25**, 2473 (1992).
- [159] E. A. Korsunsky, N. Leinfellner, A. Huss, S. Balushev, and L. Windholz, *Phase-dependent electromagnetically induced transparency*, [Physical Review A](#) **59**, 2302 (1999).
- [160] W. Maichen, R. Gaggl, E. Korsunsky, and L. Windholz, *Observation of Phase-Dependent Coherent Population Trapping in Optically Closed Atomic Systems*, [Europhysics Letters](#) **31**, 189 (1995).
- [161] M. S. Shahriar and P. R. Hemmer, *Direct excitation of microwave-spin dressed states using a laser-excited resonance Raman interaction*, [Physical Review Letters](#) **65**, 1865 (1990).
- [162] K. Yamamoto, K. Ichimura, and N. Gemma, *Enhanced and reduced absorptions via quantum interference: Solid system driven by a rf field*, [Physical Review A](#) **58**, 2460 (1998).
- [163] P. Roushan, C. Neill, A. Megrant, Y. Chen, R. Babbush, R. Barends, B. Campbell, Z. Chen, B. Chiaro, A. Dunsworth, A. Fowler, E. Jeffrey, J. Kelly, E. Lucero, J. Mutus, P. J. J. O'Malley, M. Neeley, C. Quintana, D. Sank, A. Vainsencher, J. Wenner, T. White, E. Kapit, H. Neven, and J. Martinis, *Chiral ground-state currents of interacting photons in a synthetic magnetic field*, [Nature Physics](#) **13**, 146 (2017).
- [164] S. Shevchenko, S. Ashhab, and F. Nori, *Landau-Zener-Stückelberg interferometry*, [Physics Reports](#) **492**, 1 (2010).
- [165] A. Baksic, H. Ribeiro, and A. A. Clerk, *Speeding up Adiabatic Quantum State Transfer by Using Dressed States*, [Physical Review Letters](#) **116**, 230503 (2016).
- [166] B. B. Zhou, A. Baksic, H. Ribeiro, C. G. Yale, F. J. Heremans, P. C. Jerger, A. Auer, G. Burkard, A. A. Clerk, and D. D. Awschalom, *Accelerated quantum control using superadiabatic dynamics in a solid-state lambda system*, [Nature Physics](#) **13**, 330 (2017).
- [167] L. Robledo, H. Bernien, I. van Weperen, and R. Hanson, *Control and Coherence of the Optical Transition of Single Nitrogen Vacancy Centers in Diamond*, [Physical Review Letters](#) **105**, 177403 (2010).
- [168] Y. Chu, N. de Leon, B. Shields, B. Hausmann, R. Evans, E. Togan, M. J. Burek, M. Markham, A. Stacey, A. Zibrov, A. Yacoby, D. Twitchen, M. Lončar, H. Park, P. Maletinsky, and M. Lukin, *Coherent Optical Transitions in Implanted Nitrogen Vacancy Centers*, [Nano Letters](#) **14**, 1982 (2014).
- [169] E. Neu, P. Appel, M. Ganzhorn, J. Miguel-Sánchez, M. Lesik, V. Mille, V. Jacques, A. Tallaire, J. Achard, and P. Maletinsky, *Photonic nanostructures on (111)-oriented diamond*, [Applied Physics Letters](#) **104**, 153108 (2014).

- [170] D. A. Golter, T. Oo, M. Amezcua, K. A. Stewart, and H. Wang, *Optomechanical Quantum Control of a Nitrogen-Vacancy Center in Diamond*, [Physical Review Letters](#) **116**, 143602 (2016).
- [171] M. J. Burek, J. D. Cohen, S. M. Meenehan, N. El-Sawah, C. Chia, T. Ruelle, S. Meesala, J. Rochman, H. A. Atikian, M. Markham, D. J. Twitchen, M. D. Lukin, O. Painter, and M. Lončar, *Diamond optomechanical crystals*, [Optica](#) **3**, 1404 (2016).
- [172] M. J. Burek, C. Meuwly, R. E. Evans, M. K. Bhaskar, A. Sipahigil, S. Meesala, B. Machielse, D. D. Sukachev, C. T. Nguyen, J. L. Pacheco, E. Bielejec, M. D. Lukin, and M. Lončar, *Fiber-Coupled Diamond Quantum Nanophotonic Interface*, [Physical Review Applied](#) **8**, 024026 (2017).
- [173] C. Hepp, T. Müller, V. Waselowski, J. N. Becker, B. Pingault, H. Sternschulte, D. Steinmüller-Nethl, A. Gali, J. R. Maze, M. Atatüre, and C. Becher, *Electronic Structure of the Silicon Vacancy Color Center in Diamond*, [Physical Review Letters](#) **112**, 036405 (2014).
- [174] L. J. Rogers, K. D. Jahnke, M. W. Doherty, A. Dietrich, L. P. McGuinness, C. Müller, T. Teraji, H. Sumiya, J. Isoya, N. B. Manson, and F. Jelezko, *Electronic structure of the negatively charged silicon-vacancy center in diamond*, [Physical Review B](#) **89**, 235101 (2014).
- [175] T. Schröder, S. Mouradian, J. Zheng, M. E. Trusheim, M. Walsh, E. H. Chen, L. Li, I. Bayn, and D. Englund, *Review Article: Quantum Nanophotonics in Diamond*, [ArXiv e-prints](#) (2016).
- [176] T. Müller, C. Hepp, B. Pingault, E. Neu, S. Gsell, M. Schreck, H. Sternschulte, D. Steinmüller-Nethl, C. Becher, and M. Atatüre, *Optical signatures of silicon-vacancy spins in diamond*, [Nature Communications](#) **5**, 3328 (2014).
- [177] J. N. Becker, J. Grlitz, C. Arend, M. Markham, and C. Becher, *Ultrafast all-optical coherent control of single silicon vacancy colour centres in diamond*, [Nature Communications](#) **7**, 13512 (2016).
- [178] B. Pingault, D.-D. Jarausch, C. Hepp, L. Klintberg, J. N. Becker, M. Markham, C. Becher, and M. Atatüre, *Coherent control of the silicon-vacancy spin in diamond*, [Nature Communications](#) **8**, 15579 (2017).
- [179] L. J. Rogers, K. D. Jahnke, M. H. Metsch, A. Sipahigil, J. M. Binder, T. Teraji, H. Sumiya, J. Isoya, M. D. Lukin, P. Hemmer, and F. Jelezko, *All-Optical Initialization, Readout, and Coherent Preparation of Single Silicon-Vacancy Spins in Diamond*, [Physical Review Letters](#) **113**, 263602 (2014).
- [180] B. Pingault, J. N. Becker, C. H. H. Schulte, C. Arend, C. Hepp, T. Godde, A. I. Tartakovskii, M. Markham, C. Becher, and M. Atatüre, *All-Optical Formation of Coherent Dark States of Silicon-Vacancy Spins in Diamond*, [Physical Review Letters](#) **113**, 263601 (2014).

-
- [181] L. J. Rogers, K. D. Jahnke, T. Teraji, L. Marseglia, C. Mller, B. Naydenov, H. Schauffert, C. Kranz, J. Isoya, L. P. McGuinness, and F. Jelezko, *Multiple intrinsically identical single-photon emitters in the solid state*, [Nature Communications](#) **5**, 4739 (2014).
- [182] A. Sipahigil, K. D. Jahnke, L. J. Rogers, T. Teraji, J. Isoya, A. S. Zibrov, F. Jelezko, and M. D. Lukin, *Indistinguishable Photons from Separated Silicon-Vacancy Centers in Diamond*, [Physical Review Letters](#) **113**, 113602 (2014).
- [183] K. D. Jahnke, A. Sipahigil, J. M. Binder, M. W. Doherty, M. Metsch, L. J. Rogers, N. B. Manson, M. D. Lukin, and F. Jelezko, *Electronphonon processes of the silicon-vacancy centre in diamond*, [New Journal of Physics](#) **17**, 043011 (2015).
- [184] Y.-I. Sohn, S. Meesala, B. Pingault, H. A. Atikian, J. Holzgrafe, M. Gundogan, C. Stavarakas, M. J. Stanley, A. Sipahigil, J. Choi, M. Zhang, J. L. Pacheco, J. Abraham, E. Bielejec, M. D. Lukin, M. Atatüre, and M. Lončar, *Engineering a diamond spin-qubit with a nano-electro-mechanical system*, [ArXiv e-prints](#) (2017).
- [185] M. L. Goldman, M. W. Doherty, A. Sipahigil, N. Y. Yao, S. D. Bennett, N. B. Manson, A. Kubanek, and M. D. Lukin, *State-selective intersystem crossing in nitrogen-vacancy centers*, [Physical Review B](#) **91**, 165201 (2015).
- [186] D. Pegg, *Two-photon resonance with combined amplitude and frequency modulation*, [Optics Communications](#) **57**, 185 (1986).
- [187] M. M. Mehrabadi, S. C. Cowin, and J. Jaric, *Six-dimensional orthogonal tensorrepresentation of the rotation about an axis in three dimensions*, [International Journal of Solids and Structures](#) **32**, 439 (1995).
- [188] B. Schottstaedt, *The Simulation of Natural Instrument Tones using Frequency Modulation with a Complex Modulating Wave*, [Computer Music Journal](#) **1**, pp. 46 (1977).
- [189] V. M. Acosta, E. Bauch, M. P. Ledbetter, A. Waxman, L.-S. Bouchard, and D. Budker, *Temperature Dependence of the Nitrogen-Vacancy Magnetic Resonance in Diamond*, [Physical Review Letters](#) **104**, 070801 (2010).

Acknowledgement

When I came to Basel in October 2013 and joined the Quantum Sensing group, I did not know what to expect. How would it be to live in Basel? Would I get along with my new colleagues and (more importantly) with my new boss? And what about the research I would be doing? Now, about four years later, I am really happy and grateful that Miriam dragged me to this wonderful place in the sunny and warm north of Switzerland. I had a really great time, both in- and outside of the university, I learned a lot and found new friends. In my opinion, the results of a PhD are never just the work of only one person, but reflect the effort of many. I would therefore like to express my gratitude to all members of the Quantum Sensing Group, the administrative and technical staff of the department, my family and my friends for their tireless support during the last four years.

In particular, I would like to thank Patrick Maletinsky for giving me the opportunity to do a PhD in his group. Dear Patrick, I had a wonderful time! Given how little I knew about spin physics and optics, I am still quite surprised you hired me four years ago. It was certainly a good thing that happened to me. I enjoyed your supervision during the last years very much and am grateful for always feeling your support for and your trust in my work. For the future I wish you all the best for your still young group and your personal career (and of course many other PhD students who like playing tricks on you once in a while)! Also, I would like to especially thank the members of team nanomechanics – Jean Teissier, Mark Kasperczyk, Johannes Kölbl and David Jäger – for working together on the same topic under such a nice and productive atmosphere. Jean, thank you very much for teaching me the secrets of all sorts of optical elements and how to properly align them, but also for explaining the basic idea of our experiment to me over and over. I can say that, in contrast to four years ago, I now know what Rabi oscillation are. Johannes, it was a pleasure for me to work with you. Even if you might not think so, I learned a lot from you and am grateful for this experience. Mark, thanks for correcting my endless grammar mistakes and for pushing the quantum Beat. I am pretty sure it would have taken us much longer to publish without your help! A huge *thank you* goes to my fellow PhD student Lucas Thiel. Lucas not only helped me with the measurement software (and even got me interested in programming – at least a little), he also always offered to help when I got stuck. In addition, he managed to bring some variation to my daily life of a PhD student, which I enjoyed very much (I am still wondering how long it took Patrick to find the scotch tape under his mouse AND on his spare batteries). Lucas, thank you very much for four awesome years. I think we became good friends and I will miss the time we had together! I would also like to thank Elke Neu for helping me with fabrication and taking care of the ICP, Brendan Shields for always taking the time to answer one of my numerous questions and Michael Steinacher and Sascha Martin for their help with electronic and mechanical problems. Finally, I would like to thank all SNI PhD

students (especially the INASCON 2015 team) for having a great time at all the SNI events we attended together. Thank you, Claudia and Audrey, for taking care of the administrative work regarding my SNI project!